SYNTHESIS, CHARACTERIZATION AND CATALYTIC STUDIES OF HETEROATOMS INCORPORATED ZnO

A THESIS SUBMITTED TO THE
UNIVERSITY OF PUNE
FOR THE DEGREE OF
DOCTOR OF PHILOSOPHY
IN CHEMISTRY

BY
MAITRI MAPA

CATALYSIS DIVISION
NATIONAL CHEMICAL LABORATORY
PUNE 411 008
INDIA

Dr. CHINNAKONDA S. GOPINATH
(RESEARCH GUIDE)
August 2009

DECLARATION BY RESEARCH SCHOLAR

I hereby declare that the thesis "**Synthesis, Characterization and Catalytic studies of heteroatoms incorporated ZnO"** submitted for the degree of Doctor of Philosophy to the University of Pune has been carried out by me at the Catalysis and Inorganic Chemistry Division, National Chemical Laboratory, Pune – 411 008, India, under the supervision of Dr. Chinnakonda S. Gopinath. Such material as has been obtained by other sources has been duly acknowledged in this thesis. I declare that the present work or any part thereof, has not been submitted to any other University for the award of any other degree or diploma.

Date: /08/09   **Maitri Mapa**
Catalysis Division,
National Chemical Laboratory,
Pune 411 008,
Maharashtra,
India

CERTIFICATE BY RESEARCH GUIDE

This is to certify that the work incorporated in the thesis entitled, "**Synthesis, Characterization and Catalytic studies of heteroatoms incorporated ZnO**" submitted by **Maitri Mapa,** for the Degree of **Doctor of Philosophy,** was carried out by the candidate under my supervision in the Catalysis Division, National Chemical Laboratory, Pune – 411 008, India. Such material as has been obtained from other sources has been duly acknowledged in the thesis. To the best of my knowledge, the present work or any part thereof has not been submitted to any other University for the award of any other degree or diploma.

Date: 08/09   **Dr. C. S. Gopinath**
Catalysis Division   **(Research Supervisor)**
National Chemical Laboratory,
Pune 411 008,
Maharashtra,
India

DEDICATED

TO

MY BELOVED PARENTS,

BHAI and SAPTARSHI

Acknowledgement

Table of Content

Chapter 2: Experimental Methods

Chapter 3:Charaterization and Catalytic Activity Studies of [(ZnO$_{1-x}$N$_x$)] and [(ZnO$_{1-x-z}$N$_x$S$_z$)]

Chapter 4: Characterization and Catalytic Activity Studies of Solid Solution of GaN in ZnO [(Zn$_{1-z}$Ga$_z$)(O$_{1-x}$N$_x$)]

Chapter 5: Characterization and Catalytic Activity Studies of Solid Solution of InN in ZnO [$(Zn_{1-z}In_z)(O_{1-x}N_x)$]

Chapter 6: Conclusions and Future Outlook

List of Publications

ABBREVIATIONS

AAS	Atomic Absorption Spectroscopy
BE	Binding Energy
BET	Braunauer-Emmett-Teller
CB	Conduction Band
CVD	Chemical Vapor Deposition
DTA	Differential Thermal Analysis
ECR	Electron Cyclotron Resonance
EDAX	Energy Dispersive Analysis of X-rays
EPR	Electron Paramagnetic Resonance
GC	Gas Chromatography
GSAS	General Structure Analysis System
HTXRD	High Temperature Powder X-ray Diffraction
LRS	Laser Raman Spectroscopy
MBE	Molecular-Beam Epitaxy
MOCVD	Metal Organic Chemical Vapor Deposition
PLD	Pulsed Laser Deposition
PL	Photoluminescence
PVD	Physical Vapor Deposition
SEM	Scanning Electron Microscopy
SIMS	Secondary Ion Mass Spectrometry
SCM	Solution Combustion Method
TG	Thermo Gravimetry
UCV	Unit Cell Volume
VB	Valence Band
WHSV	Weight Hour Space Velocity
XRF	X-ray Fluorescence
XRD	X-ray Diffraction
XPS	X-ray Photoelectron Spectroscopy

Chapter 1
Introduction

1   Introduction

1.1   **General Background**

Catalysis is an experimental fact now; however, it was a subject of debate prior to the introduction of the concept by Berzelius in 1835. He defined catalyst as "*a power of substances that enables to awaken the affinities, which are asleep at reaction temperature by their mere presence and not by their own affinity*" [1]. Throughout the rest of 19th century, the term catalysis remained heavily debated until around 1900; Wilhelm Ostwald proposed its valid definition in terms of the concepts of chemical kinetics. In 1909, Ostwald was awarded the Nobel Prize in chemistry for his contributions to catalysis [2]. Nowadays catalysis has a dramatic impact in our daily life as well as in industrial processes.

Catalysts are materials that change the rate of a chemical reaction but do not change the thermodynamics of the reaction, without undergoing any change in itself. In addition to the remarkable increase in the activity of the reactants, catalyst offers a remarkable selectivity towards the certain desirable reaction products. Often this higher selectivity is of greater importance than increased reactivity since a highly selective process reduces the generation of waste by-products [3].
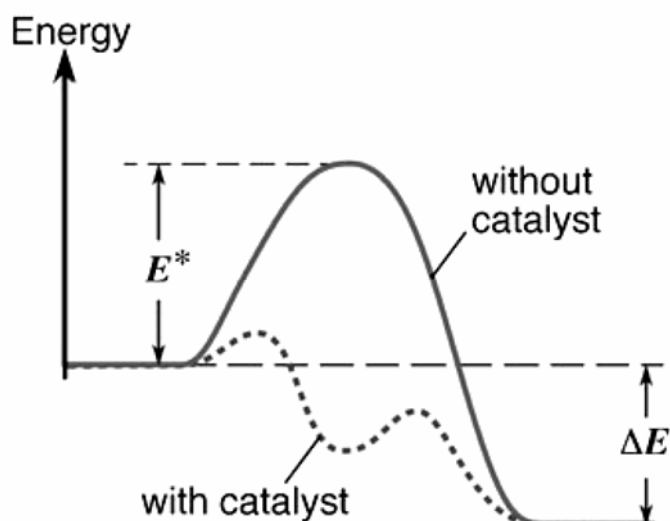
Figure 1.1: *Energy diagram illustrating the progress of a chemical reaction with and without catalyst.*

A chemical reaction involves in breaking of bonds between atoms and the formation of new ones. This process is associated with transformation of energy and the energy diagram illustrating the progress of reaction $A + B \rightarrow C$ is shown in Figure 1.1. The activation energy E^* is usually provided by thermal energy kT, where k is the Boltzmann's constant and T is the temperature. Among all molecular encounters only a fraction given by probability factor $e^{-E^*/kT}$ is usually successful. Hence, the reaction rate can be increased if the activation energy E^* is lowered either by increasing the temperature or by using a catalyst [4].

The catalytic approach is facilitated through the formation of short-lived intermediate compounds. Molecules involved in the reaction provide an alternate reaction path as sketched by the dashed line in Figure 1.1, which is associated with smaller activation barrier and hence, higher in overall reaction rate could be achieved.

Based on phase of the reactant and the catalyst, these can be classified into homogeneous and heterogeneous catalysis. In homogeneous catalysis, both reactant and catalyst are in the same phase (eg, Ziegler Natta polymerization). Generally, homogenous catalysts are such compounds or coordination complexes, which are miscible with the reactants in the reaction medium under reaction condition.

The other type is heterogeneous catalysis where the reactant and catalyst are in different phases. Normally, these catalysts are solids and dispersed in gaseous or liquid reaction mixture, like Haber process and Fischer-Tropsch processes. In the petrochemical alkylation process, both catalyst (acid) and reactant (hydrocarbon) are liquid but exist in different phases. The main advantage of the heterogeneous catalyst over homogeneous catalyst is that, it can be employed continuously in a flow reactor without interruption. Further, the catalyst is present in a different phase from that of the reactants as well as products, so it can be separated very easily from the reaction mass at the end of the reaction.

1.2 Heterogeneous Catalysis

Heterogeneous catalysts cover almost 90% of the industrial catalytic processes. Due to its definite technical advantages, like production process, competitiveness and economy, heterogeneous catalysts are gaining more and more

importance to the world's economy, to convert the inexpensive raw materials into value added fine chemicals and fuel in an economic, environmental efficient manner and also in the production of pharmaceuticals.

These catalysts are sometimes called surface catalysts because the active sites are present on the surface and all the catalytic reactions go on these active sites. Diffusion of the reactant through a boundary layer surrounding the catalyst surface is the first step of any heterogeneously catalyzed process. This is followed by the adsorption of the reactant molecules on the active sites of the catalyst surface. The atoms in the surface layer of a solid have fewer neighbors than those in the bulk, hence are chemically unsaturated. These atoms may form new bonds (chemisorptions) with suitable molecules impinging from the adjacent gas or liquid phase. Adsorption is the main step of any heterogeneously catalyzed reaction. The formed surface species may jump from one site to neighboring ones to react with others to form new adsorption complex. Then the new complexes decompose and the reaction products leave the catalyst surface (desorption). The activity of a heterogeneous catalyst is defined by the number of revolutions of the catalytic cycle per unit time.

In addition to the fundamental properties that define the efficiency of a heterogeneous catalyst, i.e. activity and selectivity, industrial application requires that should be (i) regenerable, (ii) thermally and mechanically stable, (iii) reproducible, (iv) economical, i.e. inexpensive, can be prepared from cheap raw material, (v) suitable morphological characteristics like high surface area, high number of active sites per unit area and crystallinity.

Heterogeneous catalyst can either be metal (noble/non-noble/transition), semiconductor or metal oxides which in term may be crystalline or amorphous. Each type has its own merits and demerits based on their application.

1.3 Metal Oxides as Catalysts

Metal oxides represent one of the most important and widely employed categories of heterogeneous catalysts either as active phases or as support. The versatility of the use of oxide systems can be seen in many organic reactions like oxidation, hydrogenation, dehydrogenation, condensation, cracking, isomerization

and alkylation etc [5]. Hence, oxide catalysts are important from commercial point of view and have been used for manufacturing many valuable products [6].

Classifying metal oxide catalysts is quite tedious since it involves a variety of crystal systems of different compositions with a wide range of physico-chemical properties. Oxides have an ability to bring about electron- and proton- transfer and they can be used in both redox and acid base reactions. Therefore, depending on their nature, oxide catalysts fall broadly into two general categories either acid/base catalysts or oxidation catalysts.

Acid/base catalysts are mainly those in which the cationic material has a single oxidation state and are mostly insulating in nature. They have stoichiometric M:O ratios. The *s* and *p* group metal oxides and the zeolites fall into this category. Alkali and alkaline earth metal oxides act as base catalyst and these are active and selective for many reactions such as isomerization, dehydrogenation, aldol condensation etc [7]. The *p*-block metal oxides are mainly acid catalyst like alumina, silica, and silica–alumina in their various modified forms and have been evaluated as catalyst for alkylation, acylation and cyclization reactions. Some of the oxides have both acidic and basic properties; these are normally oxides of weakly electropositive metals like ZnO, SnO_2. These amphoteric oxides react as basic oxides with acids and as acidic oxides with bases.

The other type of oxides which is commonly used in oxidation reactions and photocatalysis, are semiconductor or conducting oxides. A semiconductor is a material that has electrical conductivity between those of a conductor and insulator, which is characterized by a filled valence band and an empty conduction band. These are normally transition metal oxides where metal ion has variable oxidation state.

1.3.1 Transition Metal Oxides

Transition metal oxides are extensively used as heterogeneous catalysts for a number of organic transformations such as oxidation, oxidative/non-oxidative dehydrogenation, reduction, ammoxidation, metathesis (production of long chain alkenes), and esterification as well as for water gas shift reaction [8]. The high catalytic activity of transition metal oxides is mainly attributed to their multiple

valences. Transition metal ions exhibit variable oxidation states, due to intrinsic oxidation-reduction processes or by catalytic reactions [9] and that can occur at the same or different cationic sites.

Among the transition metal oxides, superior behavior could be obtained from the catalysts where metal ion species are relatively easy to interchange between two different valence states. This can involve two different oxidation states under reaction conditions as can be found in Fe_2O_3, V_2O_5, TiO_2, CuO or NiO, or the inter conversion between the positive ion and neutral metal, with the more easily reduced oxides such as ZnO and CdO.

1.3.2 **Doped Metal Oxide**

Sometimes metal oxides may not be active enough to achieve the highest performance of any catalytic transformation. To obviate the above limitation doping with suitable heteroatom is required as metal-support interaction helps to change the electronic properties and acid–base properties, thus helps to accomplish the desirable performance. The material chosen as appropriate dopants depends on the atomic properties of both the dopant and the material to be doped. It is believed that doping in metal oxides brings dramatic change in physical and chemical properties of the catalyst. The importance of doping on the catalytic activity of a given material can be understood by considering the following examples.

Oxidation and reduction temperature of any metal can be varied according to the demand in reaction condition by choosing the suitable material to be doped. For example, pure Co_3O_4 gives two reduction peaks at 327ºC and 540ºC. Reported TPR studies demonstrated that cobalt oxides in different environment undergo reduction of Co ion at different temperatures, such as cobalt supported on alumina shows four different reduction regimes. The temperature at which reduction of cobalt ion occurs is strongly influenced not only by the oxidation state of the cobalt, but also by the nature of neighboring metal cations and/or metal oxide phases. In Co and Cu doped on ceria, the presence of neighboring Cu and Ce ions strongly influences the reducibility of Co cations, which can be seen by decrease in reduction temperature of cobalt species in that sample [10]. Co or Cu doped on ceria does not offer good catalytic activity for preferential oxidation of CO under excess hydrogen atmosphere

at low temperature however, copper-cobalt supported on ceria gives the best result. No catalytic poisoning, coking or solid-state transformation of catalyst is observed up to 30 h of reaction time. This gives the evidence for strong synergism between Co and Cu supported on ceria catalyst. Sometime metal support interaction can help to keep dopants present in its unusual oxidation state. Further, metal can be active in its zero oxidation state, but lack in stability could be solved by choosing a proper support.

Change in Electronic Structure: Band gap of material can also be tuned by proper choice of dopants. In visible light, metal oxides may not show its desirable photocatalytic activity; however, by doping proper element, band gap can be lowered to make material active under visible light [11]. For example, though the presence of metal ions in titania (TiO_2) does not modify the position of the valence band edge, it introduces new energy levels into the band gap of TiO_2 which can be confirmed from the relative positions of metal (*d* and *f*) and O ($2p$) levels obtained from the X-ray photoelectron spectroscopy (XPS) [12].

By suitable doping, thermal stability of the material can be enhanced by means of improving the mechanical strength of unstable phase of materials. Improvements in thermal stability of smaller size alumina crystallites are obtained by incorporating yttrium species during the aerogel preparation. When temperature increases, the presence of yttrium significantly delays the lattice rearrangement in new phase(s), as normally experienced by the undoped alumina. Incorporation of Ni in cobalt oxide lattice enhances its electrical conductivity, but due to tetragonal distortion in the spinel structure, the thermal stability decreases. In contrast, zinc does not affect the cubic structure of the spinel and steadily improves the thermal stability with increased doping concentration.

Photo catalyzed reactions are normally governed by semiconductor catalysts [13]. The high rate of electron–hole pair recombination in semiconductor photocatalysts reduces catalytic activity. To overcome this disadvantage, noble metal such as Pt, Rh, Pd or Ru can be loaded on the semiconductor surfaces. When semiconductor is doped with suitable metal, the rate of electron transfer to metal is faster than that to semiconductor. This effect decreases the rate of recombination of electron–hole pair, which in turn, increases the efficiency of photocatalytic activity in degradation of dye or water splitting reactions. The photocatalytic activity varies with

parameters like nature of metal, way of loading, extent of loading and nature of semiconductor. Normally, the amount of metal loading varies from 0.1 to 1 % to obtain the optimum activity [14]. Higher metal loading causes very narrow space charge region which hinders the penetration of light in the catalyst.

Among the semiconductor photocatalysts, TiO_2 is widely used both as oxidation catalyst like CO oxidation reaction as well as photocatalyst in water splitting reaction. Due to faster electron transfer to molecular oxygen, TiO_2 is found to be efficient for photocatalytic degradation of pollutants, however, doping by noble metal in TiO_2 makes it more effective [15]. ZnO appears to be a suitable alternative to TiO_2 since its photo degradation mechanism has been proven to be similar as that of TiO_2.

ZnO belongs to II-VI binary compound semiconductors where Zn is group-II element and oxygen belongs to group-VI. ZnO exhibits a unique property of wide band-gap (3.37 eV) that is suitable for short wavelength optoelectronic material [16] and for photocatalytic applications under UV radiation. Consistently, it is becoming a key technological material, as it is inexpensive, non-hazardous, easily preparable, mechanically hard and optically active even with high dislocation densities. Except few fields like oxidative reforming of CH_3OH and water gas shift reaction, ZnO has not considerably been explored as a catalyst.

1.4 Zinc Oxide (ZnO)

Research on the ZnO crystal has been continued for many decades due to its use as a commodity chemical and also for possessing unique physical properties. The non-centro-symmetric nature of Wurtzite, combined with large electromechanical coupling, results in strong piezo-electric and pyro-electric properties which enable ZnO to be used in mechanical actuators, field emission and piezoelectric sensors. ZnO has electron conductivity and transparent conducting oxide properties. Thin polycrystalline ZnO is a popular transparent conductor being used in solar cell contacts and flat panel displays. Therefore, ZnO has versatile applications ranging from catalysis, gas sensing, UV light emitters, ceramic varsitors, transparent high power electronics, surface acoustic wave devices and piezoelectric transducers. Moreover, raw materials for its production are abundant in the earth's crust and are

nontoxic. Suitable doping of heteroatoms either in the place of zinc (Zn) or oxygen (O) can widen the application domain of ZnO [17]. Preparation procedures of ZnO differ based on their applications. A detailed discussion on preparations and the role of ZnO as a catalyst are presented at the end of the section.

1.4.1 **Structure of Zinc Oxide**

Most of the group-II-VI binary compound semiconductors crystallize in either cubic zinc-blend or hexagonal Wurtzite structure where each anion is surrounded by four cations at the corners of a tetrahedron and vice versa. The structure of ZnO can generally be described as a number of alternating planes composed of tetrahedrally coordinated O^{2-} and Zn^{2+} ions, stacked alternately along the *c*-axis. Though tetrahedral coordination is in typically sp^3 covalent bonding, however, these materials also have a substantial ionic character. Ionicity resides at the borderline between covalent and ionic semiconductor.

(a) (b) (c)
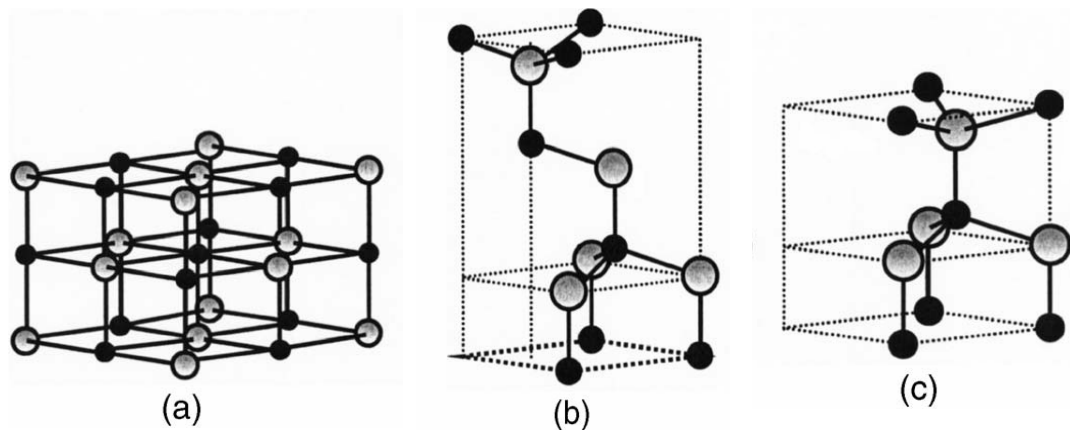
Figure 1.2: *Stick and ball representation of ZnO crystal structures: (a) cubic rock salt (B1), (b) cubic zincblende (B3), and (c) hexagonal Wurtzite (B4). The shaded gray and black spheres denote Zn and O atoms, respectively.*

The crystal structures present in ZnO are (a) cubic rock salt, (b) cubic zincblende and (c) hexagonal Wurtzite, as schematically shown in Figure 1.2. Jaffe and Hess [18] described the ground-state total energy of ZnO in Wurtzite, zinc-blend, and rock salt phases as a function of unit cell volume. The total energy in ZnO crystals was calculated to be -5.658 eV for Wurtzite, -5.606 eV for zinc-blend, and -5.416 eV for rock salt phases [16]. Using the local density approximation (LDA)

calculation technique, the equilibrium cohesive energy of ZnO is reported to be minimum in Wurtzite structure compared with the other two and thus, can be considered as the most energetically preferable ones.
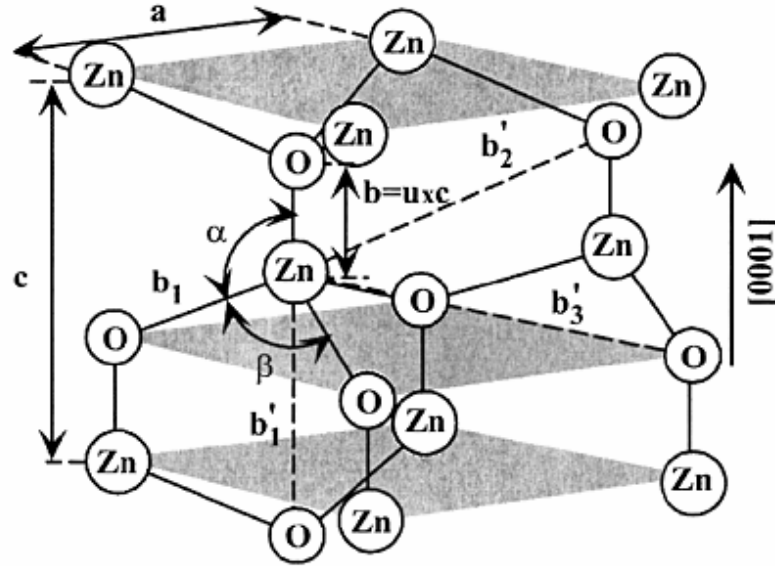
Figure 1.3: *Schematic representation of a Wurtzite ZnO structure having lattice constants a in the basal plane and c in the basal direction.*

Experimental measurements along with the theoretical calculations have shown Wurtzite ZnO belongs to the space group of $C4_{6V}$ or $P6_{3mc}$ with lattice parameters, $a = 3.296$ Å and $c = 5.20$Å [14] at room temperature. A schematic representation of the Wurtzite ZnO structure is shown in Figure 1.3. The structure is composed of two interpenetrating hexagonal-close-packed (hcp) sub lattices. Each of sub lattice consists of one type of atom displaced with respect to each other along the three fold *c*-axis by the amount of $u = 3/8 = 0.375$ (in an ideal Wurtzite structure the *u* parameter is defined as the length of the bond parallel to the *c* axis, in units of *c*). The *c/a* ratio and *u* parameter may vary in a slightly wider range, from 1.593 to 1.6035 and from 0.383 to 0.3856, respectively. The deviation from that of the ideal Wurtzite crystal is probably due to lattice stability and ionicity.

Each sub-lattice includes four atoms per unit cell and every atom of one kind (group-II atom) is surrounded by four atoms of the other kind (group-VI), or vice versa, which are coordinated at the edges of a tetrahedron. In a real ZnO crystal, the Wurtzite structure deviates from the ideal arrangement, by changing the *c/a* ratio or

the *u* value. A strong correlation exists between the *c/a* ratio and the *u* parameter. When the *c/a* ratio decreases, the *u* parameter increases in such a way that those four tetrahedral distances remain nearly constant through distortion of tetrahedral angles due to long-range polar interactions.

Another important characteristic of ZnO crystal is the presence of polar surfaces. The most commonly occurring polar surface is the basal plane. The oppositely charged ions produce positively charged Zn^{2+} (0001) and negatively charged O^{2-} (0001) surfaces, resulting in a normal dipole moment and spontaneous polarization along the *c*-axis as well as a divergence in surface energy. To maintain a stable structure, the polar surfaces generally have facets or exhibit massive surface reconstructions, but ZnO (0001) are exceptions: they are atomically flat, stable and without reconstruction.

1.4.2 Size and Shape Dependent Properties of Zinc Oxide

By changing the size and suitably adjusting the morphology of semiconductor particles, it's optical and electronic properties can be tuned for achieving better application. ZnO is one of the few oxides with a reasonably wide and experimentally accessible size range (<7 nm) that facilitates a substantial tunability of the band gap. There is a systematic and substantial shift of the absorption edge to lower energies with growth in the average particle size of ZnO [19].

As demonstrated by Gao and Wang [20] ZnO nanopropeller arrays consist of six triangular-shaped blades of 4-5 μm in length and propeller arrays with a diameter of ~10μm synthesized by using solid-vapor deposition process. In a lower temperature (600 to 700ºC) region, due to a relatively slower surface diffusion and lower supply of vapor, ZnO particles form a triangular-shaped structure. However, at medium temperature (800 to 900ºC) region, a faster diffusion of the ZnO vapor occurs and higher surface mobility leads to the formation of uniform and longer nanoblades. There have also been reports on the growth of ZnO tetrapod structures.

Park *et al.* prepared vertically aligned, uniform, homogeneous ZnO nano-rods by metal-organic vapor-phase epitaxial (MOVPE) at 400ºC without employing any metal catalysts [21]. However, the mean diameter was smaller than that of prepared

by other deposition methods though the high optical quality was achieved. Nano-belts are nano-wires with well-defined geometrical shape. Nano-belts of ZnO are usually grown by sublimation of ZnO powder without a catalyst. Semiconductor nano-belts are ideal candidates for cantilever applications, since they are structurally defect-free single crystals, so can provide a significant improvement in the cantilever sensitivity due to their reduced dimensions.

ZnO tubes formed by metal organic chemical vapor deposition (MOCVD) at temperatures of 350–450ºC have hexagonal shape as reported by Zhang *et al*. [22]. The characteristics of the tubes are found to be dependent strongly on both growth temperature and reactor pressure. Therefore, the tube density and size can be modified by changing either the growth temperature or the reactor pressure. However, no ZnO tubes found to be formed at 500ºC.

ZnO nano-needles with needle tips in the range of 20–50 nm in diameter can be obtained through chemical-vapor deposition (CVD). Excellent field-emission performance is caused by nanosize perturbations on the nano-needle tips. The high emission current density, high stability, and low turn-on field make the ZnO nano-needle arrays one of the promising candidates for high brightness field-emission electron sources and flat-panel displays [23].

ZnO nano-rods and nano-belts have been successfully utilized for field effect transistors (FETs). Single-crystal ZnO nano-wires synthesized using chemical vapor deposition method (CVD) are configured as FETs, and these are also utilized for O_2 detection. Oxygen is chemisorbed to ZnO surface at vacancy sites, forming O_2^- and resulting in a surface charge depletion layer, thus leading to a reduction in the electrical conductivity. Moreover, detection sensitivity increases with decreasing nanowire radius from 270 to 20 nm [24].

1.4.3 Doping of Zinc Oxide

In order to optimize the potential offered by ZnO, doping is required for both high-quality *n*- and *p*-type ZnO. Doping can change the electronic properties leading to change in band gap of the materials. It is easy to obtain strong *n*-type ZnO, but very difficult to create consistent, reliable and highly conductive *p*-type material.

Undoped ZnO films always exhibit *n*-type conductivity with typical carrier concentration of 10^{17} cm^{-3}, which is far below from the demand of device applications. Thus, high conductivity controlled by intentional doping is necessary. To enhance the optoelectronic properties based on ZnO, both *p*-type and *n*-type ZnO films are necessary. Therefore, ZnO have been doped with elements of the group-Ia and IIIb-VIIb, like Ga, In, N, Al, Sn, P, etc. Doping is not usually carried out with transition elements of the groups Ib, IIb, and VIIIa due to the incompatibility in the electron affinity or in the ionic radii of such elements with Zn.

p-type ZnO can be grown using an intentionally added acceptor species and some success has been achieved with N, P, As, and Sb doped as impurities. Nitrogen is most common among these because of its similar ionic radius and electronegativity with oxygen. Although a variety of nitrogen sources and different growth techniques have resulted in *p*-type ZnO:N, specific growth and post processing conditions are particularly important in realizing stable *p*-type material.

In the catalytic scenario, ZnO can act as a support in various types of conventional and nonconventional reactions. In hydrogenation reaction, Pt metal supported on ZnO is a very good catalyst. However, it has been observed that bimetallic species formed by noble metal and Zn are more promising catalyst than Pt doped on ZnO.

1.4.3.1   *n*-type Doping

ZnO with a Wurtzite structure naturally deviates from its stoichiometry, thus automatically forms an *n*-type semiconductor due to presence of intrinsic defects such as O vacancies (V_o) and Zn interstitials (Zn_i) [25]. Although it is experimentally known that unintentionally doped ZnO is *n*-type, whether the donor is Zn_i or V_o is still controversial.

For *n*-type doping, Zn or O should be replaced with atoms which contains one more electron in the outer shell. Thus, the group-III elements Al, Ga and In can replace Zn ion and group-VII elements Cl and I can be substitutional elements for O. According to equation (1.1):

$$D^0 \rightarrow D^+ + e^-$$
(1.1)

where D^0 and D^+ are the neutral and ionized donors, respectively. Preparation of Al, Ga and/or In doped *n*-type ZnO films has been attempted by many research groups with various techniques [26]. Al doped ZnO films prepared by photo assisted MOCVD (Metal Organic Chemical Vapor Deposition) method and Ga doped ZnO films grown by chemical-vapor deposition (CVD) show high conductivity.

Indeed, electron concentration beyond 10^{20} cm^3 is obtained in ZnO:Al or ZnO: Ga, which even at room temperature results in a degenerate electron gas in the conduction band. A degenerate carrier gas is characterized by the fact that the Fermi energy (or chemical potential) is located in the band and no longer in the band gap, and that consequently Fermi–Dirac statistics is mandatory for an adequate description.

Though doping with group-VII elements on the anion site is another promising possibility for *n*-type doping, however, it has not been investigated adequately for ZnO. Furthermore, it has been shown that hydrogen in ZnO is a very good donor [27]. Therefore, it is worth mentioning that small deviation from its stoichiometry and doping with proper donor help in developing *n*-type ZnO successfully.

1.4.3.2   *p*-type Doping

It is very difficult to obtain *p*-type doping in wide-band-gap semiconductors such as GaN, ZnO and ZnSe. The difficulties to form shallow acceptor level arise mainly from (i) low solubility of the dopant in the host material, (ii) compensation of dopants by low energy native defects, like, Zn_i or V_o or background impurities, and (iii) deep impurity level.

To overcome the above mentioned difficulties, one would expect that the *p*-type doping in ZnO may be possible by substituting either group-I elements, like Li, Na, and K for Zn sites or group-V elements as N, P, and As for O sites [28].

Group-I elements can act as deep acceptors with ionization energy around a few hundred meV, [14, 29] which is much larger than $k_B T$ at room temperature. According to equation (1.2):

$$A^0 \rightarrow A^- + hole \qquad (1.2)$$

where A^0 and A^- are the neutral and ionized acceptors. It has been shown that group-I elements could be better *p*-type dopants than group-V elements in terms of shallowness of acceptor levels. However, being smaller in atomic radii, group-I elements prefer to occupy the interstitial sites, rather than substitutional sites, and therefore, act mainly as donors instead. Moreover, significantly larger bond length for Na and K than ideal Zn–O bond length (1.93 Å) induces lattice strain, results in more native defects such as vacancies, which compensates the doping effect. These are among the many causes leading to difficulties in attaining *p*-type doping in ZnO. Because of these problems, a lot of research presently concentrates on *p*-type doping with the group-V elements i.e. N, P or As on oxygen site. However, reproducibility remains to be a great concern [30]. From As and P, similar behavior as that of group-I is observed. It then appears that, perhaps the best candidate for *p*-type doping in ZnO is N due to (i) smallest ionization energy, (ii) it does not form the NZn antisite, and (iii) AX center of N is only metastable. Nitrogen cannot be incorporated in the ZnO lattice in the form of N_2 using pure nitrogen source (e.g. during the growth in air), however, it can be introduced as single atom or ion using nitrogen plasma source. Furthermore, nitrogen acceptor has even smaller ionization energy than other standard acceptors.

1.4.3.3 **Nitrogen Doping**

From the above discussion, it is clear that nitrogen is a suitable dopant for *p*-type ZnO. Various research groups have expended a good deal of effort in an attempt to realize *p*-type ZnO using nitrogen (N) as a possible shallow acceptor dopant by using various types of nitrogen sources including N_2, NO, N_2O, NH_3, and Zn_3N_2 depending on the growth technique.

Several groups have tried *p*-type doping ZnO by MBE method using pure N_2 or mixture of O_2 and N_2 through RF plasma source. High nitrogen surface concentration of 10^{19} cm^{-3} in ZnO film was obtained, although formation of *p*-type ZnO does not take place [27]. Some promising results were reported recently by Look *et al.* [31] to produce *p*-type ZnO by MBE with N doping using Li-diffused semi-insulating ZnO substrates and an N_2 RF plasma source. Nitrogen-surface concentration (10^{19} cm^{-3}) in the N-doped ZnO film measured by secondary-ion-mass spectrometry (SIMS) was two orders of magnitude higher than that in undoped ZnO.

It is found that sometimes oxygen vacancies are one of the primary reasons for hindrance to nitrogen doping. To suppress the oxygen vacancies, various oxygen sources have been used with nitrogen including H_2O vapor. High H concentration was obtained instead of N while using water vapor in metal organic MBE method. In spite of that, *p*-type conductivity was observed which suggests that H incorporation may be the reason for p-type conductivity [32]. It is also reported the use of mixture of NH_3 in O_2 or H_2 gas as a nitrogen source [33] for dc reactive magnetron sputtering to prepare nitrogen doped ZnO. However, Wang *et al.* [34] argued that as NH_3 flux in the MOCVD chamber increases, the amount of nitrogen doping decreases. 100% ammonia environment facilitates O–H bond formation on the surface, which is stronger than Zn-N bond. Therefore, they have prepared ZnO:N under optimum ammonia environment. They have calculated surface nitrogen concentration through XPS analysis and obtained O:Zn:N ratio is about 40:46:14. Lu *et al.* studied *p*-type ZnO growth as a function of ammonia concentration in NH_3–O_2 ambient using dc reactive magnetron sputtering [35]. It was shown that in the pure oxygen environment intrinsic ZnO film formed, while, 100% NH_3 environment resulted in zinc polycrystalline film. 1:1 ammonia and O_2 mixture ambient produce nitrogen doped ZnO, with better electrical properties and high hole concentration of 7.3×10^{17} cm^{-3}. In spite of several reports, concentration of nitrogen is still controversial.

Another approach to reduce oxygen vacancies could be to use an O_2 and N_2 mixture to provide oxygen along with N_2. Even though various ratios of O_2 and N_2 have been employed but efforts did not turn out to be successful to obtain *p*-type conductivity. Some researchers used N_2O gas as a nitrogen source, which is a mild oxidizing gas and the dissociation energy and ionization potential of N_2O are lower than those of N_2. In this vein, N_2O plasma was used for nitrogen doping in ZnO film by pulse laser deposition (PLD) [36]. It was found that nitrogen doping was enhanced by using the active N formed by N_2O gas flowing through an electron-cyclotron-resonance (ECR) source. The prepared material has shown *p*-type conductivity with a high hole concentration in the range of 10^{18} cm^{-3}. Based on first principle studies, it was proposed that the NO gas without an ECR plasma source could be more efficient N source than N_2O or N_2 [37]. The model indicated that the defect formation energy of N on oxygen site (N_o) from NO should be lower than that from N_2O. The formation

energy of N_o from N_2O is much larger than that from NO. Therefore, it is suggested that NO molecules could spontaneously be incorporated to form N_o defects in ZnO.

Scientists have reported *p*-type doping with varying zinc source also. Wang *et al.* attempted nitrogen doping in ZnO films using diethyl zinc as zinc source and pure N_2 gas as nitrogen source, in plasma-assisted MOCVD but they did not achieve *p*-type doping. However, it was claimed to successfully prepare *p*-type ZnO films, by reacting same zinc source (as mentioned above) with NO gas as nitrogen source [38]. Here, NO gas was used to supply both O and N for *p*-type doping. Therefore, results imply that NO can more efficiently incorporate nitrogen in the ZnO film rather than using pure nitrogen source. Results also indicated that N can be incorporated into ZnO films without plasma or high-temperature process and a high N concentration was obtained only under Zn-rich conditions as predicted by Yan *et al.* [37]. A nitrogen doped zinc oxide film has been prepared by MOCVD technique from oxygen/diethyl zinc mixtures injected in an argon/nitrogen atmosphere. A nitrogen content was about 0.5 atom % which was determined by elastic recoil detection (ERD) analysis but Infrared spectroscopy and mass spectrometry measurements suggest that nitrogen is present mostly as –C=N [39]. *p*-type ZnO by nitrogen-ion implantation of ZnO films using RF magnetron sputtering was obtained by Lin *et al.* [40]. The *p*-type ZnO films implanted with N^+ dose showed good electrical properties and high hole concentration. While most studies on N-doped *p*-type ZnO have been based on deposition methods, other approaches such as oxidation have been attempted as well.

Perkins *et al.* prepared nitrogen-doped films of ZnO grown by two methods, MOCVD technique and reactive sputtering, and nitrogen amount was estimated by XPS analysis [41]. Systematic differences in the N chemical states were observed between films grown by sputtering and MOCVD. In RF sputtering method zinc metal target was sputtered by mixture of $N_2 + O_2$. In the case of reactively sputtered ZnO: N films having atomic nitrogen concentrations >1.2%, where as in the film prepared by MOCVD method contains 2.6% atom nitrogen.

Another successful approach to make nitrogen doped ZnO was thermal annealing of zinc oxynitride alloy or by oxidizing Zn_3N_2 films. Zinc oxynitride alloy films grown at a relatively low substrate temperature of 200°C and were subjected to post growth thermal annealing, resulting in the transformation from ZnON alloy to N

doped ZnO. With the variation in annealing temperature, behavior of the material changes. Due to calcination in oxygen ambient all the N dopants from ZnO film desorbed and replaced by O, thus when annealing temperature is above 1000°C pure ZnO with better crystalline quality was obtained. When Zn_3N_2 oxidized at 500°C showed *p*-type characteristics with a comparable hole concentration. However, oxidization at a higher temperature of 550°C resulted in *n*-type conductivity, which was stated to be due to insufficient N atoms to form N acceptors. These results indicate that there is a trade off between N-doping efficiency and crystalline quality [42]. Kobayashi *et al.* [43] also predicted that N is a good candidate for a shallow *p*-type dopant in ZnO although N is not very soluble. It was also suggested that N doping can be achieved by ion implantation as well.

Further studies by other groups to enhance N doping by thermal treatment of ZnO were also carried out. Garces *et al.* [44] observed the formation of nitrogen acceptors in N-doped ZnO crystals using photo induced electron-paramagnetic-resonance (EPR) method after annealing in air or nitrogen atmosphere at a temperature range of 600–900°C. Solid source chemical vapor deposition was also used for nitrogen doping of ZnO. In this method zinc acetate dehydrate [$Zn(CH_3COO)_2 \cdot 2H_2O$] and ammonium acetate [$CH_3COONH_4$] were used as Zn precursor and the nitrogen source, respectively.

Despite the above-mentioned reports on successful growth of *p*-type ZnO films by N doping, there are also a number of reports in which the authors could not be able to reproduce these results even when the same growth methods, growth conditions, and N precursors were thoroughly followed [45]. It is expected that some progress can be made by co-doping, i.e., by using either two different acceptors simultaneously (e.g. ZnO:N, As) or by combining a moderate concentration of donors with a higher concentration of acceptors (e.g. in ZnO:Ga, N). Therefore, even if one assumes that the reported results truly represent the *p*-type ZnO, the reproducibility remains to be a major concern.

1.4.3.4   **Co-doping with: Nitrogen + Group- III Metal Ion**

Although nitrogen has been considered as the best candidate for *p*-type doping for ZnO [44-56], however, till date it is well known that the low solubility of N in

ZnO is the main problem. Therefore, it is necessary to find methods that can enhance the solubility limit of nitrogen in ZnO. For this purpose, a donor-acceptor co-doping method has been proposed in order to realize highly conducting *p*-type ZnO and a number of experimental studies have been performed based on this approach. Recently, Yamamoto and Katayama-Yoshida proposed the co-doping method based on electronic band-structure calculations to solve the unipolarity in ZnO [46]. They explained that formation of co-doping ion pair between donor and acceptors enhances the solubility limit of nitrogen and lowers the acceptor level in the band gap due to strong interaction between N acceptors and reactive donor codopants. It was noted that the overall Madelung energy decreases when group-III elements are codoped with nitrogen, indicating localization of the N states. Moreover, an N-Ga–N complex would be more soluble than N alone, and be a shallower acceptor as well. A SIMS study showed that due to co-doping, N solubility enhances 400 times as compared to that in N-implanted ZnO.

For Ga and N co-doping method, Joseph *et al.* [47] successfully grew *p*-type ZnO films by a PLD system combined with a plasma gas source using N_2O gas as the nitrogen source and simultaneously introduced N as an acceptor. Hall and Seebeck coefficient measurements confirm *p*-type conductivity; however, the very low mobility brings the *p*-type conductivity in question. It was also indicated that low-temperature formation is essential for inequilibrium growth in the co-doping technique. Although *p*-type conductivity was observed in codoped ZnO films, but the origin of *p*-type characteristics is not yet clear due to the lack of characterization. Ohshima *et al.* [48] attempted to synthesize *p*-type ZnO by PLD using various co-doping methods including the ablation of ZnO:Ga target in NO gas, and Al and N co-doping using an ion gun and a microwave ECR source. Although they could identify the presence of Ga–N bond in ZnO, but *p*-type ZnO film could not be achieved.

From the reported works it is found that the types of conductivity and carrier concentration in Ga and N codoped ZnO are dependent on the O_2 partial pressure in the sputtering gas mixture as V_o and Zn_i are suppressed in the presence of O_2. *n*-type conduction obtained from deposited films for oxygen partial pressure varies between 0% and 40%. But, the films deposited with oxygen partial pressure higher than 50% showed *p*-type conduction. Since, the conduction type is dependent on oxygen partial

pressure; oxygen vacancies play an important role in determining the type of conductivity. There are also investigations on co-doping experiments in which indium and aluminum were used as group-III co-doping metals, and ultrasonic ultra spray pyrolysis method was used for growth. The aqueous solutions $Zn(CH_3OO)_2 \cdot H_2O$, CH_3OONH_4 and $In(NO)_3$ were used as the precursor of Zn, N, and In, respectively. Al and N codoped *p*-ZnO have been prepared by dc reactive magnetron sputtering at 500°C by the growth of ZnO films in a N_2O+O_2 atmosphere on glass substrates. With high N concentration in codoped sample though dramatic decrease in resistivity was observed, but does not show *p*-type conductivity. The study on modification of preparation procedure and condition is under process.

1.4.4 **Preparation of Doped Zinc Oxide**

The above discussion leads to the fact that activity and selectivity of any catalytic process and material application are dependent on preparation parameters of that material including catalyst, as with changing the preparation procedure the crystal structure, changes take place in crystallinity and cation distribution. These facts suggest that materials as well as preparation of catalysts are the critical factor. Recently, a number of fundamental studies concerning the influence of preparation procedures on the catalyst performance have been published [49]. ZnO and doped ZnO can be prepared by various methods like (i) precipitation method [50], (ii) sol-gel method [51], and (iii) combustion method depending on the nature of the doping element. Since, for nitrogen doping these conventional methods can not be applicable, sophisticated methods like pulsed laser deposition, molecular beam epitaxy, metal organic chemical vapor deposition are being attempted.

1.4.4.1 **Precipitation Method**

Precipitation is one of the most important, easiest and economic methods for the synthesis of solid catalyst. A scientific approach was introduced by Marcilly [52] for catalyst preparation by precipitation route. Formation of the precipitate from a homogeneous liquid phase may occur as a result of physical transformation (change in temperature, solvent, or solvent evaporation), however, most often it is obtained as by-product of chemical processes (addition of bases or acids, use of complex forming agents) when super saturation with respect to the precipitating solid is ensured.

However, factors like pH, temperature, nature of reagents, and presence of impurities and method of precipitation also determine the morphology, texture, structure and crystallinity of the precipitate [53].

In the synthesis of multi-component systems such as codoped ZnO, the problems are even more complex. In a system with two or more metallic compounds, the composition of the precipitate depends on the differences in solubility between the components and the chemistry occurring during precipitation. The formations of the coprecipitate followed by hydrothermal treatments are used to transform amorphous precipitate to crystalline materials which have improved thermal- and mechanical-stability.

1.4.4.2 Sol-gel Method

Sol-gel process originally developed to control the texture of the pure metal oxide phases has become universally acclaimed technique for preparation of various modern advanced catalytic materials. The method is a homogeneous process which results in a continuous transformation of solution into a hydrated solid precursor (hydrogel). The method is based on the hydrolysis and gelation (for instance by controlled addition of water) of alkoxides or other reactive compounds in alcoholic solution [54]. The chemistry of the processes that occurs during the formation of porous structure is controlled by changing the various parameters, such as pH, solvent, temperature, amount of water added for reaction and rate of addition of water during preparation. The sol-gel processing presents with wide opportunities not only for defining the chemical funtionalization of porous materials but also careful control of texture.

1.4.4.3 Combustion Synthesis

Combustion technique is a versatile process leading to syntheses of single phase, solid solutions, composites as well as complex compound oxide phases in homogeneous form. These syntheses involve a self-sustained reaction between an oxidizer, typically precursor metal nitrates and fuels such as glycine, urea and hydrazine after dissolution in water. Combustion synthesis may be classified into two types: (a) solution combustion synthesis, wherein glycine, urea or hydrazine is used as fuel and (b) gel combustion synthesis or Pechini process [55], where citric acid is

used as fuel. By keeping in moderate temperature preheated chamber, the reaction mixture turns to be viscous liquid followed by a self-ignition process. Due to the high exothermic nature of the system, the combustion temperature rapidly reaches ~ 800ºC and converts the precursor material to fine crystallites. Moreover, the high temperature reached during the combustion process and short preparation time (few seconds) along with a large amount of gas evolution promote the nanoparticles growth of the intended phase composition. Typically two types of reaction modes are adopted *viz.*, self-propagating high temperature synthesis (SHS) mode where the reaction initiates locally and follows a wave-like propagation through the medium, and volume combustion synthesis (VCS) where the reactants are heated uniformly and reaction occurs simultaneously throughout the mixture. Owing to the above-mentioned advantages, this process has been widely used for preparation of variety of advanced materials [56].

1.4.4.4   Pulsed Laser Deposition

Pulsed laser deposition (PLD) is a thin film deposition (specifically a physical vapor deposition, PVD) technique where a high power pulsed laser beam is focused inside a vacuum chamber to strike a target of the desired composition. The material is then vaporized from the target and deposited as a thin film on a substrate, such as a silicon wafer facing the target. This process can take place in ultra high vacuum or in the presence of a background gas, such as oxygen which is commonly used for depositing fully oxygenated oxide films [57].

1.4.4.5   Molecular Beam Epitaxy

The main advantage of molecular beam epitaxy (MBE) is its precise control over the deposition parameters and in-situ diagnostic capabilities. Zn metal and O_2 are usually used as the source materials for ZnO thin-film MBE. High-purity Zn metal is evaporated from an effusion cell, where the cell temperature can be varied to examine the effect of the Zn flux on the growth rate and material properties. The source of oxygen radical beam can be generated by an electron cyclotron resonance (ECR) or RF plasma source or oxygen microwave plasma source. The advantage of the ECR sputtering system is that it enables the production of highly ionized plasma under low gas pressures. The ZnO films deposited by ECR sputtering exhibit a high electrical

resistivity ($\rho > 10^{10}$ Ω cm) and good piezoelectric and optical properties [58]. NO_2 is another potential source for preparing N doped ZnO through MBE method [59].

1.4.4.6 Chemical Vapor Deposition

Chemical vapor deposition (CVD) is a chemical process used to produce high-purity, high-performance solid materials in large scale production. The process is often used in the semiconductor industry to produce thin films and optoelectronic devices. In a typical CVD process, the correct choice of reactants is very important; normally it varies from halides, carbonyls, and alkoxides to organic complex. The equipment used to perform CVD is relatively simple. In a closed/open reactor, depending upon the method applied, the pretreated support is exposed to one or more volatile or vapor precursors, which react and/or decompose on the substrate surface to produce the desired deposit. Frequently, volatile by-products are also produced, which are removed by gas flow through the reaction chamber [60].

CVD is being widely used in microfrabication processes to deposit materials in various forms, likely monocrystalline, polycrystalline, amorphous, and epitaxial. These materials include silicon, doped silicon, carbon nanofibers, filaments, carbon nanotubes, SiO_2, tungsten, titanium nitride and various high-k dielectrics. The ZnO films grown by this method show high crystal, electrical and luminescence properties.

1.4.4.7 RF Magnetron Sputtering

One of the most popular growth techniques for ZnO film preparation is sputtering method (dc sputtering, RF magnetron sputtering and reactive sputtering). As compared to sol-gel and chemical vapor deposition, the magnetron sputtering is a preferred method because of its low cost, simplicity and low operating temperature [61]. ZnO films grow on a certain substrate temperature by sputtering from a high-purity ZnO target using an RF magnetron sputter system [62].

The growth is usually carried out in the ambient environment with various O_2/Ar+O_2 ratios ranging from 0 to 1 at a pressure of 10^{-3} to 10^{-2} Torr. Here O_2 serves as the reactive gas and Ar acts as the sputter enhancing gas. ZnO can also be grown by dc sputtering from a Zn target in an Ar+O_2 gas mixture. The RF power applied to the plasma is tuned to regulate the sputtering yield rate from the ZnO target. For these

experiments, the target is often presputtered for 5–15 min before the actual deposition. To dope nitrogen in the ZnO lattice O_2 gas is mixed with definite ratio of N_2 or NH_3.

1.4.4.8   **Scope of Combustion Synthesis over Conventional Routes**

For the production of many advanced materials, the combustion method proves to be an energy-efficient simple process. This process is preferred for its additional characteristic features such as (i) rapid heating rates, (ii) high temperature, (iii) short reaction time, (iv) use of relatively simple equipment, and *(v)* formation of products with virtually any size and shape etc. Thus, this process leads to the formation of final products with higher order of purity and better mechanical properties [63]. The high exothermicity of the combustion reaction within a short duration of time is considered as an advantage to design the final phase composition. Due to the high-temperature process, only the thermodynamically stable phases can be prepared. However, controlling the rapid heating and cooling rates enables to obtain metastable materials with new and unique properties. Deshpande *et al*. [64] proved that proper choice of fuel and its concentration could invariably produce materials with improvement in composition and properties.

Because of the above advantages, combustion process finds applications in ceramic reinforcements, hydrogen storage, catalytic materials, high temperature superconductors and friction materials. Li *et al*. [65] reported that combustion synthesis is advantageous compared to the conventional method to produce (a) Co-Cr-Mo alloys for using in orthopedic implants, and (b) high efficiency hydrogen storage Mg-Ni-Cu system. Combustion synthesized NbB_2 induces superconductivity at -265ºC, whereas the conventionally prepared sample shows no superconductivity [66]. Julien *et al*. [67] prepared layered $LiNi_{1-y}Co_yO_2$ by glycine assisted combustion synthesis for Li batteries. The lithium-based cathodes synthesized by this method show superior properties than its conventional counterparts. Spinel $Zn_{1-x}Co_{2+x}O_4$ material prepared by combustion method shows ferromagnetism up to 680ºC, making the material suitable for many practical applications including Li ion battery anode material [68].

In addition to the above addressed features of combustion synthesis, Bera *et al*. [69] highlighted that combustion synthesis paves the way for ionic dispersion of

active species in the support lattice, unlike the other known conventional methods like wet-impregnation and coprecipitation. Even the noble metals like Pt, Pd and Au could be advantageously dispersed in ionic form over ceria lattice, thereby promoting the catalytic activity. In overall perspective, combustion synthesis is found to be a novel route for preparation of catalytic materials with improved properties. Exploring this route will further enable to obtain a wealth of information that could be advantageous for designing catalytic materials with greater efficiency. Hence, in the present study novel synthesis procedure for the preparation of N, N and S, Ga and N, and In and N codoped ZnO has been explored.

1.4.5 **Zinc Oxide as a Catalyst**

ZnO has very promising and wide variety of applications in (i) liquid phase acylation reaction, (ii) photocatalytic dye degradation, (iii) water splitting, and (iv) vapor phase dehydrogenation reaction. Beyond those, being amphoteric in nature and having good surface area it can act as a very good support in variety of reactions.

ZnO is a highly efficient catalyst for the Friedel-Crafts acylation reaction of activated and unactivated aromatic compounds including variety of alcohols, phenols and amines with acid chlorides or acid anhydrides. It gives high yields at room temperature under very mild reaction condition [70]. Alkylation of ethylenediamine with alcohols using $ZnO/CuO/Al_2O_3$ has also been reported. Cu-Zn-Al catalysts derived from a hydrotalcite-like precursor have been studied for oxidative reforming of CH_3OH and water gas shift (WGS) reaction. Good results in terms of CH_3OH conversion and H_2 yield, along with low CO production, have been observed [71]. This catalyst is also used to carry out for syngas to methanol conversion.

ZnO supported palladium based catalysts have been shown to be both active and selective towards the steam reforming of methanol, although they are still considered to be less active than traditional copper based catalysts. The activity of Pd/ZnO catalysts can be significantly improved by supporting them on alumina. Datye *et al.* [72] showed that the $Pd/ZnO/Al_2O_3$ catalysts have better long-term stability when compared with commercial catalysts. The $Pd/ZnO/Al_2O_3$ catalysts can be easily regenerated by oxidation in air followed by re-exposure to reaction conditions, while the Cu/ZnO based catalysts don't recover their activity after

oxidation. However, even after such extreme treatment, the catalyst activity is regained with time on stream under reaction condition alone, leading to highly stable catalyst.

The copper zinc ferrite catalyst acts as a potential candidate for selective production of N-methyl aniline from aniline. Though Cu seems to be the active species for aniline methylation, however, heterogeneous distribution of zinc plays a significant role, likely as an "active spacer cum stabilizer". Zinc ions hinder the reduction of active Cu and contribute to prolonged activity of N-alkylation reaction of aniline [73]. Apart from acting as spacer, zinc oxide can also act as promoter in the *n*-heptane (*n*-C7) hydroisomerization reaction. It is investigated that catalytic performance of $Pt/WO_3/ZrO_2$ catalyst in addition with only 3.4 wt % of ZnO would achieved 81% of *n*-C7 conversion and 89% of C7 isomer selectivity. Both WO_3 and ZnO can stabilize the tetragonal phase of ZrO_2 under reaction condition, thus helps to continue the reaction for longer time [7 e].

The formation of the ordered 1:1 Pd-Zn intermetallic compound by deposition of Pd on zinc oxide increases the average Pd-Zn coordination number and the WGS turnover rate. The bonding of adsorbed CO changes from 80% bridging on pure Pd to 90% linear on the 1:1 Pd-Zn intermetallic compound, which can be correlated linearly with the WGS rate per Pd molecule on the surface [74]. This compound is also very good catalyst for ester and 1-3, butadiene hydrogenation [75].

Gas phase hydrogenation of crotonaldehyde gives crotyl alcohol with high selectivity at 80ºC over Pt/ZnO catalyst at atmospheric pressure. Lambert *et al*. explained that the chemo selective activity of hydrogenation product was due to intrinsic property of the well-defined intermetallic compound Pt/Zn and independent of any influence from solid support [76].

In recent years, environmental and economic considerations have aroused strong interest in redesigning commercially important processes so that the use of harmful substances and the generation of toxic wastes can be avoided. ZnO can also be used as an efficient catalyst for the photocatalytic degradation of pollutants by "advanced oxidation processes" (AOPs), based on the generation of very reactive species such as hydroxyl radicals which oxidize a broad range of organic pollutants

quickly and non-selectively. Its efficiency has been reported to be particularly noticeable in the advanced oxidation of pulp mill bleaching wastewater and in photo catalyzed oxidation of phenol. Nanostructured ZnO is active in water splitting, but amount of H_2 production is less than compared to other commercial catalysts. Recently Domen *et al*. reported solid solution of GaN-ZnO supported Ru nanoparticles as a photocatalyst for overall water splitting under visible light in the order of mmol /h /gm of catalyst [77].

Researchers have found that catalytic activity is indirectly related to the surface area; specifically it depends on the surface density of active sites. Although solid-state defects have been proposed to be the active sites in heterogeneous catalysis, active centers have rarely been conclusively identified. The catalytic activity of ZnO increases linearly with the increase in surface area, though few exceptions prevail. The catalytic formation of methanol over ZnO is a structure sensitive reaction, requiring the presence of polar ZnO facets. According to the most recent model (Figure 1.4) of the methanol synthesis reaction on ZnO surface, oxygen vacancies formed on the surface of ZnO crystals serve as the active sites [78].
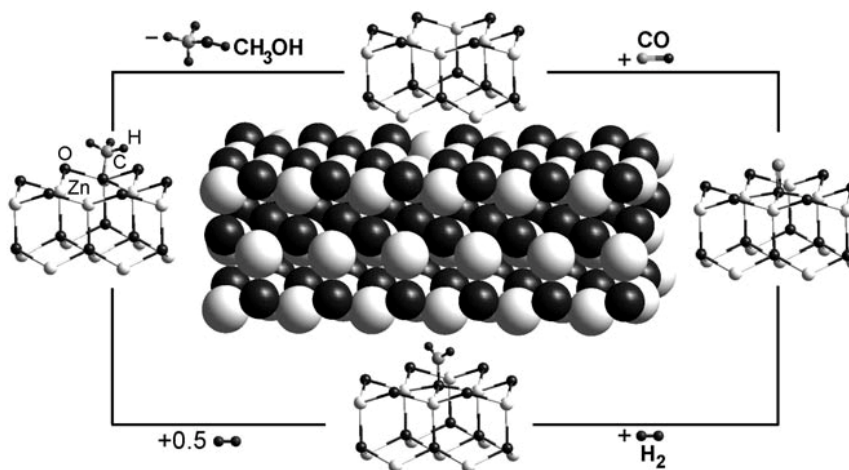
Figure 1.4: *Model for the activity of ZnO in the hydrogenation of CO.*

ZnO can promote the dehydrogenation reaction of many alcohols like cyclohexanol, butanol etc. Dehydrogenation of primary and secondary alcohols to the corresponding aldehyde or ketones plays a fundamental role in organic synthesis owing to the versatility of the carbonyl group as a building block. Traditionally, the oxidation of alcohols is mainly performed by using stoichiometric quantities of

oxidants containing chromium. Those oxidants are expensive and the systems using chromium-containing oxidants generate large volumes of waste water containing heavy metals. There is a growing demand for atom efficient catalytic methods that can utilize clean oxidants such as H_2O_2 and even O_2, to meet the economical and environmental issues. In practice, the dehydrogenation of alcohols is performed in liquid phase as well as in vapor phase, depending mainly on the thermal stability and volatility of reactants and products. However, for industrial applications, liquid phase reaction is not favored due to the selectivity problems.

1.5 Objectives of the Thesis

A survey of literature reports since past few decades reveals that doping in ZnO can change its electronic as well as its electrical properties. With change in its electronic property, it can easily influence its band gap by altering the position of valence band (VB) and conduction band (CB) or forming a mid gap state. In other words, donor impurities create states near the CB while acceptors create states near the VB. ZnO acts as a very good catalyst, both in conventional and unconventional systems, so combination of doping strategies in its preparation can make dramatic changes in the applications. Hence, doped ZnO could be employed in better way to develop potential commodity material.

Nitrogen is one of the promising dopants in place of oxygen though the conventional preparation procedures for nitrogen doping are very much time consuming and sophisticated, and it leads to zinc loss due to high temperature procedure. In spite of considerable research work being done to dope with N, the amount of surface nitrogen achieved is only 6 atom % and there is a lack of understanding about the chemical state of doped nitrogen. Though some researchers reported successful preparation of N doped ZnO, reproducibility of the obtained results still remains a big challenge. Furthermore, it is also desirable to develop solution-based synthetic routes, because the process is economical and chemically superior product can be obtained as well. In addition, the application of combustion strategy as the method of synthesis can also be investigated. The synthesis, characterization and catalytic activity of N doped ZnO, codoped with elements like Ga or In has not been pursued extensively. It is also found that application of N doped ZnO in conventional catalytic system has not yet been explored.

Recently, thorough research is being carried out to modify the conduction and valence band position of the material, followed by change in band gap of semiconductor and to explore it in the visible light driven photocatalytic applications. The top of the VB of a metal oxide consists of O $2p$ atomic orbital. When other elements (e.g. N $2p$ and S $3p$) with atomic orbital of potential energy higher than O $2p$ atomic orbital are partially or fully substituted for O, the HOMO of the new material is expected to be shifted to the higher level in comparison with the parent metal oxide. Therefore, without affecting the CB of a metal oxide, new VB can be formed, which result in decreasing the band gap energy.

Both of ZnO and GaN consist of large band gap (>3 eV) and exist in Wurtzite structure with similar lattice parameter. In solid solution of GaN rich ZnO system Zn is regarded to be a substitutional atom for Ga and Zn in GaN acts as an acceptor impurity causes the formation of different acceptor levels. The bonding between Zn and N atoms is formed because of the formation of the solid solution. Density functional theory (DFT) calculations indicate that the bottom of the CB for GaN-ZnO solid solution is mainly composed of $4s$ and $4p$ orbital of Ga, while the top of the VB consists of N $2p$ orbital followed by Zn $3d$ and O $2p$ orbital. Furthermore, it is hypothesized that p-d repulsion in the GaN-ZnO solid solution (i.e., N $2p$-Zn $3d$ repulsion) may cause the top of the VB formed by N $2p$ atomic orbital to lift up to a higher potential energy, resulting in a narrower band gap for GaN. This may be responsible for the desirable optical properties and shows very good visible light photocatalytic activity. However, this phenomenon is still valid for the solid solution with stoichiometric unit cells.

Taking into consideration the above mentioned issues, a stepwise systematic approach to explore those above problems is the main objective of this thesis.

➢ To prepare and characterize nitrogen doped ZnO by solution combustion method (SCM) in order to change its electronic properties and to explore it in conventional catalytic application. State of active nitrogen and amount of nitrogen can be studied by various spectroscopic and microscopic methods.

➢ To study the effect of use of thiourea along with urea as a fuel in combustion synthesis and understand the variation in the structural properties of the resulting doped ZnO as the function of changing thiourea concentration.

➢ To prepare and characterize ZnO-GaN solid solution by SCM and explore the use of the nitride containing material in an unconventional catalytic system like nitrogen fixation at atmospheric pressure. The work should also bring out the discussion on state and amount of nitrogen and gallium in the new solid solution material. Characterization of the spent catalyst to know the reason of deactivation is also another aim.

➢ To study In as doping agent in ZnO system on the properties, selectivity and conversion efficiency of ZnO as catalyst for simple dehydrogenation reactions.

1.6 Outline of the Thesis

This thesis mainly deals with the synthesis procedure of doping in ZnO by SCM and detailed characterization of prepared materials and their catalytic activity. An attempt has been taken to dope anion as well as cation in the ZnO crystal without disturbing its lattice system. Four types of system have been discussed in this thesis, (i) Nitrogen doped ZnO ($ZnO_{1-x}N_x$ materials), (ii) Nitrogen and sulphur co-doped ZnO ($ZnO_{1-x-z}N_xS_z$ materials, (iii) Gallium and Nitrogen co-doped ZnO ($(Zn_{1-z}Ga_z)(O_{1-x}N_x)$ materials) and (iv) Indium and Nitrogen co-doped ZnO ($(Zn_{1-z}In_z)(O_{1-x}N_x)$ materials). The following is the chapter-wise outline of the present thesis work.

Chapter 1 presents the general introduction to heterogeneous catalysts with a suitable emphasis on zinc oxide. It gives a brief description to mixed metal oxides and effect of doping in it. How doping in ZnO lattice can help to obtain its utilization as optoelectronic material and in catalytic world has also been discussed. At the end of this chapter the scope of the thesis is presented.

Chapter 2 mainly deals with the experimental methods involved in the preparation of heteroatom incorporated ZnO. It includes general introduction to the physico-chemical characterization techniques. The theory and experimental procedures that have been used to characterize the prepared materials there are discussed here.

Chapter 3 is divided into two parts - **Part A** and **Part B**. **Part A** describes detailed characterization of nitrogen doped ZnO ($ZnO_{1-x}N_x$ materials). Through various physico-chemical, spectroscopic and microscopic methods the nature and amount of nitrogen in the $ZnO_{1-x}N_x$ lattice and effect of urea in the preparation mixture is discussed. The photocatalytic decomposition of rhodamine B on $ZnO_{1-x}N_x$ with UV light and vapor phase cyclohexanol dehydrogenation are presented. **Part B** brings out the effect of thiourea in the preparation mixture of nitrogen doped ZnO. This chapter also deals with vapor phase dehydrogenation reaction of isobutanol to isobutyraldehyde.

Chapter 4 describes the state, amount and effect of gallium doping in the $ZnO_{1-x}N_x$ lattice. The change in the lattice parameter and band gap of ZnO in codoped material is discussed. The effect of gallium doping in the binding energy of nitrogen is reported as well. The application of this material in N_2 fixation reaction at atmospheric pressure is also presented here.

Chapter 5 brings out the change in lattice structure and band gap of ZnO, if it is codoped with indium and nitrogen. State and quantity of nitrogen and indium in prepared material are discussed. Effect of indium doping on $ZnO_{1-x}N_x$ materials in the vapor phase dehydrogenation reaction of secondary alcohol has also been studied.

Chapter 6 summarizes the conclusions derived based on the observation and results obtain from the entire study. At the end scope of further research work in the area of the present study have also been pointed out.

1.7 **References**

1.   J. J. Berzelius, *Jber. Chem.* **15** (1835) 237.

2.   (a) W. Ostwald, *Phys. Z.* **3** (1902) 313 (b) W. Ostwald, *Ann. Naturphil.* **9** (1910) 1.

3.   G. Ertl, H. Knozinger and J. Weitkamp, *Handbook of Heterogeneous Catalysis,* Vol. **1** Wiley- VCH, Weinheim, 1997.

4.   G. Ertl. *Angew. Chem. Int. Ed.* **47** (2008) 3524.

5.   (a) H. Hattori, *Chem. Rev.* **95** (1995) 537. (b) Mark A. Barteau, *Chem. Rev.* **96** (1996) 1413.

6. (a) J. M. Thomas, *Sci. Am.* **266** (1992) 112. (b) H. Hattori, *Stud. Surf. Sci. Catal.* **78** (1993) 35.

7. (a) S. H. Joo, S. J. Choi, I. Oh, J. Kwak, Z. Liu, O. Terasaki and R. Ryoo, *Nature* **412** (2001) 169. (b) U. Ciesla, S. Schacht, D. G. Stucky, K. K. Unger and F. Schueth, *Angew. Chem. Int. Ed. (Engl.)* **35** (1996) 541. (c) A. Corma and H. García, *Chem. Rev.* **102 (**10) (2002) 3837. (d) A. Vinu, T. Mori and K. Ariga, *Sci. Technol. Adv. Mater.* **7** (2006) 753. (e) Y. Liu, Y. Guan, C. Li, J. Lian, G. J. Gan, E. C. Lim and F. Kooli, *J. Catal.* **244** (2006) 17.

8. (a) K. Tanabe, M. Misono, Y. Ono and H. Hattori, *Stud. Surf. Sci. Catal.* Vol. **51** *New Solid Acids and Bases and Their Catalytic Properties*, 1989. (b) H. L. Emerson, *Catal. Rev*. **8** (1973) 285. (c) A. Clark, *Catal. Rev.* **3** (1969) 145.

9. (a) G. M. Schwab, E. Roth, C. H. Grinzoz and N. Mavrakis, in *"Structure and properties of solid surfaces"* (R. Gomer and C. S. Smith, Eds.), Univ. Chicago Press, Chicago, 1953. (b) J. P. Suchet, *"Chemical Physics of Semiconductors",* Chap.5, p.82, Van Nostrand, London, 1965.

10. (a) P. Arnoldy and J. A. Moulijn, *J. Catal*. **93** (1985) 38. (b) L. Ji, J. Lin and H. C. Zeng, *J. Phys. Chem. B* **104** (2000) 1783. (c) T. Paryjczak, J. Rynkowski, S. Karski, *J. Chromatogr*. **188** (1980) 254.

11. (a) S. Klosek and D. Raftery**,** *J. Phys. Chem. B* **105** (2001) 2815. (b) M. Anpo, Y. Ichihashi, M. Takeuchi and H. Yamashita, *Res. Chem. Intermed.* **24** (1998) 143.

12. K. Nagaveni, M. S. Hegde and G. Madras, *J. Phys. Chem. B* **108** (2004) 20204.

13. M. R. Hoffmann, S. T. Martin, W. Choi and D. W. Bahnemann, *Chem. Rev*. **95** (1995) 69.

14. N. J. Renault, P. Pichat, A. Foissay and R. Mercier, *J. Phys. Chem.* **90** (1986) 2733.

15. L. A. Linsebigler, G. Lu and J. T. Yates, *Chem. Rev*. **95** (1995) 735.

16. (a) C. Klingshirn, *Chem. Phys. Chem.* **8** (2007) 782. (b) Ü. Ozgur, Y. I. Alivov, C. Liu, A. Teke, M. A. Reshchikov, S. Dogan, V. Avrutin, S. J. Cho and H. J. Morkoc, *J. Appl. Phys*. **98** (2005) 041301.

17. (a) A. V Singh, R. M. Mehra, A. Wakahara and A. Yoshida, *J. Appl. Phys.* **93** (2003) 396. (b) S. V Orlinskii, J. Schmidt, P. G. Baranov and D. M. Hoffmann, *Phys. Rev. Lett*. **92** (2004) 047603.

18. (a) J. E. Jaffe and A. C. Hess, *Phys. Rev. B* **48** (1993) 7903. b) J. E. Jaffe, J. A. Snyder, Z. Lin and A. C. Hess, *Phys. Rev. B* **62** (2000) 1660.

19. R. Viswanatha, S. Sapra, B. Satpati, P. V. Satyam, B. N. Dev and D. D.Sharma, *J. Mater. Chem*. **14** (2004) 661.

20. P. X. Gao and Z. L. Wang, *Appl. Phys. Lett*. **84** (2004) 2883.

21. W. I. Park, D. H. Kim, S.-W. Jung and G.-C. Yi, *Appl. Phys. Lett*. **80** (2002) 4232.

22. B. P. Zhang, N. T. Binh, K. Wakatsuki, Y. Segawa, Y. Yamada, N. Usami, M. Kawasaki and H. Koinuma, *Appl. Phys. Lett*. **84** (2004) 4098.

23. Y. B. Li, Y. Bando and D. Golberg, *Appl. Phys. Lett*. **84** (2004) 3603.

24. Z. Fan, D. Wang, P.-C. Chang, W.-Y. Tseng and J. G. Lu, *Appl. Phys. Lett.* **85** (2004) 5923.

25. T. Minami, H. Sato, H. Nanto and S. Takata, *Jpn. J. Appl. Phys. Part 2* **24** (1985) L781.

26. (a) S. Y. Myong, S. J. Baik, C. H. Lee, W. Y. Cho and K. S. Lim, *Jpn. J. Appl. Phys. Part 2* **36** (1997) 1078. (b) B. M. Ataev, A. M. Bagamadova, A. M. Djabrailov, V. V. Mamedo and R. A. Rabadanov, *Thin Solid Films* **260** (1995) 19. (c) H. J. Ko, Y. F. Chen, S. K. Hong, H. Wenisch, T. Yao and D. C. Look, *Appl. Phys. Lett*. **77** (2000) 3761. (d) V. Assuncao, E. Fortunato, A. Marques, H. Aguas, I. Ferreira, M. E. V. Costa and R. Martins, *Thin Solid Films* **427** (2003) 401.

27. (a) C. G. Van de Walle, *Phys. Rev. Lett*. **85** (2000) 1012. (b) D. M. Hofmann, A. Hofstaetter, F. Leiter, H. Zhou, F. Henecker, B. K. Meyer, S. Orlinskii, J. Schmidt and P. G. Baranov, *Phys. Rev. Lett*. **88** (2002) 045504. (c) M. D. McCluskey, S. J. Jokela, K. K. Zhuravlev, P. J. Simpson and K. G. Lynn, *Appl. Phys. Lett*. **81** (2002) 3807. (d) N. H. Nickel and K. Brendel, *Phys. Rev. B* **68** (2003) 193303. (e) Chr. van de Walle and J. Neugebauer, *Nature* **423** (2003) 626.

28. (a) C. H. Park, S. B. Zhang and S.-H. Wei, *Phys. Rev. B.* **66** (2002) 073202. (b) D. C. Look and B. Claflin, *Phys. Stat. Sol. (b)* **241(3)** (2004) 624.

29. (a) J. J. Lander, *Phys. Chem. Solids* **15** (1960) 324. (b) C. Klingshirn and E. Mollwo, *Z. Phys.* **254** (1972) 437. (c) D. Zwingel, *J. Lumin.* **5** (1972) 385. (d) D. Zwingel and F. Grtner, *Solid State Commun.* **14** (1974) 45.

30. (a) K. Iwata, P. Fons, A. Yamada, K. Matsubara and S. Niki, *J. Cryst. Growth* **209** (2000) 526. (b) X.-L. Guo, H. Tabata and T. Kawai, *J. Cryst. Growth* **237** (2002) 544. (c) S. Yamauchi, Y. Goto and T. Hariu, *J. Cryst. Growth* **260** (2004) 1.

31. D. C. Look, D. C. Reynolds, C. W. Litton, R. L. Jones, D. B. Eason and G. Cantwell, *Appl. Phys. Lett.* **81** (2002) 1830.

32. (a) Z-Z. Ye, J-G lu, H-H. Chen, Y-Z. Chen, L. Wang, B-H. Zhao and J.-Y. Huang, *J. Cryst. Growth* **253** (2003) 258. (b) A. B. M. A. Ashrafi, I. Suemune, H. Kumano and S. Tanaka, *Jpn. J. Appl. Phys. Part 2* **41** (2002) L1281.

33. K. Minegishi, Y. Koiwai, Y. Kikuchi, K. Yano, M. Kasuga and A. Shimizu, *Jpn. J. Appl. Phys. Part 2* **36** (1997) L1453.

34. J. Wang, G. Du, B. Zhao, X. Yang, Y. Zhang, Y. Ma, D. Liu, Y. Chang, H. Wang, H. Yang and S. Yang, *J. Cryst. Growth* **255** (2003) 293 .

35. J. Lu, Y. Zhang, Z. Ye, L. Wang, B. Zhao and J. Huang, *Mater. Lett.* **57** (2003) 3311.

36. X.-L. Guo, H. Tabata and T. Kawai, *J. Cryst. Growth* **237–239** (2002) 544.

37. Y. Yan, S. B. Zhang and S. T. Pantelides, *Phys. Rev. Lett.* **86** (2001) 5723.

38. (a) X. Li, Y. Yan, T. A. Gessert, C. L. Perkins, D. Young, C. DeHart, M. Young and T. J. Coutts, *J. Vac. Sci. Technol. A* **21** (2003) 1342. (b) S. Sun, G. S. Tompa, B. Hoerman, D. C. Look, B. B. Claflin, C. E. Rice and P. Masaun, *J. Electron. Mater.* **35(4)**, (2006) 766.

39. I. Volintiru, M. Creatore, W. H. van Helvoort, J. L. Linden and M. C. M. van de Sanden, *Appl. Phys. Lett.* **89** (2006) 022110.

40. C.-C. Lin, S.-Y. Chen, S.-Y. Cheng and H.-Y. Lee, *Appl. Phys. Lett.* **84** (2004) 5040.

41. C. L. Perkins, S-H. Lee, X. Li, S. E. Asher and T. J. Coutts, *J. Appl. Phys.* **97** (2005) 034907.

42. C. Wang, Z. Ji, K. Liu, Y. Xiang and Z. Ye, *J. Cryst. Growth* **259** (2003) 279.

43. A. Kobayashi, O. F. Sankey and J. D. Dow, *Phys. Rev. B* **28** (1983) 946.

44. (a) N. Y. Garces, N. C. Giles, L. E. Halliburton, G. Cantwell, D. B. Eason, D. C. Reynolds and D. C. Look, *Appl. Phys. Lett.* **80** (2002) 1334. (b) N. Y. Garces, L. Wang, N. C. Giles, L. E. Halliburton, G. Cantwell and D. B. Eason, *J. Appl. Phys.* **94** (2003) 519.

45. (a) K. Iwata, P. Fons, A. Yamada, K. Matsubara and S. Niki, *J. Cryst. Growth* **209** (2000) 526. (b) S. Yamauchi, Y. Goto and T. Hariu, *J. Cryst. Growth* **260** (2004) 1.

46. T. Yamamoto and H. Katayama-Yoshida, *J. Cryst. Growth* **214/215** (2000) 552.

47. M. Joseph, H. Tabata and T. Kawai, *Jpn. J. Appl. Phys. Part 2* **38** (1999) L1205.

48. T. Ohshima, T. Ikegami, K. Ebihara, J. Asmussen and R. Thareja, *Thin Solid Films* **435** (2003) 49.

49. (a) A. J. Marchi, J. I. Di Cosimo and C. R. Apesteguia, in *"Proceedings, 4th International Symposium on Scientific Bases for the preparation of Heterogeneous catalysts"*, Louvainla Neuve, Paper H-7, 1986. (b) A. J. Marchi, J. I. Di Cosimo and C. R. Apesteguia, in *"Proceedings, 9th International Congress on Catalysis"* (J. M. Philips and M. Ternan, Eds.), Vol. **2**, p. 529, Chem. Institute of Canada, Ottawa, 1988.

50. (a) P. Courty and C. Marcilly, in Preparation of Catalysts I, B. Delmon, P. A. Jacobs and G. Poncelet (Eds), *Stud. Surf. Sci. Catal.* **1** (1976) 119. (b) J. A. Scwarz, C. Contescu and A. Contescu, *Chem. Rev.* **95** (1995) 484.

51. (a) R. Gopichandran and K. C. Patil, *Mater. Lett.* **12** (1992) 437. (b) S. S. Manoharan and K. C. Patil, *J. Amer. Ceram. Soc.* **75** (1992) 10.

52. C. Marcilly, *Rev. Inst. Fr. Pet.* **39** (1984) 189.

53. G. Poncelet, P. Grange and J. A. Jacobs (Eds), *Stud. Surf. Sci. Catal.* **16** (1983) 485.

54. C. J. Brinker and G. W. Sherer, Sol-Gel Science, Academic Press, San Diego, 1990.

55. M. Pechini, U. S. Pat. No. 3 330 (1967) 697.

56. (a) S. T. Aruna, S. Ghosh and K. C. Patil, *Int. J. Inorg. Mater*. **3** (2001) 387. (b) S. Bhaduri, S. B. Bhaduri and E. J. Zhou, *Mater. Res*. **13** (1998) 156. (c) S. Mukasyan, C. Costello, K. P. Sherlock, D. Lafarga and A. Varma, *Sep. & Purif. Tech*. **25** (2001) 117.

57. S. Choopun, R. D. Vispute, W. Noch, A. Balsamo, R. P. Sharma, T. Venkatesan, A. Iliadis and D. C. Look, *Appl. Phys. Lett*. **75** (1999) 3947.

58. (a) M. Kadota and M. Minakata, *Jpn. J. Appl. Phys. Part 1* **37** (1998) 2923. (b) M. Kadota, T. Miura and M. Minakata, *J. Cryst. Growth* **237–239** (2002) 523.

59. P. Fons, K. Iwata, S. Niki, A. Yamada, K. Matsubara and M. Watanabe, *J. Cryst. Growth* **209** (2000) 532.

60. (a) Y. Liu, C. R. Gorla, S. Liang, N. Emanetoglu, Y. Lu, H. Shen and M. Wraback, *J. Electron. Mater*. **29** (2000) 69. (b) M. Kasuga and S. Ogawa, *Jpn. J. Appl. Phys. Part 1* **22** (1983) 794.

61. J. L. Vossen, *Phys. Thin Films* **9** (1977) 1.

62. K.-K. Kim, J.-H. Song, H.-J. Jung, W.-K. Choi, S.-J. Park and J.-H. Song, *J. Appl. Phys*. **87** (2000) 3573.

63. J. J. Moore and H. J. Feng, *Prog. Mater. Sci*. **39** (1995) 243. (b) A. G. Merzhenov, *J. Mater. Chem*. **14** (2004) 1779.

64. K. Deshpande, A. Mukasyan and A.Varma, *Chem. Mater*. **16** (2004) 4896.

65. (a) B. Li, A. Mukasyan and A.Varma, *Mat. Res. Innovat*. **7** (2003) 245. (b) L. Li, I. Saito, K. Saito and T. Akiyama, *J. Alloys Compd*. **372** (2004) 218.

66. H. Takeya, A. Matsumato, K. Hirata, Y. S. Sung and K. Togano, *Physica C* (Amsterdam) **412-414** (2004) 111.

67. C. Julien, C. Letrenchant, M. Lemal, S. Ziolkiewicz and S. Castro-Garcia, *J. Mater. Sci.* **37** (2002) 2367.

68. (a) S. Deka, R. Pasricha and P. A. Joy, *Chem. Mater.* **16** (2004) 1168. (b) Y. Sharma, N. Sharma, G. V. Subba Rao, B. V. R. Chowdari, *Adv. Func. Mater.* **17** (2007) 2855.

69. (a) P. Bera, S. T. Aruna, K. C. Patil and M. S. Hegde, *J. Catal.* **186** (1999) 36. (b) P. Bera , K. R. Priolkar, A. Gayen, P. R. Sarode, M. S. Hegde, S. Emura, R Kumashiro, V. Jayaram and G. N. Subbanna, *Chem. Mater.* **15** (2003) 2049. (c) P. Bera, K. C. Patil, V. Jayaram, M. S. Hegde and G. N. Subbanna, *J. Catal.* **196** (2000) 293.

70. M. H. Sarvari and H. Sharghi, *J. Org. Chem.* **69** (2004) 6953.

71. M. V. Twigg, editor, 2nd ed, Catalyst handbook, London: Wolfe Press, 1989, Chapter 6, Water-gas shift.

72. T. Conant, A. M. Karim, V. Lebarbier, Y. Wang, F. Girgsdies, R. Schlögl and A. Datye, *J. Catal.* **257** (2008) 64.

73. M. Vijayaraj and C.S. Gopinath, *J. Catal.* **226** (2004) 230.

74. L. Bollmann, J. L. Ratts, A. M. Joshi, W. Damion Williams, J. Pazminoa, Y. V. Joshi, J. T. Miller, A. Jeremy Kropf, W. Nicholas Delgass and F. H. Ribeiro, *J. Catal.* **257** (2008) 43.

75. (a) A. Sankany, Z. Zsoldos, B. Furlong, J. W. Hightower and L. Guczi, *J. Catal.* **141** (1993) 566. (b) P. S. Wehner and B. L. Gustafson, *J. Catal.* **135** (1992) 420.

76. E. Galloway, M. Armbrüster, K. Kovnir, M. S. Tikhov and R. M. Lambert, *J. Catal.* **261** (2009) 60.

77. K. Maeda, T. Takata, M. Hara, N. Saito, Y. Inoue, H. Kobayashi and K. Domen, *J. Am. Chem. Soc.* **127** (2005) 8286.

78. (a) M. Kurtz, J. Strunk, O. Hinrichsen, M. Muhler, K. Fink, B. Meyer and C. Wöll, *Angew. Chem.* **44** (2005) 2790. (b) S. Polarz, J. Strunk, V. Ischenko, M. W. E. van den Berg, O. Hinrichsen, M. Muhler, and M. Driess, *Angew. Chem. Int. Ed.* **45** (2006) 2965.

Chapter 2
Experimental Methods

2 Experimental Methods

Development of novel functional materials with unique properties is entirely based on the synthetic strategies followed for the preparation of such materials. Usually it requires complex procedures. However, in the present case of ZnO based materials, SCM has been employed which leads to the novel material. Success of the present materials preparation was due to favorable reaction condition produced by the reactant itself, such as in situ generation of ammonia from the decomposition of urea. Introduction and theory of various physical, structural and spectroscopic characterization techniques employed in the characterization of ZnO based materials in the investigation has also been desired.

2.1 Catalyst Preparation

Emphasis is made on SCM to prepare heteroatoms incorporated ZnO. This is an alternative synthetic method for producing a wide variety of simple and complex inorganic materials having excellent physicochemical properties. The method is gaining more interest for the preparation of variety of materials, such as, nitrides, carbides, many composite materials and to enhance metal ion distribution on oxides etc. Furthermore, it is characterized by fast heating rates, high-reaction temperatures, and short reaction times. Owing to high exothermicity of the system, combustion temperature rapidly reaches $\geq 700°C$ and converts the precursor material to fine crystallites of the desired complex oxide.

2.1.1 Aspect of Nitrogen Doped ZnO Synthesis ($ZnO_{1-x}N_x$)

Nitrogen doped ZnO ($ZnO_{1-x}N_x$) has been prepared through SCM. All the chemicals were of analytical grade and used as such without further purification. $Zn(NO_3)_2, 6H_2O$ (Merck) as Zn precursor and urea (NH_2CONH_2) (Merck) as fuel was used for the synthesis. For the synthesis of UZ1 (the numeral given in the sample codes immediately after UZ indicates the mole ratio of urea/$Zn(NO_3)_2$ used) equimolar amount (0.04 mol) of $Zn(NO_3)_2.6H_2O$ and urea was taken in a 250 ml beaker with 5 ml of distilled water. The aforementioned mixture was stirred until a uniform solution resulted, and then the mixture was inserted into a muffle furnace that was maintained at 500ºC. Water evaporated within the first few minutes, followed by

ignition of the reactant mixture with yellow flames, yielding a solid $ZnO_{1-x}N_x$ material. However, under the SCM conditions, zinc nitrate forms a gel with urea before the actual combustion begins. The solid product was collected after the completion of the combustion process. After this, selected samples were also calcined between 500ºC and 950ºC at different temperatures for 6 hrs for further studies. Other composition of $ZnO_{1-x}N_x$ also had been prepared by the same method, but with different urea/$Zn(NO_3)_2$ molar ratios of 0.8, 1, 3, 5, 7 and 10.

For evaluating the relative exothermicity of combustion reactions involving different fuels, a simplified theoretical approach has been taken. The following combustion reactions that are balanced to give pure ZnO have been considered. The combustion synthesis can be expressed (but over simplified) as follows:

(i) $(NH_2)_2CO + Zn(NO_3)_2. 6H_2O \rightarrow ZnO_{1-x}N_x$

$Zn(NO_3)_2\ 6H_2O + (\phi)(NH_2)_2CO + [1.5\phi-2.5]O_2 \rightarrow$

$$ZnO + [1+\phi]\ N_2 + \phi\ CO_2 + [6+2\phi]\ H_2O \qquad (2.1)$$

(ii) $NH_2CH_2CO_2H + Zn(NO_3)_2. 6H_2O \rightarrow ZnO$

$Zn(NO_3)_2\ 6H_2O + \phi\ (NH_2CH_2CO_2H) + [2.25\phi-2.5]O_2 \rightarrow$

$$ZnO + [1+0.5\phi]\ N_2 + 2\phi\ CO_2 + [6+2.5\phi]\ H_2O \qquad (2.2)$$
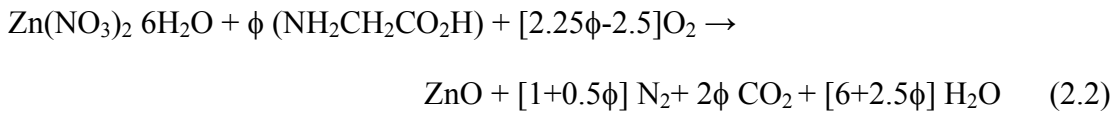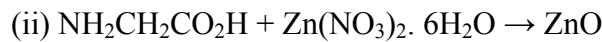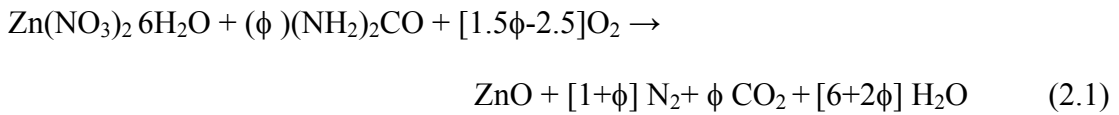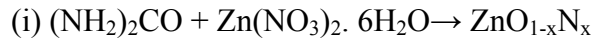
In the above equations, ϕ = ratio between fuel and metal nitrate, when ϕ = stoichiometric means that the initial mixture does not require atmospheric oxygen for complete oxidation of fuel. Depending on the fuel to metal nitrate ratio, synthesis of the ZnO powder varies. For *glycine* $\phi = 1.11$ and for *urea* $\phi = 1.66$ corresponds to the situation of an 'equivalent stoichiometric ratio', which implies that the oxygen content of zinc nitrate can be completely reacted to oxidize/consume glycine/urea exactly. As a result, ZnO, CO_2, H_2O, N_2 and oxides of nitrogen can be formed directly from the reaction between fuel and oxidizer without the necessity of getting oxygen from outside. $\phi > 1.66$ (<1.66) for urea implies fuel rich (lean) conditions. Fuel lean condition is characterized by a relatively slow, essentially flameless reaction.

Heat of combustion reaction has been determined using the relation:

$$\Delta H_{combustion} = (\Delta H_f)_{products} - (\Delta H_f)_{reactants} \qquad (2.3)$$

The combustion reactions have been found to occur on dehydration of gel at a temperature above the ambient. However, for simplification in the calculation of exothermic heat, the reaction temperature has been assumed to be 27°C. The heat evolved in the combustion will raise the reaction temperature and that of the products. In a complete combustion reaction, total reactant is converted into product in a very small time scale. With this condition, the system has been assumed to be adiabatic and the adiabatic flame temperature can be calculated by solving the equation

$$\Delta H_{combustion} = \int_{298}^{Tad} \left(\sum nC_p\right)_{product} dT \qquad (2.4)$$

Where n is the number of moles of a reaction product, T_{ad} is the adiabatic flame temperature and C_p is specific heat at constant pressure.

The values indicate that the heat of combustion is significant for urea and the heat can raise the temperature of the products (referred as T_{ad}) above 1100°C. The high value of adiabatic flame temperature suggests favorable condition for combustion to occur. It may be mentioned here that in the longer time scale the experimental condition is far from adiabatic and indeed, the temperature will rise for a very short period of time.

Table 2.1: Calculated T_{ad} of combustion reactions between fuel to zinc nitrate:

Relevant Thermodynamic data		
Compound	H_f (KJ/mol)	C_p (J/mol.K)
O_2 (g)	0	26.56 + 0.00913T
N_2 (g)	0	27.0126 +0.00556T
CO_2 (g)	0	34.177 + 0.0198T
H_2O (g)	-241.82	43.428+ 0.011508 T
Urea[c]	-333.1	-
Glycine[c]	-392.1	-
Zinc Nitrate[c]	-2304	-
Zinc Oxide[c]	350.5	39.3835
(c) = Crystalline , (g) =Gas		
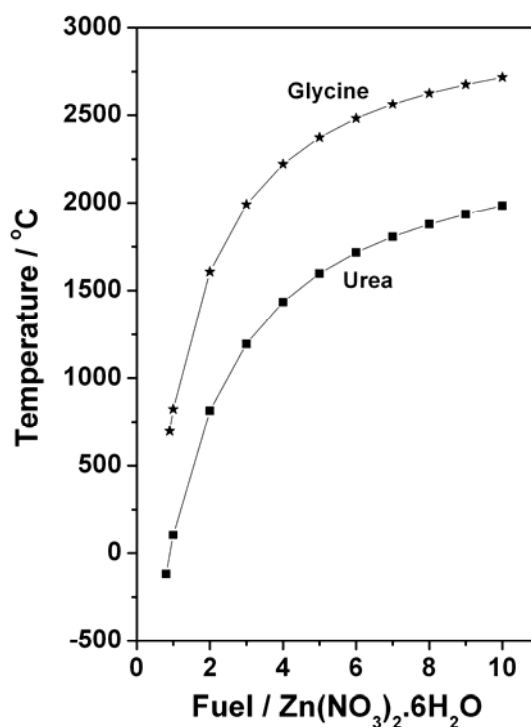
Figure 2.1*: T_{ad} as function of the molar ratio of fuel/zinc nitrate for urea and glycine.*

With increasing fuel to metal nitrate ratio, heat of formation of the reaction (ΔH_f) as well as T_{ad} value increases for both the fuels (Figure 2.1). However, in case of urea rise, in T_{ad} temperature is lesser than that of glycine by 750ºC. It is also to be noted that the estimated temperature difference remains 750ºC for a given value of fuel content. Further, the high temperature estimated with glycine indicates to be the best fuel but is also likely to lead to bigger particle. Another big difference between use of urea and glycine is the amount of nitrogen available with each mole of urea is double than that of glycine. However, in the case of nitrogen-doping preparation using various amount of urea, the nature of evolved gases varies which can be written as follows:

For 1:1 urea to metal nitrate:

$$Zn(NO_3)_2 \, 6H_2O + (NH_2)_2CO \rightarrow ZnO + NH_3 + NH_2OH + CO_2 + 5H_2O + 2NO_2 \quad (2.5)$$

For 1:6 urea to metal nitrate:

$$Zn(NO_3)_2 \, 6H_2O + 6(NH_2)_2CO + 2O_2 \rightarrow ZnO + 6NH_3 + 6NH_2OH + 6CO_2 + 2NO_2 \quad (2.6)$$
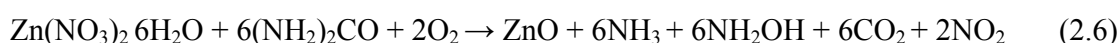
For 1:10 urea to metal nitrate:

$$Zn(NO_3)_2 \, 6H_2O + 10(NH_2)_2CO + 10O_2 \rightarrow$$

$$ZnO + 9NH_3 + 7NH_2OH + 2H_2O + 10CO_2 + 6NO_2 \qquad (2.7)$$
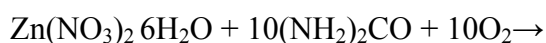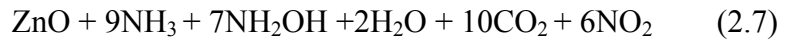
With increase in urea, more and more NH_3 and CO_2 were produced and simultaneously T_{ad} also increases which becomes the major cause to drive away the doped nitrogen from bulk towards surface. Thus with increase in urea concentration in the reactant mixture amount of bulk doped nitrogen decreases and surface nitrogen content increases.

However, for preparation of $(ZnO_{1-x}N_x)$ through conventional methods, N_2O or NH_3 has been used as a nitrogen source. Indeed, N_2O plasma was used to prepare nitrogen doped ZnO film by PLD [1]. Researchers found that nitrogen doping was enhanced using the active N formed by N_2O gas flowing through an ECR source. It has been speculated that during the preparation of the $(ZnO_{1-x}N_x)$ material through urea combustion method, ammonium nitrate was formed. At high temperature that was dissociating to produce NO_2 and NH_3. Thus in situ produced NH_3 gas at high temperature was playing a favorable role in increasing the N-content and improving the material quality.

Another approach of conventional N-doping of oxides requires ammonia treatment at high temperatures. Wang *et al*. [2] suggested that optimum NH_3 flux in the MOCVD chamber was required to dope nitrogen effectively in the ZnO lattice. Nitrogen doping decreased with enriching the amount of NH_3 in the chamber. 100 % ammonia environment facilitates O–H bond formation on the surface, which is stronger than Zn-N bond and prohibits the amount of nitrogen in the bulk. In the SCM with increasing urea concentration, more and more NH_3 and CO_2 were produced, helping to segregate nitrogen on the surface and bulk nitrogen amount decreases with the formation of $ZnCO_3$. When urea and zinc ratio was 1:1 (or below stoichiometry value) ammonia concentration in the environment and temperature of the reaction was optimum for bulk nitrogen doping.

ZnO is well known for oxygen vacancies, and a simple heating of ZnO to $\geq$ 400ºC can make it yellow in color due to oxygen vacancies; however again it becomes white in color at room temperature due to oxygen uptake. Conventional procedure for nitridation is annealing of any oxide under the flow of ammonia for several hours to few days. We have tried to combine both the aforementioned facts. It is also to be underscored that the actual combustion time is about 30-50 seconds,

although the entire preparation requires about 8-10 minutes. Time required for initial drying of reaction mixture requires few minutes, followed by increase in temperature of the solid mass and subsequent combustion. Indeed during the above combustion, in-situ production of ammonia due to urea decomposition suggests generation of an overall reduction condition and this ammonia acts as the nitrogen source. At high temperature during the reaction condition zinc oxide crystallites are in its nascent stage with lots of defects and the same has been growing under the environment of ammonia. During the growth of zinc oxide in SCM at high temperature, both zinc ion and ammonia were in their nascent form. Nascent clusters of metal oxides with plenty of defects are very likely to interact with ammonia faster to produce nitrogen doped materials. Hence, this procedure might be used to incorporate nitrogen into number of the metal oxides and it is worth exploring on this aspect.

2.1.2 Nitrogen and Sulfur Co-doped ZnO ($ZnO_{1-x-z}N_xS_z$)

Nitrogen and sulfur codoped ZnO was prepared by the same procedure as mentioned in the section 2.1.1 by SCM, using different ratio of urea and thiourea as fuel. $Zn(NO_3)_2,6H_2O$ (Merck) as zinc precursor and Urea and thiourea (NH_2CSNH_2) (Loba Chemie) as fuel was used without any further purification. In a typical synthesis of $ZnO_{1-x-z}N_xS_z$ equimolar amount (0.04 mol) of $Zn(NO_3)_2,6H_2O$ as well as fuel, but with different ratio of urea and thiourea (varied from 0 to 0.33) was taken in a 250 ml beaker with 10 ml of distilled water. Above mixture was stirred and heated up to 50ºC until a uniform solution occurs. This solution was then introduced into a muffle furnace preheated at 500ºC. Water evaporates in first few minutes followed by ignition of reactant mixture, yielding a solid $ZnO_{1-x-z}N_xS_z$ material. The solid product was collected after the completion of the combustion process. All the other composition of $ZnO_{1-x-z}N_xS_z$ material also had been prepared by the same method. The amine group of urea and -C=S group of thiourea are the main source of N and S, respectively. Furthermore, with variation in ratio of urea and thiourea average combustion temperature, reaction condition and amount of S change as well.

2.1.3 Gallium and Nitrogen Co-doped ZnO ($Zn_{1-z}Ga_z)(O_{1-x}N_x$)

($Zn_{1-z}Ga_z)(O_{1-x}N_x$) materials were prepared by the simple SCM, following the same procedure as mentioned in the section 2.1.1. In typical synthesis,

$Zn(NO_3)_2,6H_2O$ (Merck) as zinc precursor, Ga metal (Sigma-Aldrich) as Ga source and urea as fuel was used without any further purification. 100 ml of 0.1(M) gallium nitrate solution was prepared by dissolving 6.975 gm of Ga in minimum volume of concentrated nitric acid and the required distilled water was added to make up to 100 ml in a standard measuring flask. This solution was used as Ga source.

In a typical synthesis of $(Zn_{1-z}Ga_z)(O_{1-x}N_x)$, urea/(Zn + Ga) molar ratio was chosen to be either 3, 5, or 7 and Zn/Ga ratio varied between 49 and 6. Metal nitrate solution and urea was taken in a 250 ml beaker with 10 ml of distilled water. Above mixture was stirred till a uniform solution occurs. This was then introduced into a muffle furnace maintained at 500ºC. Water evaporates in first few minutes followed by ignition of reactant mixture, yielding a solid $(Zn_{1-z}Ga_z)(O_{1-x}N_x)$ material. The solid product was collected after the completion of the combustion process. Other composition of $(Zn_{1-z}Ga_z)(O_{1-x}N_x)$ has been prepared by the same method. After this, selected materials were also calcined at 300ºC, 550ºC, 800ºC for 4 hrs for further characterization and this has been mainly to explored the thermal stability of the materials.

2.1.4 Indium and Nitrogen Co-doped ZnO $(Zn_{1-z}In_z)(O_{1-x}N_x)$

Nitrogen and indium co-doped ZnO was prepared by the same procedure as mentioned in the section 2.1.3 following SCM. Instead of $Ga(NO_3)_3$, $In(NO_3)_3$ (Sigma Aldrich) solution was employed as source of indium to prepare $(Zn_{1-z}In_z)(O_{1-x}N_x)$ materials.

2.2 Method of Catalytic Activity Studies

2.2.1 Rhodamine B Degradation

Photocatalysis degradation of dye was performed with a double jacketed quartz reactor that was equipped with a 400-W Hg lamp; through the decomposition of rhodamine B. Water circulation in the outer jacket of the above reactor maintains the solution temperature at 25°C. The absorption spectrum of the rhodamine B solution was obtained from an ultraviolet-visible-light (UV-Vis) spectrometer (Shimadzu, Model UV-2500PC). Decomposition of rhodamine B was followed with 532 nm band in the absorption spectrum as a function of light exposure time.

2.2.2 **Dehydrogenation of Alcohols**

Vapor phase experiments were performed at atmospheric pressure in a fixed bed, vertical, down-flow, integral glass reactor placed inside a double-zone furnace (Geomechanique, France). Fresh catalyst was charged each time at the center of the reactor in such a way that the catalyst was sandwiched between the layers of inert porcelain beads. Catalyst and porcelain beads are separated by glass wool. The upper portion of the reactor served as a vaporizer cum pre-heater. All heating and temperature measurements were carried out using 'Aplab' temperature controller and indicator instruments. A K-type thermocouple was positioned at the center of the catalyst bed to monitor the exact temperature of the catalyst. The reactant mixture was fed into the reactor using a syringe pump (Braun, Germany) at a desired flow rate. Reaction products were collected from a condenser fixed below the reactor and circulated with ice cold water. Products were analyzed using gas chromatography (GC) equipment (Agilent, Model 6890 J-413) that consisted of a HP 5.5% phenyl methyl siloxane capillary column that was equipped for flame ionization detection (FID) and gas chromatography-mass spectroscopy (GC-MS) (Shimadzu, Model GC-17A, coupled with a Model QP 5000 mass spectrometer).

Catalytic dehydrogenation of alcohol was carried out using 1 g of catalyst with particle size between 10-20 mesh. The fresh catalyst was activated in a sufficient flow (20 ml/min) of dry N_2 at 673 K for 2 hours before the reaction and then brought to the desired reaction temperature with a stream of N_2 (20 ml/min). The reactant mixture was fed using a syringe pump without any carrier gas. Analytical grade cyclohexanol, isobutanol or 2-butanol from Merck was used in the present study. The reproducibility for different products was checked experimentally, and the measurements were repeated three times with a relative error of ± 2% for high conversion/selectivity measurements and ± 5% for low conversion/selectivity measurements. The thermal process without catalysts was negligible in all the cases.

2.2.3 **Anisole Acylation**

Anisole acylation reactions were performed in a glass (batch) reactor on a standard substrate, namely anisole and acetyl chloride. Anisole (1 mmol) was added to a mixture of ZnO (powder, 0.04 g, 0.5 mmol) and acid chloride (1 mmol) at room

temperature and stirred with a magnetic stirrer. Color (pink) developed immediately and darkened with progress of the reaction. The reaction mixture was kept at room temperature with stirring till the reaction is complete. The solid mass was then eluted with dichloromethane (CH_2Cl_2) (20 ml), and CH_2Cl_2 extract was then washed with an aqueous solution of sodium bicarbonate and dried over anhydrous sodium sulfate. Evaporation of solvent furnished practically pure product. The identification of anisole acylation products were confirmed by GC.

2.2.4 Catalytic Reactor for Nitrogen Fixation Reaction

The reactor set up used for the nitrogen fixation to ammonia consists of mass flow controllers through which the reactant gases (N_2:H_2 = 1:3) pass at a controlled flow at a rate of 60 ml/min. The gases were mixed in the mixing chamber and fed to a series of traps for removing CO_2 (anhydrous KOH), moisture (fused $CaCl_2$ and molecular sieves) and O_2 (Cu-mesh maintained at a temperature of 300ºC). The mixture of gases was then allowed to pass through a quartz reactor loaded with the catalyst, which was maintained at a temperature of 350ºC. The out going gases were then trapped in standardized H_2SO_4 (0.01N) solution. The acid trap was designed in such a way that the gases were bubbled twice in two compartments before it is escaping to atmosphere, ensuring the maximum trapping of NH_3, which is formed. Ammonia was estimated by the volumetric titration of the acid with NaOH (0.001) solution after the reaction. For rapid gas dissolution the acid trap solution was stirred on a magnetic stirrer and the trap was placed inside a beaker in the ice cold water. This ensures cooling of hot gases coming out of the reactor outlet and thus maximizes the solubility of the NH_3 in acid solution.

2.3 Physicochemical Characterization

2.3.1 Introduction

Detailed physicochemical characterization is one of the crucial aspects to understand any material including catalyst. Spectroscopy, microscopy, diffraction and methods based on adsorption and desorption are the routine material characterization techniques. It gives information about crystallinity, surface structure, nature of active sites, particle size and morphology, acidity, and other characteristic features. It also

gives the understanding of nature and chemical state of dopant. Further, how activity and selectivity change with structural and electronic properties of the catalyst is one of the major goals in catalysis research.

The materials were characterized by adopting various physico-chemical methods such as X-ray diffraction analysis (XRD), Raman spectroscopy, surface area and pore volume measurements, scanning electron microscopy (SEM), Thermo Gravimetric analysis - Differential thermal analysis (TG-DTA), X ray photoelectron spectroscopy (XPS), Electron Paramagnetic Resonance (EPR) and Secondary ion mass spectrometry (SIMS). This knowledge helps to understand the materials as well as catalyst better, so that materials can be improved or designed in better way as required. The following part gives a brief account of the theory and principle of various characterization techniques used for the current study. The procedure for each experimental technique is also described in this part.

2.3.2 Theory and Experimental Procedures

2.3.2.1 X-ray Diffraction (XRD)

XRD is one of the oldest and most frequently exploited techniques in catalyst characterization. It has been the most important technique for determining the structure of materials characterized by long-range order. It is used to identify crystalline phase(s) of the catalyst by means of lattice structural parameters and crystallinity [3]. The work presented in the thesis, emphasizes on the synthesis and characterization of heteroatom doped ZnO. Therefore, crystalline nature, impurity phase and crystal type could be identified from their XRD patterns. As the name suggests, the sample is usually in a powder form, consisting of fine grains of crystalline material.

X-rays are electromagnetic radiation with typical photon energies in the range of 1000 eV - 10000 eV. For diffraction applications, only short wavelength x-rays in the range of a few angstroms to 0.1 angstrom (1 keV -12 keV) are used. Because this wavelength of X-rays is comparable to the size of atoms, they are ideally suited for probing the structural arrangement of atoms and molecules in a wide range of materials. The energetic X-rays can penetrate deep into the materials and provide information about the bulk structure.
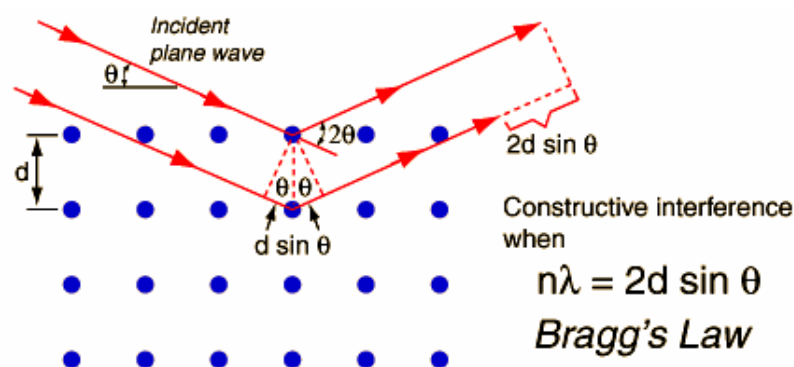
Figure 2.2: *Derivation of Bragg's Law using the reflection geometry and applying trigonometry. The lower beam must travel the extra distance (AB + BC) to continue traveling parallel and adjacent to the top beam.*

X-ray diffraction occurs in the elastic scattering of X-ray photons by atoms from the periodic lattice. The scattered monochromatic X-rays that are *'in-phase'* give constructive interference. If the distance between two periodic lattice planes is 'd' and the angle between the incoming X-rays, and the normal to the reflecting lattice plane is 'θ' and λ is the wavelength of the X-rays then the well-known Bragg's equation is

$$n\lambda = 2d\,\sin\theta \; ; \; n = 1, 2, 3 \qquad (2.8)$$

where *n* is an integer called the order of the reflection [4] (as shown in Figure 2.2).

By measuring the angle, 2θ, under which constructively interfering X-rays leave the crystal, the Bragg's equation gives the corresponding lattice spacing, which is characteristic for a particular compound. Width of the diffraction peaks signifies the dimension of the reflecting planes. It is known that the width of a diffraction peak increases when the crystallite size is reduced below a certain limit (<100 nm). Therefore, XRD patterns can be used to estimate the crystallite average size of very small crystallites from XRD line broadening is the Scherrer formula [5]

$$t = 0.9\lambda \,/\, \beta \, \text{Cos}\,\theta \qquad (2.9)$$

where *t* is the thickness of the crystallites (in Å), λ is the X-ray wavelength, θ is the diffraction angle and β is the full width half maxima of the diffraction peak.

PXRD patterns of all the catalysts reported in this work were recorded using a Rigaku Giegerflex instrument equipped with Cu Kα radiation (λ = 1.5406 Å) with a Ni-filter.

2.3.2.2 **Rietveld Refinement**

In a single crystal structure refinement, the differences between the intensities measured in a diffraction experiment and those calculated from an approximate model are minimized by adjusting the atomic parameters. Since the intensities of individual reflections in a powder pattern are often obscured by overlap in 2θ, this method cannot be applied satisfactorily to powder data. In 1969, however, Rietveld [6] developed a whole new profile fitting method for the refinement of crystal structures using neutron powder diffraction data and thereby revolutionized the scope of powder diffraction. He minimized the difference between the observed powder diffraction pattern and the pattern calculated from model. By refining the fit of the powder pattern rather than that of the individual reflection intensities (which would first have to be extracted from the powder pattern), he was able to circumvent the overlap problem. In the late 70's the method was adapted to accommodate the more complex peak shape inherent to X-ray powder patterns, and has since become the standard refinement method for all powder X-ray data. In Rietveld refinement procedure, initially a powder pattern is calculated from an approximate structural model using estimated peak shape and approximate unit cell parameters. This is compared with the experimental data and the difference between the two is calculated. This difference is then minimized by refining the profile parameters (width and asymmetry of the peaks, 2θ zero point, unit cell dimensions) and structural parameters (atomic coordinates and thermal parameters). The refinement is continued with progressively better profile and structural parameters until the difference plot approaches the statistical scatter of the data.

Generally used softwares for Rietveld refinement of the diffraction data are General Structure Analysis System (GSAS), FullProf, X-ray Rietveld System (XRS-82), Rietveld Analysis (RIETAN), DBWS, etc. In our studies, we have used GSAS for Rietveld analysis extensively; X'Pert Plus (Rietveld refinement package provided by Panalytical) is also used in some cases [7].

2.3.2.3 **Secondary Ion Mass Spectrometry (SIMS)**

SIMS is a technique used to analyze the composition of solid surfaces and thin films. It operates on the principle that bombardment of a material with a beam of ions

with high energy (1-30 keV) results in the ejection or sputtering of atoms from the material. A small percentage of these ejected atoms leave as either positively or negatively charged ions, which are referred to as 'secondary' ions. Surface of the samples are bombarded with primary ion gun in high vacuum with pressures below 10^{-4} Pascal (roughly 10^{-6} mbar). Ions of gaseous elements are usually generated with duo plasmatrons or by electron ionization, for instance noble gases (Ar^+, Xe^+), oxygen (O^-, O_2^+), or even SF_5^+ ionized molecules (generated from SF_6) and C_{60}^+ respectively. A second source type, the surface ionization source, is singularly used to generate Cs^+ primary ions. The proper choice of primary ion beam is therefore important in enhancing the sensitivity of SIMS. Oxygen primary ions are often used to investigate electropositive elements or those with low ionization potentials due to an increase of the generation probability of positive secondary ions, while cesium primary ions often are used when electronegative elements are being investigated [8]. Only charged secondary ions emitted from the material surface through the sputtering process are used to analyze the chemical composition of the material, these represent a small fraction of the particles emitted from the sample. These secondary ions are measured with a mass spectrometer to determine the elemental, isotopic, or molecular composition of the surface. The collection of these sputtered secondary ions and their analysis by mass-to-charge spectrometry gives information on the composition of the sample, with the elements present identified through their atomic mass values. Counting the number of secondary ions collected can also give quantitative data on the sample's composition. Thus, SIMS works by analyzing material removed from the sample by sputtering, and is therefore a locally destructive technique.

SIMS studies were performed with a QMS-based instrument (Hiden Analytical). Bombardment was carried out with a 5 keV O and Cs ions. The primary ion current was 400 nA for the oxygen beam and 100 nA for the cesium beam. The beam was rastered over an area of 1000 μm^2; however, the secondary ions were collected from the central area of 200 μm^2.

2.3.2.4   Surface Area Determination by BET Method

The BET (Brunauer-Emmett-Teller) method is the most widely employed procedure to determine the surface area of the solid materials by using the BET equation:

$$P/V_{ads} (P_0-P) = 1/V_mC + [(C-1)/V_mC] \times (P/P_0) \qquad (2.10)$$

where P = adsorption equilibrium pressure, P_0 = standard vapor pressure of the adsorbent, V_{ads} = volume at STP occupied by molecules adsorbed at pressure P, V_m = volume of adsorbate required for a monolayer coverage, and C = constant related to heat of adsorption.

To differentiate the adsorption mechanism between micro-pore and to that in meso and macro-pores, the *t-plot* analysis was developed by Lippens and de Boer and the same was applied [9]. The method consists of plotting the adsorption isotherm in terms of the volume of the adsorbate versus the statistical film thickness, *t*. The pore size distribution is obtained from the analysis of the desorption isotherms by applying the BJH expand model [10] which involves the area of the pore walls and uses the Kelvin equation to correlate the partial pressure of nitrogen in equilibrium with the porous solid to the size of the pores where the capillary condensation takes place.

The BET surface area and pore volume of the catalysts were determined by N_2 adsorption-desorption method at liquid N_2 temperature using Quantachrome Nova 1200 adsorption unit. Sample was degassed at 200ºC for about 2 hours till the residual pressure was $<10^{-3}$ Torr. The isotherms were analyzed in a conventional manner that includes the BET surface area in the region of the relative pressure *P/P₀* = 0.05 to 1 with the assumption for the nitrogen molecular area in an adsorbed monolayer is 0.16 nm^2. The total pore volume of each samples were taken at *P/P₀* = 0.95.

2.3.2.5 UV-Visible Spectroscopy

Absorption spectroscopy in the visible region has long been an important tool to the analyst [11]. Appearance of colour arises from the property of the colored material to absorb selectively and reflect its complementary colour which falls within the visible region of the electromagnetic spectrum. Absorption of energy leads to a transition of electron from ground state to an excited state which is governed by the following equation

$$\Delta E = h\nu = hc/\lambda \qquad (2.11)$$

where *h* represents Planck's constant, *v* is the frequency of radiation, *c* is the velocity of light and λ is the radiation wavelength.

Thus from the equation it seems that the UV-energy is quantized and hence a single discrete line should be obtained from a single electronic spectrum. However, this is not the case of reality as excitation of electronic energy levels would also involve excitation of the embedded vibrational and rotational energy levels of an atom, thus giving rise to a broad absorption band [12]. The intensity of the absorption band depends on three factors namely (a) transition probability, (b) population of states and (c) concentration or path length.

Almost all relationships between intensities of incident and transmitted radiation and the concentration and path-length is governed by Beer-Lambert's law which is written as

$$I = I_0 \exp(-\kappa c l)$$

$$\log(I_0/I) = A = \kappa c l \qquad (2.12)$$

where I = Intensity of the emitted radiation, I_0 = Intensity of the incident radiation, κ = constant, c = concentration and l = path length. A is known as the absorbance or the optical density and κ, the constant generally represented as ε, known as the molar absorption coefficient.

In a dual beam spectrophotometer, light from either the visible or ultraviolet source enters the grating monochromator before it reaches the filter. Broad band filters contained in a filter wheel are automatically indexed into position at the required wavelengths to reduce the amount of stray light and unwanted orders from the diffraction grating. The light from the source is alternatively split into one of the two beams by a rotating mirror called a chopper; one beam is passed through the sample and the other through the reference. The detector alternately sees the beam from the sample and then the reference. Its output which ideally would be an oscillating square-wave gives the ratio of I to I_0 directly i.e. the reference correction is made automatically.

Array-detector spectrophotometers allow rapid recording of absorption spectra. Dispersing the source light after it passes through a sample allows the use of an array detector to simultaneously record the transmitted light power at multiple wavelengths. These spectrometers use photodiode arrays as the detector. The light source is a continuum source such as a tungsten lamp. All wavelengths pass through

the sample. The light is dispersed by a diffraction grating after the sample and the separated wavelengths fall on different pixels of the array detector. The resolution depends on the grating, spectrometer design, and pixel size, and is usually fixed for a given instrument.

Diffuse reflectance UV-Vis measurements were performed on a spectrophotometer (Shimadzu, Model UV-2550) with spectral grade $BaSO_4$ as the reference material.

2.3.2.6 **Electron Paramagnetic Resonance (EPR) Spectroscopy**

EPR, often called Electron Spin Resonance (ESR), is a branch of spectroscopy in which electromagnetic radiation (usually of microwave frequency) is absorbed by molecules, ions, or atoms possessing electrons with unpaired spins, *i.e.* electronic spin S > 0. In EPR, the sample material is immersed in a strong static magnetic field and exposed to an orthogonal low- amplitude high-frequency field. ESR usually requires microwave-frequency radiation (GHz). With ESR, energy is absorbed by the sample when the frequency of the radiation is appropriate to the energy difference between two states of the electrons in the sample, but only if the transition satisfies the appropriate selection rules. In EPR, because of the interaction of the unpaired electron spin moment (given by two projections, *ms* = ± 1/2, for a free electron) with the magnetic field, the so-called Zeeman effect, there are different projections of the spin gain different energies.

$$E_{ms} = gm\mathrm{BB_o}ms \qquad (2.13)$$

Here, B_o is the field strength of the external magnetic field. The SI units for magnetic field is tesla, but, in EPR, gauss (1 G = 0.0001 T) is still used. Other terms in equation (2.13): *ms*- is a spin projection on the field (ms = ± 1/2 for a free electron), m*B* is the Bohr magneton [13]. EPR spectra were recorded on a Bruker EMX spectrometer operating at X band frequency and 100-kHz field modulation.

2.3.2.7 **X-Ray Photoeletron Spectroscopy (XPS)**

All solid materials interact with their surroundings through their surfaces. The physical and chemical composition of these surfaces determines the nature of the interactions. Their surface chemistry will influence factors such as corrosion rates,

catalytic activity, adhesive properties, contact potential, and failure mechanisms. Surfaces, therefore, influence many crucially important properties of the solid. Despite the undoubted importance of surfaces, only a very small proportion of the atoms of most solids are found at the surface. Nonetheless the proportion of surface contribution increases with a decrease in particle size, especially below 100nm.

XPS is based on the photoelectric [14] effect discovered by Heinrich Hertz and explained later by Albert Einstein, which involves the bombardment of a solid surface with X rays and the measurement of the concomitant photoemitted electrons. XPS is a widely used technique for obtaining chemical information of various material surfaces. The low kinetic energy ($0 \leq 1500$ eV) of emitted photoelectrons limit the depth from which it can emerge, so that XPS is a very surface-sensitive technique and the sample depth is in the range of few nanometers. Photoelectrons are collected and analyzed by the instrument to produce a spectrum of emission intensity versus electron binding (or kinetic) energy.

In general, the binding energies of the photoelectrons are characteristic of the element from which they are emanated, so that the spectra can be used for surface elemental analysis. Small shifts in the elemental binding energies provide information about the chemical state of the elements on the surface. The peak area can be used (with appropriate sensitivity factors) to determine the surface compositions of the material. Therefore, the high-resolution XPS studies can provide the chemical state information of the surface.
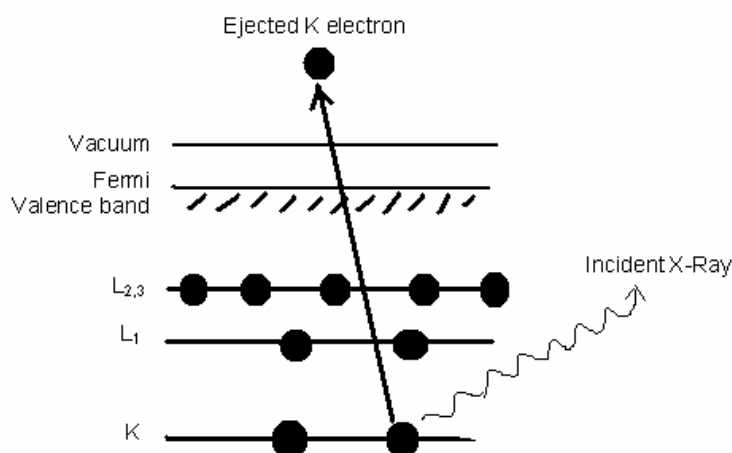
Figure 2.3: *Schematic diagram of the XPS process, showing photo ionization of an atom by the ejection of a 1s electron.*

The photoemitted electrons have discrete kinetic energy that is the characteristics of the emitting atoms and their bonding states. The kinetic energy, E_k of these photoelectrons is determined from the energy of the incident X-ray radiation (hν) and the electron binding energy (E_b) is given as

$$E_k = hν - E_b \tag{2.14}$$

The experimentally measured energies of the photoelectrons are given as

$$E_k = hν - E_b - E_w \tag{2.15}$$

where E_w is the work function of the spectrometer.

The process of photoemission is shown schematically in Figure 2.3, where an electron from the K shell is ejected from the atom (1s photoelectron). Once a photoelectron has been emitted, the ionized atom must relax in some way. This can be achieved by the emission of an X-ray photon, known as X-ray fluorescence. The other possibility is the ejection of an Auger electron through a secondary process.

All the XPS data presented in the thesis were carried out on VG Microtech Multilab ESCA 3000 spectrometer using a non-monochromatized Mg Kα X-ray source (hν = 1253.6 eV). Selected spectra were also recorded with Al Kα x-ray (hν = 1486.6 eV). Base pressure in the analysis chamber was maintained around 5×10^{-10} Torr. Binding energy (BE) calibration was performed with Au $4f_{7/2}$ core level at 83.9 eV. The error in BE values reported is ± 0.1 eV [15].

2.3.2.8 Scanning Electron Microscopy (SEM)

SEM is a type of electron microscope that is capable of inspecting topographies of sample surface and offer three-dimensional high resolution images of the sample surface. The first SEM image was obtained by Max Knoll, who in 1935 obtained an image of silicon steel showing electron channeling contrast.

SEM is a type of electron microscope that images the sample surface by scanning it with a high-energy beam of electrons in a raster scan pattern. The types of signals made by an SEM can include secondary electrons, back scattered electrons, characteristic x-rays and light. These signals come from the beam of electrons striking the surface of the specimen and interacting with the sample at or near its surface. In

its primary detection mode, secondary electron imaging, the SEM can produce very high-resolution images of a sample surface. SEM micrographs have a very large depth of focus yielding a characteristic three-dimensional appearance useful for understanding the surface morphology of a sample. This great depth of field and the wide range of magnifications (commonly from about 25 times to 250,000 times) are available in the most common imaging mode for specimens in the SEM through secondary electron imaging. Characteristic x-rays are the second most common imaging mode for an SEM. X-rays are emitted when the electron beam removes an inner shell electron from the sample, causing a higher energy electron to fill the shell and give off energy. These characteristic x-rays are used to identify the elemental composition of the sample. Back-scattered electrons (BSE) that come from the sample may also be used to form an image. BSE images are often used in analytical SEM along with the spectra made from the characteristic x-rays as clues to the elemental composition of the sample [16].

2.3.2.9   **Energy Dispersive Analysis of X-rays (EDAX)**

EDAX is a microchemical analysis technique. It is also sometimes referred to as EDX or EDS analysis. It is a technique to identify the elemental composition of the specimen or for an area of interest. It generally works as an integrated feature with SEM and cannot function on its own. During EDAX analysis the specimen is bombarded with the incident electron beam. When a voltage of 10-20 keV is used in SEM, the incident electrons knock out the inner core level electrons of the sample. The electrons from the higher energy levels fill up the vacancy thus created. During this transition X-ray is emitted which is plotted as no. of counts (intensity) with respect to the BE. The detector is made of the Li drifted Si detector, known as SiLi detector. This detector must be operated at liquid nitrogen temperatures. The photoelectron emitted is drawn into the Si detector, which creates electron-hole pairs. These electron-hole pairs are attracted towards the opposite ends of the detector by a strong electric field. The SiLi detector is often protected by Be window, hence it protects detection of soft X-rays of elements having low atomic number.

An EDAX spectrum also shows the nature of X-rays emitted which means that a transition from L-level to K-level is known as K-α peak, transition from M-level to K-level is known as the K-β peak and so on. This is shown in Figure 2.4.
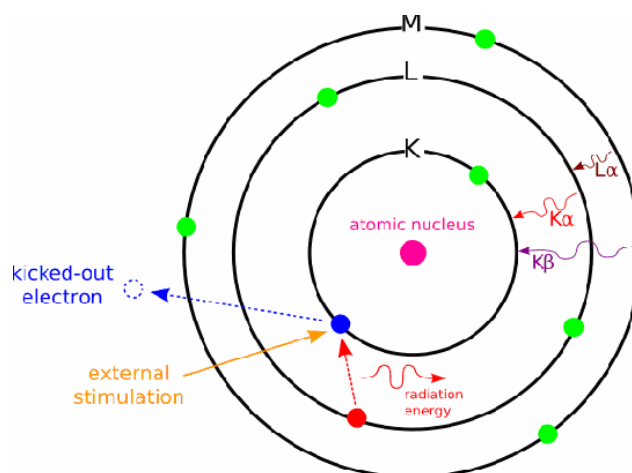
Figure 2.4: *Schematic diagram of the possible transition lines to form an EDAX spectrum.*

Elemental mapping works similarly to a scanning electron microscope: the sample is bombarded with an electron beam, and signals that come from the sample are collected. This enables the elements present within sample volumes of 10-30 cubic micrometers or less to be determined

EDAX measurements described in this thesis were performed on a Leica Stereoscan-440 scanning electron microscope instrument equipped with a Phoenix EDAX attachment. Samples for EDAX analysis were made by drop coating the solutions onto Si (111) wafers. In some cases, powder samples were also used directly on the sample-holder for the measurement [16]. Elemental mapping was carried out in above mentioned SEM system with recently equipped with an EDAX analyzer (Bruker, D451-10C Quantax 200 with X-flash detector) attachment. X-flash 4010 detector was employed for fast and high resolution real time spectrometry and elemental mapping. EDAX spectra were recorded in the spot-profile mode by focusing the electron beam onto specific regions of the sample. However, materials composition reported is based on the data collected over large areas (>300 μm^2).

2.3.2.10 Raman Spectroscopy

Raman spectroscopy is a spectroscopic technique used in chemistry to study vibrational, rotational and other low-frequency modes in a system. Since vibrational information is very specific for the chemical bonds in molecules, it therefore provides a fingerprint by which the molecule can be identified.

The laser light interacts with phonons or other excitations in the system, resulting in the energy of the laser photons being shifted up or down. The shift in energy gives information about the phonon modes in the system. A sample is illuminated with a laser beam. Light from the illuminated spot is collected with a lens and sent through a monochromator. The process where most photons are elastically scattered is called Rayleigh scattering. Raman spectroscopy is based on the Raman effect, which is the inelastic scattering of photons by molecules. The effect was discovered by the Indian physicist, C. V. Raman in 1928. Spontaneous Raman scattering is typically very weak, and as a result the main difficulty of Raman spectroscopy is separating the weak inelastically scattered light from the intense Rayleigh scattered laser light.

The energy of the scattered radiation is less than the incident radiation for the Stokes line and the energy of the scattered radiation is more than the incident radiation for the anti-Stokes line. The energy increase or decrease from the excitation is related to the vibrational energy spacing in the ground electronic state of the molecule. Therefore, the wave number of the Stokes and anti-Stokes lines are a direct measure of the vibrational energies of the molecule [12]. Raman spectra were recorded on a Horiba JY LabRAM HR 800 Raman spectrometer coupled with microscope in reflectance mode with 633 nm excitation laser source and a spectral resolution of 0.3 cm^{-1}.

2.3.2.11 Thermo Gravimetric Analysis (TGA)

TGA is an analytical technique used to determine a material's thermal stability and its fraction of volatile components by monitoring the weight change that occurs as a specimen is heated. The measurement is normally carried out in air or in an inert atmosphere, such as helium, nitrogen or argon, and the weight is recorded as a function of increasing temperature. The variation in mass of a sample is measured when it undergoes a temperature scanning in a controlled atmosphere. Such analysis relies on a high degree of precision in three measurements: weight, temperature, and temperature change. As many weight loss curves look similar, the weight loss curve may require transformation before results may be interpreted. A derivative weight loss curve can be used to tell the point at which weight loss is most apparent.

Differential thermal analysis is a technique measuring the difference in temperature between a sample and a reference (a thermally inert material) as a function of the time or the temperature, when they undergo temperature scanning in a controlled atmosphere. The DTA method enables any transformation to be detected for all the categories of materials, providing information on exothermic and endothermic reactions taking place in the sample, which include phase transitions, dehydration, decomposition, redox, or solid-state reactions. In catalysis, these techniques are used to study the genesis of catalytic materials *via* solid-state reactions where alumina is used as a reference material [17].

In TGA experiment, test material is placed into a high alumina cup that is supported on, or suspended from an analytical balance located outside the furnace chamber. The balance is zeroed, and the sample cup is heated according to a predetermined thermal cycle. The balance sends the weight signal to the computer for storage, along with the sample temperature and the elapsed time. The TGA curve plots the TGA signal, converted to percent weight change on the Y-axis against the reference material temperature on the X-axis. Thermal analysis experiments were measured in Perkin-Elmer's Diamond TG/DTA at a rate of 10ºC/min in air or N_2 atmosphere. Al_2O_3 was used as an internal standard.

2.4 References

1. X.-L. Guo, H. Tabata and T. Kawai, *J. Cryst. Growth* **237–239**, (2002) 544.

2. J. Wang, G. Du, B. Zhao, X. Yang, Y. Zhang, Y. Ma, D. Liu, Y. Chang, H. Wang, H. Yang, S. Yang *J. Cryst. Growth* **255** (2003) 293 .

3. H. P. Klug and L. E. Alexander, *X-Ray Diffraction Procedures: For Polycrystalline and Amorphous Materials*, (1974) p. 618 John Wiley and Sons, New York.

4. B. D. Cullity and S. R. Stock, Elements of X-ray Diffraction, Prentice Hall, Upper Saddle River, NJ 07458, 3rd ed. (2001).

5. N. F. M. Henry, J. Lipson and W. A. Wooster, *"The interpretation of x-ray diffraction photographs"* Macmillan and Co Ltd., London, (1951).

6. (a) H. M. Rietveld, *Acta. Crystallogr*. **22** (1967) 151. (b). H. M. Rietveld, *J. Appl. Cryst.* **2** (1969) 65.

7. A. C. Larson, R. B. Von Dreele, "*General Structure Analysis System (GSAS)*", Los Alamos National Laboratory Report LAUR 86-748 (2000)

8. *Secondary Ion Mass Spectrometry: Basic Concepts, Instrumental Aspects, Applications, and Trends*, A. Benninghoven, F. G. Rüdenauer and H. W. Werner, Wiley, New York, 1987.

9. B. C. Lippens and J. H. de Boer, *J. Catal*. **4** (1965) 319.

10. E. P. Barret, L. G. Joyner and P. H. Halenda, *J. Amer. Chem. Soc*. **73** (1951) 373.

11. R. C. Denney and R. Sinclair, *Visible and Ultraviolet Spectroscopy Analytical Chemistry by open learning series*, John Wiley and Sons, USA.

12. C. N. Banwell and E. M. McCash, *Fundamentals of Molecular Spectroscopy* Fourth Edition ed. Tata Mc-Graw-Hill Publishing Company limited.

13. (a) J. E. Wertz and J. R. Bolton, *Electron Spin Resonance: Elementary Theory and Practical Applications.* McGraw-Hill, New York, 1972. (b) S. A. Altshuler and B. M. Kozirev, Electron Paramagnetic Resonance. Academic, New York, 1964.

14. (a) T. A. Carlson, *X-ray Photoelectron Spectroscopy*, Dowden, Hutchinson & Ross: Stroudsburg, PA, 1978. (b) Practical Surface Analysis, Vol. 1: Auger and X-ray Photoelectron Spectroscopy, 2nd ed., D. Briggs and M. P. Seah, Eds., Wiley, New York, 1990. (c) S. Hüfner, *Photoelectron Spectroscopy*, Springer-Verlag: Berlin, 1995.

15. (a) M. K. Dongare, V. Ramaswamy, C. S. Gopinath, A. V. Ramaswamy, S. Scheurell, M. Brueckner and E. Kemnitz, *J. Catal*. **199** (2001) 209. (b) V. L. J. Joly, P. A. Joy, S. K. Date and C. S. Gopinath, *J. Phys. Condens. Matt.* **13** (2001) 649.

16. (a) http://en.wikipedia.org/wiki/Scanning_electron_microscope#cite_ref-7.   (b) http://www.uga.edu/caur/semnote1.htm

17. P. Gabbott (Ed.) *Principles and Applications of Thermal analysis,* Wiley-Blackwell, 2007.

Chapter 3

Characterization and Catalytic activity of $ZnO_{1-x}N_x$ and $ZnO_{1-x-z}N_xS_z$

3 Structural, Spectroscopic, Electronic Structure and Catalytic Activity Studies of (ZnO$_{1-x}$N$_x$) and (ZnO$_{1-x-z}$N$_x$S$_z$).

Part A: ZnO$_{1-x}$N$_x$ Materials

3.1 Introduction

Versatile application in wide range of area makes ZnO a key technological material [1]. However, both *n*- and *p*-type materials are required for improvement of various applications including homojunction light-emitting diodes (LEDs) and laser diodes (LDs) application. Normally, undoped ZnO acts as *n*-type semiconductor and its conductive properties are due to native donors such as zinc interstitials (Zn$_i$) and oxygen vacancies (V$_o$), though the quantification of participation from both the donors is still not clear. Synthesizing *p*-type ZnO is a big challenge because of the presence of native donor defects and low dopant solubility. Furthermore, *p*-type material often has poor quality due to low hole concentration and mobility. It tends to revert to *n*-type behavior over the course of time at room temperature.

Density functional theory (DFT) predicts that the introduction of group-I elements such as Li, Na, and K, on Zn sites could be a possible approach to obtain *p*-type ZnO [2]. However, doping with these elements typically suffer from a very high diffusivity and self-compensation effects as well. The most frequently used procedure for acceptor doping is the introduction of group-V elements, mainly N, P, or As, which generate acceptor states if incorporated in oxygen sites. However, possessing much larger ionic radii than oxygen, density functional theory suggests significantly deeper acceptor levels in *p*-type ZnO compared to doping by group-I elements. Both P and As also form significantly larger bond lengths and, therefore, produce the lattice strain. Theoretical calculations have shown that among the heteroatoms, nitrogen (N) is widely acceptable owing to its compatible size and electron affinity to oxygen (O) and it has the smallest ionization energy as well. Nitrogen cannot be incorporated in the ZnO lattice in the form of N$_2$ using pure nitrogen source (e.g. during the growth in air), however, it can be introduced as single atom or ion using nitrogen plasma source [3].

To dope nitrogen into ZnO system, many sophisticated methods such as pulsed laser deposition, molecular beam epitaxy, hydrothermal synthesis and metal oxide chemical vapor deposition have been employed and various kind of nitrogen sources like N$_2$, NO, N$_2$O, NH$_3$ and Zn$_3$N$_2$ have also been used depending on the growth techniques [4]. Indeed, poor nitrogen solubility in ZnO is a hindrance and, to date, nitrogen doping can be performed to a maximum of 10^{17} cm^{-3} [1] or to a surface doping level of 6 atom % [5]. Furthermore, the formation of Zn-O is energetically more favorable than the formation of Zn-N bonds. It is predicted that an enhancement of the doping level of nitrogen in ZnO and a reduction in the nitrogen acceptor levels are required for the fabrication of low-resistive *p*-type ZnO [6]. Hence, a suitable method to prepare ZnO with large nitrogen content could be helpful to enhance its utilization toward various applications, such as *p*-type conductors and photocatalyst, because of the delocalization effect. In spite of several reports, concentration of nitrogen in ZnO lattice is still controversial. The results showed that the nitrogen incorporation in ZnO is increased in the presence of NH$_3$, enhancing the hole concentration. In addition, ZnO is also a very good catalytic material, and hence, nitrogen doped ZnO can further be explored towards catalytic application.

Oxidation-reduction reactions play an important role in organic chemistry. Oxidation of alcohols to form aldehyde, ketone or carboxylic acids is a fundamental reaction. Primary alcohols and secondary alcohols can be oxidized to aldehyde or carboxylic acids and to ketone, respectively. One of the important alcohol oxidation reactions is cyclohexanol dehydrogenation since cyclohexanone is a very important chemical, used mainly as a starting material for the synthesis of two important polymer fibers i.e. caprolactam and nylon-6. Copper-containing catalysts have been used in the process for dehydrogenation of cyclohexanol to cyclohexanone for many years. CeO$_2$-ZnO composite catalysts have also been investigated for cyclohexanol dehydrogenation. Cyclohexanone was obtained as main product for cyclohexanol transformation reaction carried out over these mixed oxide catalysts due to dehydrogenation on basic sites.

The Friedel-Crafts acylation of aromatic compounds is also an important transformation in organic synthesis. In a typical Friedel-Crafts acylation reaction, an aromatic compound undergoes electrophilic substitution with an acylating agent in the

presence of more than 1 equiv of acid catalyst. Sharghi *et al.* identified ZnO alone can promote Friedel-Crafts acylation reaction of activated and unactivated aromatic compounds with acyl chlorides at room temperature in a very efficient way [7].

We successfully prepared up to 15 atom % N incorporated ZnO (ZnO$_{1-x}$N$_x$) by a very simple SCM. In this part (part A) we have discussed on detailed characterization of nitrogen doped ZnO to confirm the state and amount of nitrogen. The samples were characterized by powder XRD, UV-visible, XPS, Raman spectroscopy and TG-DTA. A detailed investigation has been carried out in the present chapter to explore the effect of nitrogen in ZnO lattice in the photocatalytic decomposition of rhodamine B, acylation of anisole and Cyclohexanol dehydrogenation reaction.

3.2 Results and Discussion

Throughout the chapter ZnO$_{1-x}$N$_x$ materials are denoted as UZm where m being the ratio of urea/Zn(NO$_3$)$_2$ used. Any numerical value followed by m represents calcination temperature of the corresponding material.

3.2.1 X-Ray Diffraction

To explore the structural properties of the material, powder X-ray diffraction (PXRD) was carried out. Figure 3.1 shows the PXRD pattern of ZnO$_{1-x}$N$_x$ materials. For comparison purposes, the diffractograms of the ZnO was included. It is clear from the figure that all diffraction features from ZnO$_{1-x}$N$_x$ matched with that of the pattern shown for the bulk ZnO and no additional peak was observed due to N incorporation in ZnO. The major peaks of ZnO$_{1-x}$N$_x$ material appeared at (2θ) 31.8º, 33.4º and 36.2º, which were assigned to the diffractions from the (100), (002) and (101) planes, respectively. This observation clearly demonstrates the formation of the hexagonal Wurtzite structure [8]. Rietveld refinement profiles of UZ1, UZ3 and UZ5 materials are presented in Figure 3.2. An excellent agreement between the experimental and the fitted data indicated that the XRD pattern could be indexed satisfactorily well to the Wurtzite structure with a space group P6$_3$mc. The sharp and high intensity diffraction peaks would prove the highly crystalline nature of ZnO$_{1-x}$N$_x$ materials. Compared to ZnO, small shift to higher diffraction angle associated with ZnO$_{1-x}$N$_x$ materials reveal
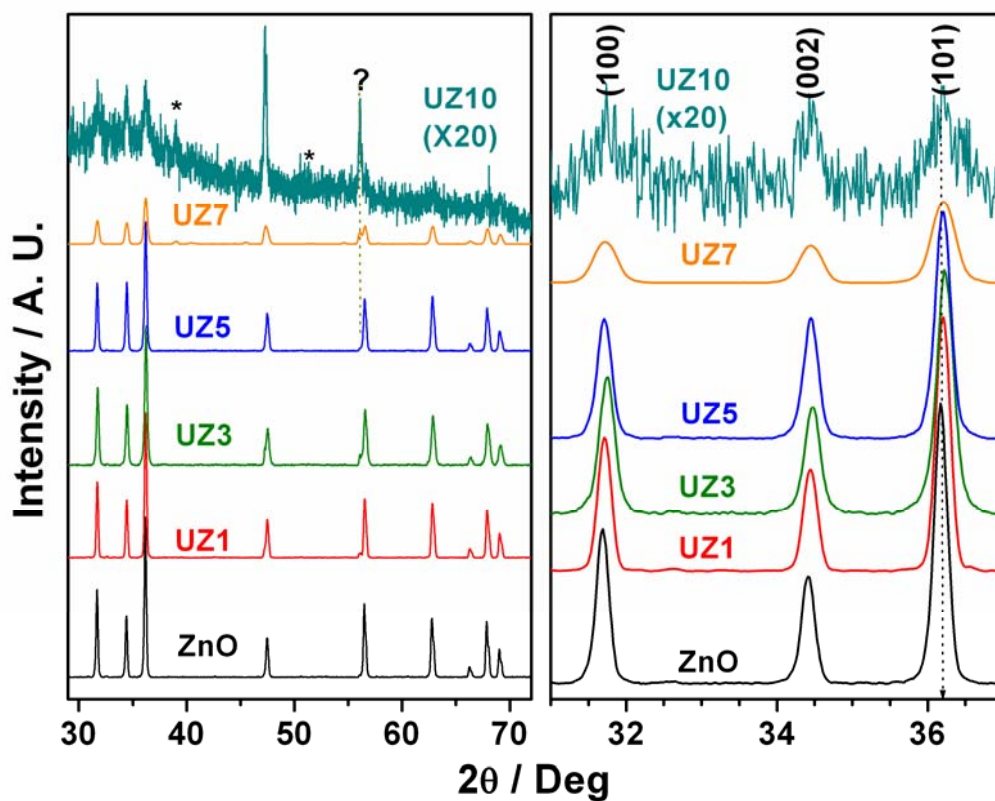
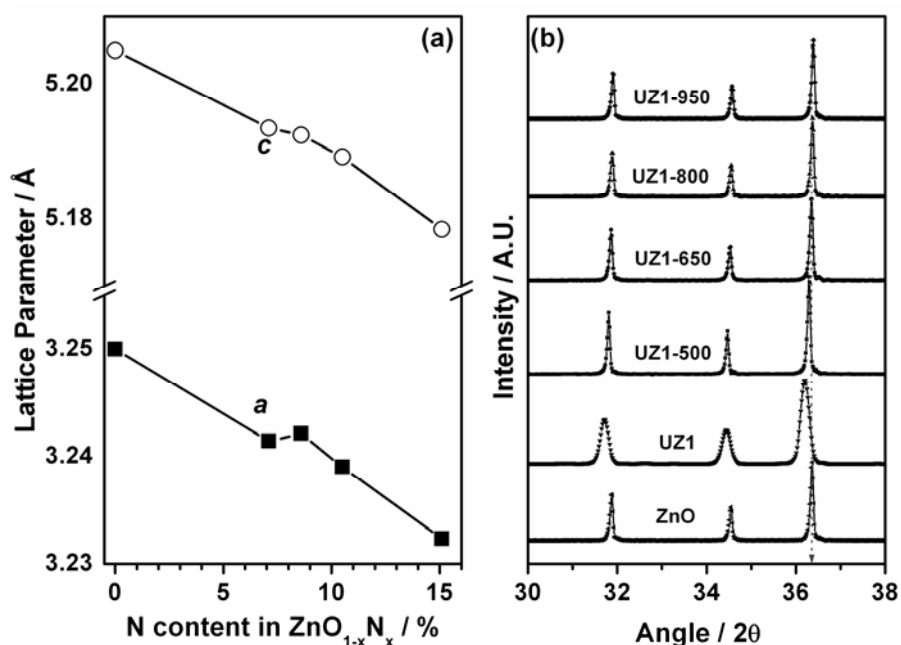**Figure 3.1:** *PXRD pattern of ZnO$_{1-x}$N$_x$ materials prepared with different urea/Zn(NO$_3$)$_2$ ratio and ZnO.*
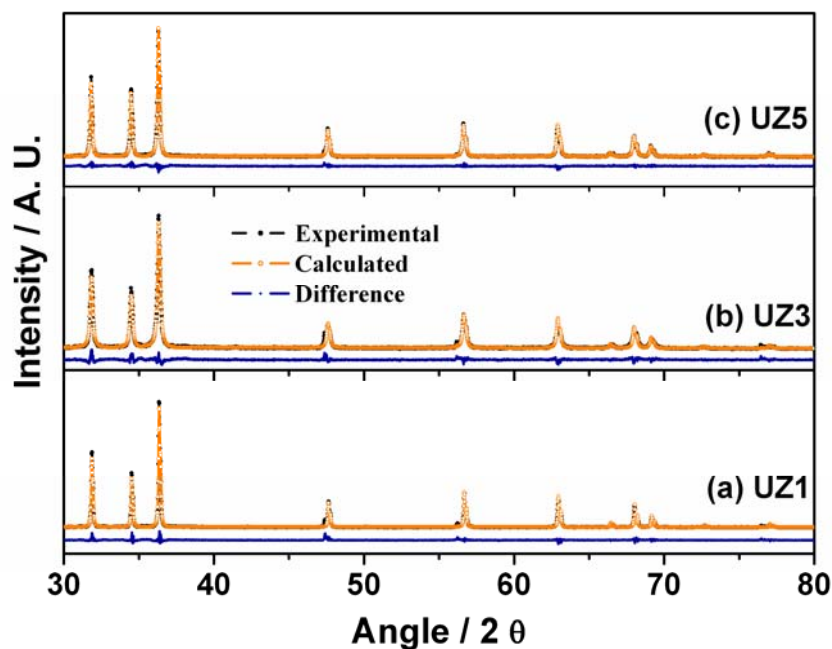
Figure 3.2: *Rietveld refinement profiles of* (a) *UZ1,* (b) *UZ3, and* (c) *UZ5 materials. Experimental data points are given in black color line and calculated intensity is given in orange open circle. The difference plot is given at the bottom.*

an overall contraction of the lattice. Indeed, there is a small change in the lattice parameters and it depends on the amount of urea employed in the preparation.

Rietveld analysis clearly suggests the largest decrease in the lattice parameters (a = 3.2323 Å and c = 5.1784 Å) observed with UZ1, which also shows maximum bulk N-content (15.1 atom %), compared to commercial ZnO (a = 3.25 Å and c = 5.205 Å) (Figure 3.3a). Moreover, with increasing urea content peak broadening occurs and peak intensity gradually decreases which indicates that an increase in urea concentration in reaction mixture deteriorates the crystallinity of the material. Further, decrease in lattice contraction was observed with increase in urea content in the reaction mixture and the lattice parameter moves closer toward ZnO as shown in Figure 3.3a. Significant amount of zinc carbonate formation is evident from the XRD patterns of UZ7 and UZ10, along with an increase in surface area and change in sample color (from light orange to white) because of the high urea content in the reaction mixture. Diffraction peaks due to zinc carbonate were also observed in the PXRD analysis and are indicated by an asterisk symbol (*) in Figure 3.1. Urea, a good fuel, produces more CO_2 along with NH_3, with increase in urea content during combustion; this causes the carbonate formation in UZ7 and UZ10 [9].

Figure 3.3: (a) *Lattice parameters of ZnO$_{1-x}$N$_x$ materials calculated from Rietveld analysis of the PXRD data.* (b) *PXRD pattern of UZ1 material calcined at different temperature compared with standard ZnO.*

Table 3.1 *Physicochemical characteristics of ZnO$_{1-x}$N$_y$ materials*

ZnO$_{1-x}$N$_y$ code[a]	Lattice Parameters[b]		Surface area (m^2/g)	density (g/cm^3)^f	Bulk and Surface atom percent[c]				Color
	a (Å)	c (Å)			Zn	O	N	(Zn/N)$_{surf}$	
UZ1[d]	3.2323	5.1784	1	5.81	24.4	60.5	15.1	72	Brownish orange
UZ1-650	---	---	1		29.7	64.3	6.01	---	Orange
UZ1-950	3.2511	5.2007	1		34.4	65.6	---	---	Off white
UZ3	3.2390	5.1892	3	5.62	24.7	64.8	10.5	7.6	Orange
UZ5	3.2421	5.1924	7	5.58	17.7	72.7	8.6	6.3	Pale orange
UZ7	3.2414	5.1934	19	5.49	16.8	72.2	7.1	2.02	Pale orange
UZ10[e]	---	---	102	5.23	14.9	55.1	0.2	0.58	White

[a] *Urea:Zn(NO$_3$)$_2$ 6H$_2$O mole ratio is given next to UZ followed by (any) calcination temperature in $^\circ$C.* **[b]** *Lattice parameters for pure ZnO (a = 3.25 Å and c = 5.205 Å).* **[c]** *Bulk and surface atomic content measured from EDAX and XPS, respectively.* **[d]** *UZ0.8 (Urea:Zn(NO$_3$)$_2$ 6H$_2$O = 0.8) shows similar characteristics as that of UZ1.* **[e]** *Bulk carbon content of UZ10 is 29.8 atom % and surface atomic ratio of Zn:C from carbonate is 0.98. Carbon content is 1 and 3.9 atom % on UZ5 and UZ7, respectively.* **[f]** *Density of ZnO is 5.606 g/cm^3.*

Carbonate formation with more urea would certainly change the atom percentage trend which was observed for materials with urea: $Zn(NO_3)_2 > 5$ (above UZ5).

Figure 3.3b shows XRD peak of UZ1 materials annealed at different temperature in static air for 6 hours and reveals that there is no change in Wurtzite structure due to calcination. However, with increasing calcination temperature there was a change in color of the material with shift of most intense peak towards higher angle. Therefore, it can be concluded that with increase in calcination temperature unit cell volume decreases and thermal contraction occurs due to loss of nitrogen from lattice and/or interstitial position which also reflects in decrease in cell parameter.

3.2.2 **Energy Dispersive Analysis of X-rays (EDAX)**

Table 3.1 describes the EDAX analysis of all $ZnO_{1-x}N_x$ materials along with surface Zn/N ratio. However, atom content measured via EDAX on individual particles differs significantly, and the values reported in Table 3.1 are the average values obtained over a large area. EDAX analysis revealed the lowest Zn/N ratio in UZ1 and it was continuously increasing with increase in urea content in preparation mixture (from UZ1 to UZ10). Brownish orange colored UZ1 contained 15.1 atom % nitrogen and UZ3 showed a decrease in the N atom content to 10.5% and a simultaneous increase in O atom content to 64.8%. This directly suggests that the introduction of nitrogen was at the expense of oxygen. In contrast, lowest Zn/N (surface) observed for UZ10 was due to preferential surface nitrogen doping along with carbonate formation. Effective combustion might be a reason for the surface segregation (or surface doping) of nitrogen on ZnO in UZ7 and UZ10. The bulk N atom content in $ZnO_{1-x}N_x$ reduced linearly as the urea content in the initial reactants mixture was increased. However, the O atom content changed to higher atom % with the urea content between UZ1 and UZ5. EDAX and XPS analyses demonstrate the presence of carbon in form of carbonate (or carbonate-like) species. The likelihood of occupancy of nitrogen atoms in oxygen lattice positions in ZnO can be confirmed from the observations mentioned above. Nevertheless, a small amount of nitrogen in extra-lattice positions might remain which could not be detected from any of the characterization methods employed in the present study.

It is to be noted that a significant difference in the density values of ZnO$_{1-x}$N$_x$ materials were observed, compared to that of ZnO (5.606 g/cm^3) (Table 3.1). UZ1 (and UZ0.8) especially exhibits higher density (5.81 g/cm^3) than all other compositions and ZnO, suggesting a considerable change in composition and/or compact nature of the material. A large amount of nitrogen and a higher density indicates that some amount of interstitial Zn might be present in the lattice.

Indeed, interstitial Zn and oxygen vacancies (EPR studies, Figure 3.10) present in the lattice are mainly present to compensate for the excess anionic charge from the significantly large nitrogen content (15%) and to maintain the charge neutrality of the entire lattice. This is further supported by a decrease in the lattice parameter with increasing nitrogen content. In view of this, the actual stoichiometry of UZ1 would be Zn$_{1+\delta}$O$_{0.85}$N$_{0.15}$, and the value of $\delta \geq 0.05$, from density values. Furthermore, the low surface area value that is observed for UZ1 (1 m^2/g) and the higher density corroborates well and supports the compact nature of UZ1. When UZ1 is subjected to air calcination at 950°C, the material turns colorless and the density value of UZ1-950 (5.62 g/cm^3) is similar to that of ZnO (Table 3.1), which supports the removal of nitrogen from the UZ1 lattice and a simple oxidation to ZnO. The low surface area observed after the aforementioned calcination with UZ1-950 is due to the sintering effect. Density values observed for UZ3 and UZ5 is comparable to that of ZnO; furthermore, the surface area also increases significantly and corresponds to decreasing nitrogen content, indicating a decreasing interstitial Zn content in UZ3 and UZ5. A large increase in the surface area and a significant decrease in the density values of UZ7 and UZ10 suggest an increasing porosity of these materials. Furthermore, the nitrogen content decreases along with a change in the nature of materials that contain more carbonates (Figure 3.1 and Table 3.1), clearly indicating that the effective introduction of nitrogen can be performed with a stoichiometric amount of urea and zinc nitrate.

3.2.3 **Scanning Electron Microscopy (SEM)**

Figure 3.4 displays the surface morphology of ZnO$_{1-x}$N$_x$ by SEM. It reveals that as-prepared sample of UZ0.8 (and UZ1) (Figure 3.4a and b) exhibits triangular and hexagonal-prism-shaped crystals with an edge length of ~400 nm to 1.5 μm; however, the triangular structure dominates over the prismatic structure. The

(a) UZ0.8   (b) UZ1

(c) UZ1-500   (d) UZ1-650
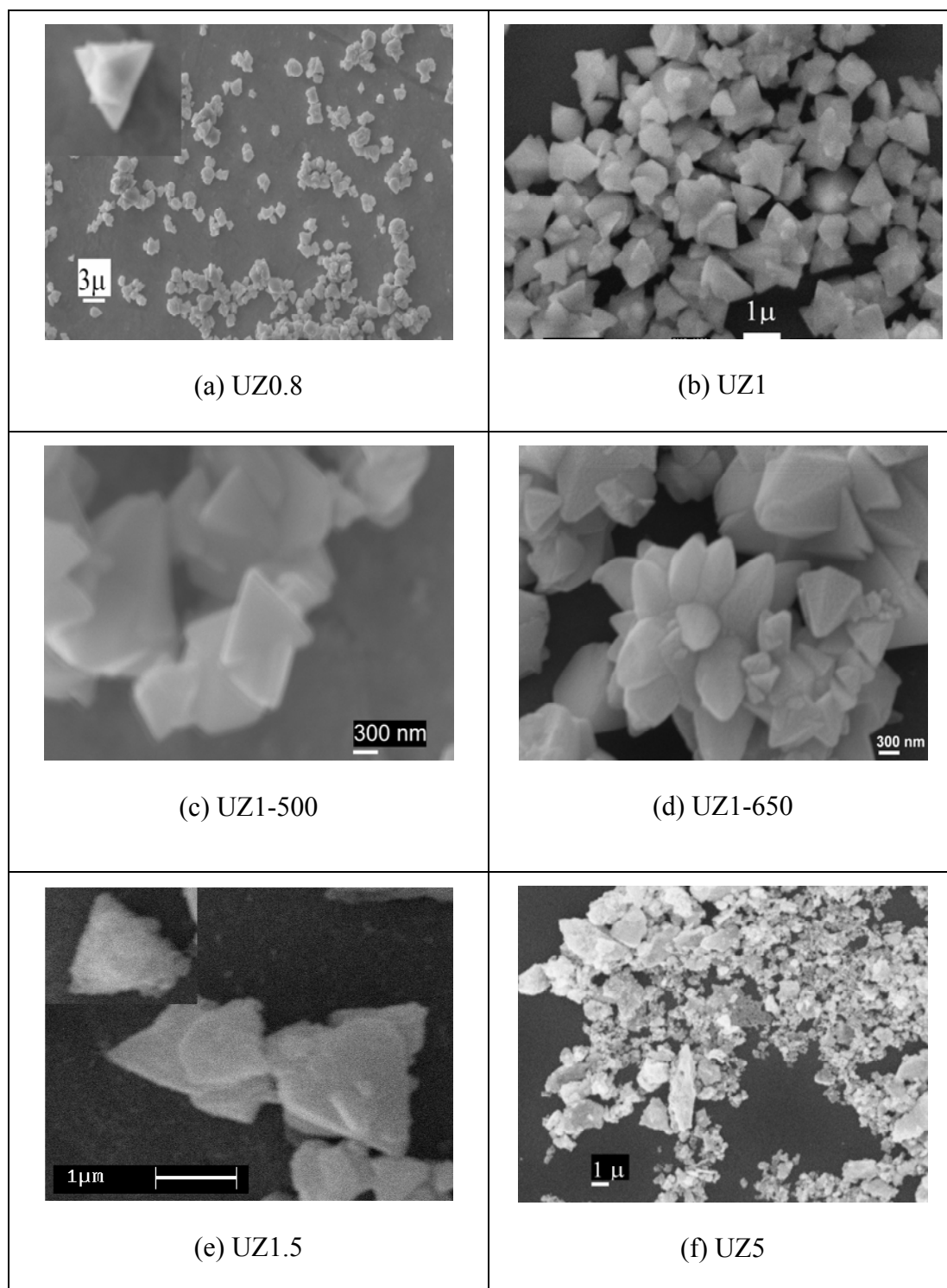
(e) UZ1.5   (f) UZ5

Figure 3.4: *SEM images of (a) UZ0.8, (b) UZ1, (c) UZ1-500, (d)UZ1-650, (e) UZ1.5 (f) UZ5.*

measured thickness of the triangular particles is ~250 nm, irrespective of the edge length. The uniform contrast that is observed within any triangular/ prismatic particle is believed to result from the stress-free and well-grown crystals, which is expected from slow crystallization. It is interesting to note that such well-grown crystals were observed from the ZnO$_{1-x}$N$_x$ materials prepared via the SCM method, which is indeed

a rapid preparation method. Thus the SEM results well support and reflect the crystalline nature of the samples found from X-ray diffraction analysis. Due to the exposure of smaller particles to relatively high-temperature zones around flame temperature (700-1000ºC) during combustion preparation, a significant amount of triangular agglomerates was also observed. This might be a reason for significantly different atomic composition of individual crystallites measured by EDAX analysis. After calcination at 500°C for 6 h, agglomeration increased in UZ1 (Figure 3.4d); however, sharp edges could still be observed. Calcination to higher temperatures (650ºC) increased the agglomeration and lotus-type agglomerates were observed on UZ1-650. As the urea/metal ratio was increased and reached stoichiometric (1.66) value, no single or unagglomerated triangle shaped particle was observed, rather particles agglomerated to form precursor structure of lotus type particle. With a ratio of urea:Zn >2 in the reaction mixture, no specific particle morphology was observed, and it is attributed to the increasing exothermicity of the combustion reaction. The high urea content in the mixture of reactants made the combustion better, and therefore in situ combustion temperature reached very high with releasing more gases emanating during SCM which helped to form micro-pores with a high surface area on UZ7 and UZ10 (Table 3.1). Hence, controlled combustion with urea content lower than a stoichiometric value (in UZ1 and UZ0.8) produced well-defined particle morphology.

The addition of NH_4NO_3, instead of urea, to zinc acetate did produce similar $ZnO_{1-x}N_x$ materials but without any specific morphology, which suggests the in situ formation of NH_2/NH_3 during combustion and the same is required for nitrogen doping, and the nitrogen source is from urea and not the nitrate nitrogen. Below Zn: urea = 0.8 the combustion was not possible as minimum oxidant concentration required was well below the stoichiometric ratio of Zn: urea = 1.66.

3.2.4 Raman Spectroscopy

Figure 3.5 displays the Raman spectra of the as-synthesized (UZ1, UZ3 and UZ5) and calcined (UZ1 at different temperature) $ZnO_{1-x}N_x$ materials. Raman spectra of the ZnO were also included for comparison purposes. ZnO exhibits a hexagonal Wurtzite structure and belongs to the C_{6v} symmetry group. Typical Raman-active phonon modes in first order spectrum E_2, $A_1(TO)$, $A_1(LO)$, $E_1(TO)$, and $E_1(LO)$ are expected

[10]. The B$_1$ modes are silent. According to the selection rules E$_2$ and A$_1$(LO) modes are expected to be observed in unpolarized Raman spectra. All the above Raman modes were found for ZnO$_{1-x}$N$_x$, rather than ZnO. A unique feature of the ZnO spectrum is that it's LO signal is weak. A strong and sharp peak observed at 437 cm^{-1} on all ZnO$_{1-x}$N$_x$ and ZnO was attributed to the typical E$_2$(high) mode. This mode corresponds to the band characteristic of the Wurtzite phase. A$_1$(TO) and E$_1$(TO) modes were observed at 380 and 415 cm^{-1} respectively. Among these Raman shift peaks, the mode at 437 cm^{-1} showed the strongest intensity and narrower line width of 9 cm^{-1}. This phenomenon indicates the high crystal quality of the material which supports the XRD analysis.

In addition to the above, three new peaks were noted at 507, 582, and 642 cm^{-1} on ZnO$_{1-x}$N$_x$ materials which don't belong to first or second order structure of ZnO. A broad peak at 582 cm^{-1} peak was attributed to A$_1$(LO) as reported by Wang *et al.* [11]
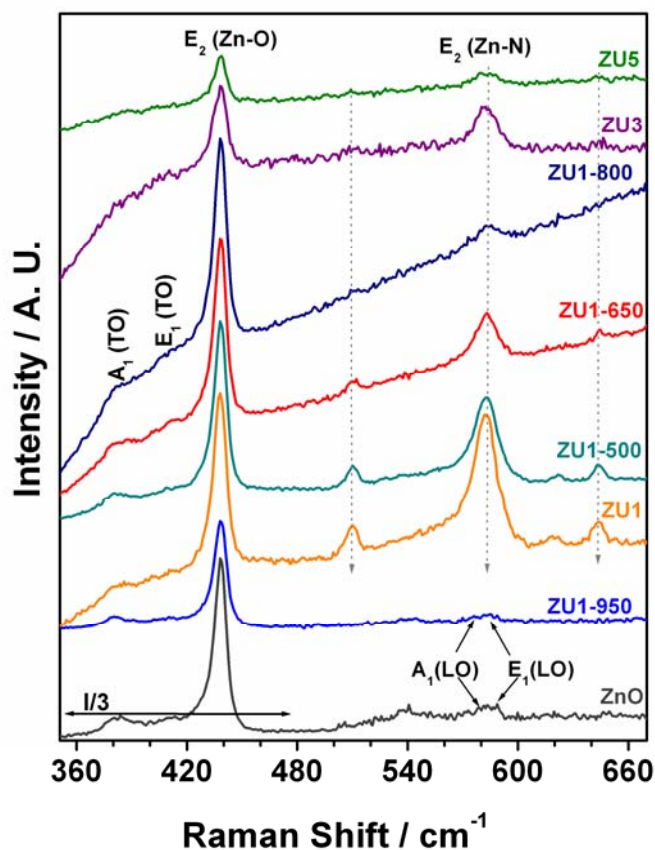
Figure 3.5: *Raman spectra of ZnO$_{1-x}$N$_x$ materials, calcined UZ1 and ZnO. Note with increasing calcination temperature Zn-N local vibrational modes intensity gradually decreases due to nitrogen loss.*

and suggested that these modes may be related to nitrogen doping. It is to be mentioned that A$_1$(LO) and E$_1$(LO) peaks at 580 cm^{-1} are low in intensity for pure ZnO, and high intensity observed at 582 cm^{-1} was attributed to the E$_2$(Zn-N) mode from ZnO$_{1-x}$N$_x$. The other two peaks (507 and 642 cm^{-1}) were also identified as Zn-N related local vibration modes (LVMs). A large content of nitrogen in UZ1 can be confirmed by comparing the intensity of Zn-N (582 cm^{-1}) to Zn-O (437 cm^{-1}). It is clear from the Raman features that the E$_2$(Zn-O) mode at 437 cm^{-1} is much higher in intensity on ZnO than on UZ1, indicating that the Zn-N features are at the expense of Zn-O features. These changes in intensity underscore the higher covalency of Zn-N than the parent Zn-O bonds.

Kaschner *et al.* [12] found that there is a proportional relationship between the intensity of the nitrogen LVM peaks and the nitrogen concentration in nitrogen-doped ZnO. A comparison of Raman spectra of as-prepared sample (UZ1) and calcined UZ1 clearly demonstrates a decrease in the intensity of Zn-N LVMs with an increasing calcination temperature, especially for the feature at 582 cm^{-1}. Hence, it can be concluded that nitrogen desorbs from the lattice of as-prepared sample during calcination >500°C. All nitrogen atoms disappeared on 950°C calcined sample and showed the identical Raman spectra as that of ZnO. However, decrease in intensity was different for different peaks. This is because of different modes of breaking probability of the nitrogen containing compounds. This provides the evidence to support the direct bonding between Zn and N in the ZnO$_{1-x}$N$_x$ system. In this system, only ZnO as well as nitrogen related LVMs were present. From calculations based on a modified valence-force model of Kane, Kaschner *et al.* obtained the values of 272 and 587 cm^{-1} for LVMs of nitrogen on a substitutional oxygen site in the ZnO lattice, which is good agreement with the observation from the present study [12]. With increasing urea concentration in reaction mixture, peaks related to LVMs of Zn-N bond were found to broaden. This supports a decrease in crystallinity of the materials. The decrease in intensity also indicates that the amount of nitrogen (bulk nitrogen) in the lattice decreases.

3.2.5 **UV-Visible Spectroscopy**

UV-visible absorption spectra of ZnO$_{1-x}$N$_x$ materials were measured and compared with pure ZnO material and the results are shown in Figure 3.6. Pure ZnO shows an

absorption cutoff edge at ~375 nm [13]. In addition to the above, a new and broad visible absorption band with an absorption onset at ~600 nm and a band maximum at ~480 nm was noticed on all ZnO$_{1-x}$N$_x$ materials, except UZ10. The energy difference between the aforementioned two features demonstrates the creation of a midgap (deep level acceptor) state in the band gap. UV-Vis absorption spectra in Kubella Munk unit (K. M. Unit) is displayed in Figure 3.6b giving the similar information. Low intensity of absorption features may be attributed to the forbidden transition from midgap state to CB. However, despite a high N content, no hole conductivity was observed and all ZnO$_{1-x}$N$_x$ materials exhibited insulating characteristics similar to that of ZnO. This observation clearly reinforces the conclusion that N 2p states are far removed from the top of the O 2p VB. UZ1 annealed at 950ºC shows no visible light absorption, because of the complete loss of nitrogen. This suggests that the visible light absorption was due to the introduction of N into the ZnO lattice and the N 2p derived midgap state. The band gap energy of the present samples was roughly estimated to be ~2.5 eV based on the absorption maximum and band in visible region of diffuse reflectance spectra, which is substantially smaller than that for ZnO (3.2 eV).
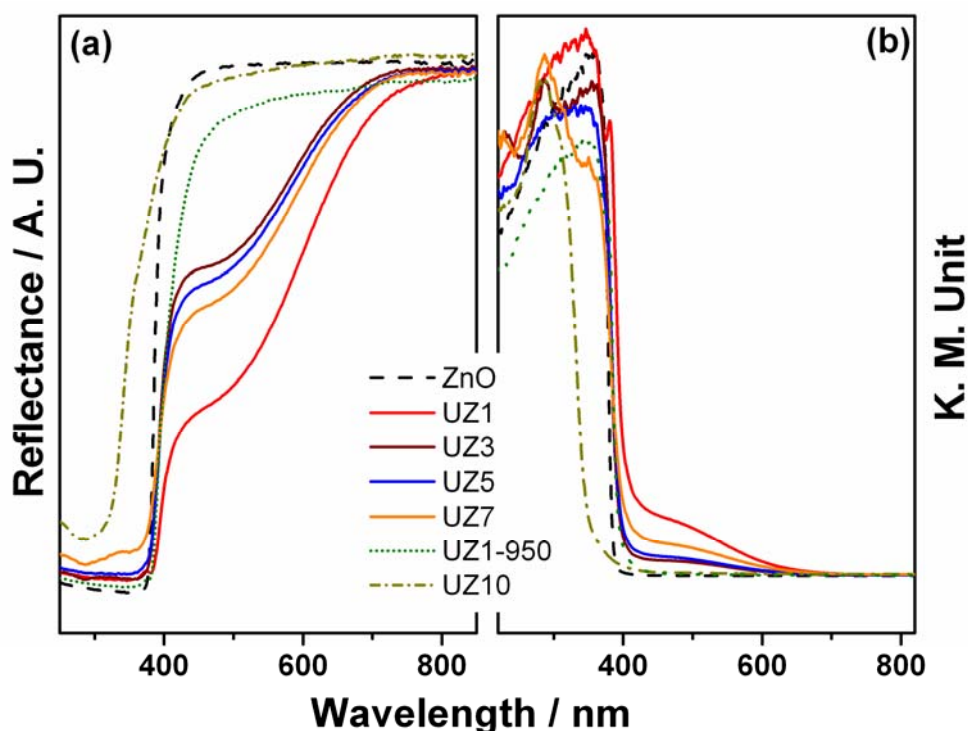

Figure 3.6: (a) *Diffuse reflectance UV-Visible spectra of the ZnO$_{1-x}$N$_x$ materials, UZ1-950 and ZnO.* (b) *UV-Vis absorption spectra of the same in K.M. unit.*

Density functional theory (DFT) calculation reveals that the bottom of the CB for pure ZnO is mainly composed of unoccupied levels consist of Zn $4s$ and $4p$ orbital, while the top of the VB consists of O $2p$ and Zn $3d$ orbital. The lower part of VB, which is located about 10 eV lower than the upper VB, is essentially composed of O $2s$ and Zn $3d$ orbital. However, doping of N $2p$ creates mid gap state between VB and CB. Based on calculations of band structures, visible-light responses for $ZnO_{1-x}N_x$ arose from band narrowing by mixing of N $2p$ and O $2p$. Nonetheless, present experimental results suggest that there is hardly any energy overlap between O $2p$ and N $2p$ states, and it is may be due to the nature of nitrogen. This will be discussed more in XPS result in section 3.2.7. $ZnO_{1-x}N_x$ powder contained not only nitrogen but also oxygen vacancies. Electronic levels due to the oxygen vacancies are slightly below the CB edge, and hence, responsible for visible-light responses. Indeed, the color intensity associated with $ZnO_{1-x}N_x$ decreased from orange-brown for as-prepared material to white after calcination at 950ºC.

3.2.6 **Thermo Gravimetric Analysis**

Figure 3.7 exhibits the result obtained from thermal analysis of the as-prepared sample (UZ1, UZ5 and UZ10) performed in simulated air atmosphere. It can be seen from Figure 3.7 that hardly any weight loss (0.4 wt %) was observed up to 800ºC for UZ1 and this indicates a high thermal stability of the sample. No considerable weight loss was observed at <500°C due to loss of any physisorbed H_2O and NH_3, or nitrate decomposition. This suggests the high purity of $ZnO_{1-x}N_x$ materials as well as the hydrophobic nature of UZ1. A broad endotherm observed from 300ºC to 850ºC in DTA suggests some desorption. Indeed, N desorption was expected above the yellow flame temperature (>600ºC). Further, it can be noted from Table 3.1 that the lattice parameter of UZ1-950 and ZnO are comparable. A marginal weight gain is normally expected to get during oxidation of $ZnO_{0.85}N_{0.15}$ (UZ1) to ZnO. However, instead of weight gain via the oxidation of $ZnO_{1-x}N_x$ to ZnO (at >600°C), an overall weight loss (0.4 wt %) was observed due to a net oxygen loss throughout the heating in the TG-DTA experiment. Further, change in color from orange to white, (UZ3 to UZ10, respectively) supports a decrease in the N content. A small but sharp change in weight loss (~1 wt %) was observed at ~550°C on UZ5, with a corresponding exothermic change in DTA (Figure 3.7a) and it is attributed to decomposition of carbonate.
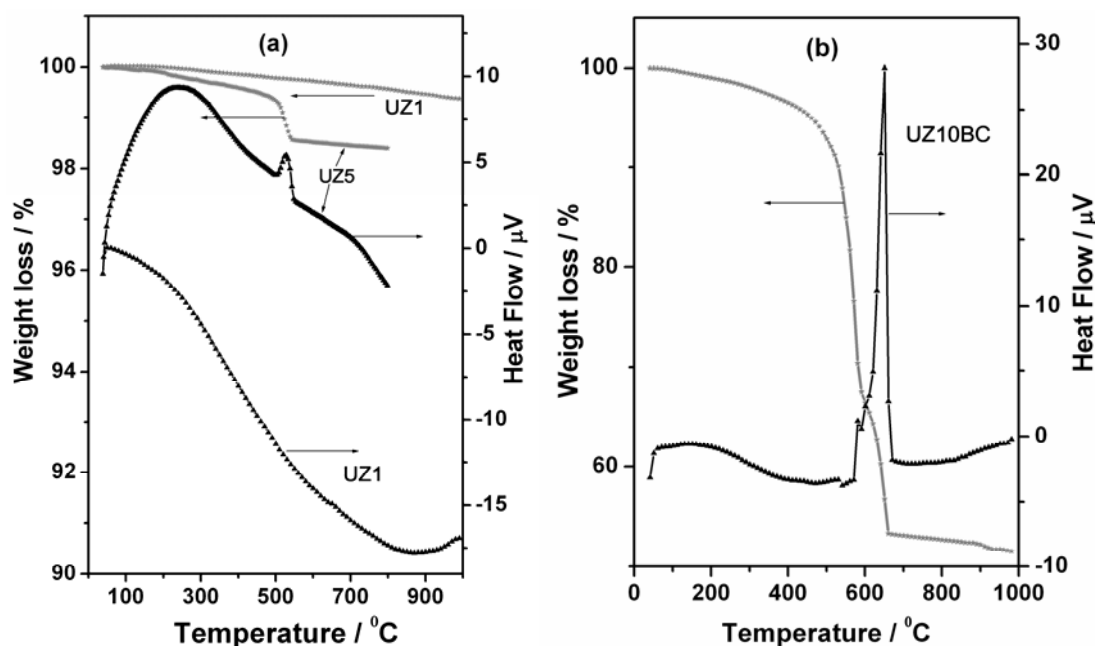
Figure 3.7: *Thermo-gravimetric and differential thermal analysis of* (a) *UZ1, UZ5 and* (b) *UZ10 carried out in air atmosphere at a heating rate of 10ºC/min.*

To explore this aspect deeper, UZ10 was also subjected to TG-DTA measurements. Very sharp and large weight loss (~40%), accompanied by an exotherm observed in DTA at ~550-660°C on UZ10 (Figure 3.7b), is attributed to the decomposition of the carbonate species. XPS results also support the formation of carbonates between UZ5 and UZ10. So, it can be inferred that when the urea content increased in the preparation (for UZ7 and UZ10), the weight loss also increases due to carbonate formation. Though a significant intensity corresponds to the carbonate decomposition peak was observed for UZ5, the absence of a carbonate feature in the XRD analysis (Figure 3.1) suggests that the carbonate formation is likely limited to surfaces, rather than the bulk. However, a large weight loss in TG and the observation of $Zn(CO_3)_2$ diffraction peaks in Figure 3.1 demonstrates the bulk nature of $Zn(CO_3)_2$ in UZ10.

3.2.7 **X-ray Photoelectron Spectroscopy**

XPS spectra of ZnO$_{1-x}$N$_x$ samples are shown in Figure 3.8 for N 1*s,* Zn 2$p_{3/2}$, C 1*s,* and O 1*s* core levels. N 1*s* core level from ZnO$_{1-x}$N$_x$ material showed a single peak and appeared at around 399.6 + 0.2 eV suggesting the nature of nitrogen, especially the charge density is similar to that of ammonia or amines. The typical nitride binding energy (BE) is reported to be ~397 eV [14], and the above mentioned observation

suggests that the electron density on nitrogen in ZnO$_{1-x}$N$_x$ is less than that of nitrides. This might be attributed to a more-covalent character of Zn-N bonds in ZnO$_{1-x}$N$_x$. However, aforementioned XPS results indicate that the surface N content increased linearly with the amount of urea used in the preparation. Although UZ10 was colorless, high surface N content suggests preferential N segregation on the surface and is further supported by EDAX results (Table 3.1). Importantly the nature of N and its charge density seems to decide the band gap modifications.
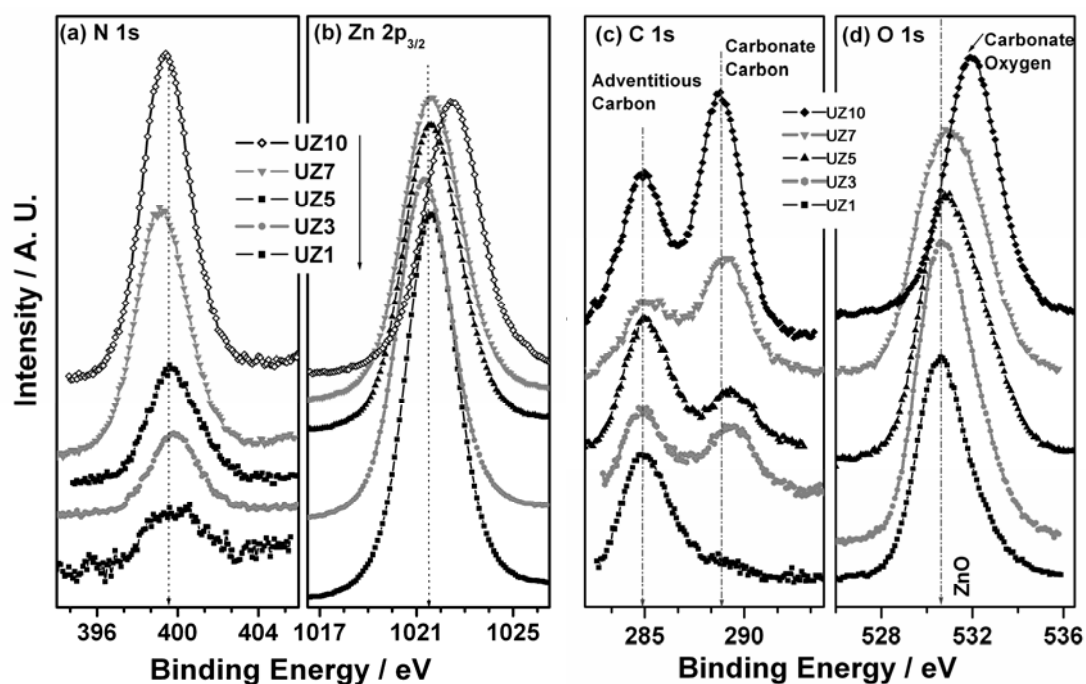
Figure 3.8: *XPS spectra collected from (*a*) N 1s (*b*) Zn 2p$_{3/2}$ (*c*) C 1s and (*d*) O 1s core levels of ZnO$_{1-x}$N$_x$ materials.*

O 1*s* peak appeared at 530.5 eV for UZ1 and it is in agreement with that of ZnO [15]. However, a broadening occurred on the high BE side with increasing urea content in the preparation. From UZ5 to UZ10 shifting of O 1*s* peak to higher BE suggests the formation of carbonate. On UZ10 presence of O 1*s* peak at 532 eV is due to carbonate formation. Furthermore, significant amount of carbonate is evident from C 1*s* spectra of UZ7 and UZ10 implies the high BE component (532.0 eV) in O 1*s* core level [16], which can be confirmed from XRD and thermal analysis. Further to mention that Zn 2*p*$_{3/2}$ core level appeared at BE 1021.6 + 0.1 eV for all ZnO$_{1-x}$N$_x$ materials, except UZ10 indicates that the electron density on Zn is slightly higher than that of ZnO.

3.2.8 **SIMS Analysis**

In the present investigations efforts to measure the nitrogen content using the Kjeldahl method with $ZnO_{1-x}N_x$ materials did not yield meaningful results, unlike that observed with organic compounds and peptides. This is the main aim for the measurement of nitrogen content in $ZnO_{1-x}N_x$ materials via analytical methods.
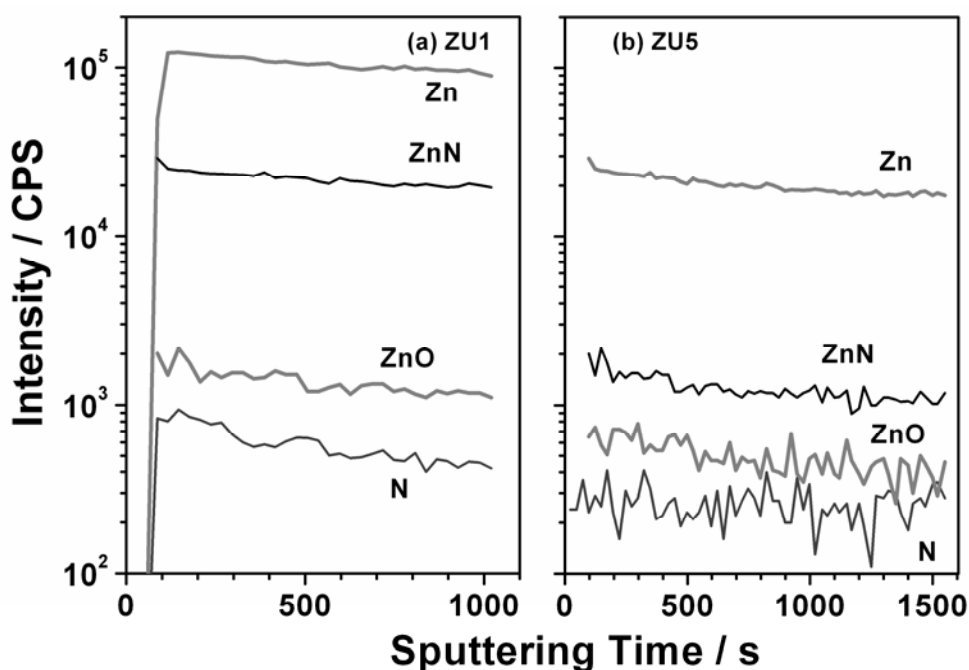
Figure 3.9: *SIMS measurements display secondary ion intensities obtained from* (a) *UZ1 and* (b) *UZ5.*

Secondary-ion mass spectrometry (SIMS) results obtained on $ZnO_{1-x}N_x$ materials are shown in Figure 3.9 with representative results from UZ1 and UZ5. Species that exhibited <100 counts/s were not considered due to high level of noise. The initially recorded mass spectrum with significant intensity illustrated the presence of different species, namely, Zn, N, ZnN, Zn-O, and O. Secondary-ion intensities of the first four species are shown in Figure 3.9, as a function of sputtering time or depth. Qualitatively, the same trend in intensity of all the species was observed on UZ1 and UZ5. No significant decrease in N and ZnN species with sputtering time emphasizes the bulk nitrogen doping in Zn-O and the uniformity of the substitution throughout the bulk. Nonetheless, Zn-N and Zn-O species counts were significantly different on UZ1 and UZ5. Considerably large Zn-N species on UZ1 underscore the fact that the level of nitrogen doping was higher than UZ5 and corresponds with the

values obtained from EDAX (as given in Table 3.1). In spite of being the host lattice, Zn-O showed the lower count rate than that of Zn-N, primarily due to different ionization capacity of emitted species. This phenomenon is strongly dependent on the local surface characteristics of the materials, known as 'matrix effect' in SIMS [17].

On the other side, another reasoning for the higher intensity of Zn-N than Zn-O can be pointed out from the fact that it is difficult to break the bonding ions from an increasing covalent character. An important point to be mentioned here is that no other N-related species, such as N_2, N_2^{2-}, NO, NO_2, NO_3^-, Zn-N-O, or NH_x, were noticed in the mass spectra, which suggests that the status of N in ZnO$_{1-x}$N$_x$ material is none of the above. The fact that only one type of N observed in all of the aforementioned characterizations underscores the status of N being unique in ZnO$_{1-x}$N$_x$ materials, and it is very likely the reason for the replacement of lattice O by N.

3.2.9 **Electron Paramagnetic Resonance Studies**

EPR studies carried out at room temperature on UZ1 and UZ1-950 is shown in Figure 3.10. This shows the features are due to Zn vacancies at $g = 2.00$, but relatively small intensity for oxygen vacancies at $g = 1.96$.
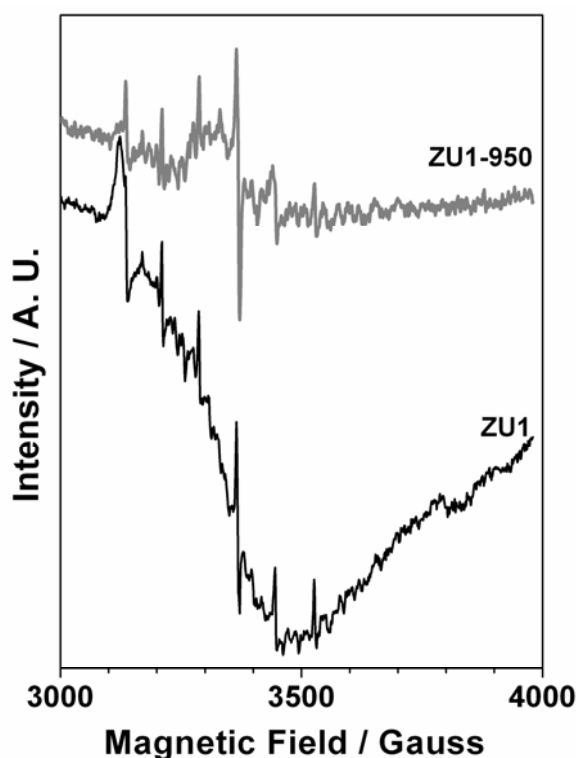

Figure 3.10: *EPR spectra of the UZ1 and UZ1-950 recorded at 298 K.*

No feature due to nitric oxide (NO) type species was observed hinting the absence of direct N-O linkages. No significant change in intensity was also marked for the above features after calcinations at 950ºC. However, an overall decrease in intensity of other features, mostly due to localized defects was observed. This is further supported by XPS studies (Figure 3.8), in which no N 1*s* peak was observed at >400 eV.

3.3 Catalytic Activity Study

3.3.1 Rhodamine B Degradation

A) Structure of rhodamine B   *B) Structure of rhodamine*
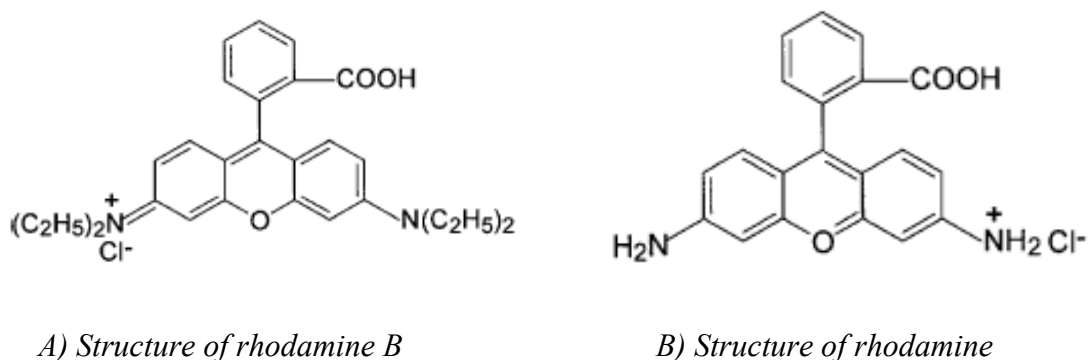
Scheme 3.1: Structure of Rhodamine B and Rhodamine

The photocatalytic degradation of harmful organic compounds is of great interest and important for environmental protection also. It has been evident from the reported studies that many organic and inorganic pollutants present in water or air stream can be fully decomposed by means of photocatalysis. Dyestuffs are ubiquitous and are one of the main classes of contaminants in wastewater, especially those from the textile and photographic industries. An efficient photocatalytic process of dye degradation usually includes the separation of electron hole pairs and the subsequent reduction-oxidation reactions. Photocatalytic activity of ZnO$_{1-x}$N$_x$, in the present research work, was examined through the photodecomposition of rhodamine B solution.

100 mg ZnO$_{1-x}$N$_x$ catalyst was suspended in 100 ml of 10 ppm rhodamine B solution and used for photocatalysis studies. The concentration of rhodamine B was determined by monitoring the intensity changes from the absorbance band at 532 nm. Figure 3.11a shows the changes in the UV-Vis absorption spectra of rhodamine B concentration for a reaction period of 3h of photocatalytic decomposition with UZ1.
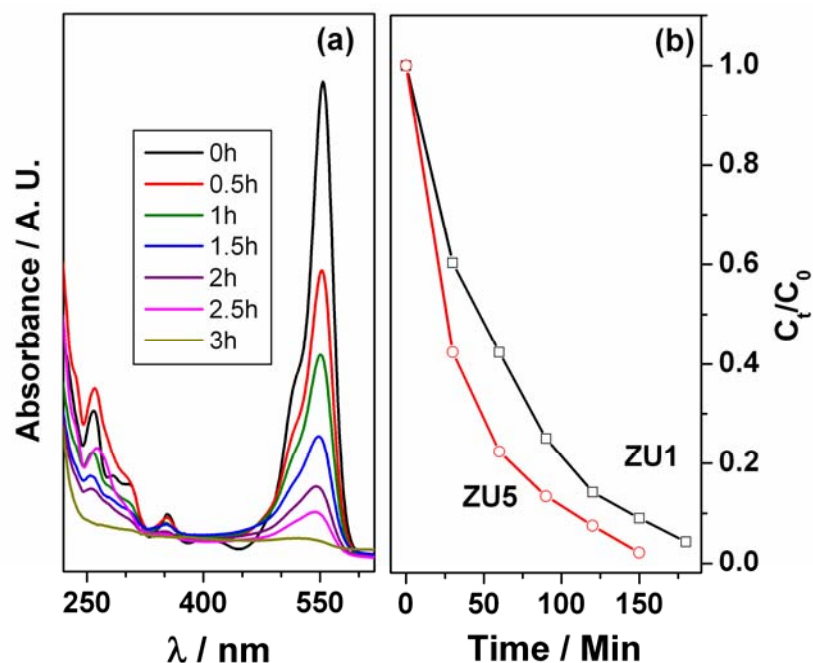
Figure 3.11:(a) *UV-Visible absorption spectra of rhodamine B decomposition plotted as a function of UV-light illumination time on UZ1.* (b) *Photocatalytic decomposition profiles of rhodamine B on UZ1 and UZ5.*

The aforementioned measurements demonstrate the complete decomposition of rhodamine B within 3 hrs for ZU1 (and ZU5). For a better understanding, the degradation rate of rhodamine B (ln (C_t/C_0)) is plotted against illumination time in Figure 3.11b for UZ1 and UZ5. The initial 10 ppm concentration of rhodamine B was taken as C_0 and C_t were the concentration measured after a specific reaction time. The rate of degradation of rhodamine B shows that it follows approximately pseudo-first-order kinetics: kt = ln (C_t/C_0), where k is the apparent reaction rate constant (the value of which was determined to be 0.017 and 0.024 min^{-1} for UZ1 and UZ5, respectively). UZ5 showed a relatively higher decomposition rate, and it is attributed to higher nitrogen content on the surface.

3.3.2 **Anisole Acylation Reaction**

It is well known that ZnO can be a dehydrogenation catalyst and a good catalytic support for many reactions, including steam-reforming reaction. Recently ZnO has been used for alkylation and acylation reaction [7] and we demonstrate here that ZnO$_{1-x}$N$_x$ exhibits acylation activity with high selectivity in a simple pot reaction at room temperature (RT).
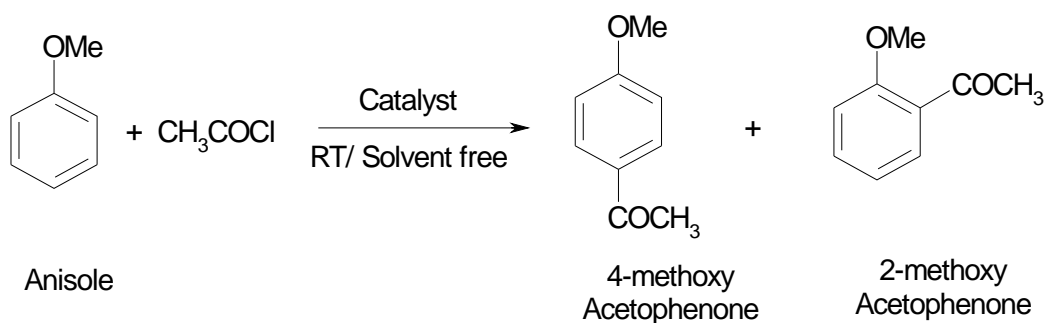
Scheme 3.2: Reaction scheme for Anisole acylation reaction.

Table 3.2: *Catalytic acylation of anisole with acetyl chloride on ZnO$_{1-x}$N$_x$ at RT*

Catalyst	Anisole conversion (Mol %)	Selectivity of the product		
		4-methoxy Acetophenone (Mol %)	2-methoxy acetophenone (Mol %)	2, 6-di-methoxy acetophenone (Mol %)
UZ1	65	90	7	3
UZ5	72	92	6	2

Conversion of anisole and selectivity towards 4-methoxy acetophenone in anisole acylation reaction was reported in Table 3.2. UZ5 shows better conversion than UZ1 which is likely due to better surface area and surface nitrogen segregation.

3.3.3 **Dehydrogenation of Cyclohexanol**

Dehydrogenation of alcohol on metal oxide catalysts has been studied for decades due to its practical importance in the chemical industry. ZnO based catalysts are known for dehydrogenation reactions. Hence, it is worth investigating ZnO$_{1-x}$N$_x$ materials for catalytic dehydrogenation of alcohols. A research for the selective catalytic dehydrogenation of cyclohexanol was carried out with ZnO$_{1-x}$N$_x$ systems.

Cyclohehexanol   **Cyclohexanone**
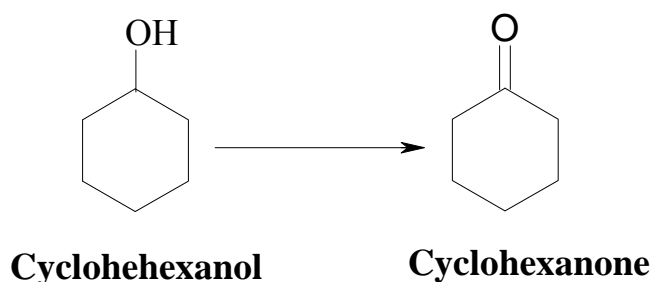
Scheme 3.3: Reaction scheme for cyclohexanol dehydrogenation.

3.3.3.1 **Effect of WHSV or Contact Time**

Figure 3.12 shows weight hour space velocity (WHSV) dependence for cyclohexanol conversion and cyclohexanone selectivity on ZnO$_{1-x}$N$_x$ (UZ5) at 400°C. Figure 3.12 demonstrates that the cyclohexanol conversion decreases with increasing WHSV. A marginal increase in conversion was observed with WHSV =4.8 h^{-1}
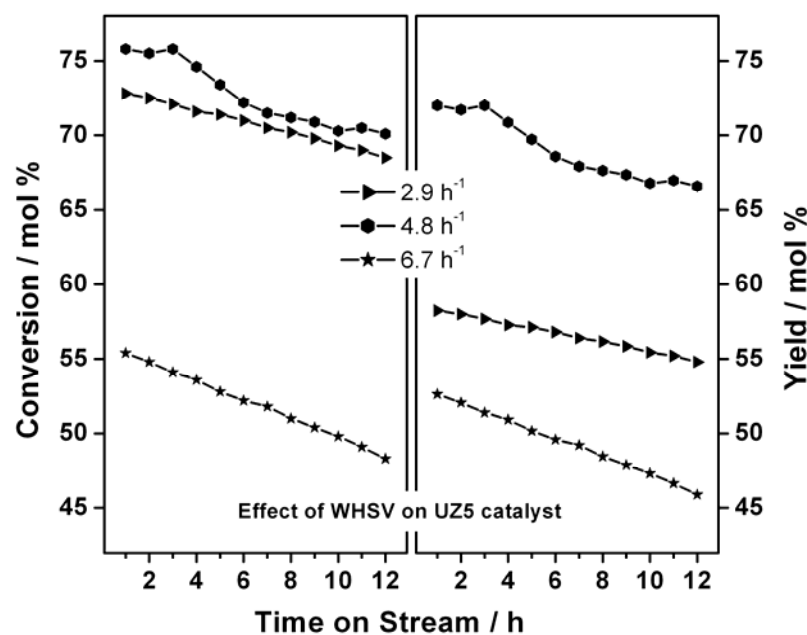
Figure 3.12: *Effect of WHSV on the catalytic activity of UZ5 with time on stream at 400°C.*

compared to 2.9 h^{-1}. Though cyclohexanol conversion is high at WHSV < 3 h^{-1} (higher contact time), but yield of cyclohexanone was low due to gaseous product and coke formation. At WHSV = 6.7 h^{-1}, conversion and yield decreases relatively rapidly hinting deactivation of the catalyst. An optimum of 72% cyclohexanol conversion with nearly 95% cyclohexanone selectivity was achieved at WHSV = 4.8 h^{-1} (or contact time = 0.21h). This above optimized WHSV was fixed for all further studies in this chapter.

3.3.3.2 **Effect of Reaction Temperature**

Effect of reaction temperatures on cyclohexanol dehydrogenation on ZnO$_{1-x}$N$_x$ (UZ5) is given in Figures 3.13. Cyclohexanol conversion and cyclohexanone yield increased significantly with increasing the reaction temperature from 350°C to 400°C. However, at high temperature (450°C), substrate conversion is high but the yield of cyclohexanone decreases mainly due to gaseous product formation like alkenes, CO$_2$.
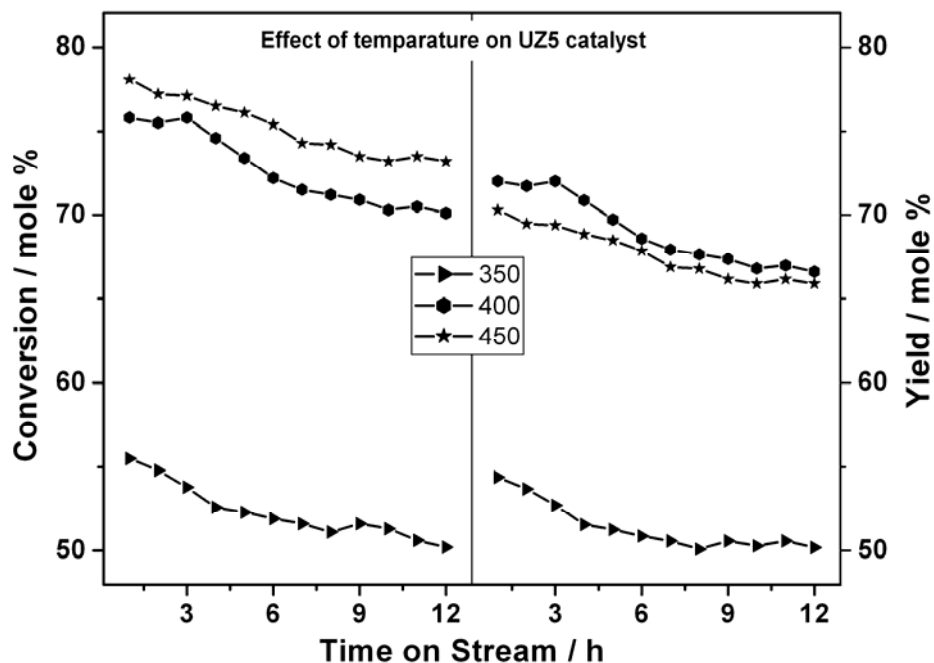
Figure 3.13: *Effect of temperature on the catalytic activity of UZ5 at a WHSV of 4.8 h^{-1} at time on stream.*

3.3.3.3   **Comparison of Catalytic Performance**

Figure 3.14a and b show the cyclohexanol conversion and cyclohexanone yield, respectively, on different ZnO$_{1-x}$N$_x$ materials at 400ºC and WHSV = 4.8 h^{-1}. Activity studies have been carried out without water in the feed. It is to be noted that UZ5 shows very high cyclohexanol conversion, compared to other two materials. For all the catalysts composition, the conversion and yield decreases with time on stream. The reason of deactivation has been discussed later part of the chapter.

Cylcohexanone selectivity remains $\geq$ 90% on all the catalyst compositions. UZ1 and UZ10 were showing 60% conversion with near about 55% yield; on ZU10 selectivity towards cyclohexanone was 90%. High urea concentration, during preparation of UZ10, increased the surface area as well as carbonate formation. Among the above series, UZ1 exhibits low surface area and UZ10 displays high surface area, but UZ10 contains a good amount of zinc carbonate. Furthermore, the surface nitrogen content is greater in UZ10 and lower in UZ1. Thus, low conversion in UZ1 is attributed to lower surface area and lower nitrogen concentration on the surface, whether in UZ10 due to carbonate formation selectivity is poor. UZ5 exhibits surface area is higher than that of UZ1, so both conversion and yield reach maximum.
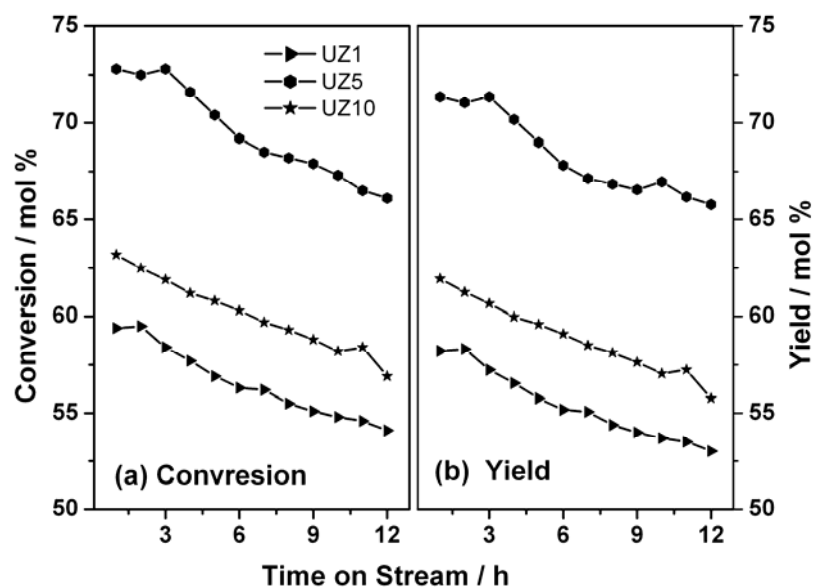
Figure 3.14: *Comparison of catalytic performance of ZnO$_{1-x}$N$_x$ with different compositions (UZ1, UZ5 & UZ10) at 400°C at a WHSV of 4.8 h^{-1}.*

3.3.3.4   Reason of Deactivation

XRD pattern and Raman spectroscopy of the fresh and the spent catalysts are compared in Figure 3.15. The spent catalysts are crystalline and all the peaks could be
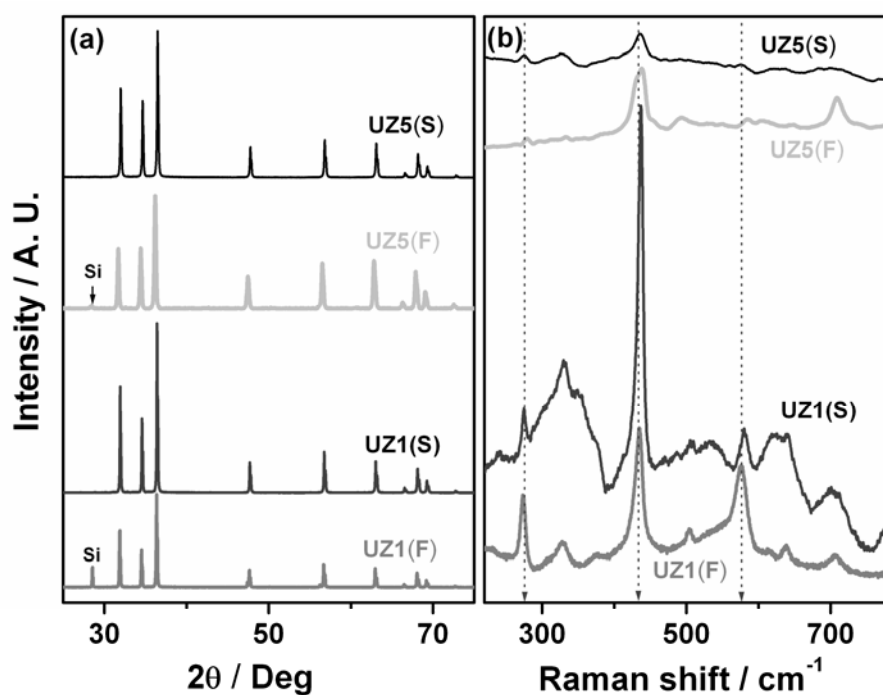
Figure 3.15: *(a) XRD and (b) Raman spectra of spent catalyst compared with fresh catalyst. Spent catalyst and fresh catalyst mentioned as (S) and (F), respectively after catalyst name.*

indexed like fresh catalyst. No significant change in the XRD pattern of spent ZnO$_{1-x}$N$_x$ materials is observed with respect to fresh catalyst. This is attributed to the structural integrity of the material retained after reaction also. However, in Raman spectra intensity of N containing peak decreases and intensity of E$_2$(high)$_{Zn-N}$ at 582 cm^{-1} decreases in intensity and that of ZnO increases at the expense of Zn-N features, which is likely due to N loss during the reaction condition. However, calcination of UZ1 under static air 500°C shows no N loss attributed another possibility of lowering the intensity of peak could be coke formation, which is blocking the N containing site.

3.4 Conclusions

ZnO$_{1-x}$N$_x$ materials were prepared using SCM, and it has been characterized by a variety of physicochemical, structural, spectroscopy, and microscopic measurements. Except for a minor lattice contraction, no significant change in the ZnO-Wurtzite structure was observed, even with 15% nitrogen in ZnO$_{1-x}$N$_x$. Density measurements suggest the presence of some amount of interstitial Zn when the nitrogen content is high (15%). Charge neutrality of the entire lattice, because of the high nitrogen content in ZnO$_{1-x}$N$_x$, was maintained by the aforementioned interstitial Zn species and some oxygen vacancies. Nanometer- to micrometer-sized and triangular/prism-shaped particles were observed via SEM. High thermal stability was identified from thermal analysis. Raman, SIMS, and optical studies demonstrate the direct Zn-N bond and the N 2*p* states forms the midgap (deep level acceptor) band, respectively. XPS indicates that the charge density of nitrogen on ZnO$_{1-x}$N$_x$ is similar to that of NH$_3$. Decomposition of rhodamine B on ZnO$_{1-x}$N$_x$ with UV light reveals its effectiveness as a photocatalyst. No significant visible-light photocatalytic activity and the insulating character of ZnO$_{1-x}$N$_x$ suggest that the N 2*p* states do not change the band gap of ZnO$_{1-x}$N$_x$, compared to ZnO, because N 2*p* states are in the forbidden region of the band gap. It is likely that suitable surface modifications of the present material with a noble metal might be a visible light driven photocatalyst and it is worth exploring further in this line. ZnO$_{1-x}$N$_x$ materials also exhibit highly selective acylation catalytic activity at RT. Visible-light absorption and a large nitrogen content observed, along with the presence of triangular or prismatic shapes, suggests a high potential associated with ZnO$_{1-x}$N$_x$ toward applications, such as low-threshold semiconductor lasers and photocatalysts such as N-doped TiO$_2$.

Part B: Solid Solution of ZnS in ZnO, ZnO$_{1-x-z}$N$_x$S$_z$ Materials.

3.5 **Introduction**

TiO$_2$ and ZnO based semiconductors are potential candidates for solar energy conversion applications, particularly as photocatalysts for H$_2$ generation from water [18]. Unlike other semiconductors such as GaP, InP, or CdTe, oxides such as TiO$_2$ and ZnO do not contain any precious metals or toxic elements. For a wide-band gap semiconductor, the addition of impurities often induces dramatic changes in its electrical and optical properties. Heteroatom doped titanium oxide (TiO$_2$) has been extensively studied for photocatalysis under UV and/or visible light, as nonmetal doping can narrow the band gap and improve the utilization of the solar spectrum [19]. The band gap reduction and photocatalytic promotion under visible light were most pronounced for sulfur-doped TiO$_2$ [20]. Both cation substitution (S^{4+}/S^{6+}) on the Ti site and substitutional anionic S on the O sites have been reported. Meanwhile, co-doping with double nonmetal elements has attracted more attention [21], such as N, S-codoped TiO$_2$. Nonetheless, there is serious concern about the efficacy of the S-TiO$_2$ [22]. However, in case of ZnO, implication to S or N-S co-doping has not yet been explored significantly.

ZnO is a multifunctional semiconductor material with versatile properties [1]. Due to their promising perspectives in these myriad areas, many approaches including both physical and chemical strategies have been developed for the preparation of this oxide. However, suitable doping of hetero atoms either in the place of zinc or oxygen can make use of ZnO in better ways. Especially, anionic impurity can introduce a new level in valence band, which provides effective modification of electronic structure, and helps to shift the threshold wavelength to the visible light [23]. In addition to the various types of dopant, its concentration and the method of doping can also broaden its application. Among the heteroatoms, N is widely acceptable. Nonetheless, sulfur can also be substituted in place of oxygen as sulfide under appropriate conditions. However, the outer shell electronic configuration of sulfur matches with oxygen which provide charge neutrality effectively in the lattice but the atomic radius of the sulfur is larger than that of oxygen. S-doping in a ZnO system is expected to modify the electrical and optical properties. This change in properties could be

assigned to the large electronegativity and size differences between S and O (r_S/r_O = 1.3) [24]. In addition, band gap engineering is possible because of the larger band gap of ZnS (3.66 eV) compared to that of ZnO. Regardless of these possibilities, S has been rarely doped in ZnO because of problems in synthesis and stabilization of ZnS owing to the significant difference in growth conditions. Interestingly, ZnO and ZnS belong to same phase. However, few reports are available on synthesis of S doped ZnO by pulse laser deposition or chemical vapor deposition method [25].

Among the transition metal sulphides, ZnS has some significant special properties, which make it a key technological material with versatile applications. ZnS is a semiconductor with a large direct band gap of 3.7 eV for the hexagonal Wurtzite phase and of 3.66 eV for the cubic zincblende phase in the UV region. It has wide range of applications like ZnO in the area of optical phase modulation, IR antireflection coatings, light guiding, in integrated optics, for the development of electroluminescent displays, in light emitting materials for color display systems, as a window layer in heterojunction photovoltaic solar cells and in multilayer dielectric filters [26]. ZnS also touted for activity of the photocatalytic decomposition of organic materials due to trapped holes arising from surface defects on the sulfide [27]. To utilize potential offered by ZnS in better way, more emphasis are given to get various sizes of ZnS starting from nano to micro size with variable morphology [28].

Here we made an attempt to incorporate sulfur predominantly along with nitrogen in ZnO lattice to vary the band gap through SCM. Thiourea and urea were used as the source of S and N, respectively. Prepared material was characterized by various spectroscopic and microscopic methods. Effect of sulfur and nitrogen co-doping was explored through alcohol dehydrogenation reaction.

3.6 **Results and discussion**

ZnO$_{1-x-z}$N$_x$S$_z$ materials prepared by SCM using various urea and thiourea ratio and physicochemical properties are listed in Table 3.3 and compared with standard ZnS, ZnSO$_4$ and ZnO materials. The metal ion to fuel ratio (urea + thiourea) was fixed to be 1, however, urea to thiourea ratio was taken as 100:0, 75:25, 50:50, 25:75 and 0:100 and as prepared materials are designated as UZ1, UZS1, UZS2, UZS3 and UZS4 respectively, through out the chapter unless stated. It is to be noted that UZ1

exhibits higher density (5.8 g/cm^3) [29] than all other composition and ZnO (5.6 g/cm^3), suggesting a considerable change in composition and compact nature of the material. It was earlier (chapter 3(A)) demonstrated with the above material that large amount of N and charge density was compensated by interstitial Zn and oxygen vacancies, and supported by EPR measurements.

3.6.1 **XRD Analysis**

Figure 3.16 presents XRD pattern of the ZnO$_{1-x-z}$N$_x$S$_z$ materials in the range of 10º to 75º, which reveals that the as prepared material also exhibited a hexagonal Wurtzite structure and its diffraction pattern was changing with ratio of urea to thiourea in the preparation mixture. For the comparison purposes, XRD patterns of ZnO, ZnS, ZnSO$_3$, Zn$_3$O(SO$_4$)$_2$ and ZnSO$_4$ were also included.
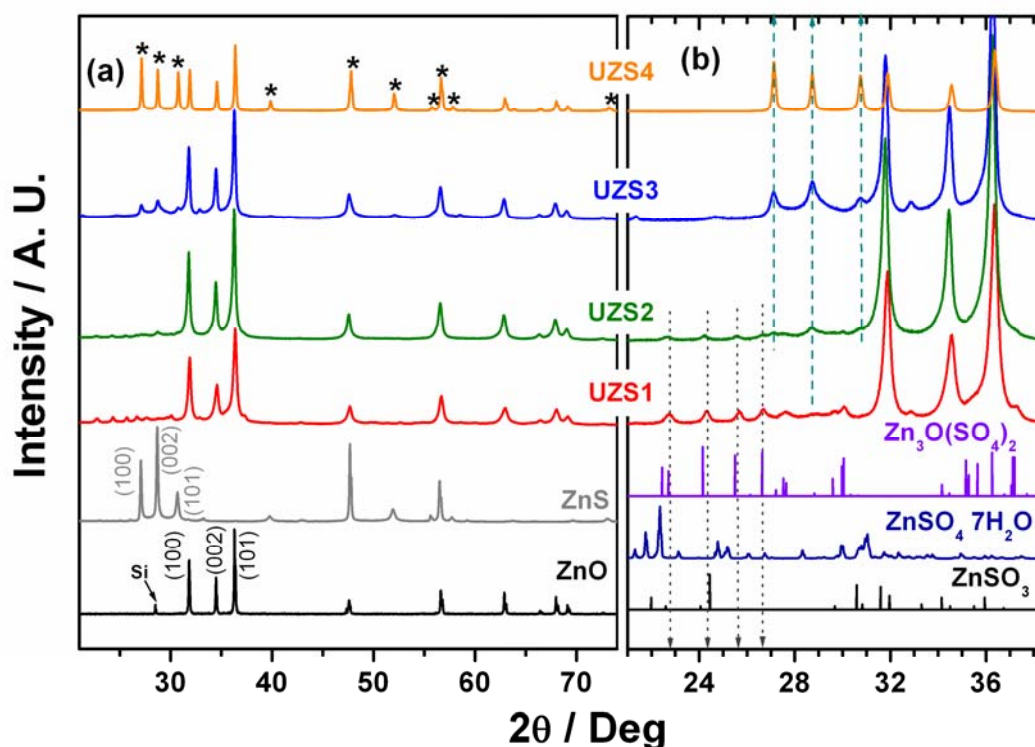
Figure 3.16: (a) *PXRD pattern of ZnO$_{1-x-z}$N$_x$S$_z$ along with ZnO and ZnS. (b) Zoomed XRD pattern of ZnO$_{1-x-z}$N$_x$S$_z$ $_z$ materials for better clarity and compared with Zn$_3$O(SO$_4$)$_2$, ZnSO$_4$ 7H$_2$O and ZnSO$_3$,. (*) indicates ZnS phase.*

XRD patterns of pure ZnO and ZnS show hexagonal Wurtzite structure, whereas ZnSO$_4$ is of orthorhombic structure and Zn$_3$O(SO$_4$)$_2$ shows monoclinic

structure [8, 25(b), 30]. Ionic radii of S (1.7 Å) is much higher than that of O (1.2 Å), and hence, the addition of small amount of sulfur containing fuel, especially thiourea in the preparation mixture prefers to form a separate phase of finely distributed sulfur related compound in the prepared materials. Furthermore, with variation in ratio of urea and thiourea average combustion temperature, reaction condition and amount of sulfur change as well. This reflects the formation of different sulfur related compounds in the as prepared material. In the case of UZS1, urea to thiourea ratio was high which leads to complete and fast combustion, as urea is known for good fuel material and with higher urea amount average combustion temperature is also high [31]. Therefore, under this combustion condition significant amount of sulfur gets oxidized to sulfite and zinc sulfate and/or zinc oxide sulfate. However, in UZS1 material 100% intense peak was indexed satisfactorily to hexagonal ZnO Wurtzite structure with space group of P6$_{3mc}$. Low intense peaks observed between 20 and 37^0 are attributed to a mixture of zinc oxy sulfate and zinc sulfate, with the former one dominating on UZS1. Very broad and low intense ZnS features could be seen on UZS1 at 28.7^0, corresponding to the 002 facets of ZnS, indicating the oxidation of surface ZnS to sulfate related features.

Table 3.3: *Preparation condition, color and surface area of the ZnO$_{1-x-z}$N$_x$S$_z$.*

ZnO$_{1-x-z}$N$_x$S$_z$ Code[a]	Urea:thiourea mole ratio in %	Color of the Samples	Surface area (m^2/g)
Zn$_{1.04}$O$_{0.84}$N$_{0.15}$ (UZ1)	100:0	Brownish yellow	1
ZnO$_{0.82}$N$_{0.08}$S$_{0.11}$ (UZS1)	75:25	off white	5
ZnO$_{0.75}$N$_{0.07}$S$_{0.17}$ (UZS2)	50:50	off white	8
ZnO$_{0.64}$N$_{0.05}$S$_{0.31}$ (UZS3)	25:75	Light yellow	15
ZnO$_{0.51}$N$_{0.03}$S$_{0.47}$ (UZS4)	0:100	Light yellow	20
ZnO	-	White	
ZnS	-	White	

[a] *The fuel (urea + thiourea):Zn(NO$_3$)$_2$ molar ratio is taken as 1. Material composition measured from energy-dispersive X-ray analysis.*

In the case of UZS2 peak intensity for ZnSO$_3$, Zn$_3$O(SO$_4$)$_2$ decreases enormously and intensity of ZnS increases notably. Unlike UZS1 and UZS2, no impurity was observed in the cases of UZS3 and UZS4. With increasing thiourea concentration in the preparation mixture, reaction atmosphere changes predominantly towards sulfides along with ammonia. This is at least partially due to no presence of oxygen in thiourea compared to urea, and hence, enough amount of oxygen was not provided by the fuel. The lack of oxygen in thiourea does not allow to form oxidized product of sulfur, and significant ZnS phase begins to form. Unlike UZS1 and UZS2, no sulfate impurity diffraction lines were observed in the cases of UZS3 and UZS4. However, ZnS phase was observed. Nonetheless, in UZS4 material strong diffraction lines of both ZnO and ZnS are found together. For UZS4 100% thiourea was used as the fuel which is likely the reason for incomplete oxidation and favors ZnS formation under such combustion condition, attesting the successful use of thiourea as a source of sulfur. Sulfur species which are not oxidized help to form large amount (50%) of hexagonal ZnS Wurtzite phase. Therefore, distinct and strong ZnS features observed in the XRD pattern along with ZnO. It is reasonable to conclude that when S^{2-} replace the O^{2-} ions in the lattice of ZnO, a lattice distortion would be created due to a large ionic radius difference between S^{2-} (1.7 Å) and O^{2-} (1.22 Å) due to which ZnS phase has been observed distinctly in cases of UZS2, UZS3 and UZS4. It is likely the structural similarity of ZnS and ZnO helps to form the solid solution of 1:1 ratio.

Not only the diffraction pattern, but also the relative intensity of the material also varied with changing thiourea concentration in the reaction mixture as well. For lower thiourea concentration, good crystallinity of the compound (UZ1 and UZS1) can be observed as it shows very sharp peak. However, with increasing thiourea concentration in the preparation mixture, crystallinity of the compound decreases and FWHM of the peaks increases with significant peak broadening due to formation of smaller crystallite sizes of ZnS. In the XRD pattern of the UZS4 material, it can be viewed specifically.

Thermal stability of the ZnO$_{1-x-z}$N$_x$S$_z$ materials have been explored with XRD after calcination of UZS4 and UZS1 at different temperatures for 4 hours in air and the results are shown in Figure 3.17. There is a strong effect of calcination on each material. In as prepared UZS4 material shows distinct peaks for ZnS and ZnO.

However, with increase in calcination temperature peak intensity of ZnS decreases and simultaneously the peak intensity for the ZnO increase. ZnS is oxidizing to ZnO under air atmosphere with an increase in calcination temperature, which directly reflects in the relative XRD intensity of ZnO and ZnS in the calcined samples. Hence, peak intensity of ZnO increases at the expense of ZnS. It is clear from the XRD patterns recorded after calcination at 300ºC and 500ºC, the peak intensity of ZnS is comparable to that of as prepared UZS4 sample. However, at 600ºC calcined sample shows relatively less ZnS intensity compared to as prepared sample. Above results are compared with XRD pattern of physical mixture of ZnO (30%) and ZnS (70%). A glance at the results indicates a difference in intensity patterns of prominent diffraction peaks in Figure 3.17a. (100) facet shows higher intensity than other facet of ZnS, however, in the physical mixture (002) facet shows higher intensity. Importantly, there is a shift of ZnO diffraction lines to lower angle (compared to pure ZnO) indicates that the materials prepared are solid solution and not physical mixture. Other characterizations provide strongly supporting evidences for this. Furthermore, 800ºC calcined sample shows pure ZnO peak.
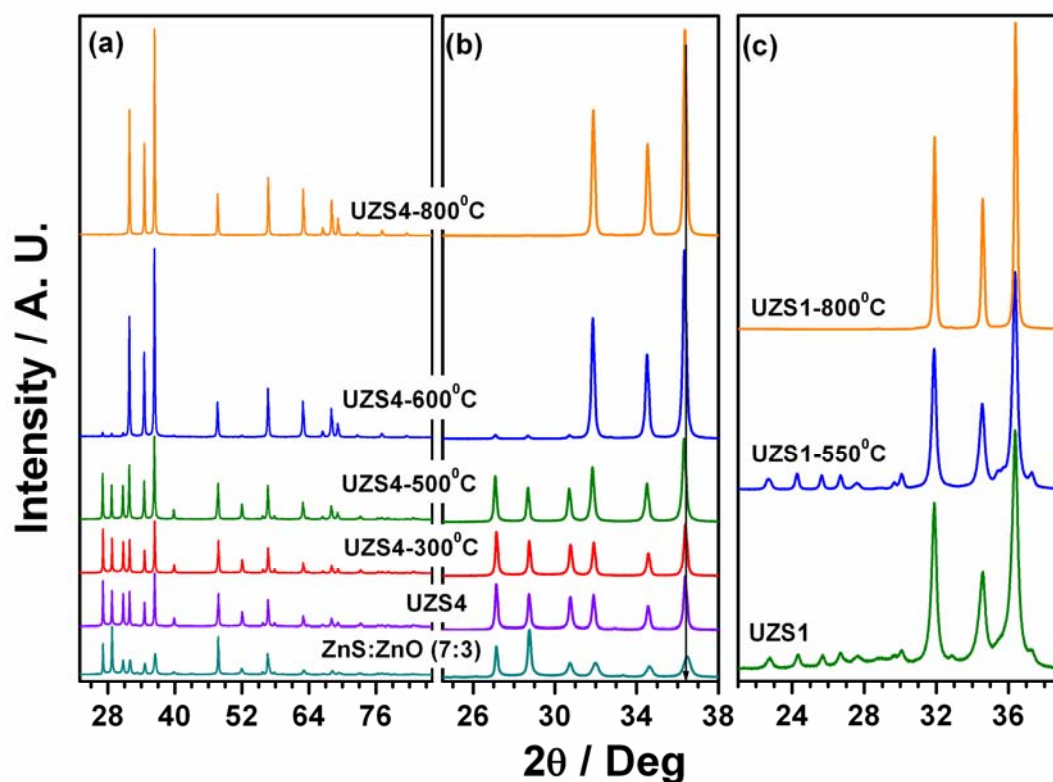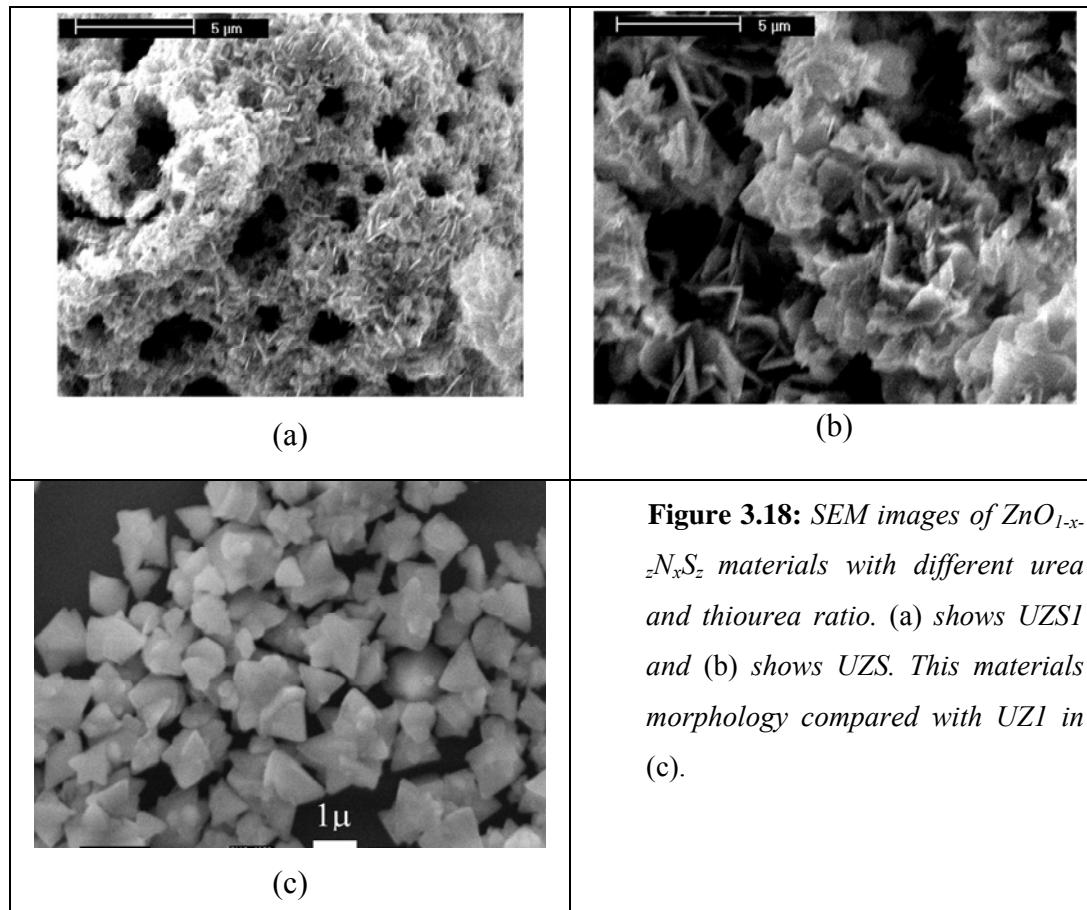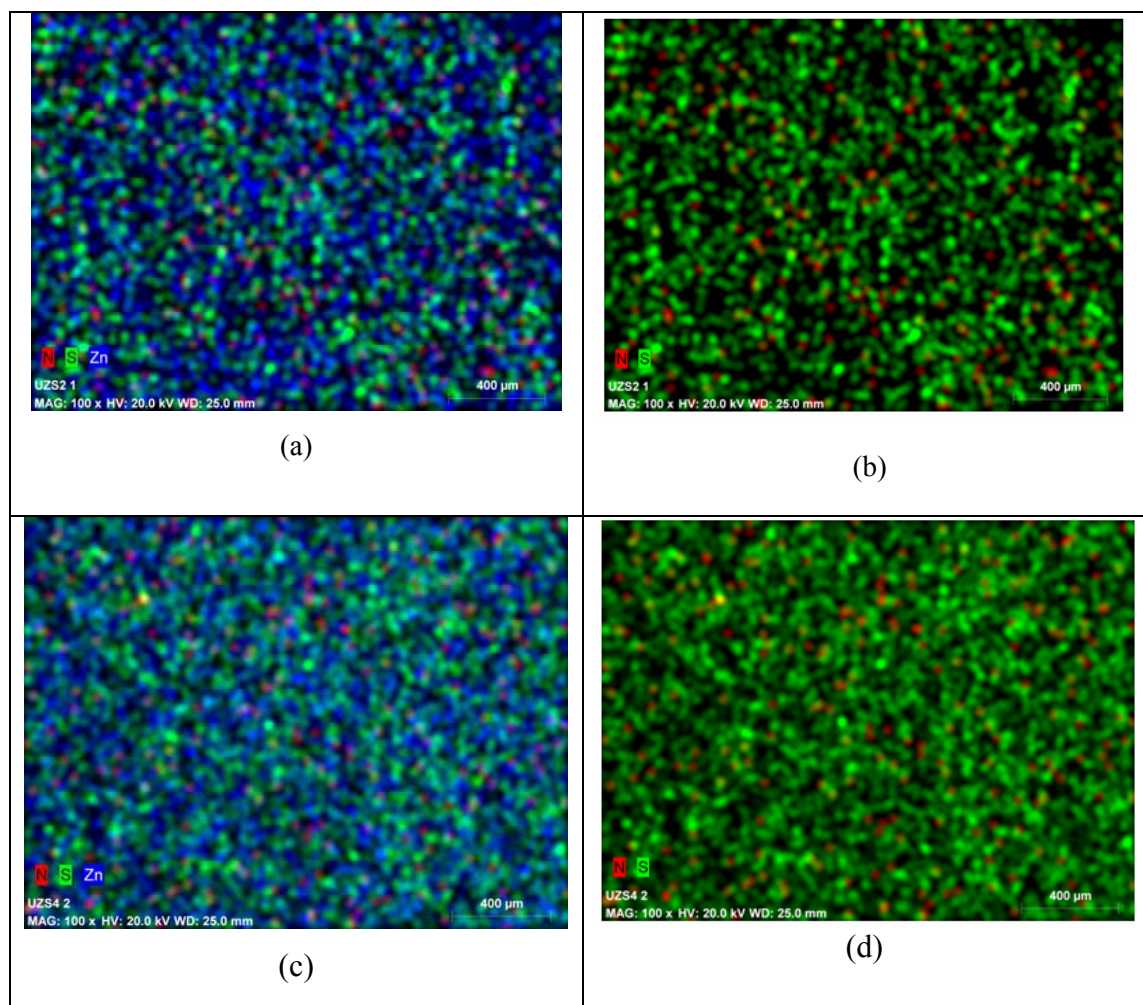

Figure 3.17: *PXRD pattern of calcined UZS4 shown in (a) and (b) compared with respective calcined materials and a physical mixture of ZnS:ZnO (7:3). (c) shows calcined UZS1.*

Except for peak narrowing, UZS1 material calcined at 550ºC (Figure 3.17b) does not show any significant changes in XRD diffraction. Upon further calcination to 800ºC it shows exclusive ZnO features. Similar trend was also observed for UZS2 material.

3.6.2 SEM Analysis

The morphology of ZnO$_{1-x-z}$N$_x$S$_z$ materials was explored using SEM. From the SEM images of as prepared material shown in Figure 3.18, it is clear that the materials exhibits pores of the order of 1-10 μm and they are significantly macro porous. It is also important to compare the morphology and textural properties of UZ1. UZ1 shows ordered hexagonal prism and triangular shape particles without any pores. Indeed the well ordered microcrystals observed in Figure 3.18c for UZ1 highlights the compact micro single crystals of ZnO$_{1-x}$N$_x$. Further, the surface area of UZ1 is also low at 1 m^2/g underscores the above points. UZS1 material shows porous structure with needle shape particle highlights the role of thiourea in changing the surface and particle morphology. Needle shape one dimensional particles observed predominantly is attributed to ZnO$_{1-x-z}$N$_x$S$_z$, and white patches observed are attributed

(a)

(b)

(c)

Figure 3.18: *SEM images of ZnO$_{1-x-z}$N$_x$S$_z$ materials with different urea and thiourea ratio.* (a) *shows UZS1 and* (b) *shows UZS. This materials morphology compared with UZ1 in* (c).

Figure 3.19: *Elemental mapping of ZnO$_{1-x-z}$N$_x$S$_z$ materials for UZS2 and UZS4, for Zn, N and S (*a *and* c*), and only N and S on* b *and* d*. Color coding for different elements are shown on the images (N – red, S – green and Zn – blue).*

to sulfate related compounds on the surface. On moving from UZS1 to UZS4, above sulfate related compounds decrease in content and the particle morphology changes drastically from needle to V-shape two-dimensional arrays with an approximate edge size of 1 μm. Indeed the surface area also increases from 5 m^2/g to 20 m^2/g from UZS1 to UZS4, respectively, indicating an increased porosity from UZS1 to UZS4.

EDAX analysis was carried out to measure the material composition as well as to find out the extent of homogeneity of uniform distribution over a large area. Representative results are given in Figure 3.19 for UZS2 (a and b), and UZS4 (c and d). Elemental mapping of all the elements have been carried out and shown with color coding for different elements. High intense and low intense (or diffused) color indicating the particular element's high and low content, respectively, in a particular

area/spot. Two or more elements in the same spot create a new color due to a combination of colors. Figure 3.19b and d shows only the nitrogen and sulfur mapping of the above materials to show the homogeneous distribution. First of all the above results confirms the homogeneous distribution of doped elements at microscopic level over a large area and indicating the effectiveness of the preparation method. A careful look at the elemental map (Fig. 3.19a and c) reveals the association of Zn and S more on UZS4 than UZS2, suggesting the large percentage of ZnS in ZnO and solid solution nature. It is also to be noted that the atom percent measured through EDAX on individual particle differs significantly, and values reported in Table 3.3 are the average values obtained over large areas (>1 mm^2), as shown in Figure 3.19. An increase in sulfur content is evident from an increase in green density from Fig. 5b to 5d. Indeed the red color (for N) could be seen better on Figure 3.19b than Figure 3.19d, indicating a decrease in N-content in UZS4. The results from XRD and EDS indicate that with lower thiourea ratio, the obtained crystals are not the simple mixtures of ZnS and ZnO, but their solid solutions. Both thiourea and urea at 500ºC dissociate and form in situ ammonia and sulfur related gaseous product, which helps to incorporate both N and S in the ZnO lattice.

3.6.3 Thermo Gravimetric Analysis

Figure 3.20 depicts the thermal analysis of (a) UZS4 material in air and N$_2$ atmosphere, (b) UZS1 material in air atmosphere and compared with that of ZnS (in a) and ZnSO$_4$, 7H$_2$O (in b) respectively. USZ1 and UZS4 show about 2% weight loss up to 150ºC is due to elimination of water and adsorbed components. Between 150 and 570ºC UZS4 material shows hardly any change in weight and a sharp weight gain of 2.5% was observed between 570ºC and 680ºC. Above 680ºC, weight loss begins and continues up to 850ºC. On comparison of UZS4 results with that of pure ZnS in air it can be inferred that the weight gain between 570 to 680ºC is mainly due to oxidation of ZnS to sulfate/sulfite like compounds. This conclusion can be supported by the XRD of calcined material at different temperature. An exothermic peak observed in DTA curve of UZS4 at 690ºC similar to that of ZnS at 660ºC supports the oxidation of sulfur. Significant shift in the temperature of the above peak for UZS4 indicating a relatively better stability for solid solution compared to bulk ZnS. However, a shift of +30ºC temperature observed in exotherm (Figure 3.20a inset) for
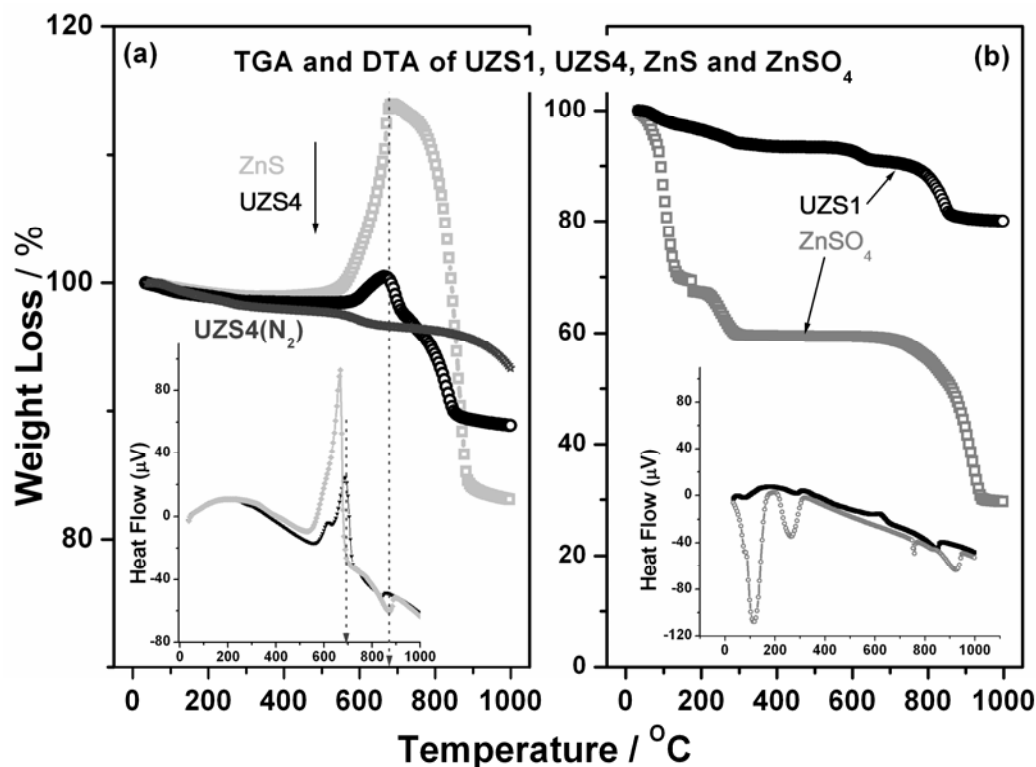
Figure 3.20: *Thermo-gravimetric of* (a) *UZS4 and (*b*) UZS1 carried out in air and nitrogen atmosphere at a heating rate of 10 °C/min compared with ZnS and ZnSO$_4$.(Inset differential thermal analysis of* (a) *UZS4 and* (b) *UZS1 carried out in air atmosphere at a heating rate of 10 °C/min compared with ZnS and ZnSO$_4$, respectively.)*

UZS4 is likely due to the distribution of smaller clusters of ZnS in ZnO lattice in UZS4. Weight loss observed between 680°C to 850°C is due to decomposition of sulfate/oxide sulfate of Zn to ZnO and it is in good correspondence with that of ZnSO$_4$ 7H$_2$O results (Figure 3.20b). No significant weight loss occurs above 850°C and supports complete removal of sulfur related species from UZS4. Thermal analysis of UZS4 material in N$_2$ atmosphere shows no weight gain between 500 and 650°C, rather a minor weight loss observed between 600 and 700°C, which clearly suggests that any oxidation is fully prevented in nitrogen atmosphere.

However, for UZS1 material weight loss pattern with increasing temperature is quite different in air atmosphere compared to UZS4. TG –DTA results of ZnSO$_4$ 7H$_2$O given in Figure 3.20b is worth comparing with that of UZS1. For pure ZnSO$_4$ 7H$_2$O sample there is initial weight loss of about 42% up to 250°C is due to loss of crystalline water. About 5-6% weight loss observed up to 270°C on UZS1 is mainly due to adsorbed and crystalline water. A sharp weight loss of 29% was observed

between 700 and 880ºC for ZnSO$_4$ 7H$_2$O is mainly due to the decomposition of sulfate to oxide. Indeed the weight loss observed between 600ºC and 850ºC (Fig. 3.20a) is due to the decomposition of ZnSO$_4$ to ZnO. The loss of SO$_2$/SO$_3$ leads to weight loss in TG. It is also to be noted that the endothermic nature of ZnSO$_4$ decomposition, in contrast to exothermic oxidation of ZnS to ZnSO$_4$ is followed by decomposition.

3.6.4 **UV-Visible Spectra**

Usually, anion doping obviously affects light absorption characteristics of any oxide material, and ZnO is not an exception. Diffuse reflectance spectra (DRS) of ZnO$_{1-x-z}$N$_x$S$_z$ were shown in Figure 3.21 and it is compared with reference materials such as standard ZnS, ZnO and a physical mixture of ZnS and ZnO (ZnS:ZnO = 7:3). ZnO$_{1-x-z}$N$_x$S$_z$ exhibits significant absorption in the visible light regime among the materials. It is to be noted that ZnS and ZnO shows absorption cut off around 340 nm and 375 nm, respectively. However, the absorption cut off is extended at least to 520 nm for UZS4; UZS1 and UZS2 also show absorption up to 470 nm. There is red-shift observed in ZnO$_{1-x-z}$N$_x$S$_z$ materials with increasing ZnS content and it has been caused by the modified chemical environment between Zn, O and S supports the formation of solid solution of ZnS and ZnO. The above observation demonstrates that the ZnO$_{1-x-z}$N$_x$S$_z$ is indeed a solid solution and not a physical mixture. It is further confirmed from the absorption spectrum recorded for a physical mixture ZnS:ZnO (7:3) which exhibits absorption due to ZnS up to 340 nm and up to 375 nm due to ZnO as expected. Physical mixture of any ratio of ZnS and ZnO does not exhibit absorption above 375 nm confirms the materials prepared are indeed solid solution of ZnS and ZnO.

Band-gap energies calculated from the DRS results for ZnO$_{1-x-z}$N$_x$S$_z$ materials show a prominent decrease with increasing ZnS content. Band gap calculated from the absorption spectrum of UZS4 is 2.85 eV suggesting a significant band gap reduction and changes in the electronic structure of solid solution compared to pure components. The band-gap diminution of the above materials has been caused by the formation of hybrid orbital in the VB. It is expected that S 3*p* and O 2*p* are likely to overlap in the VB of UZS1-UZS4. S exists as an anion (S2⁻) in UZS4 and the top of its VB may be predominantly composed of S 3*p* energy levels as they have slightly
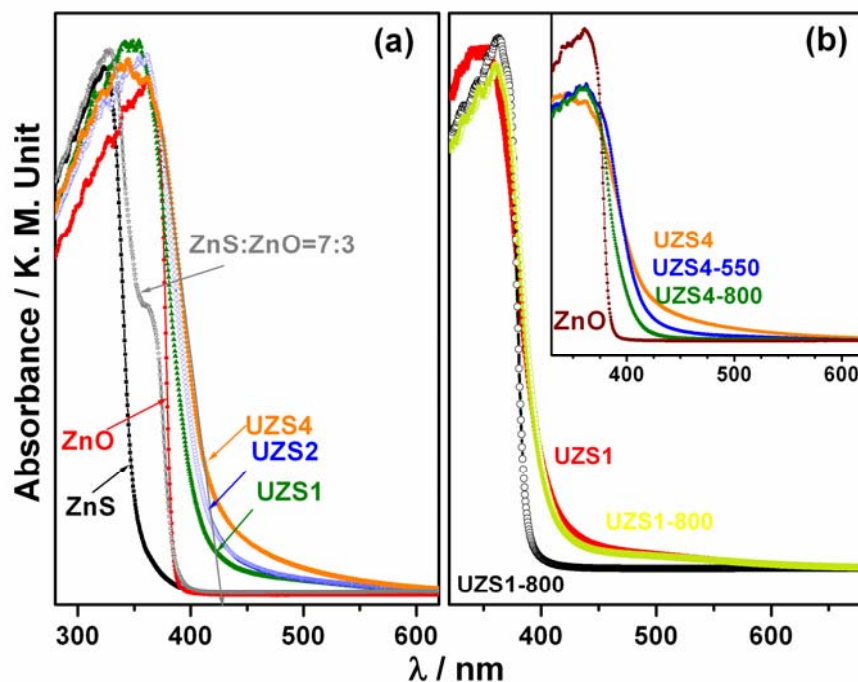
Figure 3.21: (a) *Diffuse reflectance UV-Visible spectra of the ZnO_{1-x-z}N_xS_z materials along with ZnO, ZnS and physical mixture of ZnS and ZnO (7:3).* (b) *UV-Visible spectra of calcined UZS1 and UZS4 (inset) calcined at 550 and 800°C and ZnO.*

higher orbital energies than O 2*p* levels. Thus in VB, S 3*p* and O 2*p* overlaps and broadens it than in ZnO [27a]. It is expected that the CB of UZS1-UZS4 formed by Zn 3*d* as well as S 3*d* orbitals.

UZS1 and UZS4 calcined at high temperatures have been subjected to optical absorption studies and the results are shown in Figure 3.21b. They exhibit a systematic decrease in visible light absorption with increasing calcination temperature, above 550°C. However, UZS4 exhibit some visible light absorption even after calcinations at 800°C.

3.6.5 **X-ray Photoelectron Spectroscopy**

To explore the electronic structure as well as the nature of surface of ZnO1_{-x-z}N_xS_z materials, XPS analysis has been carried out for all the composition. Core level spectra of S 2*p* Zn 2*p_{3/2}* and N 1*s* are compared in the Figure 3.22.

It can be seen from Figure 3.22a that the S 2*p* core level peak displays two different peaks at BE around 168.5 and 161.6 eV. A comparison of observed BE to

the BE values reported for different S compounds demonstrate that the oxidation state of S at 162.1 eV is -2 as in sulphide and at 169.3 eV is due to +6 as in sulfate [14]. The peak at 162.1 eV corresponds to the ZnS and demonstrates the formation of solid solution of ZnS in ZnO. In UZS1, characteristic peak for sulphide was found albeit with low intensity, along with majority of sulfate on the surface is evident. Above sulfide feature increases in intensity from UZS1 to UZS4 and directly supports the observation of XRD. Peak intensity at 168.5 eV remains constant from UZS1 to UZS3; and decreased for UZS4; however, at the same time peak for sulphide builds up its intensity from UZS1 to UZS4. The above observation supports the oxidation of sulfide species on the surface to sulfate under reaction conditions.

It is clear from Figure 3.22a that with increasing thiourea concentration in the preparation mixture total sulfur concentration on the surface also increases, which was eminently shown in elemental mapping of USZ4 as well. This can be clearly seen in as prepared material (in UZS3 and UZS4), where a prominent peak for both sulphide and sulphate was observed.
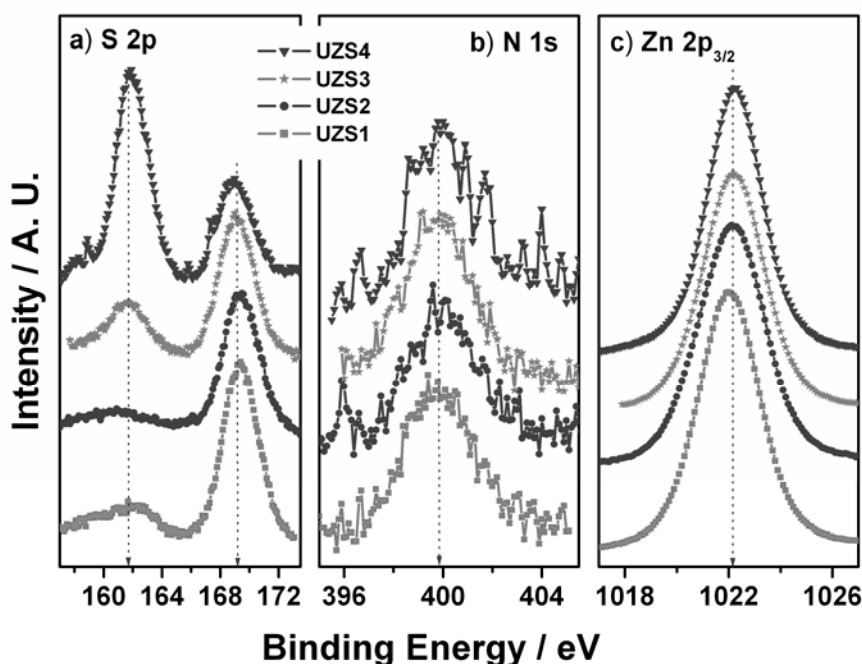
Figure 3.22: *XPS spectra collected from* (a*) S 2p* (b) *N 1s and* (c) *Zn 2p$_{3/2}$ core levels of ZnO$_{1-y-z}$N$_y$S$_z$ materials.*

N 1s core level (Figure 3.22b) appears at around 399.6 ± 0.2 eV for all ZnO$_{1-x-z}$N$_x$S$_z$ materials suggesting the nature of nitrogen on the surface, especially the charge

density, is similar to that of ammonia [29]. Nitrogen peak in XPS is attributed to the dissolution of nitrogen in the ZnO lattice and no nitride phases, such as ZnN species was found. However, the amount of surface nitrogen is very less compared to the bulk nitrogen estimated by EDAX.

The BE values for the Zn 2$p_{3/2}$ core level (Figure 3.22c) were found around 1022.2 eV, which is very close to the literature values reported for ZnO (1022 eV) and ZnS (1021.9 eV) [29, 32]. Except for a minor narrowing of core level features, BE value of the Zn 2$p_{3/2}$ region does not show a significant variation with increasing thiourea concentration, although the nature of bulk materials shows a gradual change in sulfur content from UZS1 to UZS4. Significant amount of sulfate related species on the surface, as shown by SEM results, leads to broadening of Zn 2$p_{3/2}$ core level of UZS1.

3.6.6 **Raman Spectra**

The Raman spectra of the as synthesized ZnO$_{1-x-z}$N$_x$S$_z$ (UZS1, UZS2, UZS3 and UZS4) materials along with ZnO, UZ1, ZnSO$_4$. 7H$_2$O and ZnS were measured at ambient condition and depicted in Figure 3.23. ZnO exhibits a hexagonal Wurtzite structure and belongs to the C$_{6v}$ symmetry group [10]. ZnS shows characteristic phonon modes with high intensity at 428 (2E$_2$) and 711 cm^{-1} (A$_1$/E$_1$(2LO)), and two other features at 492 and 611 (2TO) cm^{-1}. All the above four modes were observed for UZS2 to UZS4 materials. UZS1 shows broad features and it is likely due to sulfate species present in it; however, no new mode for sulfate species was observed. Indeed it is surprising that first order E$_2$ and A$_1$/E$_1$(LO) phonon modes are not observed, rather second order 2E$_2$ and A$_1$/E$_1$(2LO) modes were observed with high intensity for ZnS as well as ZnO$_{1-x-z}$N$_x$S$_z$. A strong and sharp peak observed at 433 cm^{-1} on all ZnO$_{1-x-z}$N$_x$S$_z$ materials, 437 cm^{-1} on ZnO and 429 cm^{-1} on ZnS is due to the typical E$_2$(high) mode and this mode is characteristic of Wurtzite phase. Among the above Raman modes, the E$_2$(high) mode at 437 cm^{-1} has the strongest intensity in ZnO and on all ZnO$_{1-x-z}$N$_x$S$_z$ materials indicating the high quality of the material. Presence of the above mode in ZnO$_{1-x-z}$N$_x$S$_z$ material indicates that they exhibit the same local geometry, however, intensity decreased and peak broadening occurs due to sulfur doping. Nonetheless, it is to be noted that all ZnO$_{1-x-z}$N$_x$S$_z$ materials exhibit the above 2E$_2$ mode at 433 cm^{-1} and exactly in between the E$_2$ modes of ZnO and ZnS

indicating the mixed character of the above compounds and suggesting the solid solution nature of ZnO$_{1-x-z}$N$_x$S$_z$ materials. In addition to the above, broad peaks are observed at 497 cm^{-1} on ZnO$_{1-x-z}$N$_x$S$_z$ materials which don't belong to first or second order structure of neither ZnO nor ZnS; further this mode is not observed for UZS1 suggesting that it is not due to sulfate related species.

In addition to the above, broad peaks are observed at 497 cm^{-1} on ZnO$_{1-x-z}$N$_x$S$_z$ materials which don't belong to first or second order structure of ZnO. A broad peak at 274, 507 and 582 cm^{-1} peak in UZ1 is attributed to A$_1$(LO) related to N doping [11, 29]. This is direct evidence to support the bonding between Zn and N in the ZnO$_{1-x}$N$_x$ system. However, absence of these features excludes the probability of bigger clusters of Zn-N related species. This is likely due to presence of S element in the ZnO$_{1-x-z}$N$_x$S$_z$ materials which does not allow to form Zn-N species, since S has stronger affinity towards Zn than N.
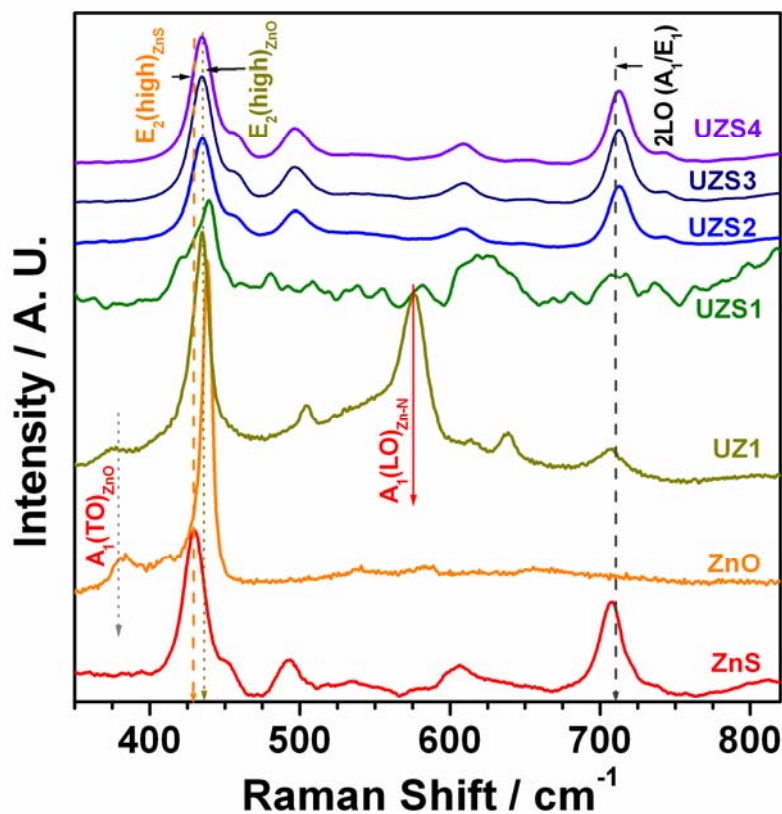

Figure 3.23: *Raman spectra of ZnO$_{1-y-z}$N$_y$S$_z$ materials, compared with UZ1, ZnS, and ZnO.*

Two new peaks are observed at 500 and 707 cm^{-1} for UZS2, UZS3 and UZS4 materials which are not present in UZS1. Above phonon modes are very characteristic

of ZnS and Raman spectrum of pure ZnS reflects that. This demonstrates that indeed ZnO$_{1-x-z}$N$_x$S$_z$ is a solid solution of ZnS in ZnO. Intensity of the above features increases from UZS2 to UZS4 suggesting the ZnS content increases linearly. Although XRD does not show prominent ZnS features for UZS2, Raman results shows the same highlighting the formation of solid solution on UZS2.

3.6.7 **SIMS Analysis**

SIMS was employed to explore the nature of different S and N related species in the prepared ZnO$_{1-x-z}$N$_x$S$_z$ materials especially the homogeneity of doping from surface to bulk, and the results obtained are shown in Figure 3.24. Species that exhibited <10 counts/s were not considered due to high noise level. The initially captured mass spectrum with significant intensity illustrated the presence of different species, namely, Zn, S, ZnO, ZnN, ZnS, N and O. Secondary-ion intensities of the first five species are shown in Figure 3.24, as a function of sputtering time or depth. No significant decrease in counts/intensity of any species with sputtering time emphasizes the bulk sulfur doping in ZnO and the uniformity of the substitution throughout the bulk. However, S related species dominate over N related species indicating the N-content is relatively lower. This is further confirmed from the SIMS results from UZ1, in which N and Zn-N exhibit considerable high intensity. It is
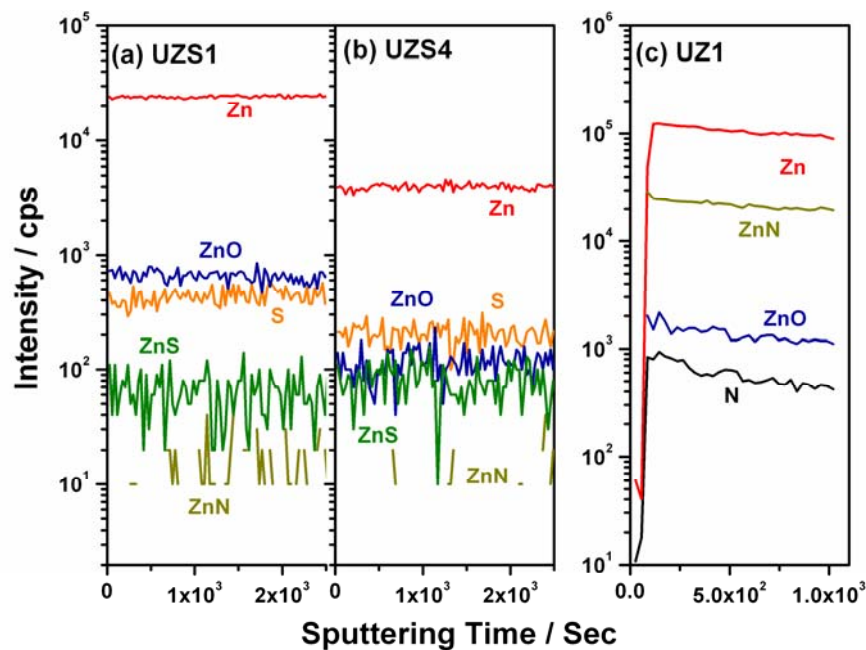

Figure 3.24: *SIMS measurements display secondary ion intensities obtained from* (a) *UZS1* (b) *UZS4 and it is compared with* (c) *UZ1.*

surprising that heavier element like S does compete to N and preferential ZnS formation occurs under SCM. Nonetheless, counts for all the species were significantly different on UZ1, UZS1 and UZS4, indicating the material characteristic are significantly different. Although bulk N-content is in UZS1 is half of that of UZ1, very low ZnN species observed on UZS1 reiterates that the ionization capacity vary for the same species from sample to sample, especially when the nature of materials changes significantly. In spite of this a decreasing ZnO count rate from UZS1 to UZS4 supports solid solution of ZnS in ZnO. An important point to be mentioned here is that no other N and S-related species, such as N$_2$, NO, ZnNO, NH$_x$, SO$_x$ (x =1-4), NS, are observed in the mass spectra, which suggests that the status of S and N in ZnO$_{1-x}$N$_x$ and ZnO$_{1-x-z}$N$_x$S$_z$ material is none of the above. It is also confirmed here that, the nature of S changes increasingly towards sulphide from UZS1 to UZS4.

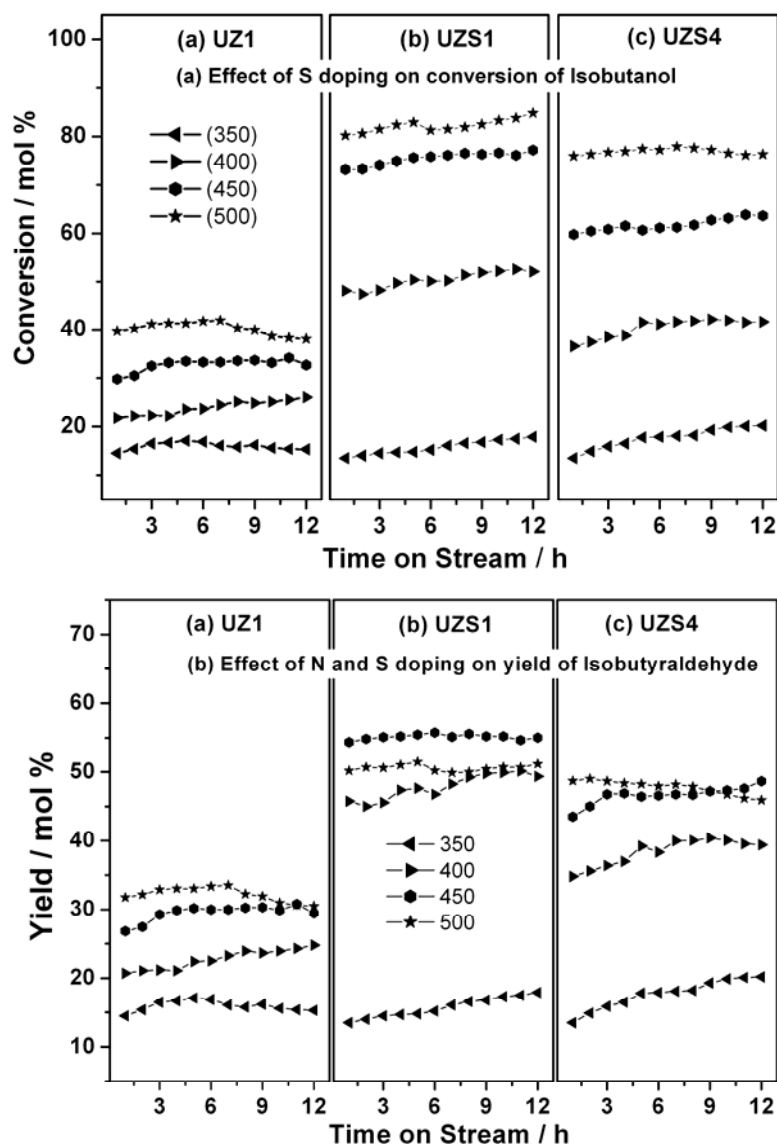## 3.7 Catalytic Activity

3.7.1 Dehydrogenation of Isobutanol

Isobutanol　　　　　**Isobutyraldehyde**
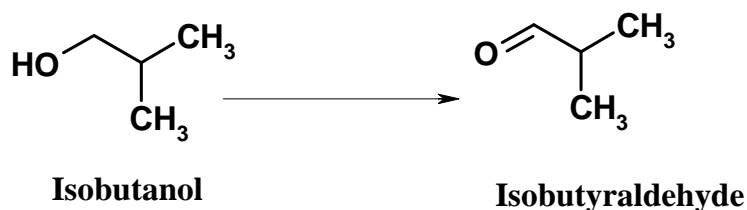
Scheme 3.4: Reaction scheme for isobutanol dehydrogenation reaction.

Isobutanol dehydrogenation reaction was carried out on ZnO$_{1-x-z}$N$_x$S$_z$ materials and it is compared with UZ1 catalyst. Isobutanol conversion examined at 400°C increases with increasing WHSV from 2.4 h^{-1} to 4 h^{-1}, but further more increase (5.6 h^{-1}) in WHSV leads to decrease in conversion which indicates a lower residence time of isobutanol on catalyst surface that leads to lower conversion, and hence, declining the yield of isobutyraldehyde. An optimum of 48% isobutanol conversion with nearly 46% isobutyraldehyde yield was achieved at WHSV = 4.0 h^{-1} on UZS1 catalyst. This above optimized WHSV was followed for all studies.

Temperature dependent catalytic activity measurements obtained up to 12 hrs are shown in Figure 3.24a. It is clear that the isobutanol conversion increases with increase in temperature on all ZnO$_{1-x-z}$N$_x$S$_z$ materials and UZ1 compositions. Further

at 400ºC, isobutanol conversion jumps to about 40-45% on ZnO$_{1-x-z}$N$_x$S$_z$ materials, compared to conversion levels below 20% at 350ºC. Indeed conversion levels are below 20% on UZ1 and it increases to about 40% at 500ºC. Low conversions associated with UZ1 are attributed to low surface area. Isobutanol conversion increases up to 75% on ZnO$_{1-x-z}$N$_x$S$_z$ materials with further increase in temperature to 500ºC. UZS1 shows somewhat higher activity than UZS4 and it is likely due to presence of S as sulfate and associated acidic sites helps to increase the conversion. However, the major contribution to the catalytic conversion originates from ZnS.

Figure 3.24: *Effect of N and S on* (a) *conversion of isobutanol dehydrogenation reaction and* (b) *yield of isobutyraldehyde with variation of temperature on the ZnO$_{1-x-z}$N$_x$S$_z$ and UZ1 materials.*

Isobutyraldehyde selectivity remains high between 90-95% on all the catalyst compositions ≤400ºC; however, it starts decreasing with increasing temperature. There is a significant effect of the temperature on the yield of isobutyraldehyde with a volcano type activity pattern with temperature. With increase in temperature yield also increases up to 450ºC, and above 450ºC yield decreases due to the formation of secondary product. With increase in reaction temperature, more gaseous side products, such as isobutene, are formed. UZS1 material shows the maximum yield of isobutyraldehyde of about 55% at 450ºC. Nonetheless, it is to be noted that the conversion and yield maintains the same value from the beginning till 12 h indicating the catalytic activity remains the same and no poisoning of the surface.

3.8 Conclusions

$ZnO_{1-x-z}N_xS_z$ materials were prepared through SCM using various ratio of urea and thiourea as fuel, and it has been characterized by a variety of physicochemical, structural, spectroscopy, and microscopic measurements. All the major peaks in XRD of prepared materials were successfully indexed to ZnO Wurtzite structure, however, with increase in thiourea content, increase in ZnS content was also observed. Lower thiourea ratio leads to formation of sulfates of ZnO. Porous structure with needle shape particles observed with small amount of thiourea changed to V-shape particles with 100% thiourea as fuel were observed via SEM. Raman, SIMS, and XRD studies demonstrate the direct Zn-N and Zn-S bond. XPS indicates that the charge density of nitrogen on $ZnO_{1-x-z}N_xS_z$ is similar to that of as in $ZnO_{1-x}N_x$. High urea content favors sulfate formation in addition to sulfide, on the surfaces of $ZnO_{1-x-z}N_xS_z$ however, with increasing thiourea content amount of ZnS increases with a subsequent decrease in sulfate and it is supported by XPS studies. Thermogravimetric analysis also demonstrates the presence of ZnS in UZS4 and the solid solution nature of $ZnO_{1-x-z}N_xS_z$ materials. Optical absorption studies demonstrate a significant decrease in band gap to 2.85 eV for UZS4 compared to higher band gap for pure components (ZnO and ZnS). The band-gap diminution of the $ZnO_{1-x-z}N_xS_z$ materials has been attributed to the formation of hybrid orbitals in the VB and CB. It is expected that S $3p$ and O $2p$ are likely to overlap in the VB of UZS1 to UZS4, and the extent of overlap increases from UZS1 to UZS4. Sulfur exists as an anion (S^{2-}) in UZS4 and the top of the VB might be predominantly composed of S $3p$ energy levels as they have higher orbital

energies than O $2p$ levels. Thus in VB S $3p$ and O $2p$ overlaps and broadens it than in ZnO or ZnS. Above studies affirms the solid solution nature of ZnO$_{1-x-z}$N$_x$S$_z$ materials and further it has been compared with a physical mixture to confirm the solid solution identity.

ZnO$_{1-x-z}$N$_x$S$_z$ materials have been evaluated for the catalytic conversion of isobutanol to isobutyraldehyde. Highly selective production of isobutyraldehyde was observed under optimum conditions highlighting the potential to be employed as heterogeneous catalyst.

3.9 **References**

1. (a) C. Klingshirn, *Chem. Phys. Chem.* **8** (2007) 782. (b) (b) U. Özgur, Y. I. Alivov, C. Liu, A. Teke, M. A. Reshchikov, S. Dogan, V. Avrutin, S. J. Cho and H. Morkoc, *J. Appl. Phys.* **98** (2005) 041301. (c) V. A. Nitienko, *J. Appl. Spectrosc*. **52** (1992) 367. (d) J. S. Jang, C.-J Yu, S. H. Choi, S. M. Ji, E. S. Kima, J. S. Lee*, J. Catal.* **254** (2008) 144. (e) M. H. Huang, Y. Wu, H. Feick, N. Tran, E. Weber and P. Yang, *Adv. Mater.* **13** (2001) 113. (f) P. M. Gao, Y. Ding, W. J. Mai, W. L. Hughes, C. S. Lao and Z. L. Wang, *Science* **309** (2005) 5741.

2. S. J. Pearton, D. P. Norton, K. Ip, Y. W. Heo and T. Steiner, *Prog. Mater. Sci.* **50** (2005) 293.

3. (a) V. A. Karpina, V. I. Lazorenko, C. V. Lashkarev, V. D. Dobrowolski, L. I. Kopylova, V. A. Baturin, S. A. Pustovoytov, A. Ju Karpenko, S. A. Eremin, P. M. Lytvyn, V. P. Ovsyannikov and E. A. Mazurenko, *Cryst. Res. Technol.* **39** (2004) 980. (b) Z. Zhang, M. Lu, H. Xu and W.S. Chin, *Chem. Eur. J.* **13** (2007) 632.

4.   I. Volintiru, M. Creatore, W. H. Van Helvoort, J. L. Linden and M. C. M. Van de Sanden, *Appl. Phys. Lett.* **89** (2006) 022110.

5.   (a) C. L. Perkins, S. H. Lee, X. Li, S. E. Asher and T. J. Coutts, *J. Appl.Phys.* **97** (2005) 034907. (b) M. Sanmyo, Y. Tomita and K Kobayashi, *Chem. Mater.* **15** (2003) 819.

6. D. C. Look and B. Claftin, *Phys. Stat. Sol. A* **201** (2004) 2203.

7. M. H. Sarvari and H. Sharghi, *J. Org. Chem.* **71** (2006), 6652.

8. E. H. Kisi and M. Elcombe, *Acta. Crystallogr. Sect. C* **45** (1989) 1865.

9. H. Effenberger, K. Mereiter and J. Zemann, *Z. Kristallogr.* **156** (1981), 233.

10. (a) U. Haboeck, A. Hoffmann, C. Thomsen, A. Zeuner and B. K. Meyer*, Status Solidi B* **242** (2005) R21. (b) L. L. Kerr, X. Li, M. Canepa and A. J. Sommer, *Thin Solid Films* **515** (2007) 5282.

11. J. Yu, H. Xing, Q. Zhao, H. Mao, Y. Shen, J. Wang, Z. Lai and Z. Zhu, *Solid State Commun.* **138** (2006) 502.

12. A. Kaschner, U. Haboeck, M. Strassburg, M. Strassburg, G. Kaczmarczyk, A. Hoffmann, C. Thomsen, A. Zeuner, H. R. Alves, D. M. Hofman and B. K. Meyer, *Appl. Phys. Lett.* **80** (2002) 1909.

13. J. Lu, Q. Zhang, J. Wang, F. Saito and M. Uchida, *Power. Technol*. **162** (2006) 33.

14. http://srdata.nist.gov/xps/

15. D. N. Hendrickson, J. M. Hollander and W. L. Jolly*, Inorg. Chem*. **8** (1969) 2642.

16. C. S. Gopinath, S. G. Hegde, A. V. Ramaswamy and S. Mahapatra, *Mat. Res. Bull*. **37** (2002) 1323.

17. P. Chakraborty, *'Ion Beam Analysis of Surfaces and Interfaces in Condensed Matter Systems'*, Ed.; Nova Science Publishers: New York, 2002.

18. K. Maeda, T. Takata, M. Hara, N. Saito, Y. Inoue, H. Kobayashi and K. Domen, *J. Amer. Chem. Soc.* **127** (2005) 8286.

19. X. Chen and S. S. Mao, *Chem. Re*v. **107** (2007) 2891. (b) M. R. Hoffmann, S. T. Martin, W. Choi and D. W. Bahnemann, *Chem. Rev.* **95** (1995) 69.

20. (a) S. Yin, K. Ihara, Y. Aita, M. Komatsu and T. Sato, *J. Photochem. Photobiol A* **179** (2006) 105. (b) K. Takeshita, A. Yamakata, T. A. Ishibashi, H. Onishi, K. Nishijima and T. Ohno, *J. Photochem. Photobiol. A* **177** (2006) 269. (c) F. H. Tian and C. B. Liu, *J. Phys. Chem. B* **110** (2006) 17866. (d) T. Umebayashi, T. Yamaki, H. Itoh and K. Asai, *Appl. Phys. Lett*. **81** (2002) 454. (e) T. Umebayashi, T. Yamaki, S. Yamamoto, A. Miyashita, S. Tanala, T. Sumita and K. Asai, *J. Appl. Phys.* **93** (2003) 5156. (f) T. Ohno, T. Mitsui and M. Matsumura, *Chem.*

Lett. **32** (2003) 364. (g) T. Ohno, M. Akiyoshi, T. Umebayashi, K. Asai, T. Mitsui and M. Matsumura, *Appl. Catal. A:Gen* **265** (2004) 115.

21. (a) M. Sathish, R. P. Viswanath, C. S. Gopinath, *J. Nanosci. Nanotechnol.* **9** (2009) 423. (b) J. Yu, M. Zhou, B. Cheng and X. Zhao, *J. Mol. Catal. A: Chem.* **246** (2006) 176.

22. E. M. Rockafellow, L. K. Stewart and W. S. Jenks, *Appl. Catal. B: Environ.* **91** (2009) 554.

23. A. Ohtomo, M. Kawasaki, T. Koida, K. Masubuchi, H. Koinuma, Y. Sakurai, Y. Yoshida, T. Yasuda and T. Segawa, *Appl. Phys. Lett.* **72** (1998) 2466.

24. (a) G. Shen, J. H. Cho, J. K. Yoo, G.-C. Yi and C. J. Lee, *J. Phys. Chem. B* **109** (2005) 5491. (b) J. W. Lee, S. Lee, S. Cho, S. Kim, I. Y. Park and Y. D. Choi, *Mater. Chem. Phys.* **77** (2002) 254.

25. (a) Y. Z. Yoo, Z. W. Jin, T. Chikyow, T. Fukumura, M. Kawasaki and H. Koinuma, *Appl. Phys. Lett.* **81** (2002) 3798. (b) B. Y. Geng, G. Z. Wang, Z. Jiang, T. Xie, S. H. Sun, G. W. Meng and L. D. Zhang, *Appl. Phys. Lett.* **82** (2003) 4791. (c) S. Y. Bae, H. W. Seo and J. Park, *J. Phys. Chem. B* **108** (2004) 5206.

26. (a) S. G. Hussain, D. Liu, X. Huang, K. M. Sulieman, J. Liu, H. Liu and R. U. Rasool, *J. Phys. D: Appl. Phys.* **40** (2007) 7662. (b) L. V. Zavyalova, A. K. Savin and G. S. Svechnikov, *Displays* **18** (1997) 73. (c) X. J. Liu, X. Cai, J. F. Mao and C. Y. Jin, *Appl. Surf. Sci.* **183** (2001) 103. (d) I. O. Oladeji and L. Chow, *Thin Solid Films* **339** (2002) 148.

27. (a) C. Kim, S. J. Doh, S. G. Lee, S. J. Lee and H. Y. Kim, *Appl. Catal. A:Gen.* **330** (2007) 127. (b) H. Fujiwara, H. Hosokawa, K. Murakoshi, Y. Wada and S. Yanagida, *Langmuir* **14** (1998) 5154.

28. (a) H. Zhou, T. Fan, Di Zhang, Q. Guo and H. Ogawa, *Chem. Mater.* **19** (2007) 2144. (b) M. Ali and D. D. Sarma, *J. Nanosci. Nanotechnol.* **7** (2007) 1960. (c) C. Yan and D. Xue, *J. Phys. Chem. B* **110** (2006) 25850. (d) G. H. Yue, P. X. Yana, D. Yana, J. Z. Liua, D. M. Qua, Q. Yanga and X. Y. Fana, *J. Crys Growth* **293** (2006) 428. (e) S. G. Hussain, D. Liu, X. Huang, S. l. Ali and M. H. Sayyad, *J.*

Phys. Chem. C **112** (2008) 11162. (f) C. Yan and D. Xue, *J. Phys. Chem. B* **110** (2006) 25850.

29. M. Mapa and C. S. Gopinath, *Chem. Mater.* **21** (2009) 351.

30. L. Bald and R. Guren, *Naturwissenschaften* **68** (1981) 39.

31. (a) K. C. Patil, S. T. Arunab and T. Mimania, *Current Opinion in Solid State and Materials Science* **6** (2002) 507. (b) B. Murugan, D. Srinivas, C. S. Gopinath, V. Ramaswamy and A. V. Ramaswamy, *Chem. Mater.* **17** (2005) 3983.

32. D. Briggs and M.P. Seah .John Willey & Sons. Vol. 1, second edition 1993.

Chapter 4
Characterization and Catalytic Activity of Solid Solution of GaN in ZnO $[(Zn_{1-z}Ga_z)(O_{1-x}N_x)]$

4 Solid Solution of GaN in ZnO, $[(Zn_{1-z}Ga_z)(O_{1-x}N_x)]$.

4.1 Introduction

Band gap engineering of electronic materials is taking the center stage of research since exploration of this aspect is capable of providing new life to the known materials to use with desired and/or refined properties. Especially III–V and II–VI semiconductors with d^{10} electronic configuration are believed to be advantageous as photocatalysts due to the suitability of the CB and the energy overlap of s and p orbitals of metals ions. The large dispersion of hybridized s and p orbitals leads to an increased mobility of photogenerated electrons in the CB and thus high photocatalytic activity. ZnO is such II–VI semiconductor material and used in applications ranging from optoelectronics to gas sensing via catalysis to cosmetics [1]. Doping in the ZnO lattice helps to reach many of the above mentioned applications in a better way. In ZnO VB consists of hybridized orbitals of Zn $3d$ and O $2p$. Addition of other metals containing $3d$ orbital having comparable energy with Zn $3d$ can shift VB_{max} to higher levels. In this case Ga fits very well as the ionic radius of Zn^{2+} (0.74 Å) is comparable to Ga^{3+} (0.61 Å). Only N-doping in ZnO ($ZnO_{1-x}N_x$) was expected to create acceptors close to the valence band (VB) and can introduce (a) p-type conductivity in N-ZnO [2] and (b) deep acceptor levels that cannot induce p-type doping [1,3,4]. Nitrogen doping in ZnO was explored significantly, but not able to be reproduced by other research groups even when the experimental conditions are the same [3]. N-ZnO films have been prepared by many sophisticated methods for optoelectronics applications, and there is no breakthrough yet. A maximum of 6 % N-doping in ZnO has been reported till date, and it is due to the poor solubility of N in ZnO [1-3]. However, large amount of nitrogen could be introduced in ZnO lattice by SCM [4], and N $2p$ states occupy mid-gap states without any change in band gap. Nevertheless, oxygen vacancy in ZnO, considered as a problem, was effectively utilized by SCM to introduce large amount of nitrogen in ZnO.

However, both donor-acceptor co-doping can facilitate the introduction of large amount of heteroatoms in better way. n-type doping causes a decrease in the Madelung energy by forming a shallow donor level while p-type doping gives rise

to an increase in the Madelung energy forming a deep acceptor level in the electronic band structure. Considering a remarkable decrease in the Madelung energy, introduction of group III elements like Al, Ga, or In, metal ion in Zn site are considered best substitution species to fabricate stable *p*-type ZnO [5]. *n*-type doping in ZnO causes the stabilization of the ionic charge distribution in the material, especially, at O sites. As the cohesive force of Ga-N bond is larger than that of ZnO, so higher affinity exists between Al or Ga and N species than between Zn and N species. Further, formation of Zn-O is energetically favourable than Zn-N bonds. Thus, both Ga and Al are suitable for use in co-doping with N acceptor. Hence, presence of Ga will enhance the incorporation of N in the ZnO lattice. Based on the analysis of a change in the lattice energy and electronic structures by the co-doping, we find that two pairs, (N and Ga) and (N, Al) are more effective. Among the group III elements Ga is a preferable element as the Ga-N bond distance (1.95 Å) in GaN being similar to the Zn-O bond distance (1.97 Å), and it reduces the elastic contribution to the energy of formation of the N-acceptor atom at O sites, thus stabilizing the system [5]. It might minimize the deformation of the ZnO lattice even with high GaN content, since both exhibit Wurtzite structure. Yamamoto [5] reported that the formation of clusters consisting of acceptor–donor-acceptor that occupy nearest neighbor sites or second-nearest ones is energetically favorable due to the strong attractive interaction between the N acceptor and Ga donors which are used as co-dopants at high doping levels. Hence, Ga and N co-doping not only helps to increase the solubility of nitrogen in the medium [5], but also decrease the Madelung energy of the system. Formation of -N-Ga-N-Ga-N- clusters that occupy near-neighbor sites is favorable due to the strong attractive interaction between them, and it helps to increase the solubility of N in ZnO. Moreover, when Ga and N are codoped in ZnO system VB and CB position changes as well.

N and Ga co-doped ZnO has been synthesized by SCM and characterizes by various physicochemical methods. This material exhibits an electronic structure that is significantly different from ZnO and/or GaN. Being a good catalyst and/or support material, ZnO deserves to be explored for catalysis applications, especially when the electronic structure is significantly modified as in the above solid solution. Ammonia spans its utility in variety of field like fertilizer industry, chemical and explosive industry and as a rocket fuel. Apart from industrial application it is also the best

model reaction for conceptual development of thermodynamics. Even though Fe based catalyst has been commercialised for nearly a century, but it suffers serious limitation of decline activity due to severe reaction condition [6]. Bimetallic nitrides are known to be good catalyst for ammonia production. Presence of GaN and Ga-N-Zn species in $(Zn_{1-z}Ga_z)(O_{1-x}N_x)$ leads us to explore for N_2 fixation through NH_3 formation at ambient pressure.

4.2 Results and Discussion

In this chapter, $ZnO_{1-x}N_x$ and $(Zn_{1-z}Ga_z)(O_{1-x}N_x)$ materials are denoted as UZx and UZxGy, respectively, with x and y being the molar ratio of urea/(Zn+Ga) and Ga atom %, respectively, unless specified.

4.2.1 X-ray Diffraction (XRD)

Figure 4.1 shows the x-ray diffraction (XRD) patterns of the $(Zn_{1-z}Ga_z)(O_{1-x}N_x)$ materials. A single hexagonal Wurtzite phase (space group $P6_3mc$) similar to the GaN and ZnO was obtained for all prepared samples [1]. All of the peaks could be indexed to ZnO lattice. The highly crystalline nature of prepared materials is evident from the sharp and high intensity diffraction peaks. With increasing Ga concentration FWHM of the peaks are increasing and it depicts a reduction in average crystallite size. Neither $ZnGa_2O_4$ nor Ga_2O_3 peaks were observed in XRD patterns up to 12% Ga doping, which implies that Ga atoms replace zinc in the hexagonal lattice. In 15% Ga doping, clear Ga_2O_3 peak was observed at 30.4º. A small amount of zinc carbonate was observed at 38.9º on nitrogen incorporated ZnO (UZ7) along with ZnO features. It is due to effective combustion of urea that produces CO_2 [4]. However, no carbonate formation was observed in XRD as well as in photoemission results on $(Zn_{1-z}Ga_z)(O_{1-x}N_x)$ materials, indicating the suppression of carbonate formation in the presence of Ga.

The positions of the (100) and (101) diffraction peaks were successively shifted to higher angles (2θ) with increasing Ga doping, indicating that the obtained samples were not physical mixtures of GaN and ZnO phases but rather solid solutions of GaN and ZnO. This peak shift is reasonable, as the ionic radius of Zn^{2+} (0.74 Å) is larger than that of Ga^{3+} (0.61 Å) [7]. In contrast, the position of the (002) diffraction
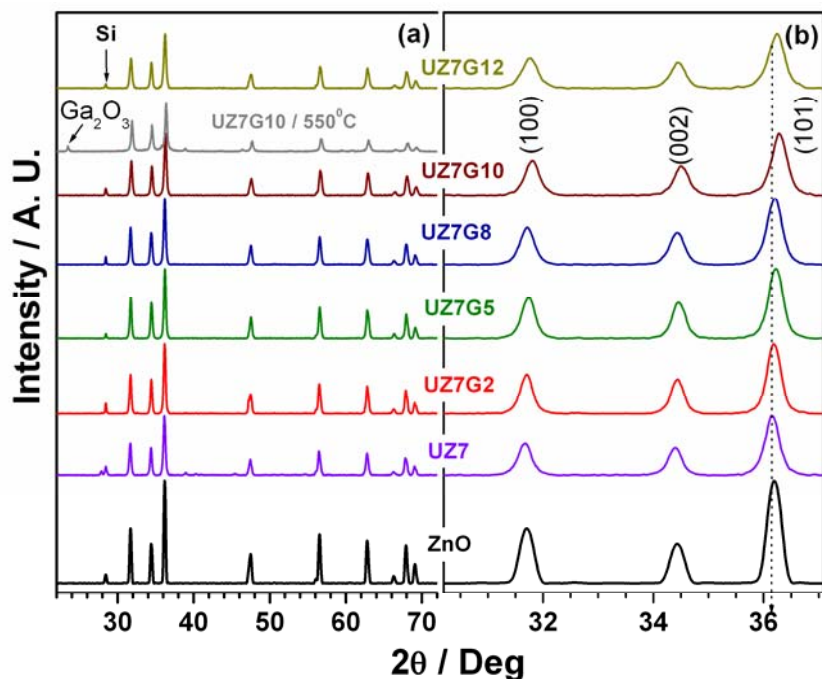
Figure 4.1: (a) *PXRD patterns of (Zn$_{1-z}$Ga$_z$)(O$_{1-x}$N$_x$), prepared with urea/(Zn+Ga) = 7, UZ7, and ZnO.* (b) *Main diffraction lines are shown in an expanded way for better clarity.*
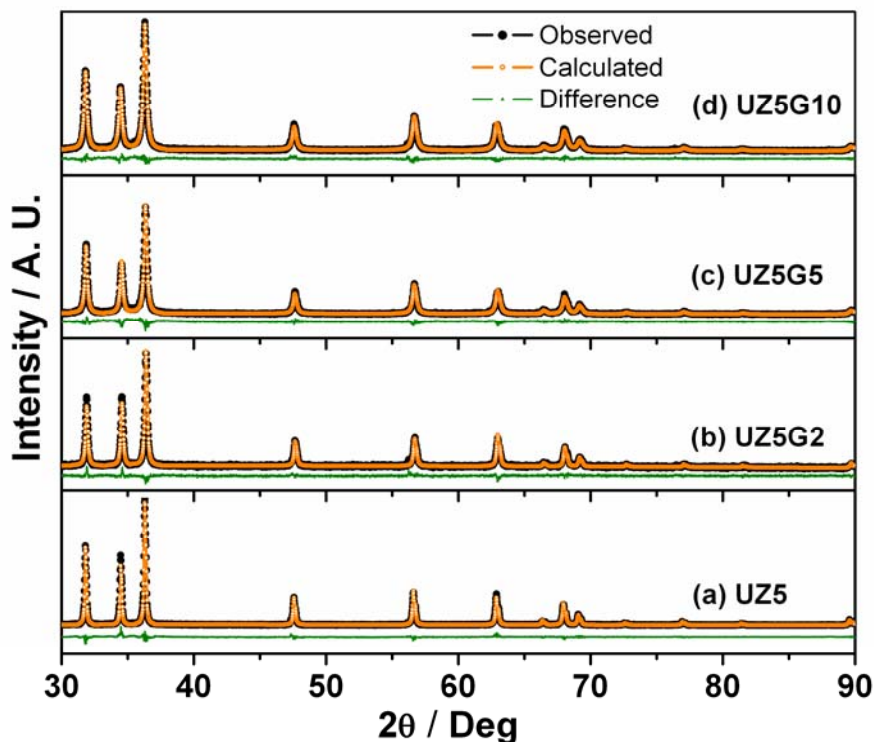
Figure 4.2: *Rietveld refinement profiles of* (a) *UZ5,* (b) *UZ5G2,* (c) *UZ5G5, and* (d) *UZ5G10 (Zn$_{1-z}$Ga$_z$)(O$_{1-x}$N$_x$) materials. Experimental data points and calculated intensity are given as orange and black colored lines. The difference plot is given at the bottom in green color.*

Table 4.1 *Physico-chemical parameters of (Zn$_{1-z}$Ga$_z$)(O$_{1-x}$N$_x$) materials.*

Material code and composition [a]	Surface area (m^2/g)	a (Å)	c (Å)
UZ5G2 - Zn$_{0.98}$Ga$_{0.02}$O$_{0.91}$N$_{0.09}$	5	3.2504 (4)	5.2052 (2)
UZ5G5 - Zn$_{0.95}$Ga$_{0.05}$O$_{0.9}$N$_{0.1}$	9	3.2405 (7)	5.1907 (2)
UZ5G8 - Zn$_{0.92}$Ga$_{0.08}$O$_{0.88}$N$_{0.115}$	12	3.2354 (5)	5.1873 (2)
UZ5G10 - Zn$_{0.9}$Ga$_{0.1}$O$_{0.84}$N$_{0.15}$	17	3.2318(8)	5.1833 (3)
UZ5G12 - Zn$_{0.88}$Ga$_{0.12}$O$_{0.85}$N$_{0.15}$	18	3.2315 (6)	5.1846 (2)
UZ5G15 - Zn$_{0.85}$Ga$_{0.15}$O$_{0.93}$N$_{0.08}$	20	3.2239 (4)	5.1731 (3)
UZ5 - ZnO$_{0.914}$N$_{0.086}$	7	3.2421 (5)	5.1924 (2)
ZnO	60	3.250	5.205
GaN	---	3.188	5.183

[a] *Urea/(Zn+Ga) = 5 and Ga atom % is given after G in sample code. Material composition was determined from XRF, EDAX and chemical analysis.*

peak did not undergo a shift, attributable to the smaller difference in c-axis lengths between GaN and ZnO compared to the difference in a-axis lengths. The same tendency was confirmed by Rietveld analysis, using the computer program X-pert plus. Rietveld refinement analysis of ZnO$_{1-x}$N$_x$ [4] and (Zn$_{1-z}$Ga$_z$)(O$_{1-x}$N$_x$) materials is given in Figure 4.2. An excellent agreement between the experimental and the fitted data indicated that the XRD pattern could be indexed satisfactorily to the hexagonal Wurtzite structure with a space group of P6$_3$mc. Composition of UZ5-series materials with lattice parameters and surface area is given in Table 4.1. A linear decrease in a and c lattice parameters with increasing Ga% was observed. A systematic incorporation of Ga^{3+} ions in the Zn^{2+} site, the lattice parameters are expected to decrease, due to the smaller ionic radius of the former compared to the latter. Indeed, a decrease in the lattice parameter from a = 3.2504 Å (c =5.2052Å) to 3.2239Å (5.1924Å) was observed from 2% Ga to 15% Ga, respectively [7(a),8]. This confirms that at least most of Ga^{3+} ions are incorporated in the zinc oxide lattice forming homogeneous (Zn$_{1-z}$Ga$_z$)(O$_{1-x}$N$_x$) solid solutions. The a- and c-axis lengths of (Zn$_{1-z}$Ga$_z$)(O$_{1-x}$N$_x$) decreased almost linearly with increasing Ga concentration (x), although the c-axis length deviated slightly from this linear relationship due to the

smaller difference in *c*-axis lengths between GaN and ZnO. However, a uniform distribution of small clusters of GaN in ZnO is unexpected, especially under the vigorous reaction conditions employed in the present work. Theoretical calculations reported by Schaefer *et al.* [9] predicts small clusters of a size between 30 and 40 oligomers of GaN under similar conditions are in good agreement with our experimental results.

Simultaneous incorporation of appropriate concentration of N and Ga introduces offsetting local lattice expansion and contraction, subsequently minimizing the lattice strain. To a large extent, charge compensation was also taken care by the above co-doping. Further, this too allows the N-acceptor to exist in a stable anionic state [5].

4.2.2 **Thermogravimetric Analysis**

Figure 4.3a depicts thermogravimetric analysis of (Zn$_{1-z}$Ga$_z$)(O$_{1-x}$N$_x$) powders in air and nitrogen atmosphere. The initial weight loss up to 1% was observed below 200ºC is attributed to water loss. Weight loss continues up to another 1-2%, depending on the material composition, until 550ºC is due to some carbon removal
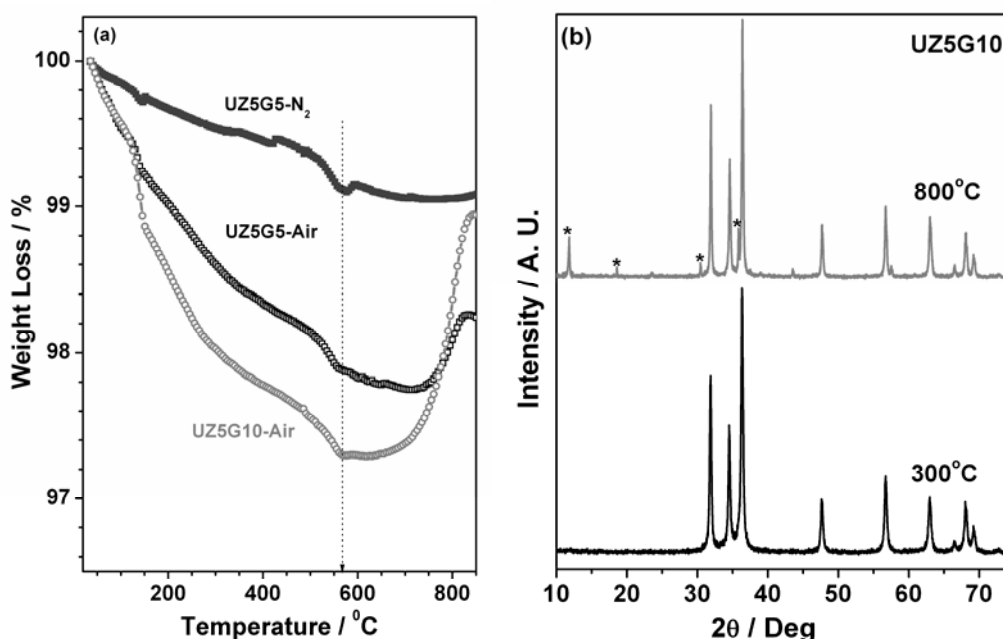
Figure 4.3: (a) *Thermogravimetric analysis of (Zn$_{1-z}$Ga$_z$)(O$_{1-x}$N$_x$) in air and N$_2$ atmosphere and* (b) *XRD patterns of UZ5G10 calcined at 300, 800^{0}C for 6 hrs in air. Formation of Ga$_2$O$_3$ is evident up on calcination from the additional peaks appear and marked with* *.

and oxygen loss. No significant weight loss was observed in nitrogen atmosphere, compared to the same material (UZ5G5) in air, supports the above conclusion. Nevertheless, a weight gain occurs above 600ºC in air atmosphere for all Ga-containing materials. The above weight gain is attributed to simultaneous N-loss and Ga_2O_3 formation. TGA in nitrogen atmosphere shows lower weight loss, and no weight gain above 700ºC confirms that the weight gain in air atmosphere is due to Ga_2O_3 formation. Further with increase in Ga % weight gain above 600ºC is increasing, indicates more amount of GaN oxidizing to Ga_2O_3.

This is further confirmed from the XRD pattern of 300ºC and 800ºC calcined UZ5G10 (Figure 4.3b). 800ºC calcined sample shows new peaks at 11.6º, 23.4º, 30.4º and 35.9º. In comparison to XRD pattern of Ga_2O_3, above new peaks can be attributed to Ga_2O_3. However, there are no peaks observed for Ga_2O_3 in 300ºC calcined sample. This clearly indicates the N-atoms in the lattice were replaced progressively by O-atom above 600ºC to Ga_2O_3 and ZnO, which is displaying in the XRD pattern of calcined sample as well.

4.2.3 UV-Visible Spectroscopy

Figure 4.4 shows UV-visible absorption spectra of $(Zn_{1-z}Ga_z)(O_{1-x}N_x)$ materials along with standard ZnO and GaN for comparison purposes. ZnO and GaN show absorption onset at 375 and 365 nm, respectively. A broad visible absorption band at 480 nm with low intensity was observed on UZ5 [4] apart from the typical absorption cut off for ZnO at 375 nm. This suggests the creation of N $2p$ derived midgap states in the forbidden gap of ZnO. As explained in chapter 3, no change in the conductivity of UZ5, compared to ZnO, underscores the generation of deep level acceptors [4].

Interestingly, co-doping of Ga and N displays an absorption onset around 550 nm and extend into UV regime gradually. Band maximum of the new band in the visible region shows a red shift from 410 to 450 nm for 2% to 12% Ga, respectively. A new band observed in the visible region shows intensity comparable to that of the band in the UV regime, suggesting the large density of states in the new band at high Ga content. Above co-doping helps to form shallow acceptor and donor levels, and decreases the band gap up to ~2.5 eV, depending on the

composition of $(Zn_{1-z}Ga_z)(O_{1-x}N_x)$. Physical mixture of ZnO and GaN does not show any absorption in the visible region underscores the true solid solution natue of $(Zn_{1-z}Ga_z)(O_{1-x}N_x)$ [5,8].
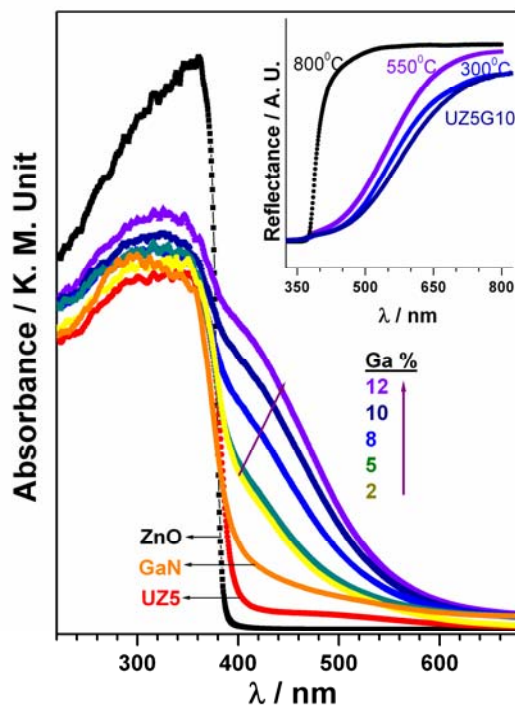
Figure 4.4: *UV-Visible absorption spectra of $(Zn_{1-z}Ga_z)(O_{1-x}N_x)$ materials prepared with urea/(Zn+Ga) = 5, GaN and ZnO. Inset shows the UV-Visible reflection spectra obtained from calcined UZ5G10 materials.*

Density functional theory (DFT) calculation revealed that the bottom of the CB for ZnO is mainly composed of unoccupied levels, consists of Zn -4s and -4p orbital while the top of the VB consists of O 2p orbital. However, doping of N 2p generates a hole at the top of the VB and mainly creates mid gap state. For the II-VI semiconductors, Wei and Zunger pointed out that the p-d repulsion repels the VB$_{max}$ upward without affecting the CB$_{min}$ [10]. Furthermore, in $(Zn_{1-z}Ga_z)(O_{1-x}N_x)$ materials the bottom of the CB composed of the Zn-Ga hybridized orbital and the presence of Ga 3d band in addition to the Zn 3d band in the upper VB further provides the p-d repulsion for the VB$_{max}$, reducing the band gap. It is likely that a strong mixing of 4s and 4p states of Zn and Ga near CB and 2p orbital of O and N in the VB is responsible for the narrow band gap. A good overlap between N 2p (from nitride) and O 2p derived states at the VB and 4s and 4p states from Ga and Zn at the CB is attributed to the above decrease in band gap.

Calcination of $(Zn_{1-z}Ga_z)(O_{1-x}N_x)$ (UZ5G10) in air at <550ºC shows only minor changes in optical absorption characteristics (inset in Figure 4.4). However, calcinations at >550ºC lead to a fast decrease in visible light absorption and a blue shift was observed. Absorption spectra recorded after calcination at 800ºC leads to a pattern resembling that of ZnO. This is in good correspondence to weight gain at >600ºC in TGA. Indeed, XRD pattern recorded for 800ºC calcined material indicates a mixture of Ga_2O_3 and ZnO and hence shows complete oxidation of the above material (Figure 4.3b). Nitrogen is replaced by oxygen at high temperatures treatment in air. Above observations confirms the visible light absorption is mostly due to N^{3-}.

4.2.4 **X- Ray Photoelectron Spectroscopy**

XPS of $(Zn_{1-z}Ga_z)(O_{1-x}N_x)$ was recorded and shown in Figure 4.5 for N 1s, Ga 2$p_{3/2,}$ Zn 2$p_{3/2}$ and O 1s core levels. N 1s peak appears at a BE 399.4 eV on UZ3 indicating the charge density on N is similar to that of ammonia or ammine [4, 11]. However, $(Zn_{1-z}Ga_z)(O_{1-x}N_x)$ shows N 1s peak at 397 eV due to N^{3-}, along with the above peak (Figure 4.5a). A decrease in BE of 3 eV, compared to $ZnO_{1-x}N_x$, indicating the presence of nitride (N^{3-}) type nitrogen. However, there is another shoulder appears at lower BE side around 394 eV is attributed to the Auger transition from Ga. Indeed, XPS analysis of GaN shows N 1s peak at 397 eV [11], and confirms the presence of N^{3-}. Amount of nitrogen also increases in Ga doped materials compared to $ZnO_{1-x}N_x$. It is also to be mentioned here that interstitial zinc and oxygen vacancies are present in the $(Zn_{1-z}Ga_z)(O_{1-x}N_x)$ material, and it is mainly to compensate for the excess anionic charge from the significantly large nitrogen content and to maintain the charge neutrality of the entire lattice. Further, nitrogen at higher binding energy (> 401 eV) was also not observed which confirms no features due to nitric oxide (NO)-type species, which suggests the absence of direct N-O linkages.

XPS for Ga 2$p_{3/2}$ core level appears at BE 1117.6 eV, indicating the Ga^{3+} state as in GaN (Figure 4.5b). It is clear that the charge density of N in $ZnO_{1-x}N_x$ is as that of NH_3, but Ga and N co-doping helps to form N^{3-} through GaN. Due to the above, optical absorption onset of $(Zn_{1-z}Ga_z)(O_{1-x}N_x)$ is shifted to higher λ. It is likely that a strong mixing of 4s/ 4p states of Zn and Ga near CB and 2p states of O and N in the VB is responsible for narrow band gap [10, 12]. XPS for Zn 2$p_{3/2}$ core level demonstrates the BE at 1021.7 eV for $ZnO_{1-x}N_x$, indicating the oxidation state of Zn
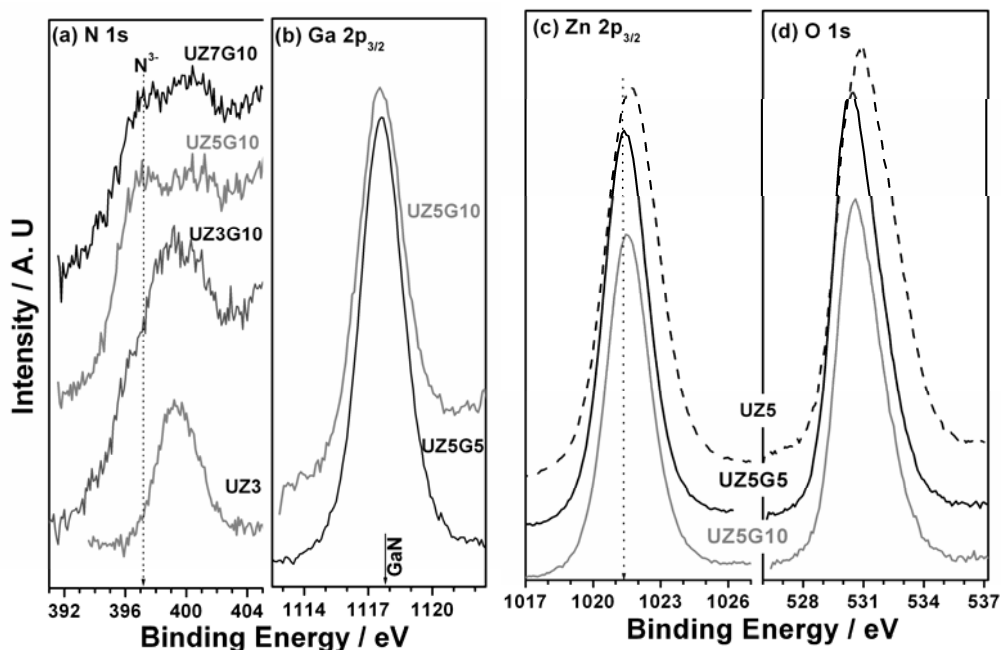
Figure 4.5: *XPS spectra from* (a) *N 1s,* (b) *Ga 2p$_{3/2}$* (c) *Zn 2p$_{3/2}$ and,* (d) *O 1s core levels of $(Zn_{1-z}Ga_z)(O_{1-x}N_x)$ materials.*

to be 2+ as in ZnO (Figure 4.5c). However, upon Ga-doping the BE of Zn $2p_{3/2}$ shifts to lower BE of 1021.7 eV indicating an overall increase in electron density on Zn and it is attributed to the presence of nitride in the lattice and it intensifying with Zn. The surface Zn concentration also decreases with Ga content as Ga is replacing Zn atom.

O 1*s* core level peak is broad for UZ5 at 531 eV compared to $(Zn_{1-z}Ga_z)(O_{1-x}N_x)$ at 530.4 eV indicating that at least two kinds of oxygen species were present on UZ5 (Figure 4.5d). Deconvolution demonstrates (not shown) a peak at 530.5 eV is due to the ZnO crystal lattice oxygen, while the peak at about 532 eV is due to carbonate oxygen. However, there is no carbonate observed in Ga-containing materials. UZ5G5 and UZ5G10 show a narrow O 1*s* peak around 530.5 eV corresponds to that of ZnO. The above details from XPS suggest that the nature of Zn and O is relatively electron rich compared to its UZ5 counterpart; however, lower width also suggests a uniform distribution of GaN in ZnO.

4.2.5 **Raman Spectroscopy**

Figure 4.6 presents Raman spectra of as synthesized $(Zn_{1-z}Ga_z)(O_{1-x}N_x)$ materials and it is compared with standard ZnO and $ZnO_{1-x}N_x$ material. A strong and sharp peak observed at 437 cm^{-1} on all synthesized and standard ZnO is

attributed to E$_2$(high) Raman active phonon mode of ZnO, [12] and its intensity decreases very significantly on (Zn$_{1-z}$Ga$_z$)(O$_{1-x}$N$_x$). However, Raman active phonon modes of GaN [13] is also observed in (Zn$_{1-z}$Ga$_z$)(O$_{1-x}$N$_x$) materials at 560, 579, and 730-740 cm^{-1} corresponding to E$_1$(TO), E$_2$(high), A$_1$(LO) and E$_1$(LO) mode, respectively. However, in Ga doped samples as Ga and N content increases, four impurity modes appear at 510, 582, 642 and 734 cm^{-1}. A broad peak at 582 cm^{-1} is attributed to A$_1$(LO) and E$_1$(LO) mode of ZnO$_{1-x}$N$_x$ [4]. It is to be noted that this peak is low in intensity for pure ZnO and high intensity is observed on ZnO$_{1-x}$N$_x$. Some of the above modes overlap around 575 cm^{-1} and a broad feature observed for z≤5% in (Zn$_{1-z}$Ga$_z$)(O$_{1-x}$N$_x$) is due to heterogeneous near-neighbour environments. However, it becomes sharper at high z (>5 %) values hinting a more homogeneous environment and supporting the solid solution nature of the materials. A new peak at 730 cm^{-1} observed which is assigned as A$_1$(LO) mode of GaN compound and the peak at 570 cm^{-1} contains contributions from both the E$_1$(TO) mode and the high frequency E$_2$ mode of both Zn-N and Ga-N bond. E$_2$(high) and A$_1$(TO) clearly weaken with the increase in Ga content [12,14].
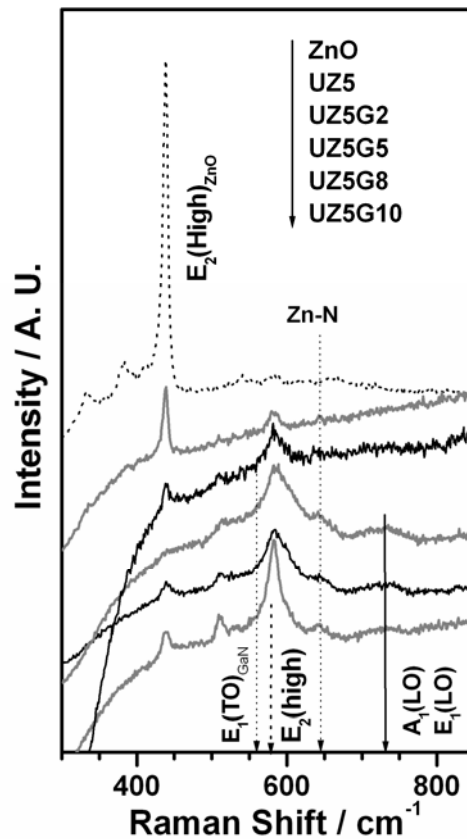

Figure 4.6: *Raman spectra of ZnO, UZ5 and (Zn$_{1-z}$Ga$_z$)(O$_{1-x}$N$_x$) materials.*

Two peaks at 510 and 642 cm^{-1} are due to Zn-N related modes [13] and the high frequency E_2 mode of both Zn-N and Ga-N bond. This is direct evidence to support the direct bonding between Ga and N in the $(Zn_{1-z}Ga_z)(O_{1-x}N_x)$ system. A sharp decrease in the intensity of E_2(high)(ZnO) at the expense of Zn-N and Ga-N related Raman active features suggests an increase in co-valent character of the material and very widely and uniformly distributed GaN crystal in the medium.

4.2.6 **Secondary Ion Mass Spectrometry Analysis**

Figure 4.7 shows the SIMS data of UZ5, UZ5G5 and UZ5G10. Secondary ion intensities of different species as a function of sputtering time reflect the presence of the corresponding constituents as a function of depth. Same trend was observed in case of UZ5G5 and UZ5G10 materials. Presence of N (from N and ZnN) was observed on all the materials, apart from the expected species, such as Zn, ZnO, Ga, and GaN of the corresponding constituents as a function of depth. Additionally, the direct observation of GaN from UZ5G5 and UZ5G10 underscores the solid solution of GaN in ZnO. Zn-N-Ga species suggests a direct interaction between N^{3-} to Zn also.
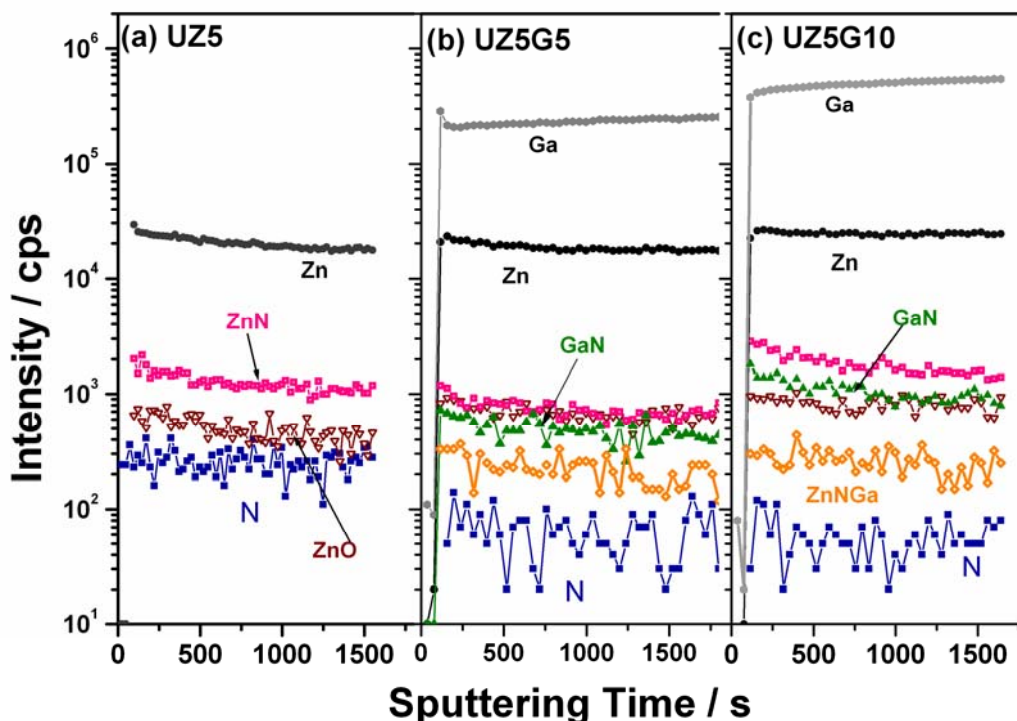
Figure 4.7: *Secondary ion intensities of various species as a function of sputtering time are given for* (a) *UZ5,* (b) *UZ5G5 and* (c) *UZ5G10.*

However, counts of N species are lower in the UZ5G5 and UZ5G10 than UZ5, is likely due to formation of GaN. Further, counts for GaN and ZnN species are higher in case of UZ5G10 compared to UZ5G5, which directly suggests that with increase in Ga concentration in corresponding material, nitrogen incorporation also increases. Crucially, signal intensities remain constant at deeper levels highlights the solid solution nature and uniform distribution for all the materials. This conclusion corroborates well with Raman spectra and XPS results. No observation of Ga$_2$O$_3$ and nitric oxide (NO) species suggests the efficacy of combustion method to introduce N^{3-} in the ZnO lattice in overall reductive atmosphere. No feature due to N-O type species is observed also in electron paramagnetic resonance studies, which suggests the absence of direct N-O linkages. It is to be noted that the intensity of ZnO and Zn is relatively lower compared to that of ZnN, Ga or GaN, despite the fact that the volume content of ZnO (parent) is much higher than the doped species. This is attributed to the fact that the ionization efficiency of certain emitted species is dependent on local surface chemistry of the sample, known as "matrix effect" in SIMS [15].

4.3 Catalytic Activity Studies

4.3.1 Ammonia synthesis

Ammonia synthesis from its elemental constituents is one of the crucial reactions. In view of drastic changes in electronic structure of (Zn$_{1-z}$Ga$_z$)(O$_{1-x}$N$_x$), such as decrease in optical band gap to 2.5 eV, direct Zn-N and Ga-N bonds, Zn-N-Ga species, solid solution nature etc ammonia synthesis reaction was explored significantly.

Representative results are given in Table 4.2. ZnO$_{1-x}$N$_x$ materials (UZ5 and UZ7), does not show any significant activity towards NH$_3$ formation. UZ5G10 shows almost same activity (0.44 mmol/h g) for the first three hours and then decreases rapidly. The maximum NH$_3$ formation activity of 1.51 mmol/h g was observed on UZ7G10 for the first hour, and then it decreases with increasing time on stream.

Catalytic activity of UZ7G10 is comparable to that of Co$_3$Mo$_3$N [16]; however, the activity is an order of magnitude less than that of commercial or Cs-promoted Co$_3$Mo$_3$N catalysts (15 to 30 mmol/h g). It is to be noted that the above

Table 4.2 *Ammonia synthesis activity on (Zn$_{1-z}$Ga$_z$)(O$_{1-x}$N$_x$) in mmol/hr.*

Time on Stream (h)	UZ5G10	UZ7G10
1	0.44	1.51
2	0.48	0.74
3	0.42	0.24

activity reported with commercial or Cs-promoted bimetallic catalysts was measured at 400ºC, 100 bar, and with electronic promoters [17]. It is also to be mentioned that the present reaction was at ambient pressure, at 350ºC, without any promoter, and the nitride content is far less than that of bimetallic nitrides [17]. This underscores the potential nature of (Zn$_{1-z}$Ga$_z$)(O$_{1-x}$N$_x$) towards NH$_3$ synthesis. Amount of nitrogen present in 1gm of UZ7G10 is 0.026gm. However, the amount of ammonia produced in the first three hrs is 2.5 mmol and this corresponds to 0.0425 gm nitrogen. This large amount of nitrogen involved in produced NH$_3$ indicates that indeed the reaction is catalytic and nitrogen source is from reactant and not from lattice N.

Addition of promoters may facilitate the dissociation of N$_2$ molecule as well as enhance desorption of NH$_3$ which is of has fundamental importance. Using this concept potassium was used as electronic promoter to increase the turn over number of the reaction. Potassium (5 wt % and 10 wt %) impregnated (Zn$_{1-z}$Ga$_z$)(O$_{1-x}$N$_x$) catalyst was prepared through wet impregnation method using potassium nitrate as potassium precursor. It is known that addition of 0.5% potassium oxide in Fe-alumina increase ammonia production [18]. This leads to conclusion that K can act as very good electronic promoter. A three to four fold increase in ammonia production was observed and reaction got extended upto 5th hr with 5 wt % potassium loaded UZ7G10 attesting the effectiveness of addition of K as promoter. It is likely that, the presence of potassium enhances the desorption of adsorbed ammonia from the surface, making more sites available to chemisorbed dinitrogen to dissociate by donating electron from the surface. Therefore, increase in the rate of ammonia synthesis was observed. However, more increase in K (10 wt %) loading leads to more increase in ammonia formation in the 1st hour, though activity decreases drastically in the next 3 hours.

4.3.2 **Deactivation Mechanism**

To know the reason of deactivation, structural and optical studies of the spent catalyst has been carried out and compared with the corresponding fresh catalyst. XRD pattern and UV spectra of spent catalyst were compared with fresh catalyst and results are depicted in Figure 4.8.

Compared to fresh catalyst, spent catalyst shows that there is no significant change in structural integrity. However intensity of K$_2$O peak decreases significantly on spent catalyst and it inferred that less amount of K was present in the bulk of spent catalyst. So, it can be concluded that K ion helps to keep catalyst active for longer time; however, during reaction, K ions are diffusing towards the surface and getting segregated on the surface. It is well known that addition of K as electronic promoter helps to increase ammonia formation, but with more K in the catalyst leads to faster formation of K$_2$O on surface and this leads to faster deactivation with 10 wt % K loaded catalyst.

From optical absorption spectra, it is clear that there is not much change in visible light absorption on spent catalyst compared to fresh catalyst. It has been already demonstrated that that nitride nitrogen is responsible for visible light absorption in (Zn$_{1-z}$Ga$_z$)(O$_{1-x}$N$_x$) materials. So retention of visible light absorption underscores that there is no loss of nitride nitrogen from the catalyst due to the reaction. Hence, for ammonia formation elemental N$_2$ was utilized and it is not from the lattice nitride nitrogen.

XPS of spent catalyst was recorded and the results have been compared with fresh catalyst. Core level binding energy of Ga 2$p_{3/2}$, O 1s, K 2p and N 1s are shown in Figure 4.9. Binding energy of K 2p shows a peak at 293.0 eV both in fresh and spent catalyst indicating oxidation state of K is +2. From the result, it is clear that there is no change in nature of K in both fresh and spent catalyst. However, compared to fresh catalyst, spent catalyst shows huge amount of K on the surface, which also reflects as an additional peak in O 1s core level. Binding energy of O 1s in the fresh catalyst shows a peak at 530.5 eV, which is only for ZnO. However, on the spent catalyst a new hump as well as peak broadening was also observed at 532.0 eV, which is due to K$_2$O. XRD pattern of the spent catalyst also shows less amount of K$_2$O,
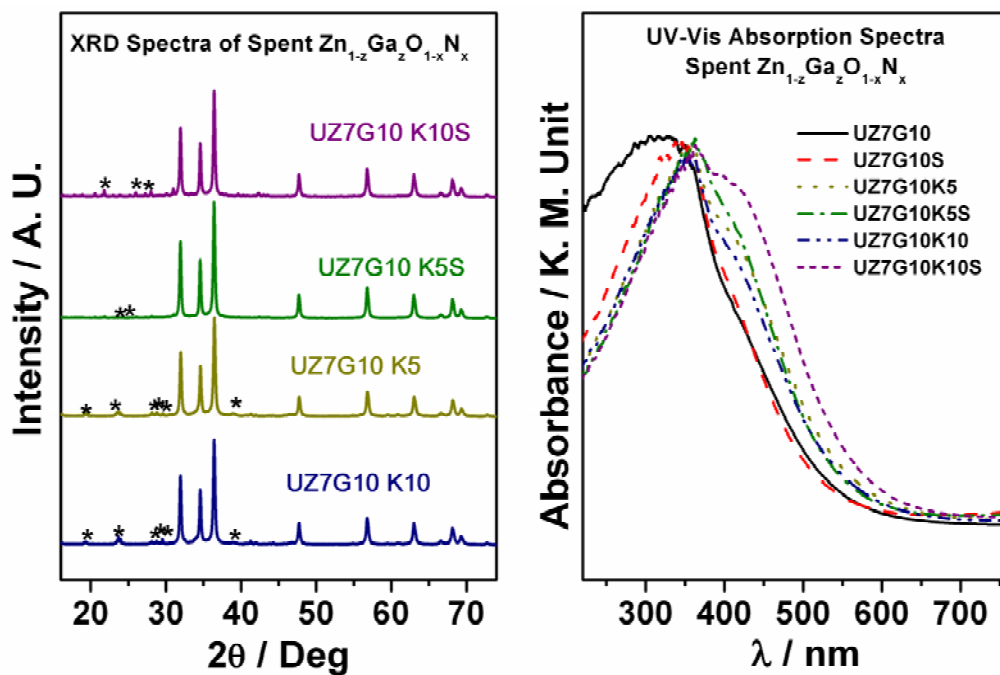
Figure 4.8: (a) *PXRD pattern and (*b*) UV-Visible spectra of fresh and spent K incorporated (Zn$_{1-z}$Ga$_z$)(O$_{1-x}$N$_x$), prepared with urea/(Zn+Ga) = 7. * indicates contribution due to K$_2$O.*
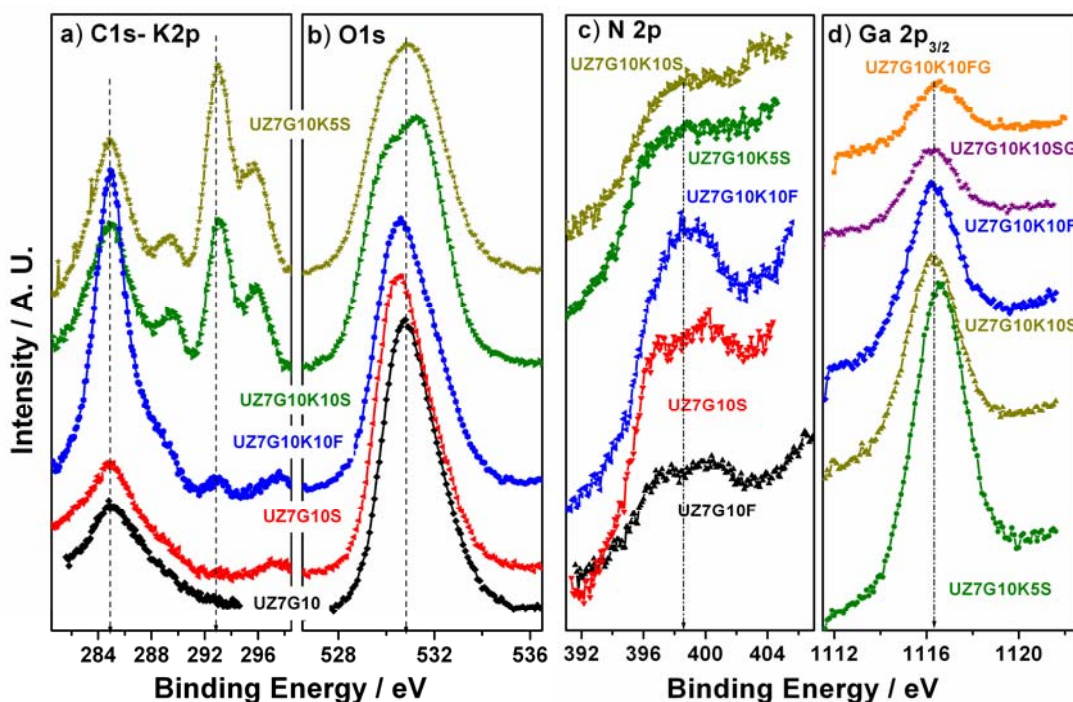
Figure 4.9: *XPS spectra from* (a) *C 1s-K 2p* (b) *O 1s* (c) *N 1s and* (d) *Ga 2p$_{3/2}$ core levels of fresh and spent UZ7G10 and K incorporated UZ7G10.*

which is due to leaching of K ion towards the surface from the bulk. Thus, the XPS results well support and reflect the result of XRD analysis of spent catalysts.

There is no significant change in the nature and amount of surface nitrogen in the fresh and used catalyst. Spent catalysts show two types of nitrogen as that of fresh catalyst. One type of nitrogen is like nitride nitrogen which shows a peak at 397.0 eV and other one is ammonia type nitrogen. These observations indicate that there is no change in nitrogen oxidation state in the catalyst during reaction. However, less amount of Ga was observed on the surface compared to fresh catalyst. This is due to surface segregation of K_2O, which masks other species.

4.4 Conclusions

Solid solution of GaN in ZnO {$(Zn_{1-z}Ga_z)(O_{1-x}N_x)$ (x and z = 0-0.15)} has been prepared by SCM. XRD studies confirm the presence of hexagonal Wurtzite phase, and no extra peak was found due to nitrogen incorporation or Ga doping. The electronic spectra show visible light absorption and an optical band gap decreased to 2.5 eV compared to 3.4 eV with ZnO and GaN. Raman spectroscopy and SIMS results suggest the presence of Zn-N and Ga-N bonds. Two types of nitrogen were found in XPS, charge density of one of the nitrogen in $(Zn_{1-z}Ga_z)(O_{1-x}N_x)$ is similar to that of ammonia/ammines, and another one is like nitride. Calcination of $(Zn_{1-z}Ga_z)(O_{1-x}N_x)$ in air <550ºC leads to minor changes in optical absorption characteristics. However, calcination >550ºC leads to fast decrease in visible absorption band, and 800ºC calcined material shows an optical absorption similar to that of ZnO. Above observations indicate the visible light absorption is mostly due to nitride. XRD pattern of 800ºC calcined samples shows a mixture of Ga_2O_3 and ZnO and confirms the oxidation of GaN. Above results suggest the N 2p states from nitride occupy the states just above the O 2p VB and reduces the band gap. The presence of GaN in $(Zn_{1-z}Ga_z)(O_{1-x}N_x)$ and supported by physicochemical analysis underscores the importance of reaction atmosphere generated in the present experimental conditions.

Catalytic activity towards N_2 fixation was observed at atmospheric pressure at 350ºC on $(Zn_{1-z}Ga_z)(O_{1-x}N_x)$ indicates its potentiality as a catalyst. Further, addition of potassium as electronic promoter helps to increase NH_3 production and keeps catalyst active for longer time. However, leaching of K ion from bulk to surface and formation of huge K_2O on the surface are possibilities for deactivation. Hence, it is worthwhile to look similar type nitride base materials for NH_3 production in ambient condition.

4.5 **References**

1. (a) C. Klingshrin, *Chem. Phys. Chem.* **8** (2007) 782. (b) U. Özgur, Y. I. Alivov, C. Liu, A. Teke, M. A. Reshchikov, S. Dogan, V. Avrutin, S. J. Cho and H. Morkoc, *J. Appl. Phys.* **98** (2005) 041301. (c) V. A. Karpina, V. I. Lazorenko, C. V. Lashkarev, V. D. Dobrowolski, L. I. Kopylova, V. A. Baturin, S. A. Pustovoytov, A. Ju. Karpenko, S. A. Eremin, P. M. Lytvyn, V. P. Ovsyannikov and E. A. Mazurenko, *Cryst. Res. Technol.* **39** (2004) 980. (d) D. C. Look and B. Claflin, *Phys. Stat. Sol. B* **241** (2004) 624. (e) S. Velu, K. Suzuki and C. S. Gopinath, *J. Phys. Chem.* B **106** (2002) 12737.

2. (a) K. Minegishi, Y. Koiwai and K. Kikuchi, *Jpn. J. Appl. Phys.* **36** (1997) L1453. (b) M. Joseph, H. Tabata and T. Kawai, *Jpn. J. Appl. Phys.* **38** (1999) L1205. (c) D. C. Look, D. C. Reynolds, C. W. Litton, R. L. Jones, D. B. Eason and G. Cantwell, *Appl. Phys. Lett.* **81** (2002) 1830. (d) G. Xiong, J. Wilkinson, B. Mischuck, S. Tuzemen, K. B. Ucer and R. T. Williams, *Appl. Phys. Lett.* **80** (2002) 1195. (e) C. L. Perkins, S. H. Lee, X. Li, S. E. Asher and T. J. Coutts, *J. Appl. Phys.* **97** (2005) 034907.

3. (a) K. Iwata, P. Fons, A. Yamada, K. Matsubara and S. Niki, *J. Cryst. Growth* **209** (2000) 526. (b) X.-L. Guo, H. Tabata and T. Kawai, *J. Cryst. Growth* **237** (2002) 544. (c) S. Yamauchi, Y. Goto, T. Hariu, *J. Cryst. Growth* **260** (2004) 1.

4. M. Mapa and C. S. Gopinath, *Chem. Mater.* **21** (2009) 351.

5. (a) T. Yamamoto and H. Katayama-Yoshida, *Jpn. J. Appl. Phys.* **38** (1999) L166. (b) T. Yamamoto and H. K. Yoshida, *Physica B* **302-303** (2001) 155. (c) T. Yamamoto, *Thin Solid Films* **420-421** (2002) 100. (d) A. V. Singh, R. M. Mehra, A. Wakahara and A. Yoshida, *J. Appl. Phys.* **93** (2003) 396. (e) T. Ohshima, T. Ikegami, K. Edihara, J. Asmussen and R. Thareja, *Thin Solid Films* **435** (2003) 49.

6. J. Sehested, C. J. H. Jacobsen, E. Tornqvist, S. Rokni and P. Stoltzey, *J. Catal.* **188** (1999) 83.

7. (a) R. D Shannon, *Acta Crystallogr. Sect. A* **32** (1976) 751. (b) M. Yashima, K. Maeda, K. Teramura, T. Takata and K. Domen, *Chem. Phys. Lett.* **416** (2005) 225.

8. (a) K. Maeda, K. Teramura, D. Lu, T. Takata, N. Saito, Y. Inoue and K. Domen, *Nature* **440** (2006) 295. (b) K. Maeda, K. Teramura, T. Takata, M. Hara, N. Saito, K. Toda, Y. Inoue, H. Kobayashi and K. Domen, *J. Phys. Chem. B.* **109** (2005) 20504.

9. A. Y. Timoshkin, H. Schaefer and H. F. III, *J. Phys. Chem. A* **112** (2008) 13180.

10. (a) S. H. Wei and A. Zunger, *Phys. Rev. B* **37** (1988) 8958.

11. (a) http://srdata.nist.gov/xps/ (b) N 1s spectra were recorded with Mg Kα, to ensure that no contribution from Ga-L2M45M45 Auger level (~392 eV with Al Kα) to N 1s region.

12. K. Ikarashi, J. Sato, H. Kobayashi, N. Saito, H. Nishiyama and Y. Inoue, *J. Phys. Chem. B.* **106** (2002) 9048.

13. (a) D. Wang, H. W. Seo, C. C. Tin, M. J. Bozack, J. R. Williams, M. Park, N. Santhitsuksanoh, A. Cheng and Y. H. Tzeng, *J. Appl. Phy.* **99** (2006) 113509. (b) U. Haboeck, A. Hoffmann, C. Thomsen, A. Zeuner and B. K. Meyer, *Phys. Stat. Sol. B* **242** (2005) R21. (c) A. Cingolani, M. Ferrara, M. Lugara and G. Scamarcio, *Solid State Commun.* **58** (1968) 823.

14. (a) N. Hasuike, H. Fukumura, H. Harima, K. Kisoda, H. Matsui, H. Saeki and H. Tabata, *J. Phys. Cond. Matt.* **16** (2004) S5807. (b) H–L. Liu, C–C. Chen, C–T. Chia, C–C. Yeh, C–H. Chen, M–Y. Yu, S. Keller and S. P. DenBaars, *Chem. Phys. Lett.* **345** (2001) 245.

15. P. Chakraborty, *"Ion beam analysis of surfaces and interfaces in condensed matter systems"*, Ed. P. Chakraborty, Nova Science Publishers, New York (2002).

16. (a) C. J. H. Jacobsen, *Chem. Commun.* (2000) 1057. (b) C. J. H. Jacobsen, S. Dahl, B. S. Clausen, S. Bahn, A. Logardottir and J. K. Norsov, *J. Amer. Chem. Soc.* **123** (2001) 8404.

17. C. J. H. Jacobsen, M. Brorson, J. Sehested, H. Teunissen and E. Tornqvist, U. S. Patent, (1999) 6, 235.

18. S. Dahl, A. Logardottir, C. J. H. Jacobsen and J. K. Norsov, *App. Cat. A:Gen.* **222** (2001) 19.

Chapter 5
Characterization and Catalytic Activity
of Solid Solution of InN in ZnO
$[(Zn_{1-z}In_z)(O_{1-x}N_x)]$

5 Solid Solution of InN in ZnO [$(Zn_{1-z}In_z)(O_{1-x}N_x)$]

5.1 Introduction

Co-doping method is widely explored in case of ZnO in order to achieve better potential offered by it. The importance of ZnO in gas sensing to UV light emitters and ceramics is well-known [1]. Furthermore, suitable choice of metal ion is required to achieve desired activity in both physical and chemical applications point of view. N has been considered as the best candidate for doping in ZnO, however the *p*-type behavior obtained in N doped ZnO ($ZnO_{1-x}N_x$) is not reproducible, and controversies still exist [2]. Further, N-monodoping creates a deep acceptor level, which is unfavorable to induce *p*-type conductivity. 15 atom % of N incorporated ZnO lattice can be prepared by SCM [3], however, without *p*-type conductivity, since N 2*p* states are found to be in the forbidden-gap. Further, the charge density of N on $ZnO_{1-x}N_x$ is not as in any typical nitride, but resembles to that of ammonia/ammines. However, co-doping method was followed to change the status of N into N^{3-} and to enhance the N^{3-} content as well. Nonetheless, there is limited success with thin-film materials prepared by various methods, especially in increasing N solubility [4]. Our recent studies on co-doping of Ga and N in ZnO lead to a solid solution of nanoclusters of GaN in ZnO with a significant decrease in the optical band gap up to 2.5 eV, from 3.37 eV for ZnO [5]. In addition, the above method also stabilizes good amount of N as N^{3-}. However, unlike Ga-N co-doping, very few reports are available on co-doping of In and N in ZnO. Similar method was adapted here to dope In and N in ZnO lattice simultaneously. Chen *et al.* [6a, b] recently reported on the synthesis of *p*-type ZnO films by means of In and N co-doping and Raman spectroscopy measurements were made by Kong *et al.* [6c]. Hole density was observed ranging around 10^{18} cm^{-3}.

Although In (0.84 Å) is slightly bigger than Zn (0.72 Å), Zn could be substituted for In due to the structural similarity, and InN possesses the hexagonal Wurtzite crystal structure (*a* = 3.537 Å, *c* = 5.704 Å) as that of ZnO (*a* = 3.250 Å, *c* = 5.205 Å), but with a band gap of 0.7 eV [7]. Further, there is void space available in the Wurtzite (B4) (and zincblende (B3)) structure makes it feasible to accommodate bigger ions. In view of this, if In could be doped successfully, then the chances of

forming a solid solution of InN in ZnO is easy. At present, the III–V nitride compounds such as AlN, GaN, and InN and N-doping in oxides, particularly TiO_2 have received considerable interest because of their potential applications in microelectronic and optoelectronic devices, and they are chemically and mechanically stable [8]. Furthermore, the co-doping technique is an effective approach in producing *p*-type ZnO, regardless of Al–N, Ga–N, or In–N pairs [4, 5].

In this chapter, we are going to discuss the effect in ZnO if we dope, up to 14 atom % N and up to 8 atom % In into ZnO as InN through SCM. These prepared materials have been characterized by various physicochemical, spectroscopic and structural methods, and alcohol dehydrogenation reaction was explored via heterogeneous catalysis. In the present case, the resulting solid solution of InN in ZnO, ($Zn_{1-z}In_z$)($O_{1-x}N_x$), exhibits an electronic structure that is markedly different from ZnO and/or InN. Indeed ($Zn_{1-z}In_z$)($O_{1-x}N_x$) materials exhibit an optical band gap of about 2.3 eV due to the N 2*p* states from N^{3-} occupying the states above O 2*p* VB.

5.2 *Results and Discussion*

Throughout the chapter $ZnO_{1-x}N_x$ and ($Zn_{1-z}In_z$)($O_{1-x}N_x$) materials are denoted as UZx and UZxIny, respectively, with x and y being the ratio of urea/(Zn+In) and In atom %, respectively, unless specified.

5.2.1 **X-ray Diffraction:**

Figure 5.1 shows the characteristic XRD patterns of various materials ($Zn_{1-z}In_z$)($O_{1-x}N_x$) synthesized in the present investigation and compared with $ZnO_{1-x}N_x$, ZnO, InN and In_2O_3. Figure 5.1a shows the XRD patterns obtained with different ratios of urea/(Zn+In) (3, 5 and 7) for 5% In concentration. The XRD pattern of pure ZnO and InN shows a hexagonal Wurtzite structure. A sharp and well refined ZnO pattern is observed for UZ5In5. However, there is significant peak broadening observed for both UZ3In5 and UZ7In5 with In_2O_3 features which were clearly observed at 2θ = 30.76º (JCPDS data card No. 71-2194). In_2O_3 features was also observed for materials prepared with In % higher than 5 with urea/(Zn+In) ratio other than 5. In view of this, observation of most of results has been presented from UZ5Iny, unless specified.
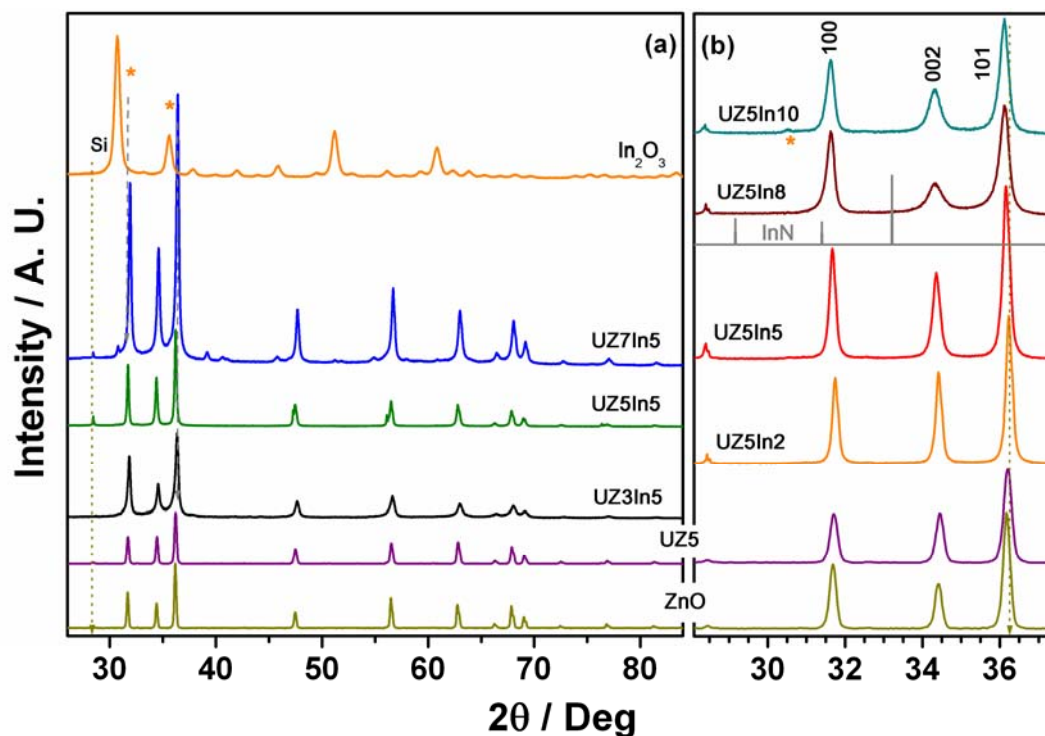
Figure 5.1: *Powder X-ray diffraction pattern of* (a) *(Zn$_{0.95}$In$_{0.05}$)(O$_{1-x}$N$_x$), prepared with urea/(Zn+In) = 3, 5 and 7, and* (b) *(Zn$_{1-z}$In$_z$)(O$_{1-x}$N$_x$) prepared with urea/(Zn+In) = 5 with In-content between 0 and 10 atom percent. UZ5, In$_2$O$_3$, InN and ZnO are also plotted for comparison. Si has been used as an internal standard. * indicates contribution due to In$_2$O$_3$.*

Table 5.1 *Physico-chemical characteristics of (Zn$_{1-z}$In$_z$)(O$_{1-x}$N$_x$) materials*

Material code [a]	Surface area (m^2/gm)	a (Å)	c (Å)
UZ5In2 - Zn$_{0.98}$In$_{0.02}$O$_{0.90}$N$_{0.10}$	7	3.25258(2)	5.2080(2)
UZ5In5 - Zn$_{0.95}$In$_{0.05}$O$_{0.86}$N$_{0.14}$	10	3.25515(6)	5.2103(8)
UZ5In8 - Zn$_{0.92}$In$_{0.08}$O$_{0.85}$N$_{0.15}$	18	3.26203(5)	5.2132(2)
UZ5In10 - Zn$_{0.9}$In$_{0.1}$O$_{0.87}$N$_{0.13}$	22	3.26555(8)	5.2150(5)
UZ5 - ZnO$_{0.914}$N$_{0.086}$	7	3.2421(5)	5.1924(2)
UZ7 - ZnO$_{0.93}$N$_{0.071}$	19	3.2414(7)	5.1934(4)
ZnO	50	3.250	5.205
InN	---	3.533	5.693

[**a**] *The urea:metal molar ratio is given after "UZ", followed by In atom %.* [**b**] *Bulk and surface atomic content, measured from EDAX and XPS, respectively.*

Figure 5.1b shows the XRD patterns obtained from UZ5Iny (y≤ 10) and compared with standard reference materials. Well resolved high intensity reflections have been observed up to In = 8% without any impurity phases; especially no peak corresponding to impurities such as In$_2$O$_3$ and ZnIn$_2$O$_4$ was observed even up to 8 atom % In containing materials. It is worth noting that the as-prepared In containing materials are highly crystalline (Figure. 5.1b), attesting the effectiveness of the SCM to induce in situ crystallization during the material formation.

However, with increasing In content, the full width at half maximum (FWHM) value of all the peak increases, implying decreasing crystallite size due to incorporation of In and N atoms. The lattice parameter 'a' (c) value increases from 3.250 Å (5.205 Å) for pure ZnO to 3.26203 Å (5.2132 Å) for 8 atom In % (Zn$_{1-z}$In$_z$)(O$_{1-x}$N$_x$) (Table 5.1). This suggests that In^{3+} replaces Zn^{2+} in the ZnO lattice with a concomitant increase in the lattice parameters due to larger size of In^{3+}. It is also to be noted that percent increase in unit cell parameter 'a' is significantly higher than that of 'c' (Table 5.1) with increasing In-content. This also indicates that the materials prepared are not physical mixtures of InN and ZnO, rather a solid solution of InN and ZnO. XRD pattern of InN given close to UZ5In8 demonstrates that the broadening observed at higher In-content (≥ 8%) is due to InN. It is likely that nano InN clusters might be dispersed homogeneously in the ZnO lattice system attributing that there is no peak specific to InN was observed, rather a shift to lower angle is observed.

Attempts to synthesize materials with higher In loadings lead to a mixed phase of (Zn$_{1-z}$In$_z$)(O$_{1-x}$N$_x$) and In$_2$O$_3$. Reflection corresponds to In$_2$O$_3$ was observed when In % ≥10. Further urea to metal ratio of 7 and 3 employed also leads to In$_2$O$_3$ phase, especially with In % >5. A new peak appears at 2θ = 30.76º, which indicates the formation of In$_2$O$_3$. Urea being a good fuel, complete combustion takes place and the average combustion temperature increases with urea content [9]. This underscores the necessity of optimum temperature for effective preparation of (Zn$_{1-z}$In$_z$)(O$_{1-x}$N$_x$) which is achieved around a ratio of urea/(Zn+In) = 5. The Rietveld refinement profiles of materials prepared by SCM using urea/(Zn+In) = 5 with different In loadings are presented in Figure 5.2. An excellent agreement between the experimental and the fitted data indicated that the XRD pattern could be indexed reasonably well to the Wurtzite structure with a space group P6$_{3mc}$.
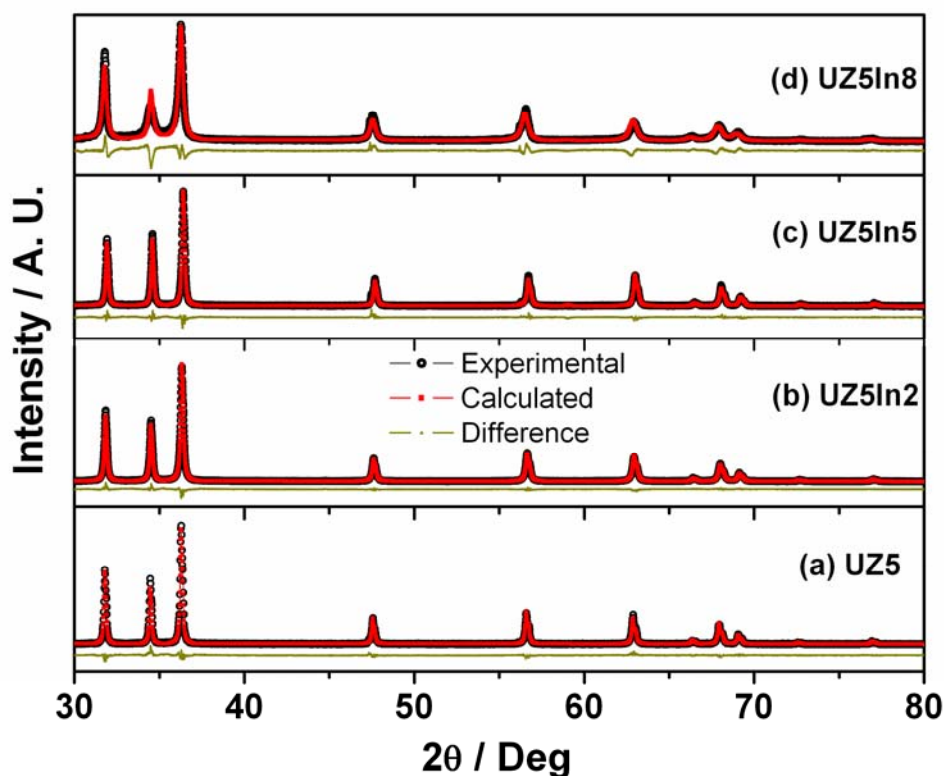
Figure 5.2: *Rietveld refinement profiles of (a) UZ5, (b) UZ5In2, (c) UZ5In5, and (d) UZ5In8 materials. Experimental data points are given in open circle and calculated intensity is given in red color line. The difference plot is given in dark yellow color at the bottom.*

The positions of major (100, 002 and 101) diffraction peaks were successively shifted to lower angles (2θ) with increasing In content, indicating that the $(Zn_{1-z}In_z)(O_{1-x}N_x)$ materials were indeed, solid solutions of InN in ZnO (Figure 5.1b). Peak shift is considerable, as the ionic radius of In^{3+} (0.84 Å) is higher than that of Zn^{2+} (0.72 Å) [10]. However, the covalent bond length of In-N (2.4 Å) is larger than that of Zn-O (1.97 Å), and In substituted at Zn sites would increase the lattice parameter as well as volume, thus justifying the peak shift to the lower angle. It is clear from the above observations that N and In atoms occupied the O and Zn lattice positions, respectively.

It is known that InN begins to decompose with loss of nitrogen between 425 and 550ºC [11]. To explore the stability of the $(Zn_{1-z}In_z)(O_{1-x}N_x)$ materials prepared, calcination at different temperatures and thermal analysis experiments were performed. As already indicated, the materials prepared by SCM get exposed to high temperatures during synthesis and hence, a better thermal stability is expected.
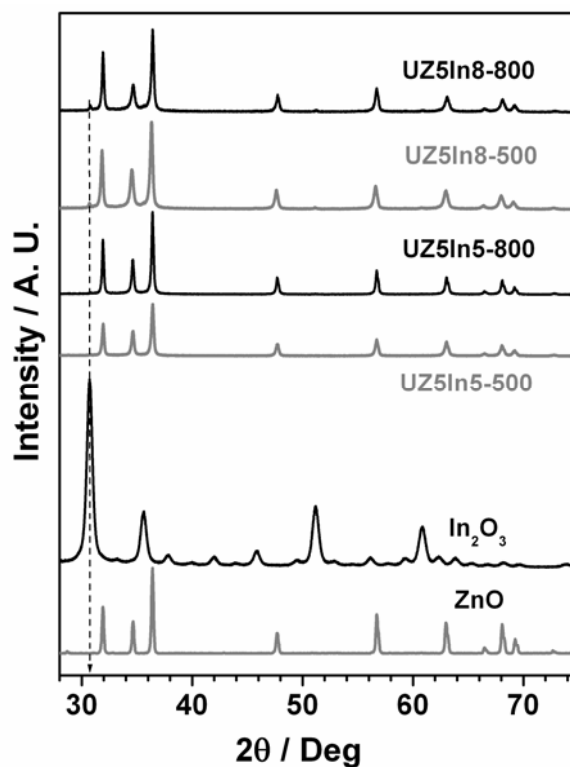
Figure 5.3: *Powder X-ray diffraction pattern of calcined $(Zn_{1-z}In_z)(O_{1-x}N_x)$, prepared with urea/(Zn+In) = 5, In_2O_3 and ZnO.*

Indeed the XRD pattern measured for UZ5In5 after calcination at 800ºC does not show any impurity peak (Figure 5.3); however, UZ5In8 exhibits an additional peak at 30.76º and a clear peak broadening at 36.5º was observed as well. Above new features are attributed due to the formation of In_2O_3. Due to calcination in static air InN gets oxidized to In_2O_3 which does not belong to Wurtzite phase and reflects in the XRD patterns. However, with In-content ≤5% no formation of In_2O_3 was observed, indicating that the smaller InN clusters are might be stable and resistant to oxidation at least up to 500ºC.

5.2.2 **Thermogravimetric Analysis**

It is necessary to understand the oxidation mechanism of InN in $(Zn_{1-z}In_z)(O_{1-x}N_x)$ materials at high temperatures in air and N_2 atmosphere, mainly to understand the thermal stability at high temperatures. The oxidation process of pure InN films is rather complicated since the oxygen incorporation and the nitrogen desorption occur simultaneously [12]. During this process, InN oxidizes to cubic bixbyite In_2O_3 phase. Thermal analysis of UZ3In5, UZ5In5 and UZ7In5 (Figure 5.4) was carried out in air

atmosphere up to 1000ºC. A sharp change in weight loss (about 4 wt %) was observed between 500 and 560ºC on UZ3In5 with corresponding exothermic change in DTA (Figure 5.4). In addition to the above weight loss, another feature was observed between 370 and 440ºC with UZ7In5 with corresponding exothermic change in DTA. Weight loss observed with exothermic peaks between 370 and 560ºC, suggests decomposition and it is attributed to the decomposition of carbonate species.
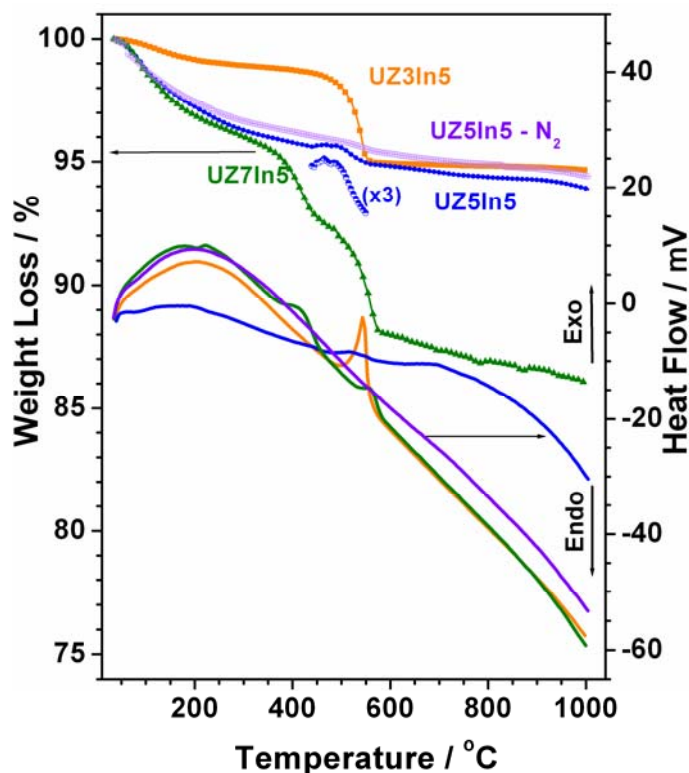
Figure 5.4: *Thermogravimetric and differential thermal analysis of UZ3In5, UZ5In5 and UZ7In5 carried out in air atmosphere. UZ5In5 analysis carried out in nitrogen atmosphere is also given. Weight gain observed on UZ5In5 around 500ºC (feature multiplied 3 times for clarity) in air atmosphere supports the oxidation of InN to In$_2$O$_3$.*

Interestingly, no such weight loss due to carbonate was observed on UZ5In5, rather a mild weight gain was observed around 500ºC. This is attributed to the oxidation of InN to In$_2$O$_3$. To validate this conclusion, similar experiment has been carried out in nitrogen atmosphere. TG-DTA result from UZ5In5 in N$_2$ atmosphere does not show any weight gain around 500ºC confirms the above conclusion. Further, no weight gain feature was observed on UZ3In5 and UZ7In5 is mainly due to overlapping of carbonate burning weight loss feature and oxidation weight gain feature. Considerable weight loss was observed at < 400ºC due to loss of physisorbed

H$_2$O, NH$_3$ or nitrate decomposition on all samples. Nonetheless, after calcination to high temperatures around 800°C, none of the (Zn$_{1-z}$In$_z$)(O$_{1-x}$N$_x$) materials shows any nitrogen and it is affirmed from the XPS results. With increase in In content weight loss also increases, which proves that there is more amount of nitrogen introduction with higher In %. No In$_2$O$_3$ feature observed in XRD on UZ5In5 after heating at 800°C might be due to smaller cluster sizes.

5.2.3 **Textural Properties**

The morphology of the as prepared samples was examined by SEM. Figure 5.5 shows representative SEM images of UZ5In2 and UZ5In5 material. As-prepared materials exhibit a good distribution of fine primary particles with an average size of about 200-300 nm. However, some bigger particles are also observed. No particular particle shape has been observed, unlike the predominant triangle shape of UZ1 [3], however, with UZ5 there is no particle morphology and random distribution was observed (Section 3.2.3).

To find out the distribution of particle sizes, dynamic light scattering (DLS) measurements have been carried out with the above materials dispersed in isopropanol solvent (Figure 5.6). It has been assumed that all of the particles are spherical in shape. Majority (90%) of particles from UZ5In5 exist in a size range between 230 and 330 nm, and the remaining (10%) shows higher diameter between 1050 and 1250 nm. Both SEM and DLS experimental results are in good agreement with each other, and confirms the nano size regime of (Zn$_{1-z}$In$_z$)(O$_{1-x}$N$_x$) materials, although the preparation method adopted was SCM, which involves high temperature between 700 and 1000°C.

EDAX analysis carried out to measure the material composition as well as to find out the extent of doping homogeneity. Representative results are given in Figure 5.7 for UZ5In5 (a and b), and UZ5In10 (c and d). Elemental mapping of all the elements has been carried out and shown with color-coding for different elements. High intense and low intense (or diffused) color indicating the particular elements high and low content in a particular area/spot. Figure 5.7b and d depicts only the N mapping of the above materials to show the homogeneous distribution over a large area. First of all the above results confirm the homogeneous distribution of doped
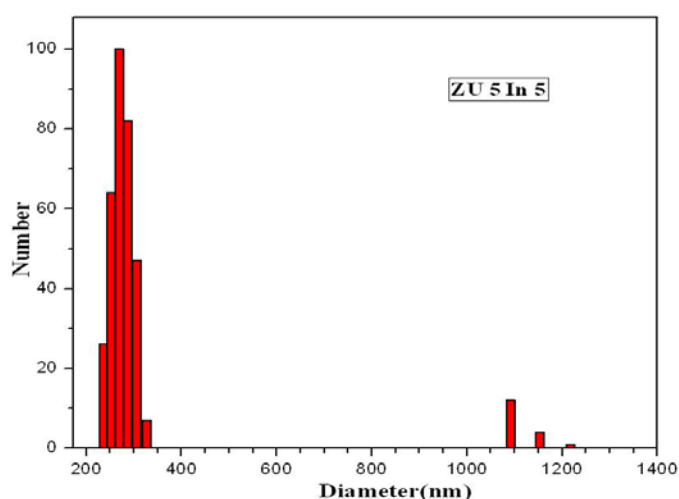
elements at microscopic level and indicating the effectiveness of the preparation method. A careful look at the elemental map (Figure 5.7a) reveals the association of In and N more than Zn and N, suggesting the solid solution of InN in ZnO.
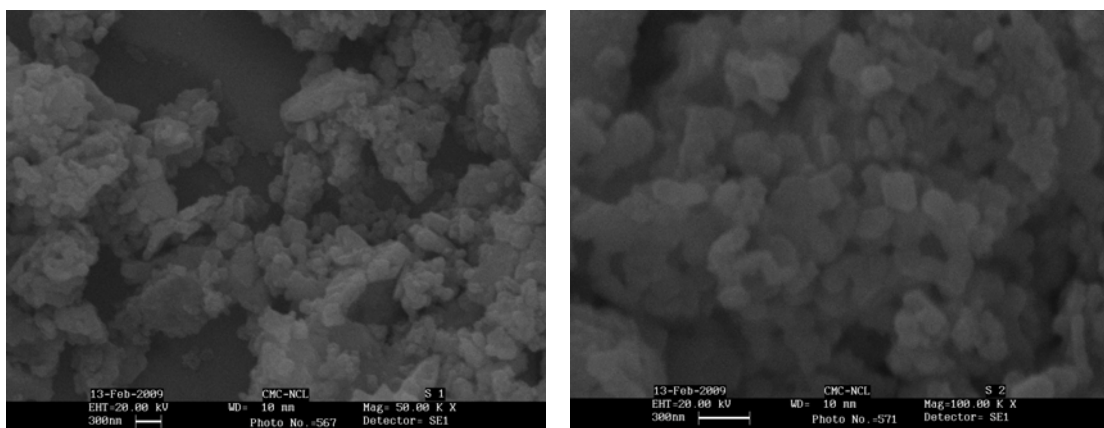

(a) UZ5In2

(b) UZ5In5

Figure 5.5: *SEM images of as prepared (*a*) UZ5In2 and (*b*) UZ5In5.*

d(nm)	G(d)	C(d)	d(nm)	G(d)	C(d)	d(nm)	G(d)	C(d)
194.1	0	0	397.7	0	95	815.0	0	95
207.2	0	0	424.5	0	95	869.9	0	95
221.1	0	0	453.1	0	95	928.6	0	95
236.0	26	8	483.7	0	95	991.2	0	95
251.9	64	26	516.3	0	95	1091.7	12	99
268.9	100	55	551.1	0	95	1152.7	4	100
287.1	82	79	588.2	0	95	1217.1	1	100
306.4	47	93	627.9	0	95	1285.1	0	100
327.0	7	95	670.2	0	95	1356.9	0	100
349.1	0	95	715.3	0	95	1432.7	0	100
372.6	0	95	763.6	0	95	1564.7	0	100

Figure 5.6: *Particle size analysis data by DLS of UZ5In5 material. Table shows the cumulative distribution of particle size. 90% of the particles are in the size range between 230 and 330 nm. Similar particle size trend has been observed for other compositions.*

(a)

(b)

(c)

(d)
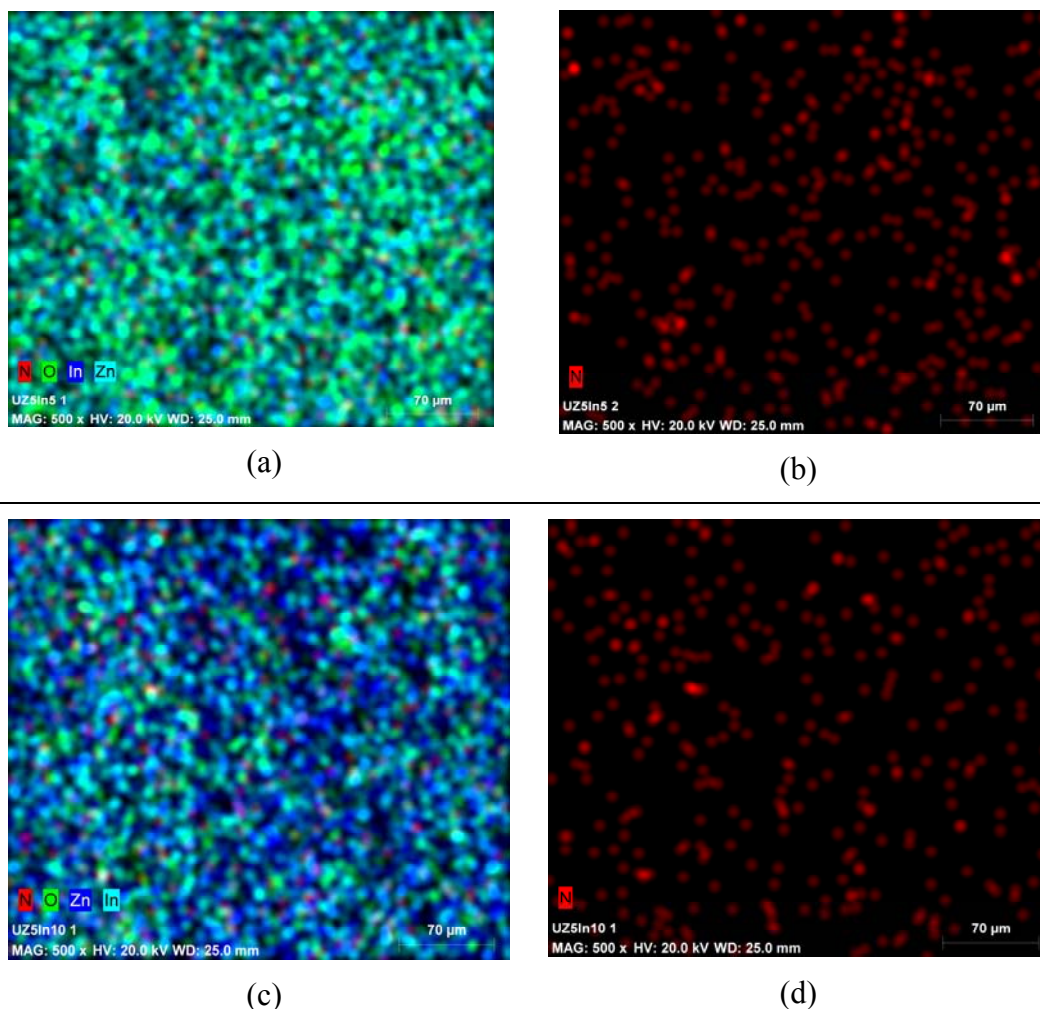
Figure 5.7: *Elemental mapping of $(Zn_{1-z}In_z)(O_{1-x}N_x)$ materials (*a *and* b*) UZ5In5, and (*c *and* d*) UZ5In10, (*a *and* c*) for all constituent elements, and (*b *and* d*) for nitrogen, respectively. Color coding for different elements are shown on the images.*

It also confirms the microscopic homogeneous uniform distribution of doped elements seen over the large area of 360 x 310 μm^2 and indicating the effectiveness of the preparation method. It is also to be noted that the atom percent measured through EDAX on individual particle differs significantly, and values reported in Table 5.1 are the average values obtained over large areas, as shown in Figure 5.7a and c. A glance at UZ5In5 (Figure 5.7a) and UZ5In10 (Figure 5.7c) highlights the change in surface composition from the former to the latter. First of all there is an increase N-content with higher In % as seen in Figure 5.7d, compared to Figure 5.7b. Indeed the red color (for N) could be seen better on Figure 5.7c than Figure 5.7a. Although apparent N-distribution and content seems similar on both materials, quantitatively it could not be shown as the decrease in relative oxygen content is small. Further the change in predominantly fluorescent green on UZ5In5 (Figure 5.7a) to blue + cyan on UZ5In10

(Figure 5.7c) underscores the change in composition from predominantly ZnO on the former to ZnO + InN on the latter, respectively. Measurement of nitrogen content of $(Zn_{1-z}In_z)(O_{1-x}N_x)$ materials through chemical method did not yield meaningful results which lead us to follow analytical method.

5.2.4 **Optical Absorption**

Optical absorption spectra of as prepared $(Zn_{1-z}In_z)(O_{1-x}N_x)$ and calcined materials have been measured, and the results are shown in Figure 5.8 along with UZ5, In_2O_3, and ZnO. Pure ZnO shows a well defined absorption cut-off edge at 380 nm; however In_2O_3 shows a gradual decrease in absorption from 370 to 440 nm [13]. A new visible absorption band with low intensity is observed at 480 nm on UZ5 material.

Our recent studies [3] confirm the creation of a mid-gap state by N $2p$ states between VB and CB, and hence, there is no change in resistivity. Evidently, after doping In and N, visible light absorption onset is extended, at least, upto 550 nm as shown in Figure 5.8a. Further, the new visible light absorption band of $(Zn_{1-z}In_z)(O_{1-x}N_x)$ materials, around 450 nm, shift to higher wavelength and the absorption coefficient increases with increasing In content up to 8% as well. There is a characteristic shift in color from pale greenish yellow for In_2O_3 to brown color $(Zn_{1-z}In_z)(O_{1-x}N_x)$, and it is unlikely that there is any In_2O_3 in the co-doped materials containing In $\leq$ 10%. N and In co-doping helps to form a shallow donor and acceptor levels from N $2p$ and In $5s/5p$, respectively, and effectively decreases the band gap by about 1 eV to 2.3 eV. Our VB studies with XPS (section 5.2.6) demonstrate that nitride contributes to a large extent towards band gap reduction.

$(Zn_{1-z}In_z)(O_{1-x}N_x)$ materials were subjected to calcinations at different temperatures and UV-Vis. absorption spectra were recorded subsequently. Representative result from UZ5In5 is given in Figure 5.8b. Significant changes in absorption characteristics could not be marked from UZ5In5 calcined up to 400ºC. However, on calcination at 500ºC, there is a considerable increase in absorption coefficient, and apparently a new absorption band develops around 440-450 nm. Similar observation was recorded for UZ5In8 after calcinations at 500ºC. This new feature is definitely not due to In_2O_3, as it exhibits absorption below 440 nm, and thus

it still contains the scope for further explorations. However, on further calcination at temperatures > 500ºC, as mentioned above, new band gradually disappears, and 800ºC calcined material shows cut off edge as that of a physical mixture of ZnO and In_2O_3, since all InN was oxidized to In_2O_3. There is a good correspondence between the features in visible light region for In_2O_3 and UZ5In5-800ºC demonstrates that all InN got oxidized to In_2O_3. Nevertheless, the important point is that the visible light absorption is exclusively due to two types of nitrogen that is combined with In and Zn. Similarly, color of UZ5In8-500ºC material is yellowish brown, which turns to very pale yellow after calcination at 800ºC. As shown in XRD, UZ5In8-800ºC exhibits a new peak at $2\theta = 30.76º$ which corresponds to the In_2O_3 peak.
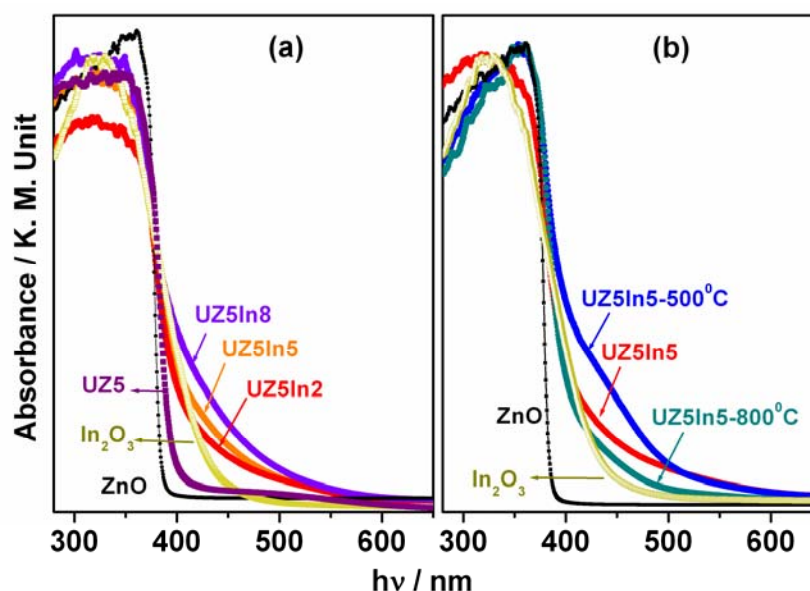
Figure 5.8: *UV-Visible absorption spectra of (Zn_{1-z}In_z)(O_{1-x}N_x) materials prepared with urea/(Zn+In) = 5 for (a) different In-content, and (b) after calcination at different temperature for UZ5In5, and compared with In_2O_3 and ZnO.*

There are few suggestions on the mechanism of band gap reduction by Inoue *et al*. [14] and Domen *et al*. [15] especially on fully-filled d^{10} systems (such as ZnO-based, GaN-based, Ge_3N_4-based), such as *p-d* repulsion or *p-d* coupling responsible for shifting the VB maximum (VB_{max}) and hence, a decrease in the band gap. For the II-VI semiconductors, Wei and Zunger [16] pointed out that the *p-d* repulsion shifts the VB_{max} upward without affecting the CB minimum (CB_{min}). However, in the present $(Zn_{1-z}In_z)(O_{1-x}N_x)$ materials there is less possibility of interaction of In 4*d* and N 2*p* states, since the In 4*d* orbital is located as shallow core levels around 18 eV in

valence band XPS. As the energy difference between N/O 2p and In 4d levels is high (12-16 eV), it is unlikely that N/O 2p - In 4d repulsion is likely to play any role. However, the possibility of lowering the CB$_{min}$ also to be considered, which is composed of Zn 4s/4p and In 5s/5p orbitals [17].

5.2.5 **Raman Spectroscopy**

Figure 5.9 shows the Raman spectra of (Zn$_{1-z}$In$_z$)(O$_{1-x}$N$_x$) with different In content and compared with ZnO and In$_2$O$_3$. ZnO exhibits a hexagonal Wurtzite structure and belongs to the C$_{6v}$ symmetry group [18]. InN exhibits two strong optical phonons at 490 cm^{-1} (E$_2$(high)), and 583 cm^{-1} (A$_1$(LO), which can be easily observed with common excitation sources [6c, 19]. A strong and sharp peak observed at 436 cm^{-1} on all synthesized and standard ZnO is attributed to characteristic nonpolar E$_2$(high) of the Wurtzite structure. Phonon mode centered at 488 cm^{-1} is attributed to E$_2$(high) mode of InN and it is in good agreement with literature reports [19 b,c]. However, this phonon mode shifts to higher frequency (504 cm^{-1}) and broadened with lower In-content (2 and 5%), indicating the smaller cluster sizes of InN. Moderate intense peak at 582 cm^{-1} is attributed to A$_1$(LO) and E$_1$(LO) modes of (Zn$_{1-z}$In$_z$)(O$_{1-x}$N$_x$), especially for Zn-N as well as In-N related mode. This peak is not observed for pure ZnO and it is characteristic for typical nitrides, such as GaN, InN and ZnO$_{1-x}$N$_x$ [3,5,18,19]. E$_2$(high) and A$_1$(TO) modes of ZnO clearly weakened with an increase in In content in (Zn$_{1-z}$In$_z$)(O$_{1-x}$N$_x$) supports the solid solution nature. In fact, all Zn-N and In-N related phonon modes intensity increased with N and In co-doping. This is a clear evidence to support the direct bonding between Zn/In and N in the (Zn$_{1-z}$In$_z$)(O$_{1-x}$N$_x$) system. A$_1$(LO) phonon mode of InN at 582 cm^{-1} overlaps with that of Zn-N related and difficult to resolve, since they appear at the same frequency. Interestingly, E$_2$(high) of In$_2$O$_3$ observed at 303 cm^{-1} is not observed on (Zn$_{1-z}$In$_z$)(O$_{1-x}$N$_x$) suggesting that the present co-doping leads to exclusive solid solution of InN in ZnO. This observation is in agreement with XRD results and confirmed by XPS studies.

The lowering of the intensity of ZnO modes with a concomitant increase in In-content in (Zn$_{1-z}$In$_z$)(O$_{1-x}$N$_x$) indicates a breaking of the total symmetry of the ZnO molecular structure. Especially, the FWHM value of E$_2$(high) at 436 cm^{-1} is found to be ~18 cm^{-1} for (Zn$_{1-z}$In$_z$)(O$_{1-x}$N$_x$) compared to 11 cm^{-1} for ZnO. This indicates the presence of nano-sized InN clusters in the samples synthesized by SCM.
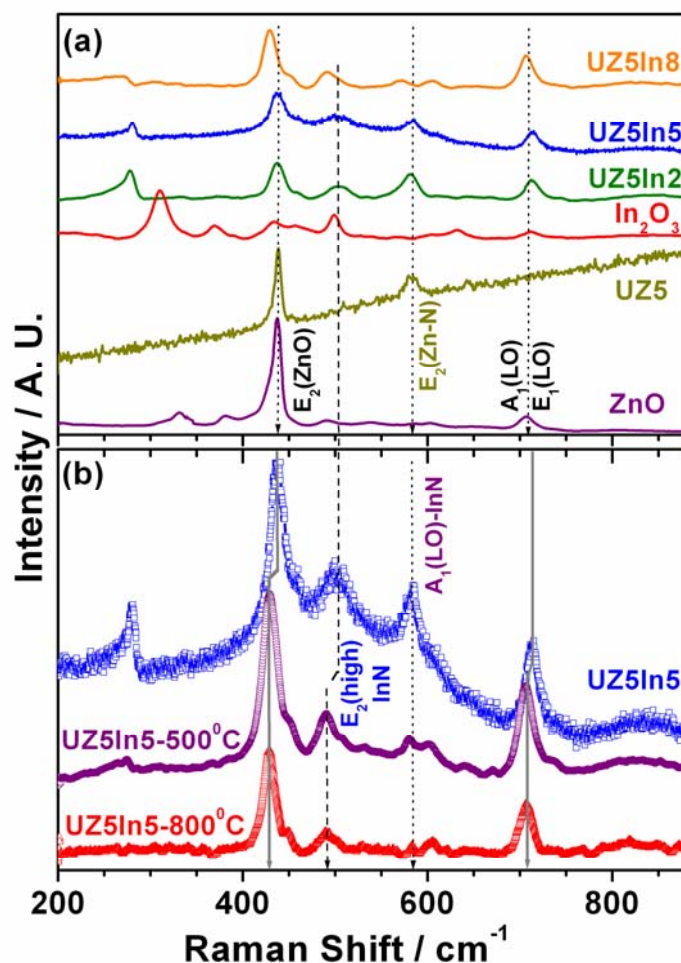
Figure 5.9: *Raman spectra of* (a) *(Zn₁₋ᵤInᵤ)(O₁₋ₓNₓ) with metal to urea ratio 5 and compared with ZnO, UZ5 and,* (b) *UZ5In5 and the same calcined at 500 and 800°C.*

Raman spectra recorded after calcination of UZ5In5 at 500 and 800°C are shown in Figure 5.9b. E_2(high) phonon modes around 436 and 490 cm^{-1}, exhibit a shift towards lower frequency and a simultaneous decrease in FWHM. In addition, InN phonon modes (E_2(high) and A_1(LO)) intensity decreased dramatically with increasing calcination temperature supporting the disappearance of InN. Nevertheless, no In_2O_3 phonon mode has been observed on calcined materials is likely due to smaller clusters.

5.2.6 Photoelectron Spectroscopy

XPS measurements have been performed mainly to examine the electronic structure details such as VB, oxidation states of constituent elements and surface composition of $(Zn_{1-z}In_z)(O_{1-x}N_x)$ materials.

Figure 5.10a displays the XPS results from N 1*s* core level of UZ5, UZ5In5, UZ5In5-500ºC, UZ5In8, and UZ5In8-500ºC. Deconvolution has been carried out to show the overlapping N components. On $ZnO_{1-x}N_x$ materials, N 1*s* core level appears to be a sharp and symmetrical peak at a BE value 399.7 eV (FWHM = 2.4 eV) indicating the charge density on N is similar to that of ammonia type nitrogen [3, 20]. However, N 1*s* peak is broad (FWHM = 3 eV) and appears around 398.8 eV for $(Zn_{1-z}In_z)(O_{1-x}N_x)$ materials hinting that there is more than one component. Deconvolution of N 1*s* core level reveals two components and the feature at 399.7 eV is same as in $ZnO_{1-x}N_x$ materials. In addition, a low BE component appears at 398.1 eV. The peak at 398.1 eV could be attributed to nitrides as in GaN/InN (397.1 eV) [20].

Indeed the BE observed here for nitride is higher than the typical nitrides, and it is attributed to the influence of surrounding majority oxide (ZnO) environment $(Zn_{1-z}In_z)(O_{1-x}N_x)$ which is likely to make it somewhat electron deficient. Elemental mapping also definitely shows a uniform distribution of nitrogen in ZnO environment,
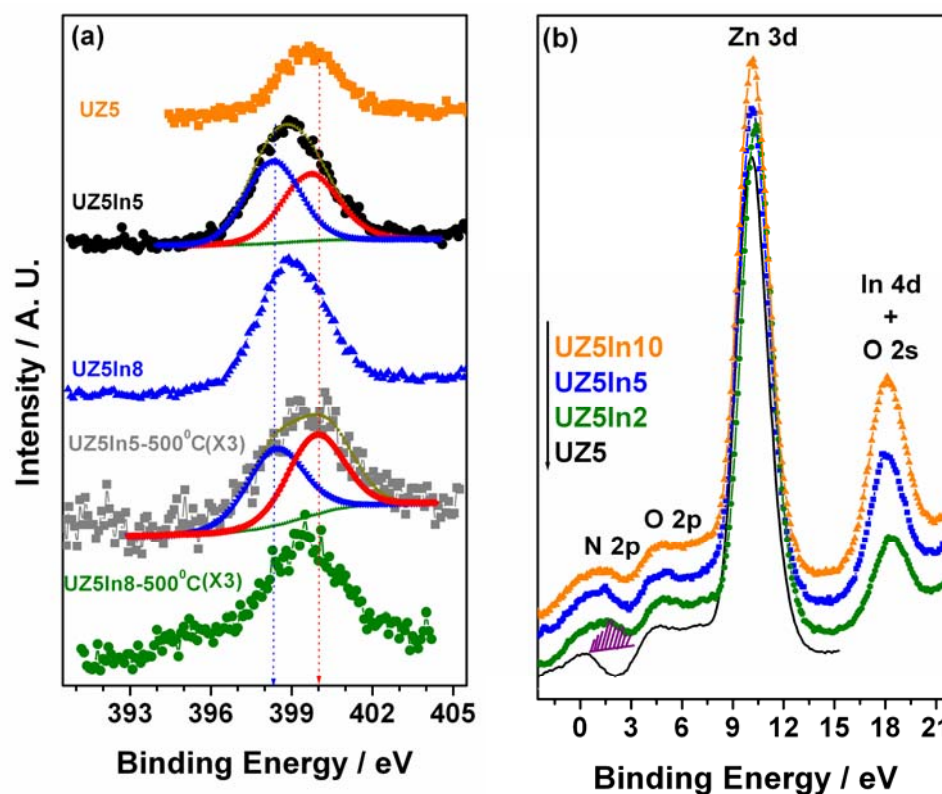
Figure 5.10: (a) *XPS spectra from N 1s core level of UZ5, UZ5In5, UZ5In5-500ºC, UZ5In8, and UZ5Ins8-500ºC.* (b) *Valence band photoelectron spectra measured from UZ5 and $(Zn_{1-z}In_z)(O_{1-x}N_x)$ materials. Feature observed around 2 eV is due to nitride 2p features.*

and it is likely to influence to some extent. UZ5In8 also shows similar feature as that of UZ5In5. Generally, In doping enhanced the nitrogen content very significantly and it is evident from XPS as well as EDAX results.

Valence band photoelectron spectra of UZ5 and (Zn$_{1-z}$In$_z$)(O$_{1-x}$N$_x$) materials have been measured with Al Kα X-ray source and shown in Figure 5.10b. Prominent Zn 3d and O 2p VB features were observed for all the above materials around 10 and 3-7 eV. For UZ5 (or ZnO$_{1-x}$N$_x$) materials, there is a band observed at Fermi level, E$_F$ = 0 eV, is because of satellite contribution from Zn 3d which is due to secondary X-ray radiations associated with Al Kα at energies higher by 9.8 and 11.8 eV than the parent radiation component [21]. Nonetheless, for all (Zn$_{1-z}$In$_z$)(O$_{1-x}$N$_x$) materials, a new and distinct VB band feature was observed between 1-3 eV, and this is in addition to the above satellite contribution. This indicates the intrinsic nature of this feature to (Zn$_{1-z}$In$_z$)(O$_{1-x}$N$_x$) materials. Indeed the above new band (hatched area in Figure 5.10b) is attributed to the N 2p contribution, especially from nitride. Lower BE for nitride feature observed in N 1s core level also supports the above conclusion. A shift of VB by 0.5 eV was observed earlier by Nambu *et al* [22] for nitrogen doped TiO$_2$ due to N-induced features, compared to TiO$_2$ surfaces. New VB feature underscores the major change in electronic structure of the (Zn$_{1-z}$In$_z$)(O$_{1-x}$N$_x$) materials due to nitride formation compared to ZnO$_{1-x}$N$_x$. Further, this also demonstrates the change in the nature of the VB from O 2p dominated on ZnO$_{1-x}$N$_x$ to nitride dominated on (Zn$_{1-z}$In$_z$)(O$_{1-x}$N$_x$) materials. It is expected that this would significantly influence various properties, including optical and catalytic properties. In 4d and O 2s shallow core levels appear around 18 eV and indicating the overlap in their energy. However, In 4d level is far away from the VB and it is unlikely to influence the VB energy due to N/O 2p – In 4d repulsion, as suggested earlier.

UZ5In5 and UZ5In8 were subjected to XPS after calcination at 500ºC for 6 hrs. Although the above calcined materials acquired brown color, the surface nitrogen content decreased. It is to be noted that the peak intensity has been multiplied 3 times to show the features with clarity and comparable intensity as that of UZ5In5/8. However, the features observed are as that of as-prepared samples at the same BE, but with lower intensity. This result combined with TG-DTA results confirms that indeed (Zn$_{1-z}$In$_z$)(O$_{1-x}$N$_x$) material undergoes oxidation, especially InN transforms to In$_2$O$_3$.

Figure 5.11a shows XPS spectra for Zn $2p_{3/2}$ core level BE appearing at around 1021.5 eV for $ZnO_{1-x}N_x$ and $(Zn_{1-z}In_z)(O_{1-x}N_x)$ materials with different In-content. The above BE is significantly lower than that of ZnO, which appears at 1022.0 eV. Although the formal oxidation state of Zn to be +2 in all of the above materials [20(a)], the relative electron density is relatively high on $ZnO_{1-x}N_x$ and $(Zn_{1-z}In_z)(O_{1-x}N_x)$ materials compared to ZnO. This is mainly attributed to the significant amount of N in the above materials, especially as nitride, which is electron rich and it is likely to influence the charge density to the neighboring cations. It is likely that there is some redistribution of electron density, at least locally on the above materials.

XPS data of In $3d$ core level shows spin-orbit doublets at 444.7±0.1 eV ($3d_{5/2}$) and 452.2±0.1 eV ($3d_{3/2}$) with an energy separation of 7.5 eV (Figure 5.11b). BE values around 444.8±0.5 eV for $3d_{5/2}$ core level has been reported for InN as well as In_2O_3 by several groups [20 a]. Apparently the BE of In $3d$ levels are not sensitive to chemical environment and it is difficult to ascertain the nature of In only from the BE values. Nevertheless, it can be concluded that In exists in the +3 oxidation state. Further, InN exhibits higher FWHM (2.1 eV), compared to In_2O_3 (1.5 eV) [23] and Figure 5.11b shows a FWHM of 2.2 eV supports that the nature of In is as in InN.
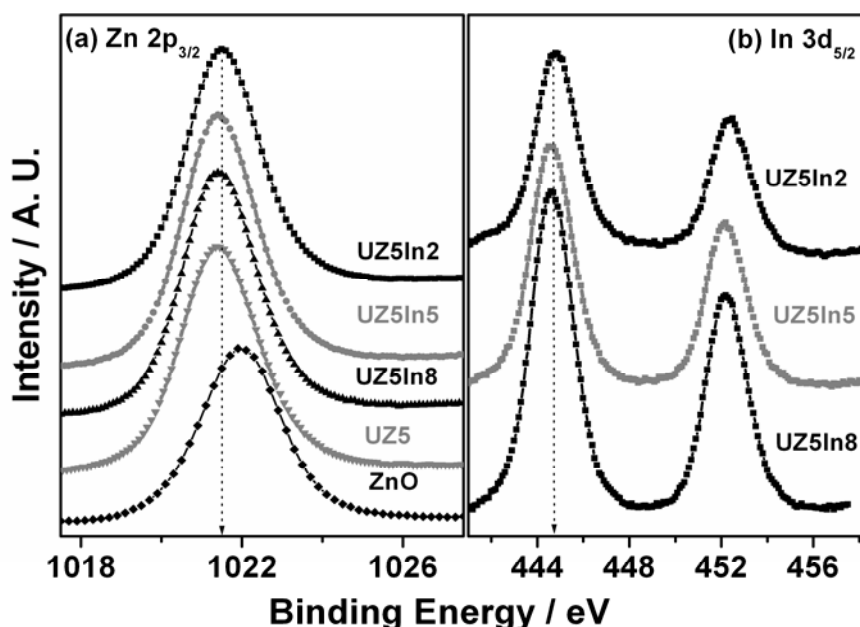

Figure 5.11: *XPS spectra from* (a) *Zn $2p_{3/2}$ and* (b) *In $3d_{5/2}$ core levels of UZ5In2, UZ5In5, UZ5In8, ZnO, and UZ5.*

5.2.7 **SIMS Analysis**

Figure 5.12 shows the SIMS data of UZ5In5 and UZ5In10. Secondary ion intensities of different species as a function of sputtering time reflect the presence of those species as a function of depth. The initially captured mass spectrum with significant intensity illustrated the presence of different species, namely ZnO, ZnN, InN, InO ZnNIn, N, Zn, and O. Secondary-ion intensities of the first five species are shown in Figure 5.12. The direct observation of InN from UZ5In5 and UZ5In10 underscores the solid solution of InN in ZnO. Additionally, presence of Zn-N-In and ZnN species suggest a direct interaction between N^{3-} to Zn as well as Zn and In together. It is surprising than InO species is also present in UZ5In5, though it was not observed through any other characterization methods.
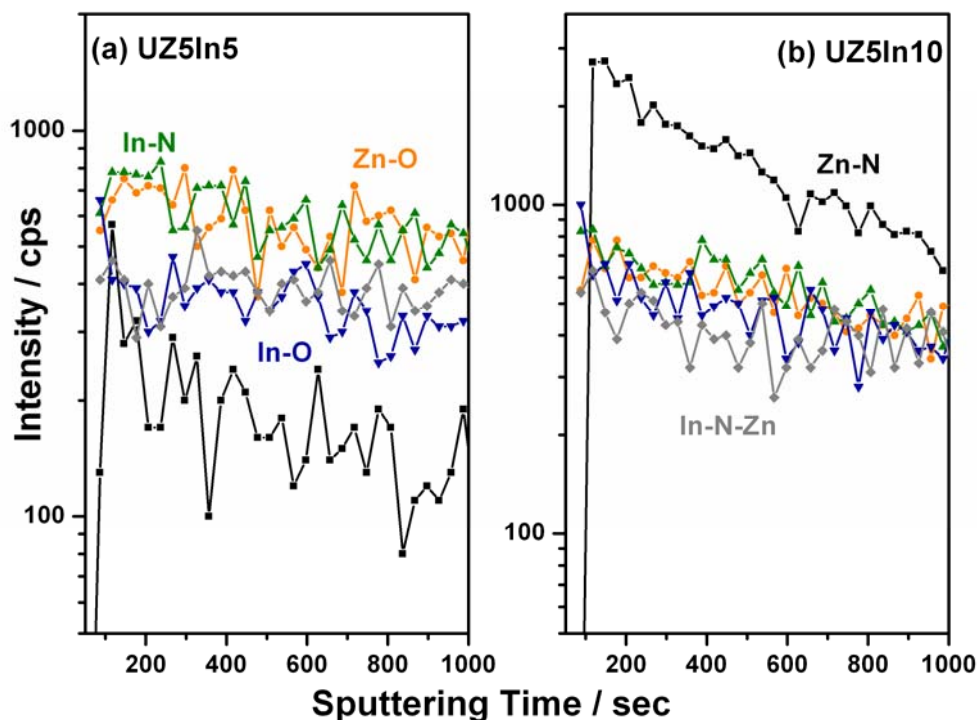
Figure 5.12: *Secondary ion intensities of various species as a function of sputtering time are given for* (a) *UZ5In5* (b) *UZ5In10.*

This is likely due to presence of highly dispersed small InN clusters which is likely to interact with ZnO at interface boundary between InN and ZnO. Crucially, signal intensities of all the species except ZnN in UZ5In10 remain constant at deeper levels highlights the solid solution nature and uniform distribution for all the materials.

5.3 Catalytic Activity

5.3.1 Dehydrogenation of 2-Butanol

ZnO being a traditional catalyst employed for dehydration and dehydrogenation reactions [24], (Zn$_{1-z}$In$_z$)(O$_{1-x}$N$_x$) materials have been explored for catalytic dehydrogenation of 2-butanol to methyl ethyl ketone (MEK) as a model reaction. MEK is a good solvent, especially for coating applications and also used in dry erase markers as the solvent for the erasable dye and refining industries. It is also an important raw material for organic chemical industries and is used for the production of MEK peroxide and oxime, as an intermediate in the perfumery industry, as an antioxidant. Currently, MEK is commercially produced using the two-step n-butylene technique. Gas phase dehydrogenation is widely used in the industry, as it involves a simpler process flow sheet and the low investment.
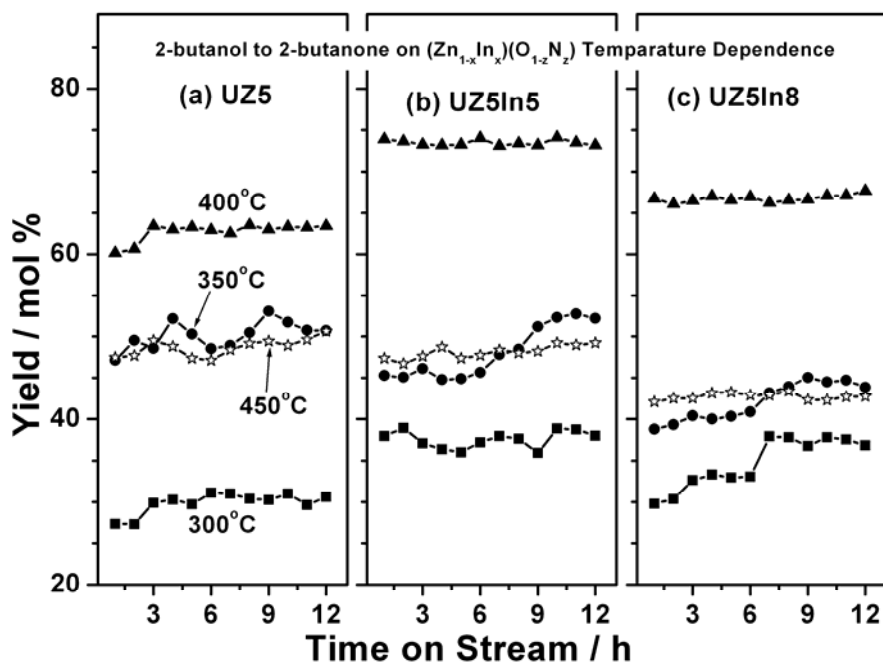

2-butanol → **2-butanone**
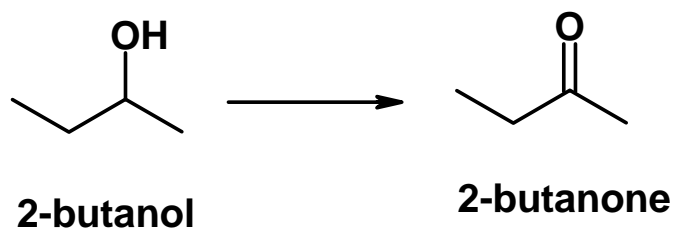
Scheme 5.1: Reaction scheme for 2-butanol dehydrogenation reaction.

Figures 5.12 and 5.13 show the catalytic conversion of 2-butanol and yield of 2-butanone as a function of time on stream for three different catalyst compositions (UZ5, UZ5In5 and UZ5In8) between 300 and 450ºC. MEK formed as a major product along with some gaseous product like CO_2 and butene. Hardly there is any catalytic activity below 300ºC for this particular reaction and without catalyst as well. Initially the reaction was carried out at different space velocity and it has been observed that at WHSV = 5 gave maximum conversion, and hence, all our studies have been carried out at this value. Catalytic conversion of 2-butanol increases steadily, with increasing temperature, from 300ºC (Figure 5.12). An important observation to be noted is the catalytic conversion remains at the same level from the beginning till 12 hrs for all catalyst compositions. 30-40% catalytic conversion observed at 300ºC for all catalyst compositions increases to 100% conversion at 450ºC for UZ5, but at 400ºC for In-containing materials.
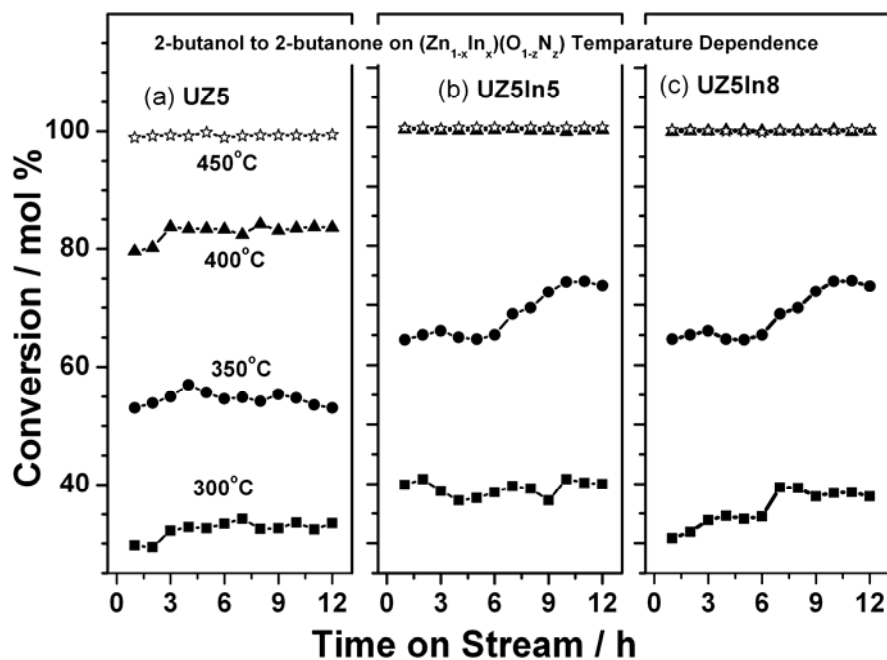
Figure 5.12: *Catalytic conversion of 2-butanol on UZ5, UZ5In5 and UZ5In8 materials in the temperature range between 300 and 450℃.*

Figure 5.13: *2-butanone yield obtained on UZ5, UZ5In5 and UZ5In8 in the temperature range between 300 and 450℃.*

100% conversion was obtained with UZ5In5 at 400℃ suggesting the influence of InN content towards better activity. However, with further increase In

concentration in the catalyst (UZ5In8 and UZ5In10) does not show any further increase in overall activity hinting the optimum activity is with UZ5In5.

Figure 5.13 displays the MEK yield observed for three different catalyst compositions between 300-450°C as a function of TOS. At 300°C, MEK yield is observed between 30 and 40 mol % irrespective of catalyst compositions. However, with increase in temperature (up to 400°C) the MEK yield increases up to 64% on UZ5. Yield decreases dramatically above 400°C and it decreases to 50% at 450°C on UZ5. Very similar trend was observed with In-containing catalysts also. However, the highest yield around 75% was observed with UZ5In5 at 400°C. The selectivity and yield of MEK decrease for all the catalysts above 400°C. It is to be noted that introduction of In induces Lewis acidity and that is likely to be responsible for higher catalytic activity, and it is well known that acid-base properties changes the catalytic activity [25]. An important point to be noted is the stable conversion and yield for all the three catalysts over the entire reaction period (12 h). No decline in activity indicates no or very less changes in the nature of the materials surface characteristics.

5.4 Conclusions

$(Zn_{1-z}In_z)(O_{1-x}N_x)$ materials were prepared by simple SCM and it was characterized by a variety of physico-chemical, structural, spectroscopy, microscopy and catalytic measurements for dehydrogenation reaction. Above detailed studies suggest that the nature of above material is a solid solution of InN in ZnO. Except for a minor lattice expansion, no significant change in ZnO Wurtzite structure was observed even up to 10% InN in $(Zn_{1-z}In_z)(O_{1-x}N_x)$ materials. Even though combustion method involves high temperatures between 600 and 1000°C, almost homogeneous nano size particles were observed by SEM. Elemental mapping of $(Zn_{1-z}In_z)(O_{1-x}N_x)$ materials displays a homogeneous distribution of doped elements and InN formation. Good thermal stability, at least up to 500°C, was identified from thermal analysis and supported by other characterization methods. A new absorption band in the visible region was observed with the onset of absorption at 550 nm. UV-Visible absorption spectral studies and valence band XPS results demonstrate the creation of a new band derived from N $2p$ states of nitride just above the O $2p$ VB, and primarily responsible for the reduction of optical band gap to 2.3 eV. Raman spectral studies directly show the linkage between Zn/In and N, and E_2(high) and

A$_1$(LO) modes corresponding to InN were clearly observed. XPS data indicates that there are two types of nitrogen on (Zn$_{1-z}$In$_z$)(O$_{1-x}$N$_x$) with different charge density; N 1s BE appeared at 398 eV (399.7 eV) corresponds to nitride (ammonia). All the above studies and characterization demonstrates that (Zn$_{1-z}$In$_x$)(O$_{1-x}$N$_x$) is indeed a solid solution of InN in ZnO. (Zn$_{1-x}$In$_x$)(O$_{1-y}$N$_y$) materials also show high selectivity and yield towards methyl ethyl ketone from catalytic dehydrogenation of 2-butanol.

5.5 **References**

1. (a) C. Klingshirn, *Chem. Phys. Chem.* **8** (2007) 782. (b) Ü. Özgür, Y. I. Alivov, C. Liu, A. Teke, M. A. Reshchikov, S. Dogan, V. Avrutin, S. J. Cho and H. Morkoc, *J. Appl. Phys.* **98** (2005) 041301. (c) I. Melian-Cabrera, M. Lopez Granados, P. Terreros and J. L. G. Fierro, *Catal. Today* **45** (1998) 251. (d) B. G. Mishra and G. Ranga Rao, *J. Mol. Cat A: Chem.* **243** (2006) 204. (e) B. M. Bhanage, S. Fujita, Y. Ikushima and M. Arai, *Green Chem.* **5** (2003) 429.

2. (a) K. Iwata, P. Fons, A. Yamada, K. Matsubara and S. Niki, *J. Cryst. Growth* **209** (2000) 526. (b) X.-L. Guo, H. Tabata and T. Kawai, *J. Cryst. Growth* **237** (2002) 544. (c) S. Yamauchi, Y. Goto and T. Hariu, *J. Cryst. Growth* **260** (2004) 1. (d) D. C. Look, D. C. Reynolds, C. W. Litton, R. L. Jones, D. B. Eason and G. Cantwell, *Appl. Phys. Lett.* **81** (2002) 1830. (e) G. Xiong, J. Wilkinson, B. Mischuck, S. Tuzemen, K. B. Ucer and R. T. Williams, *Appl. Phys. Lett.* **80** (2002) 1195. (f) C. L. Perkins, S. H. Lee, X. Li, S. E. Asher and T. J. Coutts, *J. Appl. Phys*. **97** (2005) 034907.

3. M. Mapa and C. S. Gopinath, *Chem. Mater.* **21** (2009) 351.

4. (a) K. Sato and. H. Katayama-Yoshida, *Jpn. J. Appl. Phys*. **46** (2007) L1120. (b) T. Yamamoto and K Y. Hiroshi, *Physica B*. **302-303** (2001) 155. (c) T. Yamamoto, *Thin Solid Films* **420-421** (2002) 100. (d) A. V. Singh, R. M. Mehra, A. Wakahara and A. Yoshida, *J. Appl. Phys.* **93** (2003) 396. (e) T. Ohshima, T. Ikegami, K. J. Edihara and A. R. Thareja, *Thin Solid Films* **435** (2003) 49.

5. M. Mapa, K. S. Thushara, B. Saha, P. Chakraborty, C. M. Janet, R. P. Viswanath, C. M. Nair, K. V. G. K. Murty and C. S. Gopinath, *Chem. Mater*. **21** (2009) 2973**.**

6. (a) L. L. Chen, J. G. Lu, Z. Z. Ye, Y. M. Lin, B. H. Zhao, Y. M. Ye, J. S. Li and L. P. Zhu, *Appl. Phys. Lett*. **87** (2005) 252106. (b) L. L. Chen, Z. Z. Yea, J. G.

Lu and K. P Chu, *Appl. Phys. Lett.* **89** (2006) 252113. (c) J. F. Kong, H. Chen, H. B. Ye, W. Z. Shen, J. L. Zhao and X. M. Li, *Appl. Phys. Lett.* **90** (2007) 041907.

7. (a) http://www.ioffe.rssi.ru/SVA/NSM/Semicond/InN/basic.html (last accessed on 5/09). (b) J. Wu, W. Walukiewicz, K. M. Yu, J. W. Ager III, E. E. Haller, H. Lu and W. J. Schaff, *Appl. Phys. Lett.* **80** (2002) 4741.

8. (a) S. C. Jain, M. Willander, J. Narayan and. R. V. Overstraeten, *J. Appl. Phys.* **87** (2000) 956. (b) *III-V Nitrides*, Ed. F. A. Ponac, T. D. Moustakas, I. Akasaki and B. A. Monemar, *MRS Symp. Proc. 449*, MRS, Pittsburg, 1997. (c) H. Morkoc, S. Strite, G. B. Gao, M. E. Lin, B. Sverdlov and M. Burns, *J. Appl. Phys.* **76** (1994) 1263. (d) S. Nakamura, T. Mukai and M. Senoh, *Appl. Phys. Lett.* **64** (1994) 1687. (e) J. Wu, W. Walukiewicz, K. M. Yu, J. W. Ager, E. E. Haller, H. Lu, W. J. Schaff, Y. Saito and Y. Nanishi, *Appl. Phys. Lett.* **80** (2002) 3967. (f) R. Asahi, T. Morikawa, T. Ohwaki, K. Aoki and Y. Taga, *Science* **293** (2001) 269. (g) M. Sathish, R. P. Viswanath and C. S. Gopinath, *J. Nanosci. Nanotech.* **9** (2009) 423. (h) M. Sathish, R. P. Viswanath and C. S. Gopinath, *Chem. Mater.* **17** (2005) 6349. (i) C. S. Gopinath, *J. Phys. Chem. B* **110** (2006) 7079.

9. (a) K. Deshpande, A. Mukasyan and A. Varma, *Chem. Mater.* **16** (2004) 4896. (b) R. K. Lenka, T. Mahata, P. K. Sinha and A. K. Tyagi, *J. Alloys Comp.* **466** (2008) 326. (c) C-C. Hwang and T-Y. Wu, *J. Mater. Sci.* **39** (2004), 6111.

10. (a) S. D. Dingman, N. P. Rath, P. D. Markowitz, P. C. Gibbons and W. E. Buhro, *Angew. Chem. Intern. Ed.* **39** (2009) 1470. (b) Y-R. Tzeng, P. Raghunath, S-C. Chen and M. C. Lin, *J. Phys. Chem. A.* **111** (2007) 6781.

11. (a) D. A. Neumayer and J. G. Ekerdt, *Chem. Mater.* **8** (1996) 9. (b) A. C. Jones, C. R. Whitehouse and J. S. Roberts, *Chem. Vap. Deposition* **1** (1995) 65. (c) I. Akasaki and H. Amano, *J. Cryst Growth* **146** (1995) 455. (d) I. Grzegory, J. Jun, M. Bockowski, St. Krukowski, M. Wroblewski, B. Lucznik and S. Porowski, *J. Phys. Chem. Solids* **56** (1995) 639.

12. (a) A. Bellosi, E. Landi and A. Tampieri, *J. Mater. Res.* **8** (1993) 565. (b) A. D. Katnani and K. I. Papathomas, *J. Vac. Sci. Technol. A* **5** (1987) 1335. (c) C. P. Foley and J. Lyngdal, *J. Vac. Sci. Technol. A* **5** (1987) 1708. (d) K. L. Westra, R.

P. W. Lawson and M. J. Brett, *J. Vac. Sci. Technol. A* **6** (1988) 1730. (e) I. J. Lee, J.-Y. Kim, T.-B. Hur and H.-K. Kim, *Phys. Stat. Sol. A* **201** (2004) 2777.

13. K. Kamata, K. Maeda, D. Lu, Y. Kako and K. Domen, *Chem. Phys. Lett*. **470** (2009) 90.

14. Y. Inoue, *Energy Environ. Sci*. **2** (2009) 364.

15. (a) K. Maeda and K. Domen, *J. Phys. Chem*. C **111** (2007) 7851. (b) F. E. Osterloh, *Chem. Mater*. **20** (2008) 35. (c) K. Maeda, K. Teramura, T. Takata, M. Hara, N. Saito, K. Toda, Y. Inoue, H. Kobayashi and K. Domen, *J. Phys. Chem. B* **109** (2005) 20504.

16. S. H. Wei and A. Zunger, *Phys. Rev. B* **37** (1988) 8958.

17. J. Sato, H. Kobayashi and Y. Inoue, *J. Phys. Chem. B*. **107** (2003) 7970.

18. (a) D. Wang, H. W. Seo, C. C. Tin, M. J. Bozack, J. R. Williams, M. Park, N. Santhitsuksanoh, A. Cheng and Y. H. Tzeng, *J. Appl. Phys*. **99** (2006) 113509. (b) U. Haboeck, A. Hoffmann, C. Thomsen, A. Zeuner and B. K. Meyer, *Phys. Stat. Sol. B* **242** (2005) R21.

19. (a) M. Kuball, J. W. Pomeroya, M. Wintrebert-Fouquet, K. S. A. Butcher, H. Lu and W. J. Schaff, *J. Cryst. Growth* **269** (2004) 59. (b) T. Inushima, M. Higashiwaki and T. Matsui, *Phys. Rev. B*. **68** (2003) 235204. (c) X. D. Pu, J. Chen, W. Z. Shen, H. Ogawa and Q. X. Guo, *J. Appl. Phys*. **98** (2005) 033527. (d) V. M. Naik, R. Naik, D. B. Haddad, J. S. Thakur, G. W. Auner, H. Lu and W. J. Schaff, *Appl. Phys. Lett*. **86** (2005) 201913. (e) A. Dixit, C. Sudakar, R. Naik, G. Lawes, J. S. Thakur, E. F. McCullen, G. W. Auner and V. M. Naik, *Appl. Phys. Lett*. **93** (2008) 142103.

20. (a) http://srdata.nist.gov/xps/ (b) N 1s spectra were recorded with Al Kα, to ensure that no contribution from Zn-L$_3$M$_{23}$M$_{23}$ Auger level (395-430 eV with Mg Kα) to N 1s region. (c) K. R. Reyes-Gil, E. A. Reyes-Garcı´a and D. Raftery, *J. Phys. Chem. C* **111** (2007) 14579.

21. (a) C. D. Wagner, W. M. Riggs, L. E. Davis, J. F. Moulder and G. E. Muilenberg, Handbook of X-ray photoelectron spectroscopy; Perkin-Elmer Corporation: Eden Prairie, MN, 1979. (b) C. S. Gopinath, S. Subramanian, M. Huth and H. Adrian, *J. Electron Spectrosc. Relat. Phenom*. **70** (1994) 61.

22. A. Nambu, J. Graciani, J. A Rodriguez, Q. Wu, E. Fujita and J. Fdez Sanz, *J. Chem. Phys*. **125** (2006) 094706.

23. I. J. Lee, C. Yu, H-J. Shin, J-Y. Kim, Y. P. Lee, T-B. Hur and H-K. Kim, *Thin Solid Films* **515** (2007) 4691.

24. (a) W. A. Lazier and H. Adkins, *J. Am. Chem. Soc*. **47** (1925) 1719. (b) S .Ravi, and T. S. Raghunathan, *Ind. Eng. Chem. Res*. **27** (1988) 2050. (c) V. K Raizada, V. S. Tripathi, D. Lal, G. S. Singh, C. D. Dwivedi and A. K. Sen, *J. Chem. Technol. Biotechnol.* **56** (1993) 265.

25. (a) T. Mathew, B. S. Rao and C. S. Gopinath, *J. Catal*. **222** (2004) 107. (b) T. Mathew, S. Shylesh, B. M. Devassy, C. V. V. Satyanarayana, B. S. Rao and C. S. Gopinath, *Appl. Catal. A:Gen* **273** (2004) 35. (c) S. B. Waghmode, R. Vetrivel, S. G. Hegde, C. S. Gopinath and S. Sivasanker, *J. Phys. Chem. B* **107** (2003) 8517.

Chapter 6
Conclusions and Future Outlook

6   Conclusions and Future Outlook

This chapter summarizes the present thesis work and describes the conclusions and possible future implications drawn based on the work.

Chapter 1 provides general background and introduction to heterogeneous catalysis including brief description with importance of various types of mixed metal oxides with an emphasis on ZnO system. It gives an idea on the effect of doping in lattice, electronic properties, and surface morphology of metal oxide as well. Furthermore, tuning of catalytic activity and selectivity by suitable doping in metal oxide has also been discussed. Importance of ZnO as catalyst and material is growing and it is becoming a key technological material for various applications, as it is inexpensive and environmental friendly. In fact research on ZnO crystal has been continued for many decades due to its use as a commodity chemical. In order to optimize the potential offered by ZnO, doping is required for both high-quality *n-* and *p*-type ZnO. *n*-type doping is relatively easy, but it is very difficult to create consistent and reliable *p*-type material. *p*-type ZnO can be grown using intentionally added acceptor species, and some success has been achieved with N, P, As, and Sb doped as impurities. Nitrogen is the most common among these because N-doping does not produce any lattice strain as its ionic radii and electronegativity is comparable with that of oxygen. Several efforts have been employed in the literature and has been listed using various types of nitrogen sources depending on the growth techniques applied, to get *p*-type material, however, still low solubility of nitrogen and reproducibility of the target material are the main problem. To overcome the problems co-doping method was followed exclusively with group III metal ion.

Simple SCM has been employed to prepare hetero anion (N, N and S) incorporated ZnO. **Chapter 2** mainly addresses the detailed procedures involved in the preparation methods. Use of urea as fuel and nitrogen source is proved to be successful. Urea decomposes to produce ammonia in-situ under SCM conditions along with the growth of Zn_xO_y (y/x <1) clusters from nucleation stage. Condition created above helps to introduce nitrogen into the ZnO lattice at nucleation stage under oxygen deficient high temperature conditions. Additionally at high temperature there is a deficiency of oxygen (or lattice defects) in ZnO lattice which helps nitrogen to get into the lattice position to fill up the vacancies. Thiourea was used as sulfur

source to explore the preparation of N and S codoped ZnO. Furthermore, preparation of Ga/In and nitrogen codoped ZnO has been prepared through SCM. Nonetheless, formation of solid solution of GaN in ZnO and InN in ZnO hinted at the formation of high flux of ammonia at high temperature under SCM condition. GaN, InN, ZnS and ZnO materials exhibit hexagonal Wurzite structure and this structural similarity favored the successful preparation of the above materials. Theory and experimental procedures involved in various physicochemical and spectroscopic characterization techniques were discussed.

Chapter 3 is divided into two parts - **Part A** and **Part B**. **Part A** deals with detailed studies on structural, spectroscopic and electronic structure of $ZnO_{1-x}N_x$ material through various methods. PXRD studies of $ZnO_{1-x}N_x$ demonstrate that the lattice oxygen in ZnO is replaced by nitrogen without any major change in the Wurtzite structure. However, charge compensation was partly due to interstitial Zn ions and oxygen vacancies as well. Nanometer- to micrometer-sized and triangular/prism-shaped particles were predominantly observed. Thermal analysis revealed high thermal stability and hydrophobic nature of $Zn_{0.85}O_{0.15}$. Raman spectroscopy shows typical E_2 mode of ZnO which proves that structural integrity was maintained. In addition to the above, three new peaks were observed at 507, 582, and 642 cm^{-1} on $ZnO_{1-x}N_x$ systems due to Zn-N phonon modes. Bulk nitrogen doping in ZnO and the uniformity of the substitution throughout the bulk confirmed from SIMS analysis and decrease in lattice parameters. Optical studies demonstrate that the N $2p$ states form the midgap (deep level acceptor) states and hence, no change in conducting characteristics of $ZnO_{1-x}N_x$ was observed. XPS indicates that the charge density of nitrogen on $ZnO_{1-x}N_x$ is similar to that of ammonia or amines. This might be attributed to a more-covalent character of Zn-N bonds in $ZnO_{1-x}N_x$. Photocatalytic decomposition of rhodamine B on $ZnO_{1-x}N_x$ with UV light reveals its effectiveness as photocatalyst. However, no significant visible-light photocatalytic activity suggests that the N $2p$ states do not induce any photocatalytic activity. Nonetheless, $ZnO_{1-x}N_x$ materials also exhibit highly selective cyclohexanone formation from cyclohexanol at 400ºC and anisole acylation reaction at room temperature indicating that it remains to be a conventional catalyst with better activity. The aforementioned multifunctional characteristics suggest that $ZnO_{1-x}N_x$ might be used in place of conventional ZnO for better control.

Part B brings out the effect of replacing urea to thiourea in the fuel components with $Zn(NO_3).6H_2O$ and it leads to the solid solution of ZnS in $ZnO_{1-x}N_x$ material. With increasing thiourea content, simultaneous increase in ZnS content was also observed by XRD to the extent that 1:1 ratio of ZnS:ZnO solid solution was obtained with equimolar thiourea and zinc nitrate. XPS indicates that the charge density of nitrogen on $ZnO_{1-x-z}N_xS_z$ is similar to that of $ZnO_{1-x}N_x$, however, sulfur is increasingly introduced as sulphide with increasing thiourea content in the preparation mixture. Thermogravimetric analysis corroborates with XRD and XPS analysis. Although ZnO (3.37 eV) and ZnS (3.66 eV) both are large band-gap semiconductors, the $ZnO_{1-x-z}N_xS_z$ exhibits visible light absorption, at least, up to 525 nm and demonstrates an effective reduction of optical band gap and suggests a substantial change in the electronic structure. This set of materials has shown very high selectivity of isobutyraldehyde in the catalytic conversion of isobutanol dehydrogenation.

Nature and quantity of nitrogen are expected to be changed when N is codoped with a suitable donor (Ga, In). **Chapter 4** describes the oxidation state, quantity and the effect of Ga and nitrogen co-doping and formation of solid solution of GaN in $ZnO_{1-x}N_x$ lattice. Except for minor changes in the lattice contraction, no significant change in the Wurtzite structure was observed. Visible light absorption and XPS results demonstrate that N 2*p* states of GaN occupy the states just above the O 2*p* VB, and hence, a change in optical band gap reduction occurs to ~2.5 eV from 3.37 eV for ZnO. Presence of Raman active phonon modes of GaN as well as ZnO (E_2(high)) and SIMS result in $(Zn_{1-z}Ga_z)(O_{1-x}N_x)$ confirmed the formation of solid solution of GaN in ZnO. It is also confirmed that the visible light absorption is due to nitride. The presence of GaN in $(Zn_{1-z}Ga_z)(O_{1-x}N_x)$ and supported by physicochemical analysis underscores the importance of reductive reaction atmosphere with plenty of insitu produced NH_3 in the present experimental conditions. Significant nitrogen fixation catalytic activity through NH_3 formation has been observed at ambient pressure at 350ºC on virgin $(Zn_{1-z}Ga_z)(O_{1-x}N_x)$ materials indicates its potential as a catalyst. Furthermore, addition of electronic promoter, such as K_2O, helps to keep the catalyst active for longer time. Hence, it is worthwhile to look similar type nitride catalyst system towards ammonia production at ambient conditions. Although our efforts on visible light driven photocatalytic activity towards

water splitting are not significant (not reported), post modification with noble metal and co-catalyst is worth exploring. Indeed, good visible light photocatalytic activity for water splitting on $(Ga_{1-x}Zn_x)(N_{1-x}O_x)$ observed by Domen *et al.* (*J. Am. Chem. Soc.,* **127** (2005) 8286) suggests the possibility of the present system to exhibit photocatalytic activity after post modification.

Chapter 5 addresses the change in lattice structure and band gap of $(Zn_{1-z}In_z)(O_{1-x}N_x)$ which is codoped with In and N. However, In^{3+} size is larger than that of Zn^{2+}, but void space present in ZnO lattice helps it to accommodate. Infact, a solid solution of InN in ZnO was obtained in the present study which has been thoroughly characterized by various physicochemical methods. XRD peaks are directly indexed to ZnO confirming formation of Wurtzite structure up to 10% InN in $(Zn_{1-z}In_z)(O_{1-x}N_x)$ materials. A new and distinct VB feature was observed between 1 and 3 eV in XPS indicates the intrinsic nature of $(Zn_{1-z}In_z)(O_{1-x}N_x)$ materials, and it is attributed to the N $2p$ contribution, especially from InN. XPS data reveals that there are two types of nitrogen on $(Zn_{1-z}In_z)(O_{1-x}N_x)$ with different charge density as in $(Zn_{1-z}Ga_z)(O_{1-x}N_x)$ materials. From the above mentioned observations and thorough characterization, it can be accentuated that $(Zn_{1-z}In_z)(O_{1-x}N_x)$ is indeed a solid solution of InN in ZnO. It has been evaluated for the catalytic vapor phase dehydrogenation reaction of 2-butanol to methyl ethyl ketone. Solid solution of a large amount of InN in ZnO has not yet been studied in details till date, and present study demonstrates the multifunctional nature of $(Zn_{1-z}In_z)(O_{1-x}N_x)$ materials.

$ZnO_{1-x-z}N_xS_z$, $(Zn_{1-z}Ga_z)(O_{1-x}N_x)$ and $(Zn_{1-z}In_z)(O_{1-x}N_x)$ materials exhibit certain attractive and unique features, like optical absorption in the visible region up to 550 nm and a good optical band gap reduction by upto 1.2 eV. Electronic structures of above materials are considerably different from ZnO with VB features distinctly different from O $2p$, and this reiterates that they exhibit properties/activities different from that of ZnO. Indeed, it is worth exploring specially for optoelectronics properties, visible light photocatalytic activity and sensor activity with various gases. It is also expected that more and systematic studies on the above system would lead to applications in the above mentioned areas, in addition to the applications explored in the present thesis.

List of Publications

1) MCM-41-supported platinum carbonyl cluster-derived catalysts for asymmetric and nonasymmetric hydrogenation reactions.

   Susmit Basu, **Maitri Mapa,** Chinnakonda S. Gopinath, Mukesh Doble, Sumit Bhaduri and Goutam Kumar Lahiri. *Journal of Catalysis* **239** (2006) 154.

2) Effect of spacer groups on the performance of MCM-41-supported platinum cluster-derived hydrogenation catalysts.

   Niladri Maity, Susmit Basu, **Maitri Mapa**, Pattuparambil R. Rajamohanan, Subramanian Ganapathy, Chinnakonda S. Gopinath, Sumit Bhaduri, and Goutam Kumar Lahiri, *Journal of Catalysis* **242** (2006) 332.

3) Combustion synthesis of triangular and multifunctional $ZnO_{1-x}N_x$ (x = 0.15) materials.

   Maitri Mapa and Chinnakonda S. Gopinath, *Chemistry of Materials* **21** (2009) 351.

4) Electronic structure and catalytic study of solid solution of GaN in ZnO.

   Maitri Mapa, K. S. Thushara, Biswajit Saha, Purushottam Chakraborty, C. M. Janet, R. P. Viswanath, C. Madhavan Nair, K. V. G. K. Murty and Chinnakonda S. Gopinath, *Chemistry of Materials* **21** (2009) 2973.

5) Structure, electronic Structure, optical and oxidation catalytic studies of solid solution of ZnS in $ZnO_{1-x}N_x$

   Maitri Mapa, Sivaranjani Kumarsrinivasan, Deu S. Bhange**,** Annamraju Kasi Viswanath, Biswajit Saha, Purushottam Chakraborty, and Chinnakonda S. Gopinath, *Chemistry of Materials* (communicated).

6) Synthesis and characterization of Nitrogen and Sulfur codoped ZnO.

   Maitri Mapa and Chinnakonda S. Gopinath, *Journal of Physical Chemistry C* (communicated).

7) Catalytic activity of $ZnO_{1-x}N_x$, $ZnO_{1-x-z}N_xS_z$, $(Zn_{1-z}Ga_z)(O_{1-x}N_x)$ and $(Zn_{1-z}In_z)(O_{1-x}N_x)$ towards alcohol dehydrogenation reactions.

   Maitri Mapa, Sivaranjani Kumarsrinivasan, Cimi Daniel and Chinnakonda S. Gopinath, *Applied Catalysis A: General* (Manuscripts under preparation)